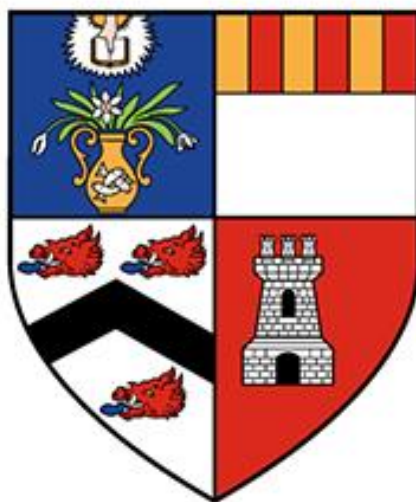**1 4 9 5**

An Investigation of the Structure and Properties of Novel Manganese Oxypnictides

Gaynor B. Lawrence

MChem, University of Aberdeen, UK

A thesis presented for the Degree of Doctor of Philosophy at the University of Aberdeen

Department of Chemistry

2021

Declaration

This thesis is submitted to the University of Aberdeen for the degree of Doctor of Philosophy. It is a record of the research carried out by the author, under the supervision of Professor Abbie C. Mclaughlin and the co-supervision of Dr Clemens Ritter. It has not been submitted for any previous degree or reward, and is believed to be wholly original, except where due acknowledgement.

<div align="right">Gaynor Lawrence</div>

<div align="right">Signed: GLawrence</div>

<div align="right">Date: 04/06/21</div>

"I am inevitable"

Thanos

"Happiness can be found in the darkest of places, if one only remembers to turn on the light"

Albus Dumbledore

"Even the smallest person can change the course of the future"

Galadriel

"You want weapons? We're in a library. Books are the best weapon in the world. This room's the greatest arsenal we could have. Arm yourself!"

The Doctor

"And I… am… Iron Man"

Tony Stark

Abstract

Oxypnictide materials have attracted significant research over the years due to their varying physical properties including superconductivity and colossal magnetoresistance (CMR) in iron and manganese pnictides respectively. $NdMnAsO_{1-x}F_x$ displays CMR, $Nd_{1-x}Sr_xMnAsO$ shows positive MR, and $PrMnAsO_{1-x}F_x$ has sizeable -MR below a structural transition. The presence of interesting properties within manganese pnictides warrants further investigation.

The layered 2322 structure, consisting of square planar oxide layers $(M(1)O_2)$ and tetrahedral pnictide layers $(M(2)_2Pn_2)$ separated by alkali earth ions, general formula $A_2M_3Pn_2O_2$, has been investigated. A sensitivity of the 2322 magnetic structure and ordering temperatures to the transition metal content is seen. $Sr_2Mn_2CrAs_2O_2$ crystallises in the tetragonal $I4/mmm$ space group and was found to contain cation ordering. Divalent chromium has a d^4 electronic configuration so, a combination of CFSE and Jahn-teller distortions results in the preferential square-planar arrangement (68% occupancy). The desired stoichiometry was not obtained, the formula of the product was $Sr_2Mn_{2.23}Cr_{0.77}As_2O_2$. There are two magnetic transitions present in the sample, the transition at 410 K is the ordering of $M(2)^{2+}$ ions into a G-type antiferromagnetic arrangement of spins parallel to the c lattice direction. Below 167 K the $M(1)^{2+}$ ions form a La_2CuO_4-like antiferromagnetic structure along the c lattice direction. A simultaneous reorientation of $M(2)$ spins occurs, forming a C-type AFM arrangement parallel to c. Both high temperature (AFM-HT) and low temperature (AFM-LT) magnetic structures are present between 167 and 135 K. At 160 K 59.8% of the sample is in the AFM-HT arrangement and 40.3% is in the AFM-LT arrangement. The magnetic phase coexistence is a result of two separate nuclear phases; the percentage occupancy of each phase matches to those of the two magnetic phases at 160 K (60:40%). One phase orders into the AFM-LT configuration at 167 K and the other at 135 K, this change in ordering temperature is due to different Cr/Mn content in the two different phases.

A novel insulator to insulator transition was discovered through the synthesis and study of a new 1111 arsenide family, $CeMnAsO_{1-x}F_x$. The transition is sensitive to sample stoichiometry, only occurring in samples when $x \geq 0.035$. The transition temperature (T_{MBL}) increases with fluorine content and small Ce deficiencies, is unaffected by As non-stoichiometry, and the transition is destroyed when Mn deficiencies are present. Like the iron arsenide superconductors, a link between

the transition and tetrahedral angle is observed. Increasing x results in the tetrahedral angles trending towards the ideal angle of 109.47°, with this the T_{MBL} increases. Prior to the new transition, the electronic behaviour of electron doped samples can be fitted to Mott 3D VRH behaviour (below 85 K). At the transition, the resistivity increases by 4 orders of magnitude before becoming immeasurable which indicates a loss of conductance at lower temperatures, as expected for a many-body localised state (MBL). AC conductance measurements displayed peak shifting with changing frequency confirming glassy behaviour in the system, a further indication of MBL. The magnetic structure in $CeMnAsO_{1-x}F_x$ series is unaffected by doping. Mn^{2+} ions form a C-type AFM arrangement of spins parallel to c at high temperatures (T_{Mn}, ~ 360 K) and undergo a spin reorientation at 34 K (T_{SR}) with spins parallel to the basal plane. Ce^{3+} ions also magnetically order at 34 K in the same arrangement as Mn^{2+} spins. Upon cooling, the crystal structure displays the usual cell contraction with a subtle anomaly at T_{SR}, so there is evidence of coupling between the nuclear and magnetic crystal structures. No connections between the nuclear or magnetic structure on cooling of $CeMnAsO_{1-x}F_x$ and the new insulating phase are observed.

Preliminary studies into 1111 oxyantimonides have been performed. The hole doped series, $Ce_{1-x}Sr_xMnSbO$ (x = 0 – 0.075), showed trends in the cell parameters indicating successful doping. The (Ce/Sr)O bond lengths decrease and the bond angles trend away from the ideal tetrahedral angle when Sr^{2+} content increases. Magnetic susceptibility measurements showed the spin reorientation transition at ~4 K in the $Ce_{1-x}Sr_xMnSbO$ series, as seen for the parent phase CeMnSbO, with the magnetic transition temperature unchanged through doping.

Publication List

1. "Electronic and Magnetic Properties of Cation Ordered $Sr_2Mn_{2.23}Cr_{0.77}As_2O_2$"- G. B. Lawrence, E. J. Wildman, G. B. G. Stenning, C. Ritter, F. Fauth and A. C. Mclaughlin, *Inorg. Chem.*, 2020, **59**, 7553-7560.

2. "Signatures of many body localisation in manganese-based layered compound, $CeMnAsO_{1-x}F_x$" – E. J. Wildman, G. B. Lawrence, S. Simpson, C. Ritter, G. B. G. Stenning, A. M. Arevalo-Lopez and A. C. Mclaughlin, in draft (to be submitted to *Nature*).

Acknowledgements

For the duration of this PhD, a great many people have been there to support and guide me along the way and without them this work would not have been possible. My first, biggest, and most heartfelt thanks has to be to my brilliant supervisor Abbie. She has been a fantastic advisor; with never wavering patience for me and she is truly a person I wholeheartedly wish to live up to some day in academia. I would also like to express my gratitude to Clemens Ritter, my excellent Institut Laue-Langevin (ILL) supervisor. He not only helped on all neutron experiments as the beam line scientist but also was a welcoming presence at a new research facility, his wealth of knowledge was truly inspiring.

I would next like to thank both the University of Aberdeen and the ILL for their financial support during the course of this PhD, for the ILL an extra thanks is due for the accepted neutron beam time. Thank you to ALBA synchrotron for the allocated beam time, as well as to Dr Francois Fauth for assistance running the experiments on the BL04-MSPD beamline. At ISIS neutron facility, Dr Gavin Stenning was key to all property measurements recorded, so I would like to show appreciation for his contributions.

Thank you to all of the members of the Solid State Chemistry group at the University of Aberdeen for all the help and friendship. Special thanks to Eve for helping me along the way in continuing your work, training me up in the lab, and thanks to Kirstie for being a terrific office mate and shoulder to lean on. Biggest thanks in the Aberdeen group to the lovely Struan who I may have labelled my replacement, but he is a truly great coworker, collaborator and amazing friend. Through the Solid State RSC Early Career Researcher meeting, a great support network was formed with some other early career solid state chemists. Together we have been there for one another and these fellow researchers have been so helpful while going through the write-up procedure of my PhD.

At the ILL, I was made welcome by a wonderful group of people, the ILL PhD student group. They all have such a diverse range of specialities that everyday something new could be learned. In France I shared an office with superb students who made every working day a joy, so a special thanks goes to Office 110. The amazing friends I made across there were an irreplaceable support

to me both scientifically and personally. Special notice to Marta, Murias and Mohamed for always looking out for me and supplying many laughs.

Finally I would like to say a massive thank you to my family for all their support and encouragement throughout the years: My mum Alwyn, my dad Alan and my brother Mark. Also thanks to my 'adopted family' Laura, my best friend in the world. She had to listen to me ramble on about my research for far too long, as well as support me through all personal struggles in this time. You are the best Simpson, thank you for everything.

Contents

Chapter 1

Introduction

The goal of this PhD research project was to synthesise, characterise and study the properties of new manganese oxypnictides. Pnictides are materials that contain pnictogen ions, from group 15 of the periodic table (Figure 1.1), the ions have three negative charge. Pnictide materials display interesting properties, and the following section is designed to introduce the properties in materials previously discovered.
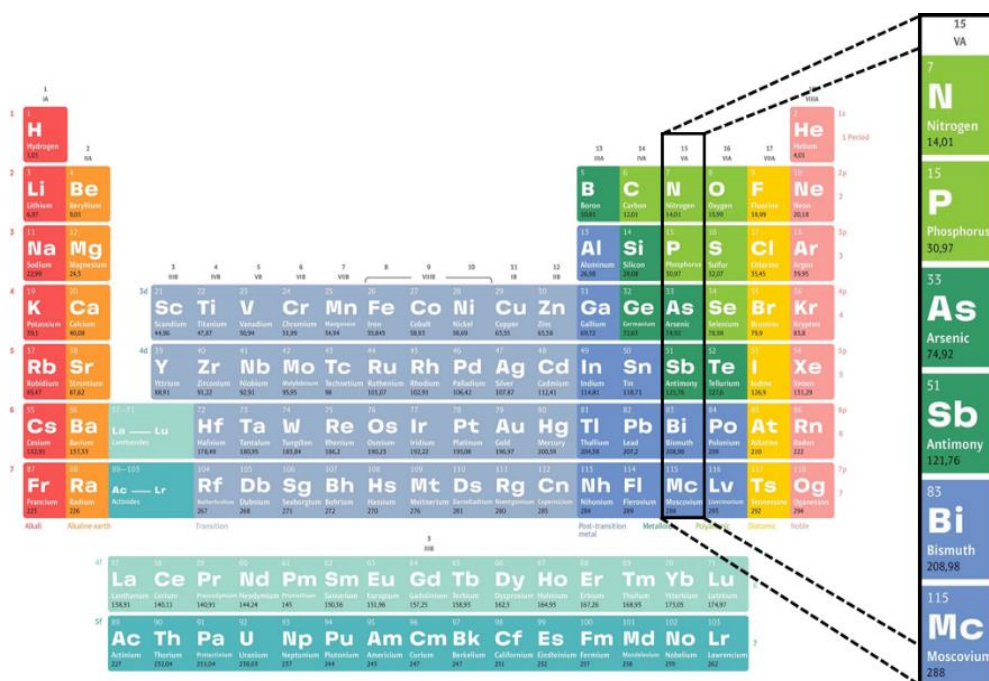
Figure 1.1: Periodic table of the elements with pnictogen column 15 highlighted[1].

1.1: Iron Pnictide Superconductivity

A surprise discovery was made in 1986 when the first high temperature superconducting transition (T_C) was observed in $La_{2-x}Sr_xCuO_4$, which then led to a large boom within the scientific community searching for other materials sharing the same behaviour. Numerous high T_C superconductors have since been found, most notably $YBa_2Cu_3O_{7-\delta}$ (YBCO) which was found in 1987 with T_C of 77 K[2]. Focus has since been shifted in finding different families of superconductors not containing copper oxide layers. The superconductivity of copper oxides is believed to be related to strong electron correlation linked with the transition metal ions, and so layered structures have been investigated as there is the ability to control the metal oxide layer carrier density. Multiple new superconductors have since been found working from this basis, unfortunately not with as high T_Cs, for example Sr_2RuO_4 [3] $T_C = 0.93$ K and KOs_2O_6 [4] $T_C = 9.6$ K.

1.1.1: 1111 Structure

In 2006 a new class of superconductor was discovered within the iron-based oxypnictide family, LaFePO[5]. Both pure and fluorine doped (6% on O site) LaFePO were investigated, reported as single phase. The pure structure is shown in Figure 1.2, first reported in 1995[6] sharing the ZrCuSiAs type structure known as 1111 type: LaFePO is composed of alternate layers of lanthanum oxide ($La^{3+}O^{2-}$) and iron phosphide ($Fe^{2+}P^{3-}$) in $P4/nmm$ space group. Lanthanum and phosphorus located on $2c$ Wyckoff site (¼, ¼, z), iron at $2b$ (¾, ¼, ½), and oxygen at $2a$ (¼, ¾, 0).
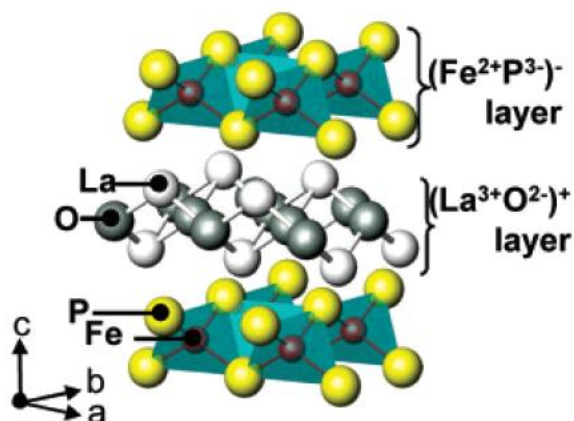
Figure 1.2: Crystal structure of superconducting LaFePO, crystallising in P4/nmm space group with alternating [LaO]$^+$ and [FeP]$^-$ layers[5].

Refinements performed on the structure showed that the FeP_4 tetrahedra are distorted resulting in two different P-Fe-P bond angles, 104.39(4) and 120.18(8)°. The structure is significantly different from previously well-known high T_C copper superconductors where Cu^{2+} occupies 4-fold square planar sites; the transition metal (Fe) instead occupies edge-sharing tetrahedra. Another key difference between these superconducting families is the determined Fermi levels. In LaFePO the Fermi levels are Fe^{2+} $3d_{xy}$ or $3d_{yz}/3d_{zx}$, rather than Cu^{2+} $3d_{x2-y2}$ in copper oxide superconductors[5]. The two superconducting families do share some qualities as both iron and copper superconductors have layered systems, the d electrons play a key role, and antiferromagnetic (AFM) order is close to superconducting transition in both phase diagrams[7]. Another trait shared by both family of superconductors is the occurrence of Jahn-Teller distortions in the structures[8,9].

Electrical resistivity measurements were performed on both pure and F-doped LaFePO samples (Figure 1.3). Both samples behave as a metal above 10 K. As the pure sample is cooled to below 5 K a sharp decrease in resistivity is seen, dropping to 0 at 3.2 K. The superconducting transition temperature is raised by F-doping and lowered by applying magnetic field indicating that the presence of magnetic field breaks the superconducting state. The zero-resistivity observed along with perfect diamagnetism confirm the presence of superconductivity in these materials.
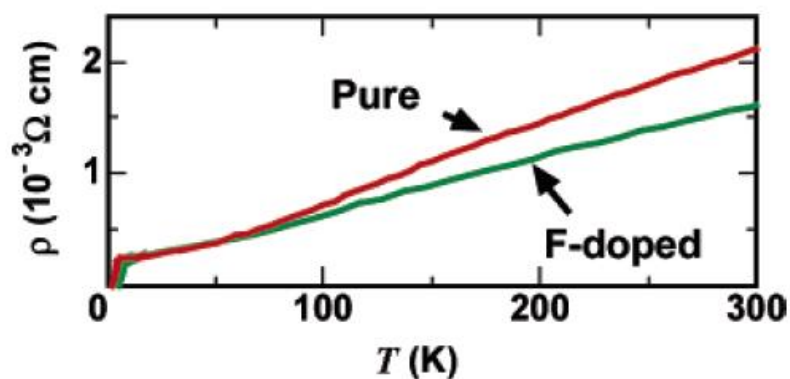
Figure 1.3: Electrical resistivity (ρ) versus temperature (T) for pure and F-doped LaFePO[5].

Chemical substitutions in this known superconducting structure has led to further discovery in the field, with $LaFeAsO_{1-x}F_x$ found to have zero resistance at 26 K[10]. LaFeAsO phase adopts the same structure as LaFePO phase, *P4/nmm* symmetry group, see Figure 1.4. The iron arsenide layers serve as a conduction path in $LaFeAsO_{1-x}F_x$ superconductor and are found sandwiched in the structure between lanthanide oxide layers.
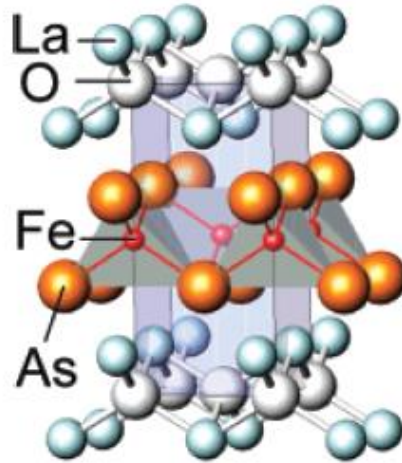
Figure 1.4: Crystal structure of LaFeAsO, displaying [La$_2$O$_2$]$^{2+}$ and [Fe$_2$As$_2$]$^{2-}$ layers[10].

Electrical resistivity measurements were performed finding that the undoped sample resistivity is not a superconductor, only the F-doped samples undergo a superconducting transition. Fluorine substitution onto the oxygen site (that results in superconductivity of this phase) is known as electron doping, as opposed to the hole doping which induced high temperature cuprate superconductivity. The substitution of fluorine for oxygen results in electron doping of the conducting iron arsenide layer. The fluorine content in the samples has to be above 4 atom % before a drop to zero resistance is observed. Electron doping into iron pnictide systems brings the number of iron 3d electrons closer to 3d electron number of cobalt in LaCoPnO (Pn = P, As), these are ferromagnetic materials with Curie temperatures of 34 and 59 K for P and As analogues respectively[11]. The transition temperature of electron doped LaFeAsO$_{1-x}$F$_x$ can be shifted to higher values through the application of pressure, with a maximum T$_C$ achieved of 43 K for 11 atom % under 4 GPa[12].

Fluorine has poor solubility, x < 0.2, into LaFeAsO structure as a stable impurity phase can form (LaOF), the high x region of the superconducting phase diagram therefore cannot be investigated in the LaFeAsO$_{1-x}$F$_x$ system[13]. Changing F$^-$ doping for H$^-$ into LaFeAsO allows for investigation of superconductivity at higher x values, x = 0.53[14]. Hydrogen substitutes into the lanthanum oxide layers also resulting in electron supply to the iron arsenide layers, so LaFeAsO$_{1-x}$H$_x$ is an electron doped system like LaFeAsO$_{1-x}$F$_x$. Superconductivity is observed for $0.08 \leq x < 0.53$, but interestingly there is a dip in the transition temperatures (x = 0.21) resulting in a two dome superconducting phase diagram, Figure 1.5.

4
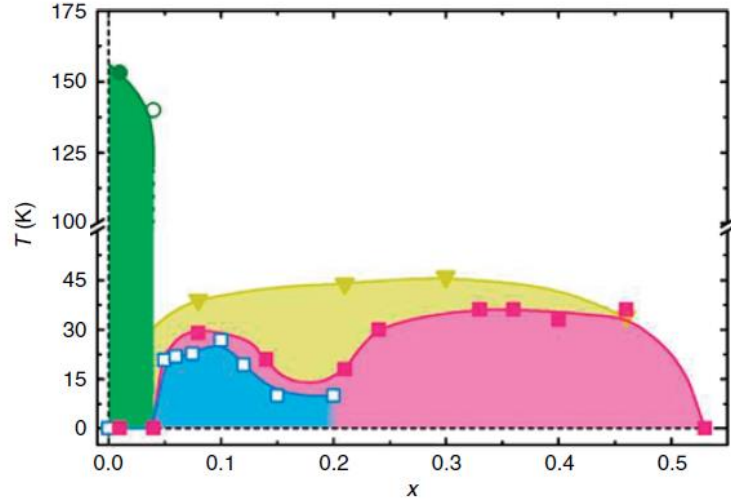
Figure 1.5: Electronic phase diagram for LaFeAsO$_{1-x}$H$_x$ (filled data points) and LaFeAsO$_{1-x}$F$_x$ (open data points). The superconducting transition temperatures displayed under ambient pressure (squares) and 3GPa (inverted triangles). The circle data points are from the kink observed in ρ-T curve at higher temperatures that is lost before superconductivity induced[14].

Within the first superconducting dome the highest T_C recorded is 29 K for x = 0.08 before a drop to 18 K for x = 0.21. The second superconducting dome appears for x > 0.21, this enhances the T_C to a maximum of 36 K for x ≈ 0.36, with superconductivity not seen above x = 0.53. The T_C enhancement under pressure is displayed in Figure 1.5. The highest T_C recorded under 3 GPa was 46 K for x = 0.3, so it is clear the double dome superconducting behaviour is lost under pressure and that transition temperature sensitivity to hydrogen content is lessened[14].

Hole doping into the LaFeAsO structure using calcium on the lanthanum site was found by Kamihara *et. al.*[10] to not show a superconducting transition. From these results it was deduced that electron doping is a critical factor for inducing superconductivity. A different study performed on La$_{1-x}$Sr$_x$FeAsO series[15] counters the argument of electron doping being key to superconductivity in LaFeAsO structure where tri-valent lanthanum is substituted for di-valent strontium. The hole doping nature of these samples was checked by measuring the Hall effect, the Hall resistivity of all Sr doped samples were positive convincing the researchers that it is indeed hole doped.
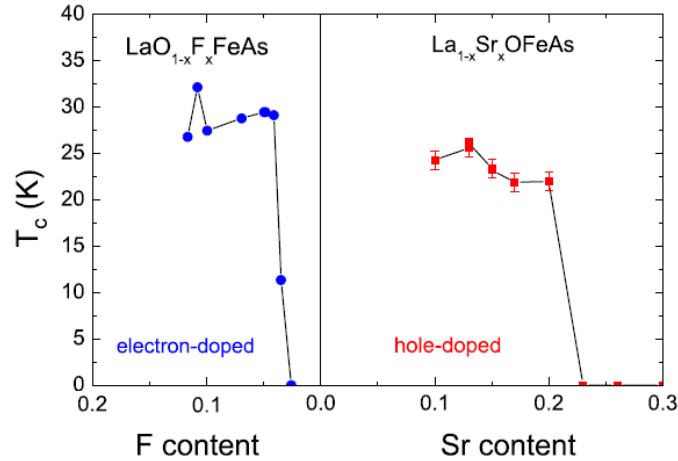
Figure 1.6: Phase diagram of the two doped LaFeAsO systems: electron doping (left) using fluorine on oxygen site and hole doping (right) using strontium on the lanthanum site[15].

For the $La_{1-x}Sr_xFeAsO$ series, as the strontium content increases the *a* and *c* lattice parameters grow, especially along *c*. The growth of the crystal lattice is expected as the ionic radius of Sr^{2+} is 1.12 Å, larger than La^{3+} radius (1.06 Å). The onset of superconductivity is stable in $La_{1-x}Sr_xFeAsO$ for x values 0.1 to 0.2, with the transition no longer observed for x > 0.23. The highest T_C is observed in $La_{0.87}Sr_{0.13}FeAsO$, the onset of superconductivity is at 25.6 K and zero resistance at 15 K. The superconducting transitions are broad in these samples, attributed to the presence of impurities. Even with this discovery of a hole doped system, electron doped LaFeAsO maintains the higher T_C and is the more optimal doping choice to induce superconductivity. Looking at the phase diagrams for both electron and hole doped LaFeAsO systems, Figure 1.6, it can be seen that the behaviour is very close to that of the cuprates[15].

Other 1111 pnictides like the aforementioned LaFePnO (Pn = P or As) using different rare earth elements (Lanthanide, *Ln*) have been synthesised and studied with general formula $LnFeAsO_{1-x}F_x$. The same layered structure is adopted by all of these materials, with tetrahedral FeAs layers present in every case.

The first non-cuprate superconductor to have a T_C above 50 K was reported as $PrFeAsO_{1-x}F_x$[16]. Samples were prepared under high pressure and resistivity measurements were performed with 0 and 9 T applied magnetic field. The temperature dependence of resistivity for 11 atom % fluorine doped PrFeAsO sample is shown in Figure 1.7. These results clearly show a drop of resistivity at

52 K and unmeasurable at 44 K. Application of a magnetic field lowers the zero transition to 35 K with the onset of superconductivity not visibly shifting.
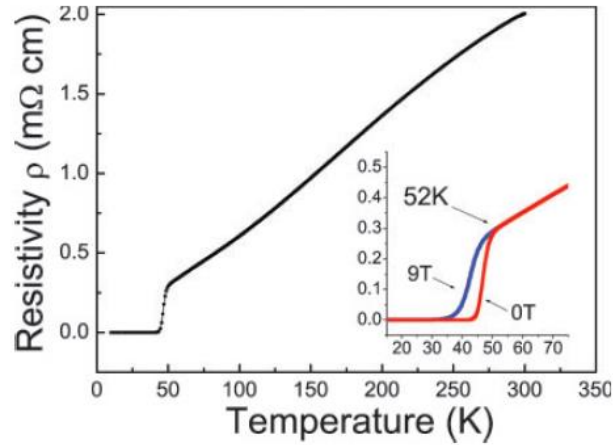
Figure 1.7: Temperature dependence of resistivity for PrFeAs[$O_{0.89}F_{0.11}$] superconductor[16].

Magnetisation measurement performed on $PrFeAsO_{0.89}F_{0.11}$ (Figure 1.8) show sharp magnetic transitions; this behaviour indicates that this superconductor is of high quality. The differential ZFC curve displays the onset of the diamagnetic transition at around 50 K. At 5 K the diamagnetic shielding signal is around 90%, indicating that the new $PrFeAsO_{0.89}F_{0.11}$ material has bulk superconductivity.
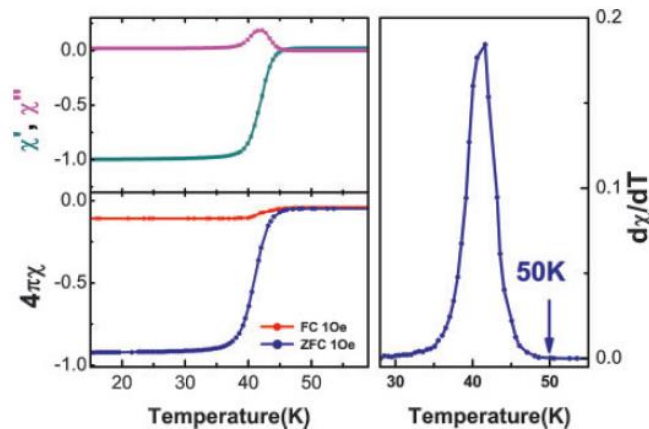
Figure 1.8: $PrFeAsO_{0.89}F_{0.11}$ temperature dependence of ac susceptibility, dc susceptibility and differential ZFC curve[16].

Multiple other LnFeAsO$_{1-x}$F$_x$ superconductors have been found; Ln = Nd, Ce, Sm[17,18,19]. The samarium analogue of the 1111 iron pnictide structure has the highest critical temperature among all known materials to this date outside of copper oxide family. Undoped SmFeAsO resistivity does not drop to zero at any point and therefore the parent compound in this case is not a superconductor. A high T$_C$ of 55 K is reported by Ren *et. al.*[19] for the 10 atom % fluorine doped samarium sample, however, due to the synthesis method used the real F-doped level is lower than nominal as fluorine is lost during the high pressure process.

Samarium has a smaller covalent radius compared to the other lanthanides discussed (La, Ce, Pr and Nd) the crystal lattice for SmFeAsO$_{1-x}$F$_x$ is therefore reduced in size. It was proposed that the increased internal chemical pressure caused by the shrunken lattice is a key factor in enhancing T$_C$[20]. Calculations carried out linked improvement of T$_C$ to increasing hopping integral, a way of doing such is through the shrinkage of crystal lattice[21], and so these Sm findings agree with the calculated model.
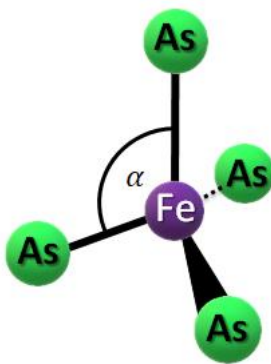
Figure 1.9: Depiction of an iron arsenide tetrahedron, with α bond angle highlighted. A regular tetrahedron is present when α = 109.47°.

An interesting feature of iron superconductors is that they display strong correlations between superconducting transition temperatures and crystal structure. As previously stated, *Ln* ion size changes the internal chemical pressure impacting the T$_C$, however, the FeAs$_4$ tetrahedral shape is believed to be a more important factor[22,23]. The transition temperature is highest when a regular FeAs$_4$ tetrahedron is attained, with α As-Fe-As bond angle of 109.47°; see Figure 1.9 for diagram of iron arsenide tetrahedra with alpha bond angle labelled. Figure 1.10 displays numerous known

iron superconductor transition temperatures plotted against the α bond angle. It is clear that close proximity of As-Fe-As angle to regular tetrahedron arrangement results in the highest T$_C$ values.
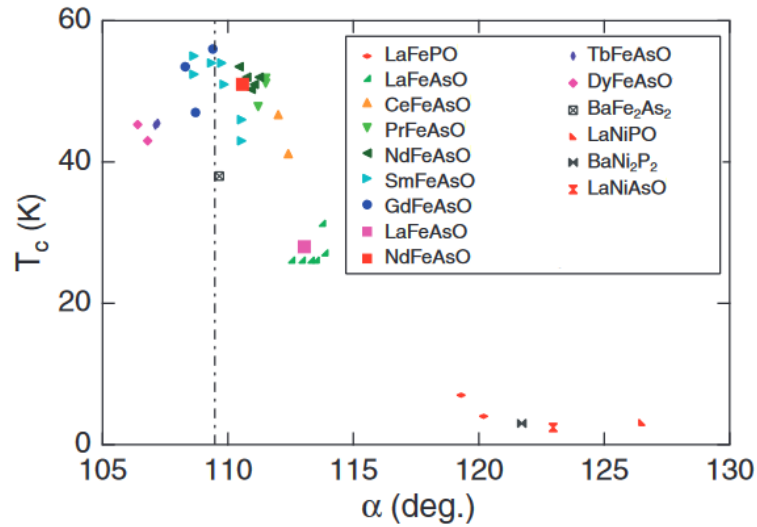
Figure 1.10: Superconducting transition temperature vs α As-Fe-As bond angles for various pnictide superconductors, displaying a clear correlation between regular tetrahedron arrangement (α = 109.47°) and high T$_C$[22].

1.1.2: Other Structure Types

Multiple other structure types have been found to exhibit superconductivity, each sharing the FeAs planes of aforementioned *Ln*FeAsO materials as basic building blocks. The three families with recorded superconducting transitions are 111, 122 and 21311(42622) types (see Figure 1.11), with FeAs layers sandwiched between other layers that influence the electrical properties of the system[24].
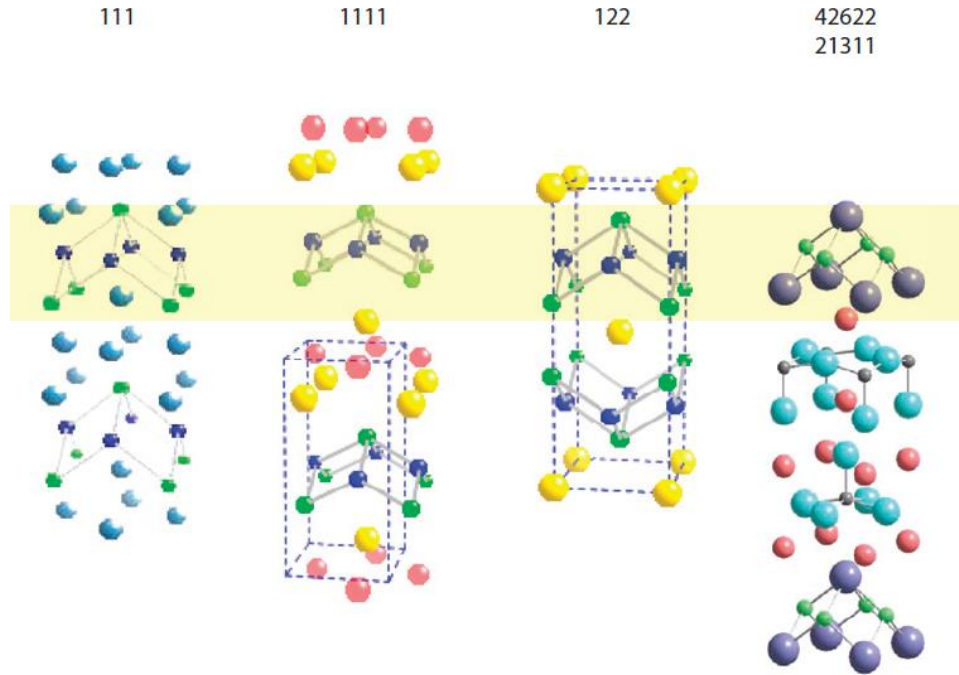
Figure 1.11: Families of confirmed iron superconductors, FePn (Pn = P or As) highlighted regions for each structure all with the same geometry[24].

Starting with the 111 geometry, superconductivity is present in the undoped LiFeAs sample[25]. LiFeAs crystallises into the tetragonal *P*4/*nmm* space group making it isostructural with PbFCl, it is similar to an 'empty' variant of LaFeAsO with $[Fe_2As_2]^{2-}$ layers containing edge-sharing tetrahedra. The pure material had a recorded transition temperature $T_C = 18$ K. The large negative thermoelectric power (around -20 µV/K) of LiFeAs indicates that the major current carriers in the system are electrons, as reported for *Ln*FeAsO systems.

A lower transition temperature for LiFeAs was reported by Wang *et. al.*[26] The superconducting onset transition temperature was found to be 16 K for the pure sample, with an 18 K transition temperature recorded for a lithium deficient $Li_{0.6}FeAs$ sample. These lower transition temperatures were disregarded by Tapp *et. al.*, thought to be a result of the non-stoichiometry, whereas their LiFeAs sample had 1:1:1 content verified through powder and single crystal x-ray diffraction, as well as ICPMS measurements.
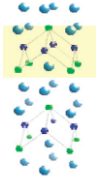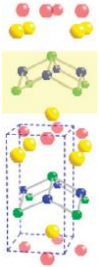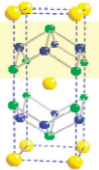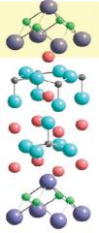
The 122 structure (Figure 1.11) is obtained through replacing the $(Ln_2O_2)^{2+}$ layers in the 1111 structure with a single large *A* atom (*A* = Sr, Ba), leading to the body-centered $ThCr_2Si_2$ structure. The *A* atom is divalent to maintain the same electron count[27]. Doping into AFe_2As_2 systems leads

to superconductivity with multiple examples found so far, such as $(Ba_{1-x}K_x)Fe_2As_2$[28], $Ba(Fe_{1-x}Co_x)_2As_2$[29], and $SrFe_{2-x}M_xAs_2$ (M = Rh, Ir, Pd)[30]. The highest T_C recorded in the 122 family was 39 K for $(Ba_{1-x}K_x)Fe_2As_2$ with x = 0.4 which introduces holes into $(Fe_2As_2)^{2-}$ layers. High doping levels through substitution of 30-40% barium ions with potassium is known to be possible as KFe_2As_2 is stable. The parent compound $BaFe_2As_2$ undergoes a structural and magnetic transition at 140 K, changing from the tetrahedral $I4/mmm$ space group to the orthorhombic space group $Fmmm$. No broadening or splitting of diffraction peaks are observed in the $Ba_{0.6}K_{0.4}Fe_2As_2$ sample and from this it is apparent that potassium substitution into the structure supresses the structural transition. The lack of a structural transition allows $Ba_{0.6}K_{0.4}Fe_2As_2$ to undergo a superconducting transition with zero resistance recorded at 37.2 K[28]. The parent compound $BaFe_2As_2$ contains distorted tetrahedral with α As-Fe-As bond angle of 111.1°. Introduction of potassium into the system decreases this angle towards the value of a regular tetrahedron which, as mentioned in previous section, increases superconducting transition temperatures[23].

The final family is the so-called 21311-type or 42622-type (Figure 1.11). This structure consists of FePn layers separated by perovskite type $M_4M'_2O_6$ layers. Two examples of such layered materials found to exhibit a superconducting transition are $Sr_4V_2O_6Fe_2As_2$[31] and $Sr_4Sc_2O_6Fe_2As_2$[32]. Both samples crystallise in $P4/nmm$ space group with very large c values; 15.6732 Å and 15.543 Å for $Sr_4V_2O_6Fe_2As_2$ and $Sr_4Sc_2O_6Fe_2As_2$, respectively. Large c values means larger distances between the iron pnictide planes. $Sr_4Sc_2O_6Fe_2P_2$ was discovered first, exhibiting superconductivity below 17 K, a higher transition temperature recorded than in the other non-arsenide iron superconductor LaFePO[32]. After this new structure was shown to display superconductivity, further research occurred and $Sr_4V_2O_6Fe_2As_2$ was investigated. This undoped sample has a superconducting transition at 37.2 K. The onset transition temperature shows very little movement in response to a field up to 9 T, the temperature of zero resistance shifts to lower temperatures rapidly with application of field, broadening the superconducting transition. The broadening effect implies that there is the presence of some weak superconducting link between individual grains of the sample. The 21311/42622 system does not require doping to induce superconductivity, like LaFeAs and LaFePO. The ability for un-doped $Sr_4V_2O_6Fe_2As_2$ to superconduct is theorised to be due to one of a few reasons. The oxygen content is easily controlled in the 21311 system, as there are multiple occupying sites, so slight deficiency of oxygen sites results in electron doping into the iron pnictide

layers resulting in superconductivity[31]. Vanadium can vary in valence and this leads to doping to the system, which could also be responsible for tuning superconductivity in $Sr_4V_2O_6Fe_2As_2$[31].

Table 1.1: Summary of superconducting iron pnictide families, T_C is the superconducting onset temperature, x column containing doping levels with highest T_C.

Structure type	Formula	T_c (K)	X
111	LiFeAs[25]	18.0	
1111	LaFePO[5]	5	
	$LaFeAsO_{1-x}F_x$[10]	> 30	0.11
	$LaFeAsO_{1-x}H_x$[14]	36	0.36
	$La_{1-x}Sr_xFeAsO$[15]	25.6	0.13
	$PrFeAsO_{1-x}F_x$[16]	52	0.11
	$NdFeAsO_{1-x}F_x$[17]	51.9	0.11
	$CeFeAsO_{1-x}F_x$[18]	41.0	0.16
	$SmFeAsO_{1-x}F_x$[19]	55	0.10
122	$(Ba_{1-x}K_x)Fe_2As_2$[28]	39	0.40
	$Ba(Fe_{1-x}Co_x)_2As_2$[29]	23	0.07
	$BaFe_{2-x}Rh_xAs_2$[30]	21.9	0.25
	$BaFe_{2-x}Ir_xAs_2$[30]	24.2	0.43
	$BaFe_{2-x}Pd_xAs_2$[30]	8.7	0.15
21311 **(42622)**	$Sr_4V_2O_6Fe_2As_2$[31]	37.2	
	$Sr_4Sc_2O_6Fe_2P_2$[32]	17.0	

1.1.3: Unconventional Superconductivity

Discoveries in the field of iron superconductors found that the superconductivity pairing was not through conventional electron-phonon coupling means[33]; superconductivity is the result of an unconventional mechanism created by electron-electron Coulomb interactions. Bardeen, Cooper and Schrieffer (BCS) described the phenomenon of conventional superconductivity in 1957[34], in which electrons pair up (so-called Cooper pairs) through an attractive interaction accompanied by a phonon. As seen in Figure 1.12a, movement of the first electron results in a lattice distortion (a phonon), this movement causes an attraction of a second electron with opposing momentum, p. Coulomb repulsion is avoided in this interaction as an electron pair is formed with time delay separation[35]. Figure 1.12b displays unconventional SC, where the electron pairs form through attractive interactions. Coulomb repulsion is avoided in this instance through opposing relative motion of the electrons. These electron pairs are favoured between electrons of different sites, pairings are unfavourable between electrons occupying the same site as the dominant interaction occurring is repulsion.
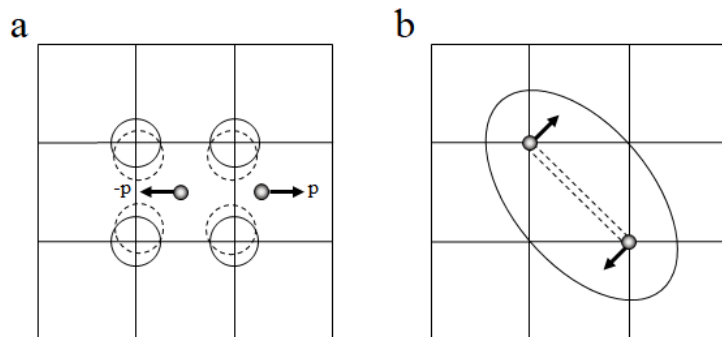
*Figure 1.12: Visible representation of electron motion in **a** conventional and **b** unconventional superconductivity[35].*

Electron-phonon coupling does not fully equate for the high T_c measured for $LaFeAsO_{1-x}F_x$ samples. Conventional superconductivity is therefore not sufficient to explain SC in the FeAs family, the superconductivity pairing in iron superconductors is as a result of unconventional pairing through electron-electron Coulomb interactions[35]. Iron superconductors have two key characteristics, which provide an indication of the unconventional superconductivity mechanism. Firstly, in FeSCs, from the phase diagram it is seen that superconductivity appears out of a 'bad-

metal' normal state. The second characteristic is that the SC phase occurs near the start of antiferromagnetic order. It is due to the presence of unconventional SC that iron pnictides have been extensively studied, with focus into the electron correlations and magnetism. As with the high T_C cuprate superconductors, the definitive theory of superconductivity in iron arsenides remains unknown.

1.2: Other Transition Metal Pnictides

1.2.1: 1111 Structure

After the successful discovery of high temperature superconductivity in the iron pnictides, other transition metal pnictide compositions were investigated based on the families of materials previously discussed. Replacing Fe with Cr, Co, Ni, and Zn results in differing electronic and magnetic properties of the 1111 family, with most crystallizing in the *P4*/*nmm* space group shown in Figure 1.13 . The nickel analogues display superconducting transitions at low temperatures; the other transition metal pnictides in this family do not.
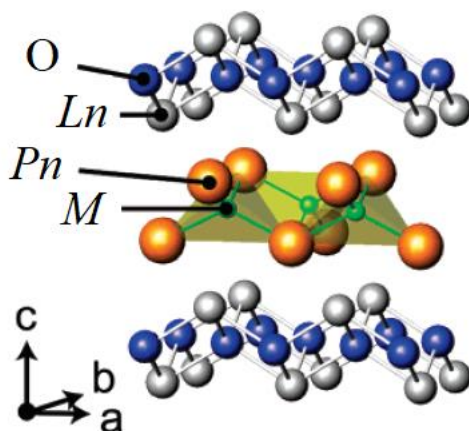
Figure 1.13: Structure of majority 1111 LnMPnO materials, crystallising in the P4/nmm tetrahedral symmetry group[36].

LaNiPO, first studied in 2007[36], crystallises in the *P4*/*nmm* structure displayed above, as do all known 1111 nickel pnictides. The NiP_4 tetrahedra are distorted with two different P-Ni-P angles

of 101.7° and 126.4°. The electrical resistance of LaNiPO was very low (1.2 mΩ.cm) at 300 K, exhibiting metallic behaviour from high temperature down to 4 K. At 4 K the electrical resistance begins to drop, with zero resistance recorded at around 2 K. With the application of an external magnetic field, the onset transition temperature shifts to lower values, with complete destruction when a 10000 Oe field is applied. The magnetic susceptibility for LaNiPO was small and almost independent of temperature from 300-4 K implying Pauli paramagnetism behaviour, the susceptibility begins to drop to negative values at around 3 K. Both electrical resistivity and magnetic susceptibility findings together agree that the material exhibits superconductivity below 4 K.

The arsenide analogue of LaNiPnO displays similar behaviour to LaNiPO, with metallic conduction behaviour at high temperature and superconducting with a T_C of 2.4 K[37]. The NiAs$_4$ tetrahedra are also distorted, more planar than regular tetrahedra, with As-Ni-As bond angles of 122.95° and 103.18°. The temperature dependence of electrical resistance for LaNiAsO was measured, revealing that the material shows metallic behaviour down to 2.4 K. The resistivity started to decrease at 2.4 K with zero resistance recorded at 2 K. Much like LaNiPO, the application of magnetic field shifted the superconducting transition temperature to lower values. The magnetic susceptibility of LaNiAsO was also nearly independent of temperature between 305 and 2.4 K, indicating Pauli paramagnetism, like in LaNiPO. At 2.4 K, the susceptibility starts decreasing, becoming negative. These results alongside the zero resistance denote a superconducting transition at 2.4 K.

LnNiAsO (Ln = Ce, Pr, Nd and Sm) parent compounds have been investigated[38, 39]. Superconductivity in the undoped LnNiAsO phases has only so far been observed in La and Pr systems. PrNiAsO has a recorded superconducting transition T_C of 1.6 K[40]. CeNiAsO does not show evidence of superconductivity down to 30 mK[38], and while there are no local magnetic moments on the nickel ions there are two antiferromagnetic transitions related to cerium ions. The cerium moments are reported to align in G-type antiferromagnetic arrangement with T_{N1} = 9.3 K, which changes to a C-type antiferromagnetic arrangement at T_{N2} = 7.3 K. G-type antiferromagnetism is when all nearest neighbour spins are antiferromagnetically aligned, both intraplanar and interplanar, in a layered structure. In C-type antiferromagnetically ordered systems the spins align antiferromagnetically intraplanar but align ferromagnetically interplanar. Sm and

15

Nd analogues both also only display AFM ordering, SmNiAsO has a T_N of 3.5 K and NdNiAsO is paramagnetic down to 2 K with a local AFM transition below 1.3 K[39].

Based on the success of electron doping into the LnFePnO system, which results in shifts of the superconducting transitions to higher temperatures, the same approach was undertaken on the LnNiAsO system. LaNiAsO$_{1-x}$F$_x$ (x = 0 – 0.15) showed only a slight increase in T_C from the pure material (Figure 1.14), however, the partial fluorine substitution greatly increases superconducting quality[41]. The highest T_C for this series recorded was 3.8 K for LaNiAsO$_{0.9}$F$_{0.1}$. Although not a large increase from 2 K recorded for the pure sample the transition width (~0.05 K) is much narrower than other superconductors in the same family, so the superconducting quality is better.
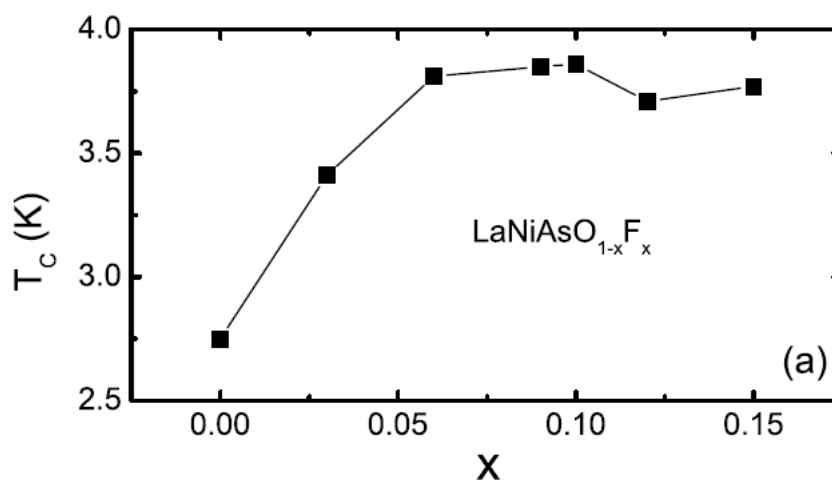
Figure 1.14: Transition temperature evolution with partial substitution of fluorine onto oxygen site in LaNiAsO[41].

Hydride substitution into LnNiAsO systems found behaviour much like fluorine doping for the lanthanum analogue; the transition temperature of LaNiAsO was increased to 3.7 K for hydride levels x = 0.07-0.17. At higher hydride levels the superconducting transition temperature quickly decreased, T_C = 1.7 K at x = 0.18. The other LnNiAsO samples (Ln = Ce, Pr, Nd) showed no increase to superconducting transition above 2 K or appearance of SC in the non-superconducting samples[40].

1111 zinc pnictide materials show differing properties to the iron and nickel pnictides, including not all samples crystallising in the tetragonal $P4/nmm$ space group. LnZnPnO (Pn = P, As, Sb)

were prepared and studied by Takano *et. al.*[42] finding that for *Ln*ZnPO (Ln = La and Ce), all *Ln*ZnAsO, and all *Ln*ZnSbO samples the *P*4/*nmm* space group adopted. The other lanthanide compounds in *Ln*ZnPO family have significantly different symmetry, belonging to the trigonal *R*$\bar{3}$*m* space group, Figure 1.15. The lattice parameters of all samples studied decreased linearly with reducing *Pn* and *Ln* ionic radii size. Looking into the electrical resistivity of these materials found no superconductivity, and the resistance decreases with atomic number of *Pn*. For the arsenide materials, a maximum resistivity is reached for *Ln* = Ce and then lowers with atomic number or *Ln*, the resistivity simply decreases with *Ln* atomic number for the zinc antimonides. Semiconducting behaviour is observed for *Ln*Zn*Pn*O (*Ln* = La, Ce, Pr, *Pn* = P, As), a metal to semiconducting electronic transition is observed for *Ln*ZnSbO (*Ln* = La, Ce), and NdZn*Pn*O (*Pn* = As, Sb) become metallic. The lanthum zinc pnictides investigated are diamagnetic materials; all other zinc 1111 pnictides are paramagnetic[42]. The effective magnetic moments of samples measured deviated from the free ion values of trivalent lanthanides. A correlation was observed between this deviation and a decrease in the electrical resistivity suggesting that the 4f electrons supply conduction electrons to the zinc pnictides. A further study into the zinc arsenide materials magnetic behaviour reported *Ln* = Ce, Pr and Nd analogues display Curie-Weiss behaviour above 100 K. SmZnAsO magnetic susceptibility does not follow a Curie-Weiss law with the susceptibility not following a linear trend, this is not unexpected as Sm^{3+} is a Van Vleck paramagnetic ion. Antiferromagnetic ordering of Sm and Gd – ZnAsO is observed at 4.6 and 3.4 K respectively, this work also reported no magnetic ordering of *Ln*ZnAsO (*Ln* = Ce, Pr, Nd)[43].
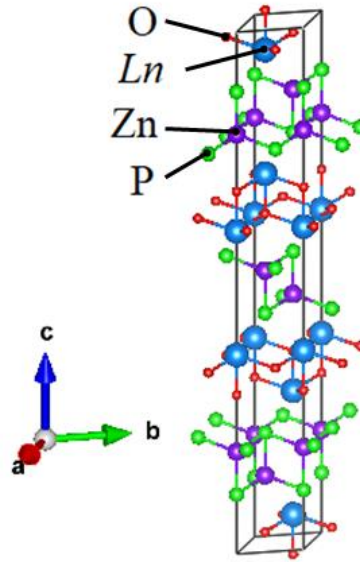
Figure 1.15: Crystal structure for LnZnAsO analogues crystallising in $R\overline{3}m$ space group[42].

Ferromagnetism is present in layered cobalt oxypnictides *LnCoPnO*[44,45] all crystallising in the *P*4/*nmm* space group. For LaCo*Pn*O (*Pn* = P, As) the lattice constants grow with increasing pnictide atomic radius and both compounds show no superconductivity with metallic behaviour observed down to 3 K[44]. Both samples are ferromagnetic with Curie temperatures of 34 and 59 K for P and As derivatives respectively, and this ferromagnetic arrangement of cobalt ions is thought to prevent superconductivity. A series of different lanthanide CoAs based ferromagnetic materials showed a dependence of the magnetic properties on the lanthanide ion[45]. As expected, the lattice constants of *Ln*CoAsO decrease with shrinking Ln^{3+} ion size with *Ln* = La-Gd investigated. Figure 1.16 displays the magnetisation of *Ln*CoAsO materials versus temperature; LaCoAsO magnetisation rapidly increases around 55 K indicating a ferromagnetic transition. The other lanthanide samples show a fast increase in magnetisation with a peak at around 70 K, revealing the ferromagnetic transitions occur at higher temperatures in these other lanthanide samples. CeCoAsO shows a second increase in magnetisation below 45 K, denoting a two-step transition exists. The sharp drop in magnetisation for *Ln* = Nd, Sm and Gd is a ferromagnetic-antiferromagnetic transition (FAFT)[45].
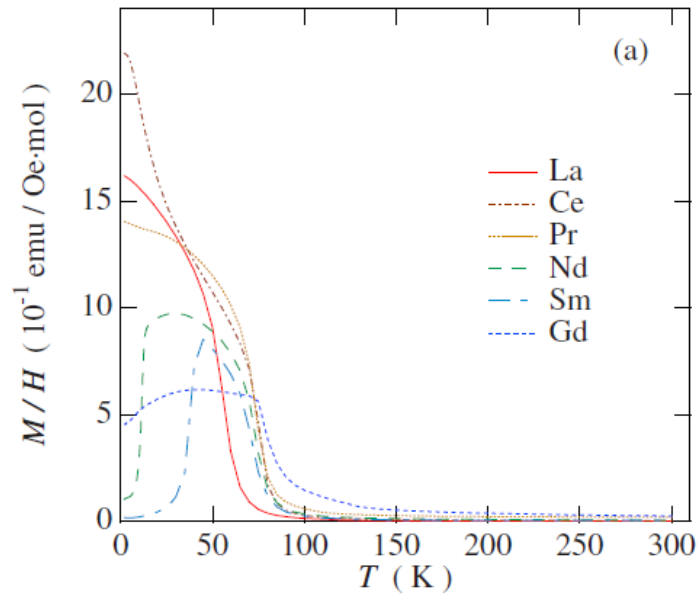
Figure 1.16: Temperature dependent magnetisation plot for LnCoAsO system with 1 kOe field, field cooled measurements for all Ln analogues excluding Ce[45].

The iron superconductors display strong electron correlations and antiferromagnetic ordering, so an ideal candidate for superconductivity in 1111 pnictide materials is thought to be a sample containing these two properties. Divalent chromium has a $3d^4$ electron configuration and a large magnetic moment, giving rise to strong electron correlation in *Ln*CrAsO system[46]. *Ln*CrAsO materials looked at so far do not show superconductivity, despite meeting the previously mentioned criteria. LaCrAsO displayed a metallic-type conduction; with an antiferromagnetic transition below 550 K into a G-type magnetic ordering of Cr spins parallel to *c* axis. Manganese doping on the chromium sites of LaCrAsO resulted in the appearance of a metal to insulator transition.

1.2.2: Other Structure Types

Multiple other crystal structures that showed superconductivity with iron pnictides have been investigated with different transition metals on the iron sites, including the 122 structure previously discussed (Figure 1.17).
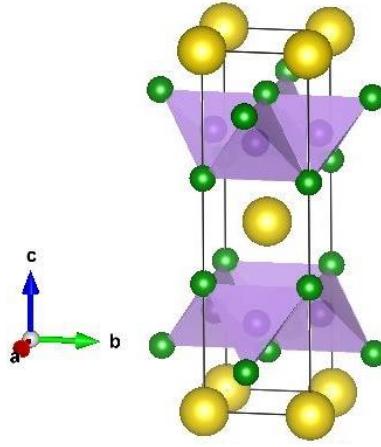
Figure 1.17: 122 crystal structure AM_2As_2, where A = alkali earth (yellow) or lanthanide and M = transition metal (purple). All samples discussed crystallise in this I4/mmm crystal structure.

Superconductivity is present in $BaNi_2As_2$ and $SrNi_2As_2$ samples without the need of doping into the structure[47,48]. $BaNi_2As_2$ goes through a first order phase transition at 130 K upon cooling, confirmed through resistivity and specific heat measurements thought to be a mixed magnetic and structural transition. Resistivity, ac-susceptibility and heat capacity measurements confirmed the presence of superconductivity at low temperatures. Bulk superconductivity onset is recorded at 1.5 K in the resistivity data with a drop to zero at 0.7 K for $BaNi_2As_2$[47]. $SrNi_2As_2$ displays bulk superconductivity at $T_C = 0.62$ K[48]. The resistivity measurements of $SrNi_2As_2$ did not show any sign of a structural transition below 400 K. It was interesting that the transition temperature was not significantly different between Ba- and Sr- analogues of 122 nickel arsenide. The two structures have different structural parameters given Sr^{2+} ions are smaller in size than Ba^{2+} ions, also there is a possible magnetic transition present in the $BaNi_2As_2$ sample not seen in $SrNi_2As_2$ but this does not appear to effect the superconductivity of the system[48].

Other transition metal 122 arsenides studied so far do not show superconductivity but have interesting magnetic structures. $LnCo_2As_2$ (Ln = La, Ce, Pr, Nd) samples prepared all showed ferromagnetic ordering of the cobalt magnetic moments along the tetragonal c axis at high temperature, $LaCo_2As_2$ has the highest transition temperature of 178 K[49]. The Ln sublattice orders magnetically at lower temperatures antiparallel to the cobalt moments, resulting in a ferrimagnetic (FiM) ground state for all $LnCo_2As_2$ samples studied. ACr_2As_2 (A = Ba, Sr)[50,51] were found to order magnetically at much higher temperatures. A study into $BaCr_2As_2$ discovered a transition into the

antiferromagnetic G-type structure of chromium ions along c axis at $T_N = 580$ K, with ordered magnetic moment of $\mu_{Cr} = 1.9$ μ_B at 2 K[50]. SrCr$_2$As$_2$ also displays G-type antiferromagnetic ordering of Cr^{2+} moments along c below $T_N = 590$ K, the ordered moment is $\mu_{Cr} = 1.9$ μ_B at 12 K. The G-type antiferromagnetic structure of chromium arsenides is displayed in Figure 1.18[51]. A mixed Cr/Fe sample BaCrFeAs$_2$ was studied, with random distribution of Cr and Fe within the transition metal sites. BaCrFeAs$_2$ also has a transition into G-type order of transition metal ions, however, at a lower temperature of 265 K and $\mu_{Cr/Fe} = 1.1$ μ_B where chromium dominates the ordered moment, only a very small contribution is associated to iron ions[50]. Antiferromagnetic ordering is unfavourable for irom magnetic moments and so the overall magnetic moment decreases with increasing iron content[50].
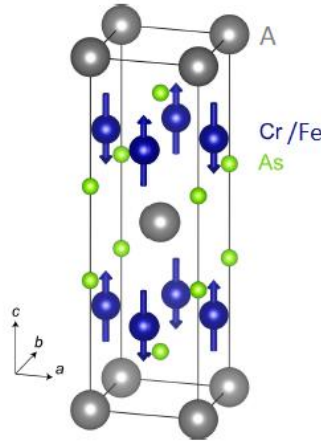
Figure 1.18: Nuclear and magnetic structure of ACr$_{2-x}$Fe$_x$As$_2$ (A = Ba, Sr) samples, with G-type antiferromagnetic order of Cr^{2+} magnetic moments. All magnetic moments are aligned antiparallel with all nearest neighbours[51].

A new multilayer structure for transition metal arsenides not discussed for iron superconductors is the 2322 family, with general formula $A_2M_2As_2O_2$ (A = Sr, Ba, M = transition metal). The crystal structure of 2322 materials is shown in Figure 1.19. It can be seen that there are two distinct transition metal layers stacking along the c axis with alkali earth metal cations distributed between them. The first transition metal site M(1) is within MO$_2$ layers, like CuO$_2$ layers in copper oxide superconductors; the second site M(2) is within tetrahedral M$_2$As$_2$ layers, like the Fe$_2$As$_2$ layering in iron superconductors. Due to the layering matching that of two superconducting families, the

2322 system is theoretically a good basis for superconductivity[52]. Manganese analogues of 2322 structure were studied in 1991 but these will be discussed in a later section.
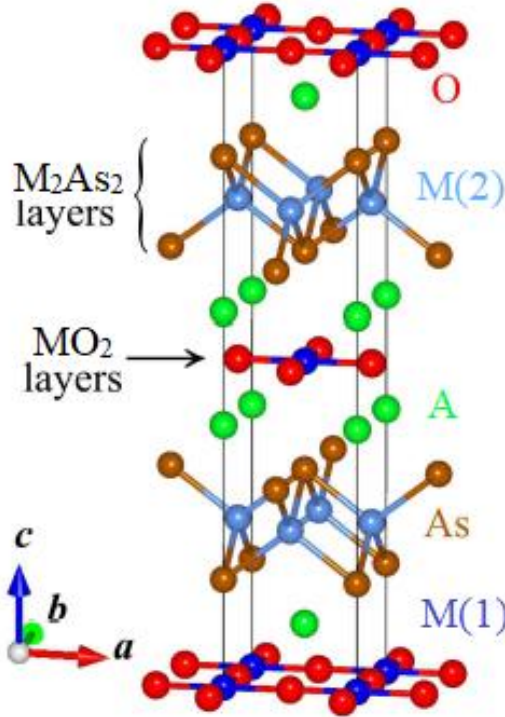
Figure 1.19: Structure for $A_2M_2As_2O_2$ materials, A = Sr, Ba, M = transition metal. Two transition metal layering types are labelled, the first M(1) is in square planar MO_2 arrangement, and other M(2) in tetrahedral M_2As_2 order[52].

$Sr_2Cr_3As_2O_2$ crystallises in the structure shown above with the *I4/mmm* space group[52]. It was originally of interest as a possible superconductor but superconductivity has not been observed under ambient pressure. Neutron diffraction experiments conducted revealed the magnetic structures of $Sr_2Cr_3As_2O_2$, which undergoes two magnetic transitions. At 590 K the $Cr(2)^{2+}$ ions in Cr_2As_2 layers order in a C-type antiferromagnetic arrangement along the *c* axis. At 300 K the calculated magnetic moment is 1.97(4) μ_B per Cr(2) ion. Below 291 K there are additional magnetic Bragg peaks in the diffraction pattern, the $Cr(1)^{2+}$ ions within the oxide planes form long-range antiferromagnetic ordering of the moments along the *c* direction, the lattice forms a K_2NiF_4 type antiferromagnetic ordering[53]. The Cr(1) magnetic moment ordering results in a spin flip of the Cr(2) ions to no longer be along *c*, now ordering in the *ab* plane, the two magnetic structures (high

22

and low temperature) are presented in Figure 1.20. At 4 K the magnetic moments are calculated to be 2.19(4) μ_B/Cr(2) ion and 3.10 μ_B/Cr(1) ion. Given the change to Cr(2) ion magnetic ordering through ordering of Cr(1) ions, there are clearly correlations between the magnetic layers.

T < 291 K   291 K < T < 590 K
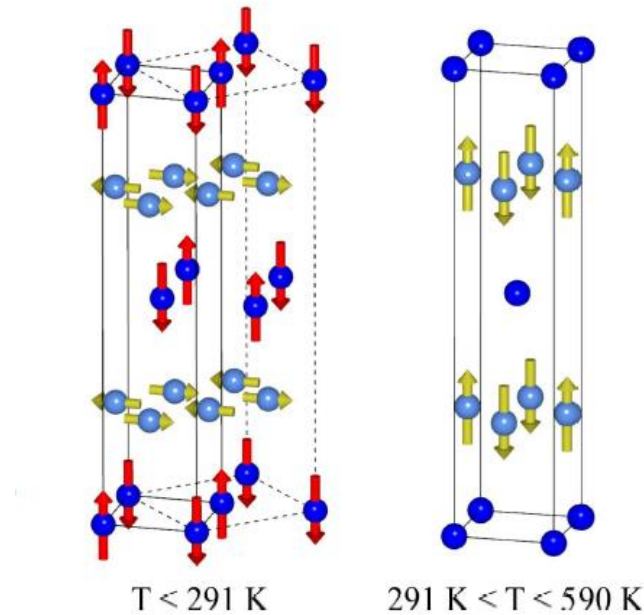
Figure 1.20: The magnetic structures of Sr₂Cr₃As₂O₂ at low and high temperatures, Cr(1) ions in dark blue and Cr(2) ions in light blue[52].

A new study from X. Xu *et. al.*[54] into $Sr_2Cr_3As_2O_2$ looked more closely into the magnetic behaviour and found a deviation from the previous studies, as well as documenting the magnetic behaviour of the barium analogue $Ba_2Cr_3As_2O_2$. For $Sr_2Cr_3As_2O_2$ the Néel temperature is estimated at around 600(10) K similar to the previously reported value of 590 K[52], the barium analogue ordered at the lower temperature of 473(10) K. From 598 – 348 K in $Sr_2Cr_3As_2O_2$ and 473 – 233 K in $Ba_2Sr_3As_2O_2$ the high temperature ordering is determined to be that as stated before[52], with the Cr(2) magnetic moments in a C-type AFM arrangement parallel to the *c* direction of the lattice. In the higher temperature range the Cr(1) magnetic moments are not ordered or contributing to the magnetic Bragg peak intensities for both samples. The high temperature magnetic ordering of the Cr(2) ions has propagation vector $k = (1\ 1\ 1)$ and forms a primitive tetragonal unit cell, with lattice parameters $a_{nucl} \times a_{nucl} \times c_{nucl}/2$ in relation to the nuclear unit cell.
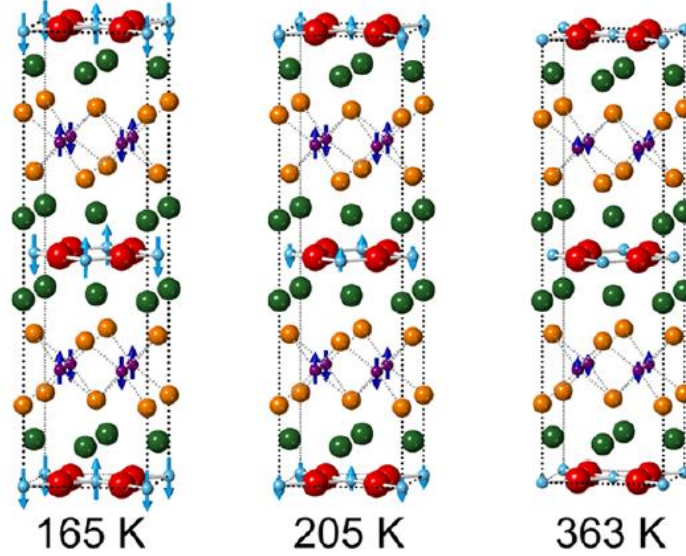
Figure 1.21: Ba$_2$Cr$_3$As$_2$O$_2$ magnetic structure evolution with temperature, Cr(1) in light blue and Cr(2) in purple[54].

New magnetic reflections appeared between 325 and 348 K down to low temperatures for the strontium analogue, with similar Bragg peaks appearing for the barium sample below 233 K. The new reflections were found in both samples to be modeled as long-range antiferromagnetic ordering of Cr(1) ions in the oxide layers with propagation vector k = (1/2 1/2 0) and a new magnetic unit cell with lattice parameters $\sqrt{2a_{nucl}} \times \sqrt{2a_{nucl}} \times c_{nucl}$. The low temperature ordering differs between the strontium and barium samples. Below 233 K for Ba$_2$Cr$_3$As$_2$O$_2$ the magnetic moments of the Cr(1) ions are antiferromagnetically arranged parallel to the c direction, like those of the Cr(2) moments in the arsenide layers. At base temperature, the two chromium magnetic moments are saturated, with both orientated parallel to the c axis as seen in the 165 K magnetic structure in Figure 1.21.

The low temperature ordering in Sr$_2$Cr$_3$As$_2$O$_2$ differs from the barium sample, as below 348 K the Cr(1) magnetic moments lie in the *ab*-plane, not along *c*. Canting of the Cr(1) magnetic moments towards the *c* direction was refined for the 297(1) K data resulting in magnetic intensities modeled more successfully. A steady reorientation of the magnetic moments for both chromium positions occurs between 297 and 248 K; Cr(1) moments in the oxide layers start in the *ab* plane and rotate to become parallel to the *c* axis, the opposite rotation occurs for Cr(2) moments in the arsenide layers so they lie in *ab* plane. The spin reorientation is determined to be complete by 247(1) K,

24

both moments realign simultaneously so it appears the chromium positions are magnetically coupled. The magnetic structure reorientation for $Sr_2Cr_3As_2O_2$ is shown in Figure 1.22.
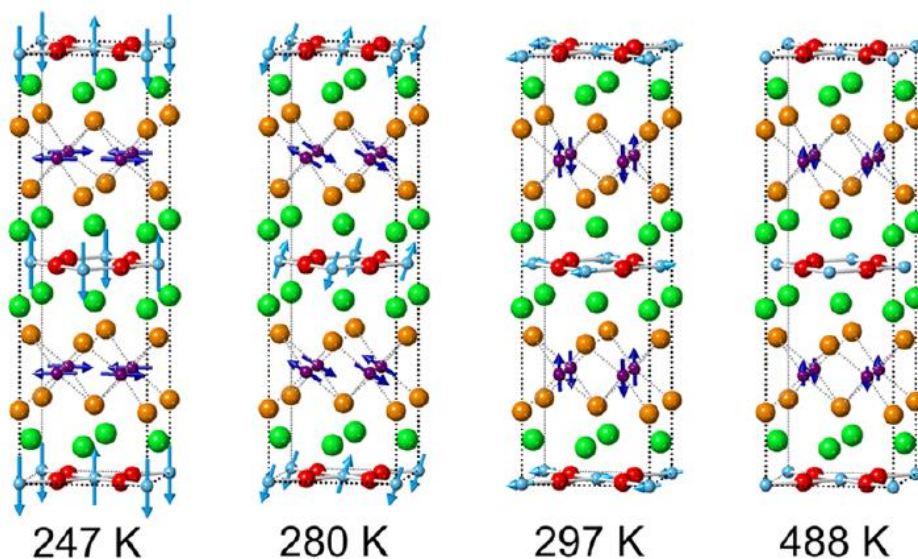
Figure 1.22: Magnetic ordering of $Sr_2Cr_3As_2O_2$ at different temperatures, highlighting the spin reorientation of Cr(1) and Cr(2) magnetic moments[54].

There are some structural differences between the Sr and Ba analogues of the material which could be key to the variation of magnetic ordering between the two samples. The Cr(1)-O and Cr(2)-Cr(2) bond lengths in $Ba_2Cr_3As_2O_2$ are 1.17% larger than those of $Sr_2Cr_3As_2O_2$ due to the extension of *a* parameter from 4.00800(2) to 4.05506 (2) Å (Sr and Ba analogue values respectively from I11 powder X-ray diffraction data). The larger bond lengths results in the lower magnetic ordering temperature. The significant structural difference between the two analogues is the significantly larger Cr(1) – As bond length in $Ba_2Cr_3As_2O_2$ (3.6630(8) Å, 3.2072(7) Å in $Sr_2Cr_3As_2O_2$). The extension of Cr(1)-As leads to larger distortions of Cr(1)O_4As_2'octahedra', where the oxygen are in square planar arrangement in CrO_2 layers and the arsenic atoms in the tetrahedral layers form the top and bottom of the octahedra. It is unknown how this distortion relates to the behaviour of $Sr_2Cr_3As_2O_2$ (as only the strontium analogue shows evidence of the two chromium positions magnetically coupling) but it is presumed that the extent of the distortion is key to the strength of a Cr(1) – Cr(2) coupling interaction[54].

A mixed chromium and iron 2322 structure $Sr_2Fe_2CrAs_2O_2$ has been investigated by N. Eguchi *et. al.*[55] The sample crystallises in the same *I4/mmm* space group as other 2322 pnictide materials,

with the Cr ions occupying the MO_2 square planar layers and Fe ions in the M_2As_2 tetrahedral layers. Rietveld refinement from powder x-ray diffraction measurements yielded lattice constants of $a = 3.9948(1)$ Å and $c = 18.448(1)$ Å. Resistivity measurements of $Sr_2CrFe_2As_2O_2$ recorded between 3 and 300 K were performed, with the material exhibiting semiconductor-like behaviour for the whole temperature range. There is no evidence of any structural or magnetic transition of the sample through resistivity measurements. Variation of magnetization with temperature was measured using a SQUID magnetometer, with very small change observed and no Curie-Weiss-like behaviour. Some small kinks in the magnetization curves were observed under fields of 1 and 10 kG, and the cause is not yet known. Ferromagnetic behaviour is seen in the magnetization measurements, however, this is thought to be due to an impurity phase, a Fe-Cr alloy. Due to slight impurities, for a proper magnetic investigation of the $Sr_2CrFe_2As_2O_2$ sample to be performed, purification is required. $Sr_2CrFe_2As_2O_2$ is not observed to display a superconducting transition even under pressure; replacement of Cr with other elements is thought to possibly lead to superconductivity emerging for the 2322 structure[55].

$A_2Zn_3As_2O_2$ (A = Ba, Sr) phases were studied and resistivity measurements indicated that both compounds are semiconductors but further studies would be required to confirm this[56]. The 2322 structure adopted by these materials leads to the unusual coordination of square planar zinc in an extended system, within the ZnO_2 layers. Given zinc is a non-magnetic ion there is no magnetic ordering within these systems. In $Ba_2MnZn_2As_2O_2$[57] there is cation ordering, with pure Zn_2As_2 and pure MnO_2 layers. The magnetic coupling in $Ba_2MnZn_2As_2O_2$ below 38 K is weak, with the non-magnetic zinc layers disturbing the magnetic ordering. Magnetisation measurements showed a divergence of ZFC magnetisation at 30 K, which is more pronounced at 12 K, this is taken to indicate spin-glass behaviour at low temperatures[57]. A further study into the physical properties of $Ba_2MnZn_2As_2O_2$ by T. Ozawa $et.$ $al.$ [58] discovered semiconducting properties through resistivity measurements. The study also finds ZFC and FC magnetisation deviations below 30 K agreeing with the proposed spin glass state. $Sr_2MnZn_2As_2O_2$ was found to not have full selectivity of Mn and Zn ions, unlike the $Ba_2MnZn_2As_2O_2$, the oxide layers are nearly fully Mn occupied with 99.6(4)% and the arsenide layers are occupied 94.0(5) and 6.0(5)% by zinc and manganese respectively[59]. The loss of zinc from the material is thought to occur through the sample preparation. $Sr_2MnZn_2As_2O_2$ has a transition in the magnetisation measurements at 55 K with no long-range order found but the ground state is taken to be a spin glass state.

1.3: Manganese Pnictides

1.3.1: 1111 Structure

Manganese pnictide compounds are of interest as Mn^{2+} has an odd number of $3d$ electrons so is predicted to form a different spin configuration than the other LaMPnO (M = transition metal, Pn = pnictides) compounds, this is due to many Mn^{2+} compounds forming half-filled stable shells with high spin d^5 configuration[60]. Within the 1111 family, investigation into different lanthanide substitution and doping strategies has led to new properties exhibited for manganese pnictides.

LaMnPO crystallises in the $P4/nmm$ space group, with the same structure as other $LnMPn$O samples discussed, containing alternating M-Pn and Ln-O layers. The magnetic moments of Mn^{2+} ions were refined to be parallel to the c axis, with a magnetic moment of 2.26(2) μ_B/Mn. The magnetic structure found to be the best fit to the data is shown in Figure 1.23. Within the manganese phosphide layers there are antiferromagnetic couplings of magnetic moments, but between the planes there are ferromagnetic interactions[60]. LaMnPO electrical and optical measurements revealed the sample to be a semiconductor with a band gap of around 1.3 eV. A variable pressure study on LaMnPO performed found that the antiferromagnetic order is destroyed through application of around 34 GPa pressure. At around 20 GPa there is also a change in the material from an antiferromagnetic insulator into an antiferromagnetic metallic state[61].
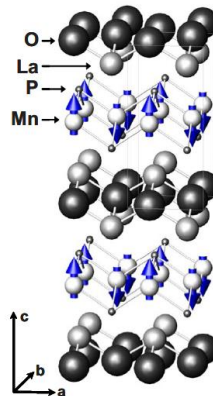
Figure 1.23: Magnetic structure of LaMnPO, with Mn^{2+} moments arranging antiparallel within the Mn-P layers but parallel between Mn-P planes[60].

LaMnAsO was found to have the same nuclear and magnetic structure as LaMnPO, with a refined magnetic moment of 2.43(1) μ_B/Mn^{2+} ion at 290 K[62]. The Néel temperature was reported in another paper on LaMnAsO magnetic properties, T_N = 360(1) K[63]. Resistivity measurements revealed the sample to be a semiconductor as well, with resistivity becoming too high to measure below 200 K. A significant magnetoresistance (MR) was observed for LaMnAsO for a large temperature range; which implies that there are strong spin-charge couplings of Mn^{2+} 3d^5 electrons. MR is the change in electrical resistivity, ρ, of a material with application of a magnetic field H, MR = $(\rho(H) - \rho(0))/\rho(0)$. The measured MR becomes negative below 380 K, increasing more with cooling with a peak around 200 K. The conductivity of LaMnAsO was modelled by three-dimensional variable range hopping (VRH) of the charge carriers, with a localisation temperature of 102 K. The variation of MR with temperature in LaMnAsO is different to that seen in colossal magnetoresistant (CMR) manganite perovskites like La$_{1-x}$Sr$_x$MnO$_3$[64] (Mn oxidation states of 3.2-3.5); the magnetoresistance mechanism is therefore thought to be different in this system[62]. A theorised explanation for the large negative MR found in LaMnAsO is due to a change of the VRH via multiple sites at higher temperatures to two site hopping below the transition. When electron tunnelling exists through more than two sites then quantum destructive interference is possible. The −MR is a result of diminished quantum destructive interference that occurs upon application of an external magnetic field, so the conductivity increase has arisen from the hops that have zero amplitude when zero field is applied[62]. Magnetoresistance that arises from quantum interference has only been seen in highly disordered semiconductors, the MR in this instance changes gradually with lowering temperature below the magnetic ordering temperature[65] like observed in LaMnAsO.

Given the success of doping into the iron superconductor systems, doping strategies were employed on the LaMnAsO system using hydride ions[66]. Synthesis of LaMnAsO$_{1-x}$H$_x$ (x = 0 − 0.73) samples revealed that substitution of O^{2-} with H$^-$ induced a transition from insulating to metallic behaviour with accompanying suppression of Mn ion antiferromagnetic ordering. The magnetic reflections seen in the neutron diffraction pattern of LaMnAsO are not observed in the hydrogen doped samples, demonstrating that the AFM ordering vanished with this doping strategy at room temperature. Ferromagnetic ordering replaces the AFM ordering as hydrogen content increases. Magnetisation measurements found the appearance of peak for x > 0.08, which increases intensity and onset temperature with increasing x, this is indicative of a ferromagnetic transition.
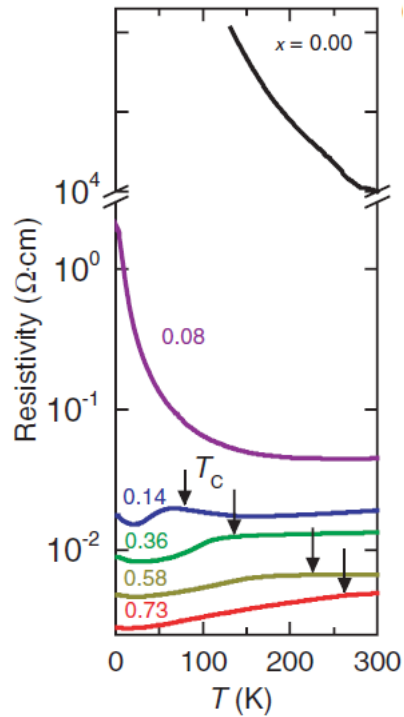
Figure 1.24: Temperature dependence of dc resistivity for LaMnAsO$_{1-x}$H$_x$ (0.00 $\leq$ x $\leq$ 0.73)[66].

The addition of hydrogen to the system dramatically changed the electrical resistivity of LaMnAsO (Figure 1.24). The resistivity recorded at room temperature is reduced by over 6 orders of magnitude by the addition of hydrogen on the oxygen sites. The resistivity temperature coefficient is reversed from the parent compound above x = 0.14; from this an insulator-to-metal (I-M) transition is indicated to occur at this doping level. No superconductivity was observed in the samples even though hydrogen substitution reduced the resistivity substantially from pure LaMnAsO. Negative MR is observed in all the LaMnAsO$_{1-x}$H$_x$ samples. For x = 0.08, an AFM insulating sample, a maximum negative MR of -63% is recorded at 8 K under H -50 kOe. The metallic sample, x = 0.14, has a lower $-$MR of -25% at 53 K. The transition of I-M accompanies the AFM-FM transition in x > 0.14. The ordering temperature T_C and saturation moment increase with x value, with values 264 K and 1.58 μ_B/Mn^{2+} respectively for x = 0.73[66].

NdMnAsO was found to have a magnetic transition at 335 K into the same magnetic structure as reported for LaMnPO and LaMnAsO (see Figure 1.23)[62]. The magnetic ordering in NdMnAsO was further investigated through variable temperature neutron and x-ray diffraction studies[67], a change in the magnetic diffraction peak intensity was observed below 23 K. The Nd^{3+} magnetic moments

align antiferromagnetically at low temperatures with moments along the *ab* plane rather than parallel to *c*, as shown in Figure 1.25. The same magnetic ordering has been reported by A. Marcinkova *et. al.*[68]. Mn magnetic moments are reported to order at higher temperature $T_N = 359(2)$ K parallel to the *c* lattice direction. As seen in Figure 1.25 there is a spin reorientation of the Mn^{2+} magnetic moments, which is found to coincide with the antiferromagnetic ordering of Nd^{3+} magnetic moments, so at base temperature both moments lie in the *ab* plane. The spin reorientation of manganese moments occurs at $T_{SR} = 23$ K. The refined magnetic moments at 1.6 K are $\mu_{Mn} = 3.72(1)$ μ_B and $\mu_{Nd} = 1.94(1)$ μ_B[68]. A further small magnetic transition at 10 K was visible in the SQUID measurements, attributed to neodymium moment ordering[62]. NdMnAsO has smaller cell parameters than LaMnAsO. Given the smaller ionic radius of Nd^{3+} over La^{3+}, this results in a reduction of *Ln*O and MnAs layer thickness and increase of tetrahedral α-angles. The reduction in layer thickness results in stronger interactions in NdMnAsO as the Mn-Mn distances are shorter, this is therefore the reason given for difference in magnetic transition temperature (T_N for Mn^{2+}) between the two analogues of LnMnAsO.
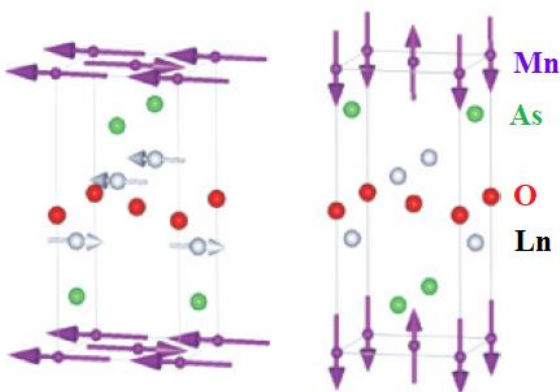
Figure 1.25: Magnetic structure of NdMnAsO at 2K (left) and 290 K (right), with low temperature ordering of Nd^{3+} magnetic moments resulting in the change of moment direction of Mn^{2+} moments[67].

NdMnAsO is also a semiconductor, in this instance the resistivity is too high to measure below 30 K[62]. The conductivity, like LaMnAsO, was modelled using three-dimensional VRH. Figure 1.26 shows there is a subtle electronic transition in NdMnAsO evidenced through change in slope of the $\ln(\rho)$ vs $T^{-0.25}$ slope between 120-180 K. As shown there is a suggested overlap of two different 3D VRH states, with localisation temperatures T_0 of 77 and 22 K for high and low temperature

respectively. The MR behaviour is the same as discussed for LaMnAsO, and different doping strategies have been investigated in NdMnAsO system to see the effect on MR properties.
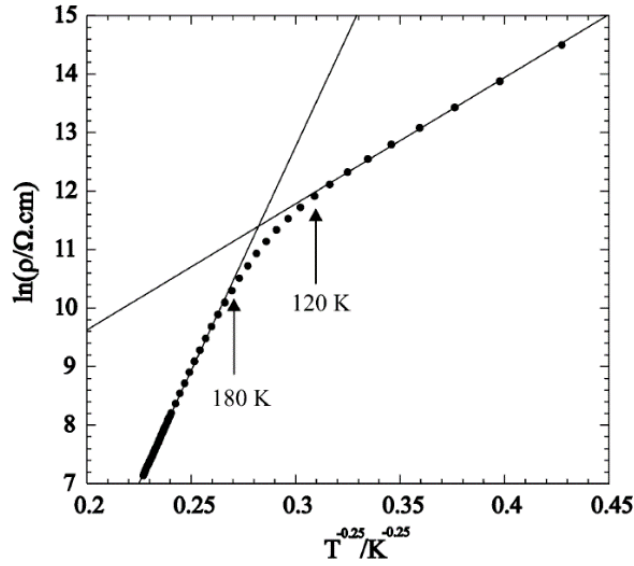
Figure 1.26: Plot of ln(ρ) vs $T^{-0.25}$ of NdMnAsO , a clear change in the slope is highlighted with the whole temperature range fitting well to the Mott VRH equation [ρ = $ρ_0exp(T_0/T)^{0.25}$] [62].

Fluorine doping of NdMnAsO system results in the emergence of colossal magnetoresistance, which is a rare phenomenon. The electrical resistivity of samples decreases by multiple orders of magnitude upon application of a magnetic field[69]. NdMnAsO$_{1-x}$F$_x$ (x = 0.05, 0.065, 0.08) were prepared and X-ray diffraction data refinements revealed that increase in fluorine content results in the decrease of *a* and *c* cell parameters of the *P4*/*nmm* crystal structure, as expected, due to the smaller ionic radii of F$^-$ than O^{2-} (1.33 and 1.40 Å respectively). The magnetic transitions recorded for the fluorine doped samples are the same as those seen in the NdMnAsO parent compound. Neutron diffraction of NdMnAsO$_{0.95}$F$_{0.05}$ confirmed the antiferromagnetic ordering of manganese moments below 356(2) K. The electron doping has no significant change in the transition temperature from the undoped structure. At 23 K the Nd^{3+} moments order so that the spins are parallel to the basal plane of NdMnAsO$_{0.95}$F$_{0.05}$ which accompanies the spin flip of the manganese moments from along *c* into the *ab* plane, like previously stated as occuring in NdMnAsO (Figure 1.25). The spin reorientation occurs as a result of the Nd^{3+} moments magnetically ordering as there is strong coupling between the MnAs and NdO sublattices.

The conduction carriers are assumed to be confined within the manganese arsenide layers and the electronic behaviour is observed to significantly change through the addition of 5% fluorine in the oxygen sites. At low temperature, CMR is observed in the $NdMnAsO_{1-x}F_x$ system, as evidenced in Figure 1.27. Negative MR occurs in all the samples below 75 K, and the magnitude of MR increases exponentially with lowering temperature and a sharp drop is clear below the spin reorientation temperature, T_{SR}. CMR does not occur in the parent compound, so the charge carriers are deduced as electrons generated through replacement of O^{2-} ions for F^-. The negative magnetoresistance is reversible with field, it reaches the highest value of -95% at 3 K with 9 T field applied. The CMR mechanism is novel, as it cannot be associated with spin polarized tunneling across domain or phase boundaries where low field MR is normally found. There are also no correlations in the CMR materials between magnetoresistance and the field variation. The electronic behaviour of $NdMnAsO_{0.95}F_{0.05}$ is fitted to 3D VRH below 75 K, inset Figure 1.27, but a subtle electronic transition occurs at T_{SR} below 20 K that is modelled by Efros Shkovskii VRH. The change in model suggests that the change in orientation of manganese spins into the basal plane enhances the Coulomb correlations between localized electrons and transport is diminished. In previously studied manganite materials the CMR behaviour appears when a magnetic field improves the ferromagnetic arrangement of spins at the boundary of paramagnetic to ferromagnetic ordering (disorder-order)[64]. In the case of $NdMnAsO_{1-x}F_x$, CMR has been shown possible in a pnictide material under a magnetic field around an antiferromagnetic-paramagnetic transition (order-disorder), so CMR is induced thanks to the competition of the different phases[69].
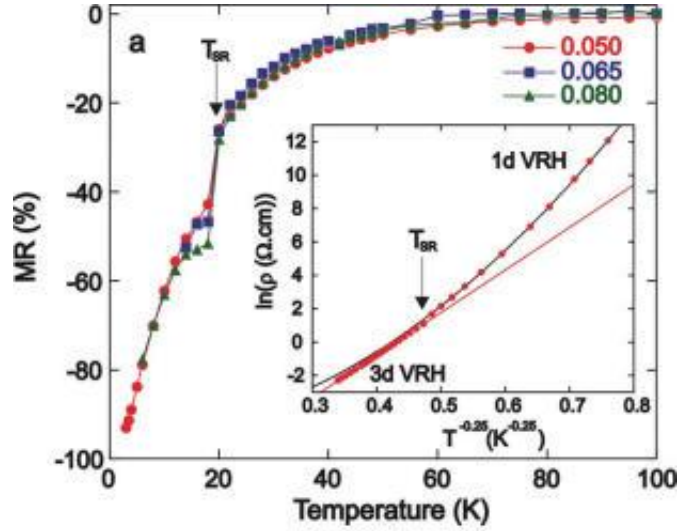
Figure 1.27: Plot of the variation of magnetoresistance at 7 T with temperature for NdMnAsO$_{1-x}$F$_x$ system, with x = 0.050, 0.065, 0.080. Inset figure displays the crossover from 3D VRH to one-dimensional VRH below T$_{SR}$ for NdMnAsO$_{0.95}$F$_{0.05}$[69].

A variable temperature study of NdMnAsO$_{0.95}$F$_{0.05}$ with synchrotron x-ray diffraction was used to check if there were any subtle crystal structure changes upon cooling[70]. There are no structural distortions evident in NdMnAsO$_{0.95}$F$_{0.05}$ down to 4 K even though multiple magnetic transitions occur. There is a small anomaly in the plot of *a* against temperature at 23 K (T$_{SR}$), which does not occur for the *c* parameter. The change at T$_{SR}$ is evidence that coupling exists between the crystal lattice and magnetic ordering. The coupling occurring in the NdMnAsO$_{0.95}$F$_{0.05}$ sample is therefore related to the electronic behaviour previously stated, resulting in the change to 1D VRH below T$_{SR}$. The CMR material NdMnAsO$_{0.95}$F$_{0.05}$ is therefore found to show coupling between the crystal lattice, electronic and magnetic degrees of freedom[70].

High pressure measurements were carried out on the NdMnAsO$_{0.95}$F$_{0.05}$ sample; unlike LaMnPO the AFM ordering is not destroyed in this system[71]. NdMnAsO$_{0.95}$F$_{0.05}$ shows no structural transition over the whole pressure range investigated up to 8.59 GPa. The antiferromagnetic ordering is retained with applied pressure with the ordering temperature T$_N$ increasing as the applied pressure increases. The sample was heated to above the T$_N$ of 360 K so no magnetic Bragg peaks were observed, with pressure then applied until the peaks re-emerged. The highest T$_N$ reached was 383 K under 4.97 GPa and the rate of T$_N$ increase determined to be 4.63 K GPa^{-1}. The increase in T$_N$ upon application of external pressure is unlikely due to a change in the charge

distribution within the [MnAs]$^-$ layers as neither doping technique (hole/electron) increases the ordering temperature. The changes seen with applied pressure are more likely due to a structural effect, with a clear decrease in Mn–As bond length with increasing pressure and temperature. The interlayer spacing within $NdMnAsO_{1-x}F_x$ structure also decreases through increasing the external parameters. Reduction of Mn–As bond length and interlayer spacing results in enhanced superexchange between manganese centres along Mn–As–Mn as well as between the planes, resulting in an increase in T_N in $NdMnAsO_{1-x}F_x$.

Different dopants were investigated for the NdMnAsO system to compare the effects doping has on the electrical properties. $Nd_{1-x}Sr_xMnAsO$ series was prepared with x = 0.05 and 0.10; this strontium substitution creates hole doping within the manganese arsenide layers[72]. The T_N were found through neutron diffraction to be 342 and 325 K for x = 0.05 and 0.10 respectively, so the addition of strontium to the system reduced the magnetic ordering temperatures, however, the magnetic structure is not altered. For both Sr doped samples investigated the resistivity measurements revealed metallic behaviour not semiconducting like NdMnAsO. For $Nd_{1-x}Sr_xMnAsO$ no large negative MR is observed between 150 and 390 K, instead at low temperatures there is positive MR, see Figure 1.28. The MR peaks appear at around 15 K, which is unrelated to the magnetic transitions. A possible cause for the positive MR seen in $Nd_{1-x}Sr_xMnAsO$ samples is that there is a change in mobility linked to altering of the band structure when temperature is decreased, like that reported for La(Fe, Ru)AsO[73]. The CMR in fluorine doped NdMnAsO samples is reported as linked to the magnetic transition and so there are clearly multiple different MR mechanisms in the *Ln*MnAsO materials.
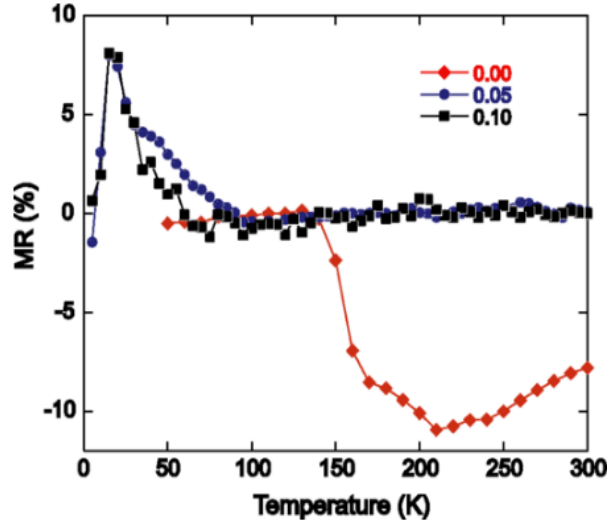
Figure 1.28: Plot of Nd$_{1-x}$Sr$_x$MnAsO 7 T MR variation with temperature, exhibiting positive MR below 100 K[72].

Nd(Mn$_{1-x}$Co$_x$)AsO$_{0.95}$F$_{0.05}$ was studied to determine the effect of cobalt doping on the colossal magnetoresistance of NdMnAsO$_{0.95}$F$_{0.05}$[74]. Cobalt doping results in arsenic and oxygen non-stoichiometry in the system, with As deficiencies from 4.9-6%. The non-stoichiometry of the two sites could result in further electron doping of the Mn cation; the electrons may be trapped by the vacancies. The magnetic structure and spin reordering temperature is unchanged through cobalt doping, however, the T$_N$ is decreased with increasing cobalt content from x = 0.00 to 0.047. There are no strong correlations between the crystal structures of Nd(Mn$_{1-x}$Co$_x$)AsO$_{0.95}$F$_{0.05}$ and cobalt content, so the reduction in T$_N$ is probably due to an increase in magnetic frustration and electron doping through substitution of Co into the Mn$_2$As$_2$ layers. There is a correlation between the value of calculated manganese magnetic moment and the arsenic occupancy level in this series, with the change in arsenic deficiencies with changing Co doping similar to the trend in manganese magnetic moments. Arsenic deficiencies in the tetrahedral layers reduces the number of nearest-neighbour AFM superexchange pathways as well as increasing e$^-$ doping in tetrahedral layers. Nd(Mn$_{1-x}$Co$_x$)AsO$_{0.95}$F$_{0.05}$ samples are all semiconductors, measured resistivities are between 1 and 40 Ωcm. The MR measured for this system showed that CMR is diminished with small additions of Co (x = 0.010 and 0.015) and not observed when x = 0.047, Figure 1.29. It is clear from the studies that the MR properties of the NdMnAsO system are very sensitive to small changes in the doping strategies and Mn magnetic moments.
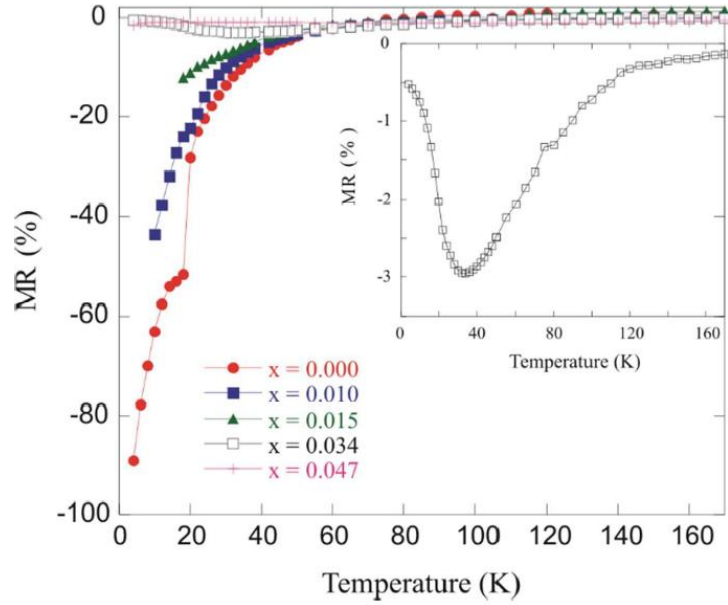
Figure 1.29: Temperature variation of 7 T magnetoresistance for NdMn$_{1-x}$Co$_x$AsO$_{0.95}$F$_{0.05}$, the inset is a closer look at the low temperature behaviour in x = 0.034 sample[74].

Changing Nd to Pr in NdMnAsO$_{1-x}$F$_x$ system also results in the loss of CMR[75]. The crystal structure of PrMnAsO$_{1-x}$F$_x$ was found through XRD refinements to change with decreasing temperature. At high temperatures the material crystallises in the tetragonal *P4*/*nmm* space group, changing to orthorhombic *Pmmn* symmetry below 35 K. Below the structural transition, PrMnAsO$_{0.95}$F$_{0.05}$ has refined cell parameters of *a* = 4.05896(1) Å, *b* = 4.06201(1) Å, and *c* = 8.89399(2) Å at 10 K. A T$_N$ was recorded at 340 K in PrMnAsO$_{0.95}$F$_{0.05}$, which corresponds to the antiferromagnetic ordering of manganese spins in the *ab* plane and ferromagnetic interactions along *c*, much like that in NdMnAsO$_{0.95}$F$_{0.05}$. The magnetic model no longer fits as well at 180 K, so a small Pr^{3+} AFM moment is added; with magnetic moments parallel to *a* and a spin reorientation of Mn^{2+} spins occurs simultaneously. The reorientation occurs over a large range of temperature, around 80 K, with moments fully rearranged by 140 K, see Figure 1.30, and the reorientation induces antiferromagnetic order of Pr^{3+} ion spins.
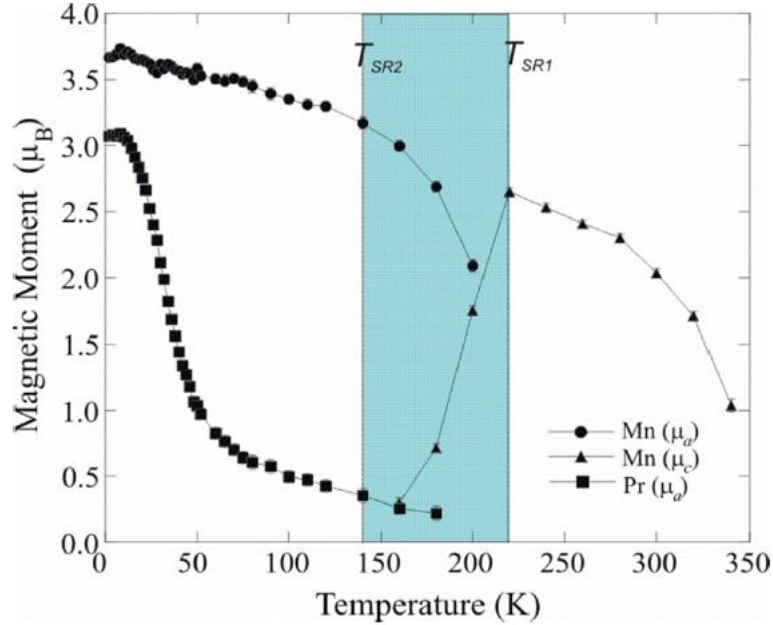
Figure 1.30: Plot of temperature variation of the manganese and praseodymium magnetic moments in PrMnAsO$_{0.95}$F$_{0.05}$. The highlighted region indicated the spin reorientation region for Mn spins, changing orientation from c direction into the basal plane[75].

Electrical resistivity measurements of PrMnAsO$_{0.95}$F$_{0.05}$ revealed semiconducting behaviour, below 95 K the resistivity can be characterised by 3D VRH of the electrons similar to NdMnAsO$_{0.95}$F$_{0.05}$. At 44 K, a subtle electronic transition is evidenced in the fit to VRH equation, with a clear change in slope. The MR variations with respect to temperature at 7 T for the Nd and Pr analogues of *Ln*MnAsO$_{0.95}$F$_{0.05}$ are shown in Figure 1.31. PrMnAsO$_{0.95}$F$_{0.05}$ does not show CMR, instead a sizeable –MR is present below the structural transition T$_s$ at around 35 K, with no MR shown above this temperature. The –MR reaches a peak at 12 K before a reduction so at 4 K the MR = -0.9% at 7 T. The behaviour seen in the praseodymium sample is very different to the neodymium analogue, and the absence of CMR is surprising. The CMR absence can be a result of multiple factors, such as the lack of 1D Efros Shkovskii VRH given the system has weakened electron correlations as the Mn-As bond lengths are extended below the structural transition. Changing of lanthanide ion in this 1111 Mn system is shown to largely effect the electronic and magnetic properties, with multiple MR mechanisms possible[75].
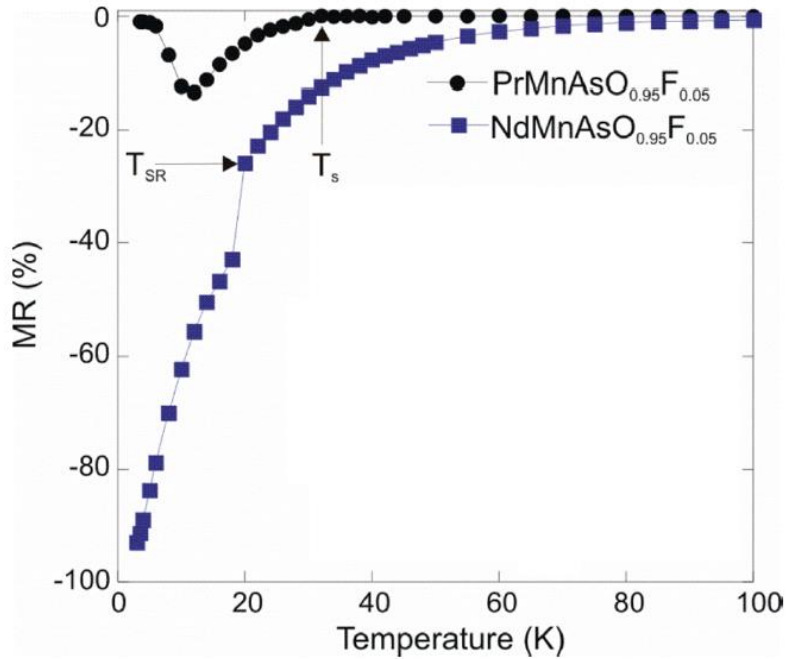
Figure 1.31: Variation of MR with temperature at 7 T for Pr and Nd analogues of LnMnAsO$_{0.95}$F$_{0.05}$ with absence of CMR clear in the praseodymium sample. The structural transition temperature (T$_s$) for PrMnAsO$_{0.95}$F$_{0.05}$ and spin reorientation transition (T$_{SR}$) for NdMnAsO$_{0.95}$F$_{0.05}$ highlighted[75].

1.3.2: Other Structure Types

The 122 structure with manganese as the transition metal has been investigated. The structure and magnetic behaviour of BaMn$_2$As$_2$ was discovered through neutron diffraction experiments[76]. A high magnetic transition temperature is recorded at 625 K. At 10 K the manganese magnetic moments have G-type AFM ordering along *c*, with antiferromagnetic interactions between all nearest neighbour spins. The crystal and magnetic structure is shown in Figure 1.32. The refined magnetic moment at 10 K is 3.88(4) μ$_B$ per manganese ion. The variation of magnetic moment with temperature suggests that the AFM transition is second order in nature; the cell parameters for BaMn$_2$As$_2$ decreases monotonically with decreasing temperature, displaying normal thermal contraction. The magnetic transition does not result in a change to the crystal structure, unlike the previously mentioned BaFe$_2$As systems, where orthorhombic distortions are associated with the

38

AFM ordering[28]. Electrical resistivity measurements of $BaMn_2As_2$ system revealed it to have a semiconducting ground state[77].
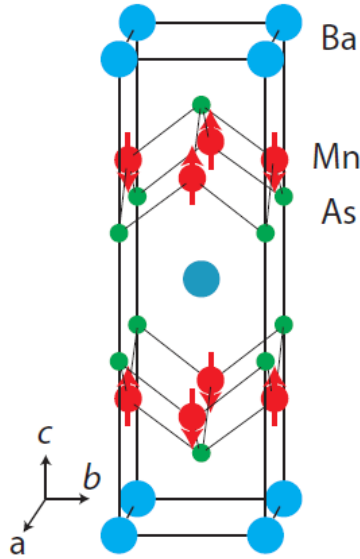
Figure 1.32: Crystal and magnetic structure of BaMn₂As₂ at 10 K[76].

$BaMn_2As_2$ has been driven to metallic behaviour through doping the barium site with potassium. $Ba_{1-x}K_xMn_2As_2$ with x = 0.05 (powder sample) and 0.016 (single crystal sample) have metallic ground states, the partial substitution of potassium leads to hole doping of the samples[78]. The resistivities at 2 K are recorded at 5.8 and 2.2 mΩ.cm for x = 0.016 and 0.05 respectively, and such values are attributed to the low concentrations of hole doping through potassium substitution. Heat capacity measurements showed agreement with the appearance of metallic behaviour in K doped samples. The magnetic behaviour for the doped samples is unchanged, other than a small reduction in the transition temperature into the AFM state, from 625 to 607 K x = 0 and 0.05 respectively. The refined magnetic moments show slight increase with potassium doping, from 3.88(4) μ_B/Mn in the undoped material to 4.21(6) μ_B/Mn for x = 0.05. The T_N and magnetic moments are not significantly changed through potassium doping, and $Ba_{1-x}K_xMn_2As_2$ in the doping range 0.016-0.05 is summarised as a hole-doped antiferromagnetic local moment metal.

$SrMn_2As_2$ and $CaMn_2As_2$ do not crystallise in the tetragonal $ThCr_2Si_2$ structure like other 122 pnictides, instead adopting the trigonal $P\bar{3}m1$ space group as seen in Figure 1.33[79]. The manganese layers form a corrugated honeycomb structure, Figure 1.33 (b), stacked along the *c* axis with alkali-

earth ions separating the layers. The nearest Mn-Mn neighbours are highlighted in the crystal structure picture, with an intra layer minimum distance of around 3 Å (d_1) being much smaller than the minimum interlayer Mn-Mn distance of around 6 Å (d_{z1}). Due to these interatomic distances, the samples are expected to have quasi-two-dimensional Mn-Mn exchange interaction connectivity.
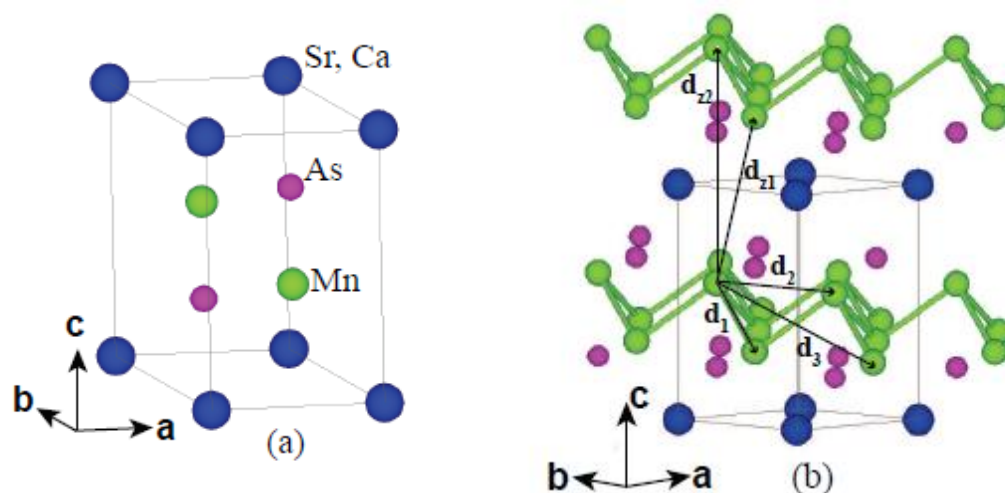
Figure 1.33: Trigonal crystal structure of of SrMn$_2$As$_2$ and CaMn$_2$As$_2$ systems, with CaAl$_2$Si$_2$-type arrangement in the hexagonal setting. (a) The outline of one unit cell containing one formula unit of (Sr,Ca)Mn$_2$As$_2$. (b) Near perpendicular to c axis view of structure displaying the honeycomb-like layers of manganese[79].

Magnetic susceptibility measurements found AFM transitions in AMn$_2$As$_2$ materials at 120(2) K and 62(3) K for A = Sr and Ca respectively. The susceptibility data indicates that the samples have hexagonal c axis as the easy axis for magnetic ordering. The manganese magnetic moments align antiferromagnetically in the ab plane. Both susceptibility and heat capacity measurements revealed strong dynamic short-range AFM connections with T$_N$ up to a minimum of 900 K. These correlations are probably linked to the quasi-two-dimensional connectivity of strong antiferromagnetic interactions between manganese spins inside the honeycomb layers that lie parallel to the ab plane of (Sr,Ca)Mn$_2$As$_2$[79].

The 2322 structure, as discussed for other transition metals, has long been known for the manganese pnictides, with the first investigation reported in 1991 by Stetson $et.$ $al.$[80] The general formula A_2Mn$_3$$Pn_2O_2$ (A = Sr, Ba, Pn = P, As, Sb) is adapted by the series, with all phases

crystallising in the body centered tetragonal *I4/mmm* space group, Figure 1.34 displays the 2322 structure for clarity. As with the other transition metal 2322 materials, there are two distinct sublattices of manganese ions, the body centered square planar $Mn(1)O_2$ sublattice, and the tetrahedral $Mn(2)_2As_2$ sublattice. $Ba_2Mn_3Pn_2O_2$ ($Pn = P$, As, Sb) were the first Mn_3 2322 systems discussed with magnetic susceptibilities from 6-300 K recorded. These initial measurements found that the samples display broad antiferromagnetic transitions, where the transition temperatures decrease as the size of pnictogen ion increases. The broad transitions seen correspond to low-dimensional AFM compounds, indicating short-range AFM coupling of manganese ions that is 2D above the T_N and three-dimensional below. T_N was taken as the maximum slope in the magnetic susceptibility vs temperature plot, $T_N = \sim90$ K, 60 K, 50 K for P, As, and Sb analogues respectively.
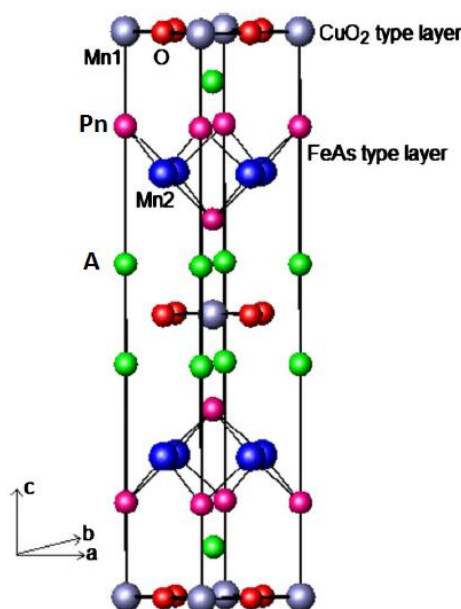
Figure 1.34: $A_2Mn_3Pn_2O_2$ crystal structure, in I4/mmm space group. Two distinct manganese layers are highlighted, both similar layer-types to high temperature superconductor families[81].

$Sr_2Mn_3Pn_2O_2$ (Pn = As, Sb) have also been studied, with the magnetic structures fully realised through neutron diffraction experiments[82]. The neutron diffraction data for the two samples were split into three regions for refinements, with the first region fit to purely nuclear structures above 300 K for Sb and 340 K for As analogues. The second region (65 - 300 K for Sb, 75 - 340 K for As) found enhancement of some neutron diffraction peaks, indexed as the addition of magnetic ordering forming a G-type AFM arrangement of $Mn(2)^{2+}$ magnetic moments along *c*. In the third

region the two samples differ from one another magnetically, with $Sr_2Mn_3Sb_2O_2$ showing multiple new reflections at low temperature. The reflections appearing index to the same arrangement of ordered K_2NiF_4 samples[53] in the manganese oxide layers, altering the magnetic cell parameters so the cell dimensions become $a_{MAG} = \sqrt{2}a$ and $c_{MAG} = c$. The low temperature structure of $Sr_2Mn_3Sb_2O_2$ shown in Figure 1.35. The low temperature diffraction pattern of $Sr_2Mn_3As_2O_2$ only shows two distinct new features with smaller peaks visible through magnification, as opposed to multiple strong reflections seen in the antimony analogue. The strongest peak that can be indexed, the (100) reflection, is of Warren type lineshape, corresponding to two-dimensional ordering on the Mn(1) position. Three dimensional ordering is not established within the $Mn(1)O_2$ sublattice for the arsenic sample even down at base temperature of 4 K[82].
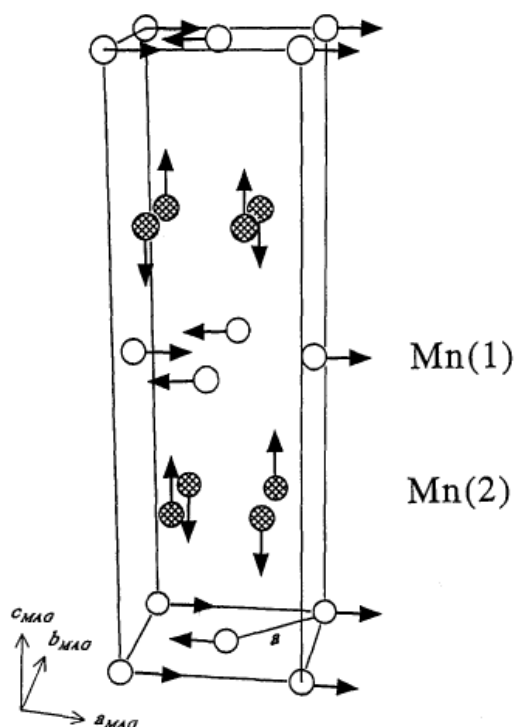
Figure 1.35: Magnetic structure of $Sr_2Mn_3Sb_2O_2$, with K_2NiF_4 type ordering of Mn(1) ions an G-type AFM ordering of Mn(2) ions, the cell dimensions are shown as $a_{MAG} = \sqrt{2}a$, $c_{MAG} = c$, with chemical cell dimension a labelled[82].

The full $A_2Mn_3Pn_2O_2$ series was reported in a further study by Brock *et. al.*[83], other than $Sr_2Mn_3P_2O_2$ where the synthesis was unsuccessful. All samples crystallise in the same structure as previously mentioned, with the Pn atoms of Mn_2Pn_2 tetrahedra pointing towards the Mn atoms

within the MnO_2 layers creating a pseudo-octahedral environment for the Mn(1) ions. The interplanar manganese to pnictide ion distance is much larger than a bond though, more on the scale of a van der Waals interaction. The Mn-Pn interplanar distance enlarges with the larger size of pnictogen anion and alkaline earth cation (changing from Sr to Ba, and As to Sb). Magnetic susceptibilities measured for all materials, except $Sr_2Mn_3As_2O_2$, show a wide maximum and very similar behaviour assigned to the coupling within MnO_2 layers. From this study, the magnetic behaviour of all barium samples are taken to be the same as refined for $Sr_2Mn_3Sb_2O_2$, as shown in Figure 1.35. The exception to this ordering is $Sr_2Mn_3As_2O_2$ as previously mentioned, where the only long-range ordering only occurs within the Mn_2As_2 layers[83].

A mixed manganese/copper version of the 2322 structure ($Sr_2Mn_2CuAs_2O_2$) was successfully synthesised and studied showing different magnetic behaviour from the purely manganese compounds[81]. Neutron diffraction measurements were analysed to determine the copper distribution within the structure. The best refinement model was obtained with copper only on the M(2) site within the arsenide layers, when Cu was allowed to refine on the M(1) position the refinement was significantly worse. The content of copper does not match to the stoichiometry of the sample, only 37% of the M(2) positioned as opposed to 50% expected for $Sr_2Mn_2CuAs_2O_2$ phase which could be due to the presence of an impurity phase. Magnetic susceptibility measurements of the sample show rapid increase below 125 K, which indicates a ferrimagnetic/ferromagnetic ordering at around 100 K. ZFC and FC susceptibilities in $H = 100$ Oe have large divergence at 90 K which is a characteristic trait of ferri/ferromagnetic materials. Neutron diffraction measurements were performed to study the magnetic structure in more detail, with the magnetic transition reduced from 340 K for Mn_3 sample to 120 K Mn_2Cu sample and Curie temperature T_C of 95(1) K. The magnetic ordering is found to be ferrimagnetic, where the ordering of M(1) ions are antiparallel to those in $M(2)_2As_2$ planes. The magnetic ordering has changed from G-type AFM to A-type ferrimagnet, where all intraplanar interactions are ferromagnetic but interplanar interactions are antiferromagnetic, the comparison of two magnetic structures is visible in Figure 1.36. The magnetic ordering in the 2322 system is clearly very sensitive to the different transition metal content, as one third substitution into the structure with copper results in the significant change of G-type AFM arrangement to A-type ferrimagnetic ordering[81].
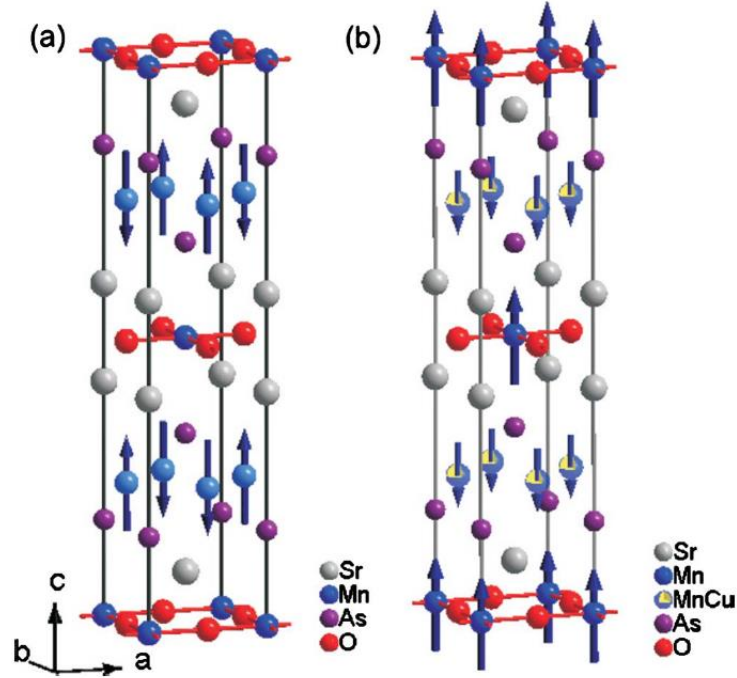
Figure 1.36: (a) Magnetic crystal structure for $Sr_2Mn_3As_2O_2$ sample, with G-type AFM arrangement of $Mn(2)^{2+}$ ions and (b) the ferrimagnetic model used for refinements of $Sr_2Mn_2CuAs_2O_2$ sample with antiparallel M(1) and M(2) moments[81].

1.4: Many-Body Localisation

1.4.1: Thermalisation

To discuss the topic of many-body localisation (MBL) it is first key to describe the terms of thermalisation and localisation. Isolated quantum many-body systems are not coupled to any external bath; so the system is not capable of exchanging heat or work with an external reservoir. To obey the second law of thermodynamics, an isolated system should move towards thermodynamic equilibrium with a state of maximum entropy and so some form of mutual interaction is required[84]. The aforementioned lack of external reservoir for isolated quantum systems means that to satisfy the second law of thermodynamics the system is considered to act as its own reservoir.

This behaviour is the basis of "thermalisation" and is generally thought to be true for all systems that obey conventional statistical mechanics. For quantum-mechanical systems, the thermalisation of isolated systems is described by the "eigenstate thermalisation hypothesis" (ETH) [85,86]. The hypothesis expresses that in a many-body quantum system, the individual eigenstates in the system behave similar to a statistical ensemble, so the behaviour of a subset of the wider system averages out over time in the same fashion as the wider system.

The ETH is not always true, a large class of systems that do not obey such a hypothesis is those that are many-body Anderson localised, to be discussed later. In recent years, many-body localisation has received greater attention as a key example of a quantum many-body system that does not thermalize and does not obey ETH. The MBL system contains strong interactions between the constituent bodies but does not have the ability to act as its own heat reservoir so cannot accomplish equipartition of energy[87]. An MBL system is incapable of thermalisation as information contained within local degrees of freedom are maintained over long time periods[88]. Before discussing why such behaviour is displayed by MBL systems and the practical applications this would have, it is vital to first address the concept of localisation from basic concepts up to an examination of many-body systems.

1.4.2: Localisation

Localised materials do not act as their own reservoirs, thus needing an external bath and so do not thermalize. The difference between thermalisation and localisation is merely dynamical with thermalisation assumed when only focusing on thermodynamic quantities. When the individual many-body eigenstates are investigated, the distinction becomes rather clear[87].

Localisation is a term used when talking about the electrical transport properties of solid-state systems, covering a range of diverse materials that can be broadly split into two main classes: Mott localisation and Anderson localisation. Mott localisation is in reference to the electron localisation in highly correlated Mott insulators[89], which are insulating due to interactions within the materials. Mott insulating states appear in materials that go through metal to insulator transitions (MIT). The simplest theory of Mott insulation is the Hubbard model[90], which in itself is an expansion of the tight-bonding model where electrons are capable of hopping between different lattice sites.

Hubbard's Hamiltonian includes an extra term, with an energy amount *U* for each electron pair inhabiting the same lattice site, signifying Coulomb repulsion. The model allows for both metallic and insulating states depending on the *U* value, a significantly large value results in the creation of an energy gap. Anderson localisation is different in that it occurs in materials with quenched disorder[91], first described by the eponymous researcher in 1958. Anderson was concerned with doped semiconducting systems and how the quantum mechanical phenomena affect the electrical transport properties, showing that the interacting spins in such materials may be unable to thermally equilibrate without assistance through lattice vibrations (phonons). It was suggested by Anderson that in an adequately disordered lattice it is possible for an electron to become partially localised on the lattice positions. Additionally, he proposed that given sufficient disorder the electron may become completely localised onto the lattice positions, resulting in no transport at zero temperature. Abrahams *et. al.* later validated this in 1978, where they also put forward a scaling relationship that could become a diagnostic for the appearance of localisation[92].

Anderson localisation has recently become a trending research topic with advancements in many-body studies including many-body molecular and optical physics as well as quantum information. Localisation is aptly understood for quantum particles and waves not interacting in a disordered medium. Experimentally, Anderson localisation has been observed in multiple different systems including phonons[93] and ultracold atoms[94], this is single-body Anderson localisation. An exploration into an Anderson-localised system was performed in 2006 to determine whether the localisation could persist at zero temperature given introduction of small interactions between close particles[95]. Perturbation theory was used to study this system, the localisation was maintained and it therefore validated the idea of the many-body (Anderson) localisation phase as a state of matter at temperatures above zero.

Many-body localisation at temperatures above zero is a phase transition of high interest. The findings by Basko *et. al.*[95] showed that MBL is characterised by a metal to insulator transition where the conductivity disappears at temperatures below this transition. This was significant progress in the field of localisation as it highlighted an experimental way of identifying a thermal state to a many-body localised state phase transition. The simplest definition of many-body localisation would be if Anderson localisation-like behaviour is observed in a many-body system, a more technical definition MBL is present in a many-body system when the ETH does not hold

true. A key difference between single-body and many-body localisation is that for MBL systems quantum entanglement spreads logarithmically from an initial non-tangled condition, in single-particle localised systems the entanglement is not spread[87].

1.4.3: Many-Body Localisation Applications

Moving away from the theory aspect to many-body localisation, it is key to look into the experimental side of this phenomenon and its possible practical applications. Experimentally a few examples of MBL have been recently reported, although only within artificial quantum systems. A disorder-induced insulating state has been shown to appear within a strongly interacting Fermi gas that is contained within an optical lattice when cooled below the Fermi temperature, the localisation remains as the temperature of the gas increases[96]. The properties discussed in the report by S. Kondov *et. al.* are expected for a MBL system. This experiment is performed within a precisely controlled system; it is free of any external heat bath (phonons for example) allowing for testing of the MBL state. An MBL phase transition has been reported to occur for interacting fermions within a one-dimensional quasirandom optical lattice[97], the phase transition in this instance was recognised through the relaxation dynamics of an initially formulated charge density wave. Unfortunately, so far there has been no evidence of MBL in a bulk material, meaning that the practical applicability of this phase is unsubstantiated. Solid-state systems pose the problem of unavoidable environmental couplings, which can dampen the expected sharp features of MBL states, where isolated systems do not have this issue[98].

MBL phases display an exciting new feature, as they have strictly zero thermal and electrical conductivity, and so are perfect insulators[99]. The DC conductivity in MBL phases must be zero, and so the disappearance of DC transport is a helpful indicator of MBL in certain systems[87]. The property which may lead to future applications of MBL materials is their ability to retain some memory of their local initial conditions over long times. The ability to retain information on the initial states in MBL systems is a large motivator for MBL studies, as this property could be used as a form of quantum 'memory'.

Quantum memory has been advised as an essential component for the progression of multiple up-and-coming quantum technologies. Particularly, quantum memories are being investigated to help

with the advancement of quantum computing; quantum mechanics can increase the speed of multiple applications in computing[100] as they can be in a superposition of states and can examine numerous variants at once. Quantum effects such as entanglement do not at the moment play a part in information processing, however, this could change in the future as they can be used to crack codes and many other applications[101]. MBL systems could prove to become key in using localisation to defend quantum computation, as localised systems undergo slow dephasing essential to the concept of quantum memory[102].

1.5: Research Aims

Following on from the results obtained on the compounds discussed within this introductory chapter, in this thesis, further investigations were undertaken to discover the effects of chemical substitution within manganese pnictide materials. Structural, magnetic and electrical properties were probed in the new samples prepared.

The effect of mixing manganese and chromium occupancy within the 2322 family of pnictides has been explored, as well as the outcome of cerium substitution into the 1111 family of manganese oxypnictides. Preliminary studies into some antimonide 1111 manganese pnictides was performed to compare the effect of pnictide ions on measured properties.

The $Sr_2Mn_{2.23}Cr_{0.77}As_2O_2$ sample was prepared and fully investigated through variable temperature neutron and synchrotron X-ray diffraction experiments, with preliminary magnetometry measurements performed as well. A $CeMnAsO_{1-x}F_x$ (x = 0 – 0.075) series was synthesised and studied through SQUID magnetometry, resistivity measurements. A thorough study of the nuclear and magnetic structures through variable temperature neutron and synchrotron X-ray diffraction experiments was performed to determine if a link is present between the structural and electronic properties. Synthesis of some antimonide manganese 1111 samples was started but only preliminary studies through laboratory X-ray diffraction and SQUID magnetometry could be performed within the timeframe of this thesis.

References

[1] iF WORLD DESIGN GUIDE, *Periodic Table Of Elements*. url: https://ifworlddesignguide.com/entry/259038-periodic-table-of-elements, accessed 01/09/2020.

[2] P. Atkins, T. Overton, J. Rourke, M. Weller and F. Armstrong, in *Shriver & Atkins' inorganic chemistry,* Oxford University Press, Oxford, 5th ed. 2010, pp.81, 478, 502-504.

[3] Y. Maeno, H. Hashimoto, K. Yoshida, S. Nishizaki, T. Fujita, J. Bednorz and F. Lichtenberg, 1994, *Nature,* **372**, 532-534.

[4] Z. Hiroi, S. Yonezawa and Y. Muraoka, 2004, *J. Phys. Soc. Jpn.* **73**, 1651-1654.

[5] Y. Kamihara, H. Hiramatsu, M. Hirano, R. Kawamura, H. Yanagi, T. Kamiya and H. Hosono, 2006, *J. Am. Chem. Soc.* **128**, 10012-10013.

[6] B. I. Zimmer, W. Jeitschko, J. H. Albering, R. Glaum and M. Reehuis, 1995, *J. Alloy. Compd.* **229**, 238-242.

[7] Z. Tesanovic, 2009, *Physics*, **2**.

[8] B. Pradhan, S. Goi, S. Behera, P. Parida and R. Mishra, 2016, *Solid State Commun.* **248**, 53-59.

[9] B. Pradhan, 2010, *Indian J. Phys.* **84**, 279-289.

[10] Y. Kamihara, T. Watanabe, M. Hirano and H. Hosono, 2008, *J. Am. Chem. Soc*. **130**, 3296-3297.

[11] X. Jin, T. Masubuchi, T. Watanabe, K. Takase and Y. Takano, 2009, *J. Phys.: Conf. Ser.* **150**, 052085.

[12] H. Takahashi, K. Igawa, K. Arii, Y. Kamihara, M. Hirano and H. Hosono, 2008, *Nature*, **453**, 376-378.

[13] H. Hosono and S. Matsuishi, 2013, *Curr. Opin. Solid St. M.* **17**, 49-58.

[14] S. Iimura, S. Matsuishi, H. Sato, T. Hanna, Y. Muraba, S. W. Kim, J. E. Kim, M. Takata and H. Hosono, 2012, *Nat. Commun.* **3**, 943.

[15] H. Wen, G. Mu, L. Fang, H. Yang and X. Zhu, 2008, *Europhys. Lett.* **82**, 17009.

[16] Z. A. Ren, J. Yang, W. Lu, W. Yi, G. C. Che, X. L. Dong, L. L. Sun and Z. X. Zhao, 2008, *Mater. Res. Innov*. **12**, 105-106.

[17] Z. A. Ren, J. Yang, W. Lu, W. Yi, X. L. Shen, Z. C. Li, G. C. Che, X. L. Dong, L. L. Sun, F. Zhou and Z. X. Zhao, 2008, *Chin. Phys. Lett.* **25**, 57002.

[18] G. F. Chen, Z. Li, D. Wu, G. Li, W. Z. Hu, J. Dong, P. Zheng, J. L. Luo and N. L. Wang, 2008, *Phys. Rev. Lett*. **100**, 247002.

[19] Z. A. Ren, W. Lu, J. Yang, W. Yi, X. L. Shen, Z. C. Li, G. C. Che, X. L. Dong, L. L. Sun, F. Zhou and Z. X. Zhao, 2008, *Chin. Phys. Lett.* **25**, 2215.

[20] W. Lu, J. Yang, X. L. Dong, Z. A. Ren, G. C. Che and Z. X. Zhao, 2008, *New J. Phys.* **10**, 063026.

[21] Q. Han, Y. Chen and Z. D. Wang, 2008, *Europhys. Lett.* **82**, 37007.

[22] C. H. Lee, A. Iyo, H. Eisaka, H. Kito, M. T. Fernandez-Diaz, T. Ito, K. Kihou, H. Matsuhata, M. Braden and K. Yamada, 2008, *J. Phys. Soc. Jpn.* **77**, 083704.

[23] C. H. Lee, K. Kihou, A. Iyo, H. Kito, P. M. Shirage and H. Eisaki, 2012, *Solid State Commun.* **152**, 644-648.

[24] H. Wen and S. Li, 2011, *Annu. Rev. of Conden. Ma. P.* **2**, 121-140.

[25] J. H. Tapp, Z. Tang, B. Lv, K. Sasmal, B. Lorenz, P. Chu and A. Guloy, 2008, *Phys. Rev. B.* **78**, 060505.

[26] X. C. Wang, Q. Q. Liu, Y. X. Lv, W. B. Gao, L. X. Yang, R. C. Yu, F. Y. Li and C. Q. Jin, 2008, *Solid State Comm.* **148**, 538-540.

[27] C. Krellner, N. Caroca-Canales, A. Jesche, H. Rosner, A. Ormeci and C. Geibe, 2008, *Phys. Rev. B.* **78**, 100504.

[28] M. Rotter, M. Tegel and D. Johrendt, 2008, *Phys. Rev. Lett.* **101**, 107006.

[29] N. Ni, M. E. Tillman, J. Q. Yan, A. Kracher, S. T. Hannahs, S. L. Bud'ko and P. C. Canfield, 2008, *Phys. Rev. B.* **78**, 214515.

[30] F. Han, X. Zhu, P. Cheng, G. Mu, Y. Jia, L. Fang, Y. Wang, H. Luo, B. Zeng and B. Shen, 2009, *Phys. Rev. B.* **80**, 024506.

[31] X. Zhu, F. Han, G. Mu, P. Cheng, B. Shen, B. Zeng and H. Wen, 2009, *Phys. Rev. B.* **79**, 220512.

[32] H. Ogino, Y. Matsumura, Y. Katsura, K. Ushiyama, S. Horii, K. Kishio and J. Shimoyama, 2009, *Supercond. Sci. Tech.* **22**, 075008.

[33] L. Boeri, O. V. Dolgov and A. A. Golubov, 2008, *Phys. Rev. Lett.* **101**, 026403.

[34] J. Bardeen, L. Cooper and J. R. Schreiffer, 1957, *Phys. Rev.* **106**, 162-164.

[35] Q. Si, R. Yu and E. Abrahams, 2016, *Nat. Rev. Mater.* **1,** 16017.

[36] T. Watanabe, H. Yanagi, T. Kamiya, Y. Kamihara, H. Hiramatsu, M. Hirano and H. Hosono, 2007, *Inorg. Chem.* **46**, 7719-7721.

[37] T. Watanabe, H. Yanagi, Y. Kamihara, T. Kamiya, M. Hirano and H. Hosono, 2008, *J. Solid State Chem.* **181**, 2117-2120.

[38] Y. Luo, H. Han, H. Tan, X. Lin, Y. Li, S. Jiang, C. Feng, J. Dai, G. Cao, Z. Xu and S. Li, 2011, *J. Phys.: Condens. Mat.* **23**, 175701.

[39] Y. Li, Y. Luo, L. Li, B. Chen, X. Xu, J. Dai, X. Yang, L. Zhang, G. Cao and Z. Xu, 2014, *J. Phys.: Condens, Mat*. **26**, 425701.

[40] S. Matsuishi, A. Nakamura, Y. Muraba and H. Hosono, 2012, *Supercond. Sci. Tech.* **25**, 084017.

[41] Z. Li, G. Chen, J. Dong, G. Li, W. Hu, D. Wu, S. Su, P. Zheng, T. Xiang, N. Wang and J. Luo, 2008, *Phys. Rev. B*. **78**, 060504.

[42] Y. Takano, S. Komatsuzaki, H. Komasaki, T. Watanabe, Y. Takahashi and K. Takase, 2008, *J. Alloy. Comp.* **451**, 467-469.

[43] I. Schellenberg, H. Lincke, W. Hermes, V. Dittrich, R. Glaum, M. H. Möller and R. Pöttgen, 2010, *Z. Naturforsch.* **65b**, 1191-1198.

[44] X. Jin, T. Masubuchi, T. Watanabe, K. Takase and Y. Takano, 2009, *J. Phys. Conf. Ser.* **150**, 052085.

[45] H. Ohta and K. Yoshimura, 2009, *Phy, Rev. B*. **80**, 184409.

[46] S.-W. Park, H. Mizoguchi, K. Kodama, S. Shamoto, T. Otomo, S. Matsuishi, T. Kamiya and H. Hosono, 2013, *Inorg. Chem.* **52**, 13363-13368.

[47] F. Ronning, N. Kurita, E. D. Bauer, B. L. Scott, T. Park, T. Klimczuk, R. Movshovich and J. D. Thompson, 2008, *J. Phys.: Condens, Mat.* **20**, 342203

[48] E. D. Bauer, F. Ronning, B. L. Scott and J. D. Thompson, 2008, *Phys. Rev. B*. **78**, 172504.

[49] C. M. Thompson, X. Tan, K. Kovnir, V. O. Garlea, A. A. Gippius, A. A. Yaroslavtsev, A. P. Menushenkov, R. V. Chernikov, N. Buttgen, W. Kratschmer, Y. V. Zubavichus and M. Shatruk, 2014, *Chem. Mater.* **26**, 3825-3837.

[50] K. A. Filsinger, W. Schnelle, P. Adler, G. H. Fecher, M. Reehuis, A. Hoser, J.-U. Hoffmann, P. Werner, M. Greenblatt and C. Felser, 2017, *Phys. Rev. B*. **95**, 184414.

[51] P. Das, N. S. Sangeetha, G. R. Lindemann, T. W. Heitmann, A. Kreyssig, A. I. Goldman, R. J. McQueeney, D. C. Johnston and D. Vaknin, 2017, *Phys. Rev. B*. **96**, 014411.

[52] J. Liu, J. Wang, J. Sheng, F. Ye, K. M. Taddei, J. A. Fernandez-Baca, W. Luo, G.-A. Sun, Z.-C. Wang, H. Jiang, G.-H. Cao and W. Bao, 2018, *Phys. Rev. B*. **98**, 134416.

[53] R. J. Birgeneau, H. J. Guggenheim and G. Shirane, 1970, *Phys. Rev. B*. **1**, 2211.

[54] X. Xu, M. A. Jones, S. J. Cassidy, P. Manuel, F. Orlandi, M. Batuk, J. Hadermann and S. J. Clarke, 2020, *Inorg. Chem.* **59**, 15898-15912.

[55] N. Eguchi, F. Ishikawa, M. Kodama, T. Wakabayashi, A. Nakayama, A. Ohmura and Y. Yamada, 2013, *J. Phys. Soc. Jpn.* **82**, 045002.

[56] S. L. Brock and S. M. Kauzlarich, 1994, *Inorg. Chem.* **11**, 2491-2492.

[57] T. C. Ozawa, M. M. Olmstead, S. L. Brock, S. M. Kauzlarich and D. M. Young, 1998, *Chem. Mater.* **10**, 392-396.

[58] A. Matsushita, T. C. Ozawa, J. Tang and S. M. Kauzlarich, 2000, *Physica B.* **284-288**, 1424-1425.

[59] T. C. Ozawa, S. M. Kauzlarich, M. Bieringer, C. R. Wiebe and J. E. Greedan, 2001, *Chem. Mater.* **13**, 973-980.

[60] H. Yanagi, T. Watanabe, K. Kodama, S. Iikubo, S. Shamoto, T. Kamiya, M. Hirano and H. Hosono, 2009, *J. Appl. Phys.* **105**, 093916.

[61] J. Guo, J. W. Simonson, L. Sun, Q. Wu, P. Gao, C. Zhang, D. Gu, G. Kotliar, M. Aronson and Z. Zhao, 2013, *Sci. Rep.* **3**, 2555.

[62] N. Emery, E. J. Wildman, J. M. S. Skakle, G. Giriat, R. I. Smith and A. C. Mclaughlin, 2010, *Chem. Commun.* **46**, 6777-6779.

[63] M. A. McGuire and V. O. Garlea, 2016, *Phys. Rev. B.* **93**, 054404.

[64] C. N. R. Rao and B. Raveau, in *Colossal Magnetoresistance, Charge Ordering and related Properties of Manganese Oxides,* World Scientific, Singapore, 1998, pp. 356.

[65] N. Manyala, Y. Sidis, J. D. Ditusa, G. Aeppli, D. P. Young and Z. Fisk, 2000, *Nature*, **404**, 581.

[66] T. Hanna, S. Matsuishi, K. Kodama, T. Otomo, S. Shamoto and H. Hosono, 2013, *Phys. Rev. B.* **87**, 020401.

[67] N. Emery, E. J. Wildman, J. M. S. Skakle and A. C. Mclaughlin, 2011, *Phys. Rev. B.* **83***, 144429.

[68] A. Marcinkova, T. C. Hansen, C. Curfs, S. Margadonna and J. -W. G. Boss, 2010, *Phys. Rev. B.* **82**, 174438.

[69] E. J. Wildman, J. M. S. Skakle, N. Emery and A. C. Mclaughlin, 2012, *J. Am. Chem. Soc.* **134**, 8766-8769.

[70] E. J. Wildman and A. C. Mclaughlin, 2016, *Sci. Rep.* **6**, 20705.

[71] E. J. Wildman, M. G. Tucker and A. C. Mclaughlin, 2015, *J. Phys.:Condens. Mat.* **27**, 116001.

[72] E. J. Wildman, N. Emery and A. C. Mclaughlin, 2014, *Phys. Rev. B.* **90**, 224413.

[73] I. Pallecchi, F. Bernardini, M. Tropeano, A. Palenzona, A. Martinelli, C. Ferdeghini, M. Vignolo, S. Massidda and M Putti, 2011, *Phys. Rev. B.* **84**, 134524.

[74] E. J. Wildman, K. S. McCombie, G. B. G. Stenning and A. C. Mclaughlin, 2018, *Dalton T.* **47**, 14726-14733.

[75] E. J. Wildman, F. Sher and A. C. Mclaughlin, 2015, *Inorg. Chem.* **54**, 2536-2542.

[76] Y. Singh, M. A. Green, Q. Huang, A. Kreyssig, R. J. McQueeney, D. C. Johnston and A. I. Goldman, 2009, *Phys. Rev. B.* **80**, 100403.

[77] J. An, A. S. Sefat, D. J. Singh and M.-H. Du, 2009, *Phys. Rev. B.* **79**, 075120.

[78] A. Pandey, R. S. Dhaka, J. Lamsal, Y. Lee, V. K. Anand, A. Kreyssig, T. W. Heitmann, R. J. McQueeney, A. I. Goldman, B. N. Harmon, A. Kaminski and D. C. Johnston, 2012, *Phys. Rev. Lett.* **108**, 087005.

[79] N. S. Sangeetha, A. Pandey, Z. A. Benson and D. C. Johnston, 2016, *Phys. Rev. B.* **94**, 094417.

[80] N. T. Stetson and S. M. Kauzlarich, 1991, *Inorg. Chem.* **30**, 3969-3971.

[81] R. Nath, V. O. Garlea, A. I. Goldman and D. C. Johnston, 2010, *Phys. Rev. B.* **81**, 224513.

[82] S. L. Brock, N. P. Raju, J. E. Greedan and S. M. Kauzlarich, 1996, *J. Alloy. Compd.* **237**, 9-19.

[83] S. L. Brock and S. M. Kauzlarich, 1996, *J. Alloy. Compd.* **241**, 82-88.

[84] R. F. Sekerka, in *Thermal Physics,* Elsevier, 1st ed. 2015, pp. 257-276.

[85] M. Srednicki, 1994, *Phys. Rev. E.* **50**, 888.

[86] M. Rogol, V. Dunjko and M. Olshanii, 2008, *Nature,* **452**, 854-858.

[87] R. Nandkishore and D. A. Huse, 2015, *Annu. Rev. Condens. Matter Phys.* **6**, 15-38.

[88] E. Altman and R. Vosk, 2015, *Annu. Rev. Condense. Matter Phys.* **6**, 383-409.

[89] N. F. Mott, 1968, *Rev. Mod. Phys.* **40**, 677-683.

[90] J. Hubbard, 1963, *Proc. R. Soc. Lond. A.* **276**, 238-257.

[91] P. W. Anderson, 1958, *Phys. Rev.* **109**, 1492–1505.

[92] E. Abrahams, P. W. Anderson, D. C. Licciardello and T. V. Ramakrishnan, 1979, *Phys. Rev. Lett.* **42**, 673–676.

[93] R. L Weaver, 1990, *Wave Motion,* **12**, 129-142.

[94] J. Billy, V. Josse, Z. Zuo, A. Bernard, B. Hambrecht, P. Lugan, D. Clement, L. Sanchez-Palencia, P. Bouyer and A. Aspect, 2008, *Nature,* **453**, 891-894.

[95] D. M. Basko, I. L. Aleiner and B. L. Altshuler, 2006, *Ann. Phys.-New York,* **321**, 1126-1205.

[96] S. S. Kondov, W. R. McGehee, W. Xu and B. DeMarco, 2015, *Phys. Rev. Lett.* **114**, 083002.

[97] M. Schreiber, S. S. Hodgman, P. Bordia, H. P. Luschen, M. H. Fischer, R. Vosk, E. Altman, U. Schneider and I. Bloch, 2015, *Science,* **349**, 842-845.

[98] T. Nguyen, N. Andrejevic, H. C. Po, Q. Song, Y. Tsurimaki, N. C. Drucker, A. Alatas, E. E. Alp, B. M. Leu, A. Cunsolo, Y. Q. Cai, L. Wu, J. A. Garlow, Y. Zhu, H. Lu, A. C. Gossard, A. A. Puretsky, D. B. Geohegan, S. Huang and M Li, 2021, *Nano. Lett.* **21**, 7419-7425.

[99] D. A. Huse, 2016, *Physics*, **9**, 76.

[100] L. K. Grover, 1997, *Phys. Rev. Lett.* **79**, 325-328.

[101] C. H. Bennett and D. P. DiVincenzo, 2000, *Nature*, **404**, 247-255.

[102] V. Khemani, R. Nandkishore and S. L. Sondhi, 2015, *Nat. Phys.* **11**, 560-565.

Chapter 2

Experimental Methods

Multiple different experimental methods were applied during the course of this research project, this chapter will inspect each by supplying theoretical background information on the techniques and an explanation of the practical capabilities operated.

2.1: Synthesis

Solid state synthesis methods were applied throughout the project for the production of all samples. Polycrystalline samples were prepared for characterization *via* powder diffraction with both X-ray and neutron sources as well as some property measurements. Electrical resistivity measurements were recorded using compressed sintered pellets.

The synthesis of final product materials first required precursor preparation steps. SrO was attained through the overnight decarbonation of $SrCO_3$ at 1200 °C, and Ce*Pn* (*Pn* = As, Sb) formed by reacting elemental pieces of Ce and corresponding *Pn* in vacuum sealed silica tubes for 33 hours at 980 °C. The final products were synthesised by combining stoichiometric amounts of the corresponding precursors, with the appropriate transition metal oxides/fluorides and sintering occurred within vacuum-sealed silica tubes. To produce $Sr_2Mn_2CrAs_2O_2$, a 2%wt deficiency of SrO was used to increase the purity of the phase. The materials made with CeMn*Pn*O parent structure only require one heating step synthesis before analysis; no regrinding, pelletisation, and heating are required as in many solid state syntheses. The full syntheses methods are outlined in each corresponding results chapter experimental section.

2.2: Powder Diffraction Techniques

2.2.1: Theory

Crystalline solids are long range ordered materials, all consisting of atoms/ions distributed in space with small repeating units called unit cells. Unit cells contain the full symmetry of the materials crystal structure. The dimensions of a unit cell, referred to as the unit cell parameters, are side lengths (a, b and c) and angles (α, β and γ)[1]. The use of diffraction techniques is important for characterizing crystalline samples, as they are capable of discovering information on the phases and structural properties of materials.

Crystalline materials are considered by Bragg's theory of diffraction, to consist of multiple layers or parallel planes that each behave as semi-transparent mirrors[2] able to reflect incident beams of radiation. Bragg's law states the relationship between the wavelength of radiation (λ), scattering angle (2θ), and the interplanar spacing between parallel planes (d). The derivation of Bragg's law is shown in Figure 2.1.
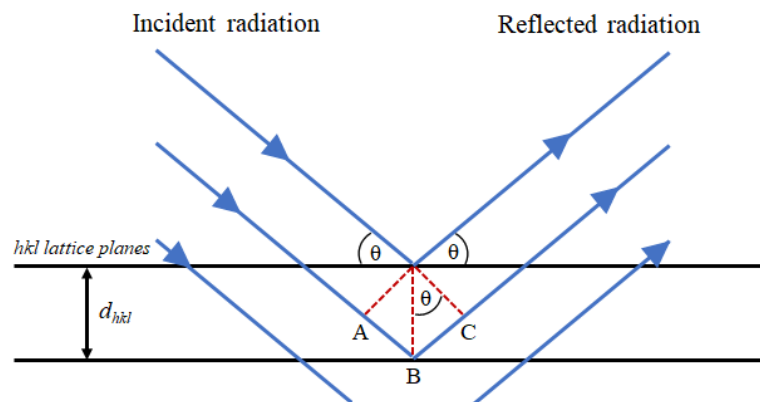
Figure 2.1: Derivation of Bragg's Law of diffraction.

The theory was first developed with X-rays as the incident radiation. As can be seen, the incoming beams with the same wavelength are reflected from the parallel planes in the crystal. The first beam will hit the upper plane, the second, however, passes through the upper plane before striking the lower plane resulting in an extra distance (ABC) being traversed. For both waves to be in phase

56

with each other and constructively interfere, the increased path length taken, ABC, is required to equal an integer of wavelengths (nλ). The relationship described by Bragg can be derived by:

$$AB = BC = dsin\theta \tag{1}$$

$$ABC = 2dsin\theta \tag{2}$$

$$ABC = n\lambda \tag{3}$$

$$2dsin\theta = n\lambda \tag{4}$$

There are conditions in Bragg's law in which the scattering angles must meet in order for reflections of the beams to occur. Only when the law is satisfied do the beams reflected interfere with each other constructively. When the angle of incidence is far from the Bragg angle (> few tenths of a degree) destructive interference can occur and cancellation of beams[3]. The integer n is usually set to 1 by convention so can be removed from the equation. For interference to occur between the scattered rays it is necessary for the incoming wavelength of radiation to be a similar magnitude to that of the inter-atomic distances (the distances between scattering centres) of the materials in question.

The perpendicular distance between pairs of adjacent planes in a sample, or d-spacing, is related to the unit cell parameters for cubic crystals in the following way:

$$\frac{1}{d^2} = \left(\frac{h^2 + k^2 + l^2}{a^2}\right) \tag{5}$$

As the systems investigated are tetragonal, the d-spacing formula for such a system is:

$$\frac{1}{d^2} = \frac{(h^2 + k^2)}{a^2} + \frac{l^2}{c^2} \tag{6}$$

From this, it is clear that peak positions in a diffraction pattern can be determined from unit cell parameters, if they are known. From experimentally observed peak positions therefore the unit cell parameters can be determined. The samples used in diffraction studies throughout this project were polycrystalline, these are samples which contain a huge number of small crystallites that can orientate in many different directions. An incoming X-ray beam that hits a polycrystalline sample will diffract in all possible directions that satisfy the Bragg condition. The diffracted X-rays form

what are known as cones of diffraction, which are made up of dots closely packed together, with each diffraction spot representing scattering from one singular crystallite[1], see Figure 2.2.
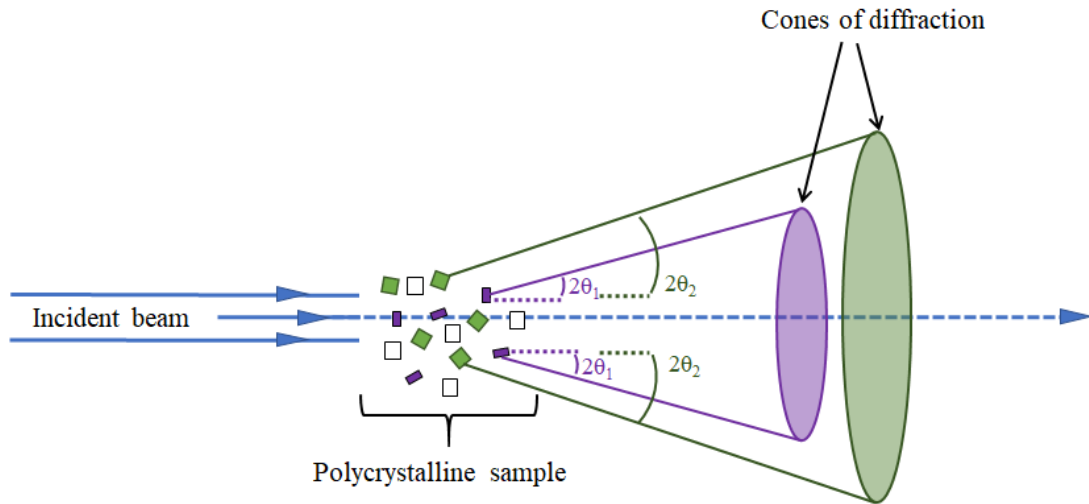
Figure 2.2: Visual representation of the diffraction cones attained by radiation beams passing through a polycrystalline sample.

In a diffraction experiment, the resultant pattern has peaks, positioned in relation to the crystallographic information, with the intensity of peaks proportional to the square of the structure factor[4]. The structure factor, F_{hkl} is the number that defines the scattering from a total unit cell and is written as[5]:

$$F_{hkl} = \sum_{j=1}^{N} f_j \, exp\left[2\pi i\left(hx_j + ky_j + lz_j\right)\right] \tag{7}$$

The f_j above represents the atomic scattering factor for atom j, hkl are miller indices of the crystal with x_j, y_j and z_j as atomic coordinates and i the imaginary number equal to $\sqrt{-1}$. The atomic scattering factor of elements is mainly reliant on the number of electrons of atom j so the structure factor is related to the electron density.

Different types of incident radiation can be used for diffraction experiments of crystalline materials, X-rays, electrons, and neutrons. This project has implemented both X-ray and neutron powder diffraction experiments to study the crystallographic structures of the novel materials investigated.

58

2.2.2: Powder X-ray Diffraction (PXRD)

X-ray diffraction is commonly used in solid state chemistry as a means to characterise crystalline materials and determine the crystal structure. Every crystalline material has its own distinctive diffraction pattern that is used for classification[6] and so XRD can be used to check the purity of prepared samples. Another use for XRD in this project was to perform structural refinements.

An XRD experiment can be broken down into basic components; the source, the sample, and the X-ray detector to measure the diffracted beam. X-rays are produced in laboratory diffractometers through a beam of electrons being accelerated towards an anode and hitting a metal target, this creates a spectrum of X-rays. The electron beam comes from the heating of a tungsten filament. To prevent the metal target from oxidising, the X-ray tube is required to be under vacuum, and the outgoing X-rays leave through beryllium "windows". Unfortunately, the production of X-rays is a very inefficient process as the kinetic energy of electrons involved is mostly converted to heat, the anode therefore requires constant cooling. Through this process only a small percentage of the energy from the electron beam is changed into X-rays[4]. The spectrum of X-rays that emerge consist of two components, one being a spectrum of white radiation (Bremsstrahlung radiation) that occurs when the electrons are slowed down/stopped by the metal target. The white radiation comprises of a range of wavelengths with a lower limit, these link to X-rays with the highest energy. The X-rays used in most diffraction experiments are the other component, produced through an indirect method that results in monochromatic X-rays. This method of X-ray production begins through the incoming electron beam ionizing some inner shell electrons from the target. An electron from a higher energy level then relaxes to the vacant site and the energy released appears as X-ray radiation of specific wavelength dependent on target metal used[7]. Copper is the common target metal in laboratory X-ray diffractometers, the copper ($1s$) electrons are ionised by the incident electron beam and then an electron from a higher level outer orbital will fall to the lower energy vacant $1s$ orbital, the resultant energy release appears as X-ray radiation. There are two transitions in copper ($K\alpha$ and $K\beta$); $K\alpha$ transition is used for XRD as it is more frequent in occurrence so creates more intense radiation[2]. The $K\alpha$ transition ($2p \rightarrow 1s$) consists of two slightly varying energies thanks to the small copper $2p$ orbital splitting; the two $K\alpha$ values are $K\alpha_1 = 1.54051$ Å and $K\alpha_2 = 1.54433$ Å, resulting in a doublet. Not all X-ray experiments can resolve the Cu $K\alpha$ doublet, so

only a singlet can be seen. The $K\alpha_2$ beam is weaker (1.54443 Å compared to 1.5406 Å) and can be removed by using a crystal monochromator[3].

X-ray diffraction does come with its downsides. The atomic scattering factor for X-rays is in proportion to the number of electrons of the atom, the atomic number of the element in question. It is therefore difficult to locate light atoms with XRD, light atoms have a small contribution to the structure-factor equation given the lower atomic scattering factor. In studies of materials comprising of elements with close atomic numbers, the structure determination can be hard with X-rays.

2.2.3: Powder X-ray Diffraction Experiments

X-ray diffraction was used throughout this project for phase identification at room temperature. The diffraction patterns were recorded on a PANalytical Empyrean powder diffractometer implementing Cu Kα1 radiation (λ = 1.540598 Å) and a Johansson monochromator. The quick scans performed were between range of 5°< 2θ < 70°, 0.0131° step size used with data collected over a period of 12-30 minutes. Longer scans were recorded for Rietveld refinements of XRD patterns to check purity and elemental content before neutron diffraction experiments. The same laboratory PANalytical Empyrean diffractometer was used for the higher resolution scans, with counting time of around 16 hours. The patterns in this case were recorded between 10 and 120° 2θ, step size of 0.003°. Synchrotron X-ray diffraction patterns were collected on the powder diffraction station on the BL04-MSPD beamline of the ALBA synchrotron in Barcelona, Spain[8]. The highest angular resolution was obtained using the so-called Multi Analyzer Detection (MAD) setup. Powder diffraction patterns were collected in the angular range 0-45° 2θ with a step size of 0.003°. Low temperatures were achieved using the lHe flow cryostat Dynaflow[9] and data were recorded from 8 to 290 K with wavelength 0.3252Å ($CeMnAsO_{1-x}F_x$) and 10 to 220 K with wavelength = 0.4123 Å ($Sr_2Mn_{2.23}Cr_{0.77}As_2O_2$) .

2.2.4: Powder Neutron Diffraction

X-ray diffraction is an easily accessible technique as laboratory diffractometers are widely available. On the other hand, neutron diffraction experiments are only available at specialist large-scale facilities. When other methods of analysis have proven inadequate to fully resolve the materials' structure neutron diffraction is used. This method is not easily accessible; in order to perform a neutron experiment it is necessary to apply for time through proposal basis, which can take a long time. The neutrons that are used in experiments have wavelengths ranging from 0.5 to 3 Å and a large sample size is required (minimum 1 mm^3) as the intensity of neutron beams is low[2]. Neutron scattering does not have the same dependence on electron density as X-ray scattering and so a primary use for neutron diffraction experiments is the study of systems with light atoms, such as hydrogen. Neutron diffraction allows the distinguishing of neighbouring elements in the periodic table from one another as well as different isotopes of the same element; these are key advantages over X-ray diffraction techniques. An added advantage neutrons pose over X-rays is that the scattering power is not dependent on 2θ due to the lack of the form factor effect, so high angle reflections in neutron diffraction experiments are more easily analysed than those produced through X-ray diffraction[7].

Neutrons can scatter from atoms in two different ways; the spin of a neutron can interact with the nucleus of the atom, or the neutrons magnetic dipole moment can interact with the spin of any unpaired electrons in the atom. As the neutron beam can have either interaction taking place, both nuclear and magnetic structures can be determined through neutron diffraction[10].

Neutron diffraction, as previously mentioned, can be used to identify the long-range magnetic ordering of materials. Even though neutrons do not have any charge they do have a magnetic moment, this moment is due to the spin angular momentum of the neutron creating a spin-half particle. An added complication to magnetic structure determination is the vectoral nature of magnetic moments; they not only have a magnitude but also a direction. A simplification of this occurs when the moments are taken to only have two directions, 'up' and 'down', they are treated as scalars as only positive or negative. Scattering from a repeating magnetic moment pattern will cause Bragg peaks to appear, as seen in non-magnetic scattering. Depending on the magnetic ordering, the magnetic Bragg peaks can overlap with the nuclear Bragg peaks with increased

intensity or can occur at new positions. This is dependent on whether the magnetic unit cell is equal to or larger than that of the nuclear unit cell. When the temperature of the sample is raised above the ordering temperature and the moments are no longer ordered (in a paramagnetic state) the magnetic contribution to the Bragg intensity is lessened and becomes incoherent background. Low angle reflections are used to determine magnetic ordering in materials as the scattering intensity decreases upon increasing 2θ angle[11]. This dependence is due to magnetic scattering requiring an atomic form factor as the scattering is from the much larger electron cloud (as in X-ray scattering) rather than the small nucleus (nuclear scattering). When 2θ goes towards zero for magnetic scattering, the combined amplitudes from all unpaired electrons are in phase, but as 2θ increases, different phases occur as the electron cloud being interacted with is comparable in size to the wavelength of the neutron beam. The form factor effect is seen in X-ray scattering also but is more pronounced for nuclear magnetic scattering as the scattering is from the outermost electronic orbitals[11]. Nuclear scattering does not lose intensity with increasing angle, as the wavelength of the beam is several orders of magnitude higher than the nuclear radii.

There are two methods of neutron beam production; one can be created either through using a high-energy particle accelerator or a nuclear reactor. When neutrons are produced, they are of very high energy (tens to hundreds of mega-electron volts) and so they have very short wavelengths, too short for the diffraction experiments. The neutrons must be slowed down before use in experiments as a result. Water or liquid hydrogen are known as 'moderating' materials with large scattering cross sections and so they are used in this slowing process, bringing the neutrons into thermal equilibrium with the surroundings. After the interaction with moderating materials, the now thermal neutrons are emitted from the surface of said moderator[12]. The process used to produce neutrons in a nuclear reactor, like that of Institut Laue-Langevin, is fission of uranium. This procedure results in neutrons with a spectrum of radiation and the beam is therefore required to go through processes to become a monochromatic beam before diffraction can occur by using a monochromator crystal. In this instance then for experiments the wavelength is fixed, the θ and *d* parameters variable.

2.2.5: Powder Neutron Diffraction Experiments

Neutron diffraction experiments were all performed for this project at the Institut Laue Langevin (ILL) in Grenoble, France. The ILL is an internationally funded neutron facility that uses a nuclear reactor to create neutron beams; it is one of the most intense neutron sources in the world. Three different beamlines were used to perform neutron diffraction experiments on $Sr_2Mn_{2.23}Cr_{0.77}As_2O_2$ and $CeMnAsO_{1-x}F_x$ samples; D1B, D2B and D20. D2B is a very high-resolution two-axis diffractometer used on powder samples. This beamline is used to characterise crystal and magnetic structures of powder samples. A range of temperatures were recorded for both $Sr_2Mn_{2.23}Cr_{0.77}As_2O_2$ and $CeMnAsO_{1-x}F_x$ samples on the D2B beamline. For $Sr_2Mn_{2.23}Cr_{0.77}As_2O_2$ high resolution measurements were taken from 1.5 to 300 K on heating and 200 – 120 K on cooling, with the $CeMnAsO_{1-x}F_x$ series having measurements recorded between 1.5 and 400 K all on heating. Both samples were inserted into 8 mm vanadium cans for measurements, and data recorded with λ = 1.594 Å for 2-3 hours per temperature. D1B and D20 are both high intensity two-axis diffractometers (Figure 2.3) used for variable temperature scans. These beamlines can be used to visualise the temperature evolution of magnetic ordering in samples. Both were used to measure the $Sr_2Mn_{2.23}Cr_{0.77}As_2O_2$ sample, with D20 used for cooling measurements from 300 - 1.5 K, and D1B recording on heating from 3 – 446 K. Depending on the doping level, the cerium series were measured in different temperature ranges but all measurements were recorded with the D20 diffractometer between 1.5 and 380 K. The ramping rates for data recording were 19 seconds per 0.1°.
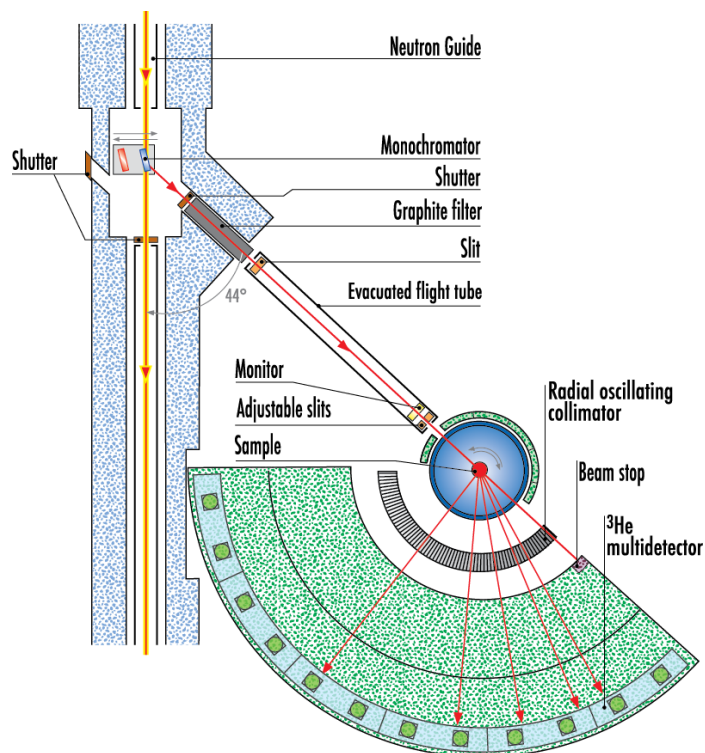
Figure 2.3: Schematic for a neutron diffraction experiment on D1B beamline, a high intensity beamline at the Institut Laue Langevin used for variable temperature scans.

2.3: Rietveld Refinement

The Rietveld method of refinement is a widely used technique, which can extract information about the crystal structure from data produced from a powder diffraction experiment. A least squares approach is applied to refine the crystal structure; this is done by fitting a calculated model to the diffraction pattern profile. The refinements are performed until a best fit is achieved between the whole diffraction pattern and calculated pattern profile[13].

The Rietveld method is not a structure solution method; it is a structure refinement method, meaning it needs an input structure to begin with. The relationship between the adjustment of parameters and the peak intensities observed are not linear. Due to this relationship, a good starting model is necessary to obtain the global minimum. If the starting model is inadequate, a false minimum of refinement can be reached.

The shape of powder diffraction peaks are a function of the sample itself and instrumental features, the shape varies as a function of 2θ. The breadth of the profiles (H), measured as a full width at half maximum (FWHM), had dependence usually modelled by the Caglioti equation. U, V, and W are refineable parameters during the Rietveld method[14].

$$H^2 = U \tan^2 \theta + V \tan \theta + W \tag{8}$$

Modelling of peak shapes is performed using a profile function, the most commonly used one for both X-ray and neutron diffraction is the pseudo-Voigt function, as used throughout this project. This function is an approximation of the Voigt function, it is a linear combination of the Gaussian and Lorentzian functions. The two following equations outline the model for the variation of FWHM as a function of 2θ for the Gaussian and Lorentzian constituents of peak shapes respectively:

$$FWHM^2 = U \tan^2\theta + V \tan\theta + W \tag{9}$$

$$FWHM = X \tan\theta + \frac{Y}{\cos\theta} \tag{10}$$

The Rietveld refinements are usually performed a few cycles at a time, some complex structures can require hundreds of cycles dependent on the complexity. The refinements of the model against the data should be closely monitored throughout the procedure[15]. The progress of the refinements is usually judged from values known as R-values, the R_{wp} value is considered most significant. For R_{wp} the minimised residual is the numerator:

$$R_{wp} = \left\{ \frac{\sum w_i \left(y_i(obs) - y_i(calc)\right)^2}{\sum w_i \left(y_i(obs)\right)^2} \right\}^{\frac{1}{2}} \tag{11}$$

The R_{wp} value can sometimes be misleading if the background being refined is high. The R_{wp} value used in the end should converge upon the statistically expected R value (R_{exp}) which corresponds to the quality of the data recorded (for example reflects the counting statistics)[16]. The following equation is an expression of R_{exp}, with N as a number of observations and P as the number of parameters being explored.

$$R_{exp} = \left[\frac{(N - P)}{\sum_{i=1}^{N} w_i y_i(obs)^2} \right]^{\frac{1}{2}} \tag{12}$$

Refinement progress can also be monitored by a third R value, known as the profile R value R_p which is calculated as follows:

$$R_p = \frac{\sum \left| y_i(obs) - y_i(calc))^2 \right|}{\sum y_i(obs)} \tag{13}$$

The main factor that is a useful indicator for the refinement progress is known as the goodness of fit, χ^2. The ideal value that this factor should approach is 1.

$$\chi^2 = \left(\frac{R_{wp}}{R_{exp}}\right)^2 \tag{14}$$

A small χ^2 value can, unfortunately, also be created due to quick data collection or from data where the estimated standard deviation of counts are incorrectly calculated[15]. Both R-values and χ^2 values are good tools for determining the improvement of a refinement but they are not the only factors that should be used to judge the refinement quality. The visible fit of the calculated pattern to the observed pattern, plus the background chemical knowledge of the systems' structure, are more important factors for the assessment of refinement quality. At the end of a refinement, the profile plot, atomic parameters, and errors of refined parameters should be carefully inspected[16].

2.4: Resistance

Resistivity is a measurement technique that quantifies the strength of a material to counter the flow of an electrical current. Resistance is related to the voltage and current by Ohm's law, but Ohm's law is only valid when the resistance is constant over a large voltage range.

$$R = \frac{V}{I} \tag{15}$$

The R, bulk resistance, of a system is related to the resistivity (ρ) and even if the system doesn't obey Ohm's law the bulk resistivity can be used to describe resistance. The resistance takes into account the length of the sample (l) and the cross-sectional area (A), producing the following equation:

$$\rho = R\frac{A}{l} \tag{16}$$

The expression only works when the current is assumed uniform across the cross-section of the wire, which is true for direct current (DC). Resistivity is temperature dependent; this temperature dependence of resistivity can be predicted from temperature coefficient of the resistance over large temperature ranges[17].

Variable temperature DC and AC electrical resistance, as well as variable frequency AC transport measurements, were recorded at the Materials Characterisation Laboratory at the ISIS Neutron and Muon Source in Oxford using the Quantum Design physical property measurement system (PPMS). Measurements were recorded between 4 and 300 K, with selected frequencies between 1 Hz and 1000 Hz. The electrical resistivity, ρ was measured using the usual four-probe method; a rectangular bar of the sintered pellet sample is attached to the PPMS "puck" using varnish and four wire electrodes. The electrodes are attached to the sample block by silver paint; a diagram of this set up is shown in Figure 2.4.
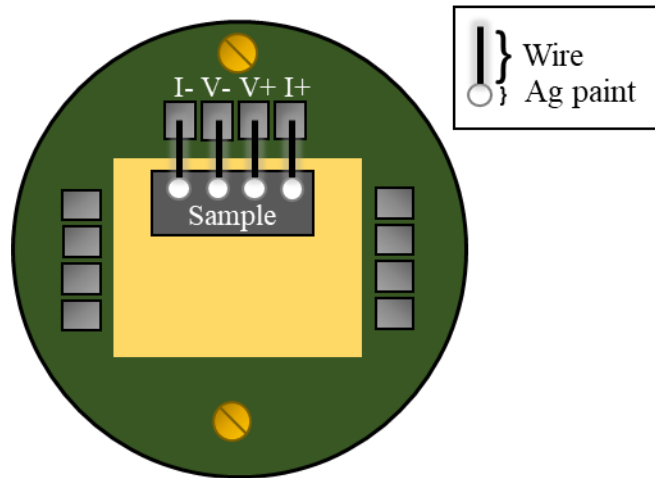
Figure 2.4: Diagram representation of the PPMS puck set up for resistance measurements using the four-probe set-up.

The small sample bar for measurements normally has dimensions of width and height resulting in an area A of around 0.05 cm^2 (A = width × height), the length of the bars is typically around 0.6 cm.

2.5: Magnetic Measurements

A magnetic property measurement system (MPMS) was used in this project to analyse the magnetic properties of all the samples to be discussed in later chapters. A SQUID, magnetometer superconducting quantum interference device, was used throughout this project and uses superconducting technology to determine the changes in externally applied magnetic fields. SQUID magnetometers are built up of two superconductors that form parallel Josephson junctions creating a superconducting loop. Josephson devices are key to high-speed measurements as they are capable of changing states in a matter of picoseconds. The two connected junctions allow an electric current to pass through them by the Josephson effect, the constant current being passed through a SQUID device has varying output voltages because of phase changes of the junctions. The phase changes in the Josephson junctions are due to variation in magnetic flux as a result of the presence of external magnetic fields. Changes in magnetic behaviour of materials can therefore be monitored using a SQUID device through analysis of the voltage changes[18].

In order to perform measurements, samples are prepared by accurately weighing some powder sample (around 100 mg) into one half of a plastic capsule. To keep the powder in the base of the capsule, PFTE tape was used to pack it down and the other capsule half enclosed it. The small capsule is then placed in a plastic straw, around halfway down, and held in place using other pieces of straw so that it couldn't move around or fall out of the straw. The plastic for the straw and capsule has a very small signal in the SQUID, which permit it to be ignored.

Using a MPMS the magnetic moment of a sample can be measured. From the magnetic moment data, calculations of magnetization and magnetic susceptibility can be performed. Samples which are exposed to external magnetic fields with strength *H,* gain magnetization *M* with the following relationship:

$$\chi = \frac{M}{H} \tag{17}$$

The magnetic properties of samples are simply based on the interactions between electron spins in structures. The χ stated is the magnetic susceptibility, this is a measurement of the ease of the electron spins within a material to align with the applied magnetic field. Samples are cooled down

to below 5 K to then be measured on heating. The cooling procedure can be performed either with a magnetic field applied (known as field-cooled, FC) or with no field (zero-field-cooled, ZFC). Typically, magnetic measurements were recorded from low temperature up to room temperature. In our measurements, the magnetisation was recorded in units of emu, which is the default for the MPMS. Magnetic susceptibility is calculated with units of $emu.Oe^{-1}mol^{-1}$.

The χ profiles measured are dependent on the different magnetic behaviour exhibited as seen in Figure 2.5. When a negative magnetic susceptibility is measured this means that the material repels the magnetic field and is diamagnetic in nature. In diamagnetic materials, the induced magnetic field is usually in the opposing direction to that of the applied field, and is a state adopted by molecules with no unpaired electron spins as well as superconducting materials. A positive χ is recorded for paramagnetic materials, which are attracted to magnetic fields[19]. Paramagnetism occurs when the unpaired electron spins align in a material under an applied field, the alignment results in an induced field, which increases applied field.
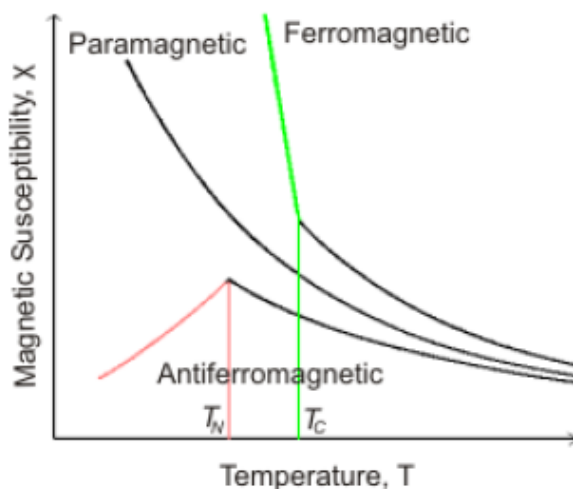
Figure 2.5: The variation of magnetic susceptibility with temperature for differently magnetic ordered systems[20].

Paramagnetism is a weak form of magnetism due to the presence of unpaired electrons in a material (illustrated in Figure 2.6). The spins of the magnetic ions in this case are randomly oriented with no ordering but become weakly magnetised by an external magnetic field, resulting in the spins aligning parallel to the field. A form of net attraction is established by the field induced spin alignment, this magnetization is not retained when the external magnetic field is removed.

69
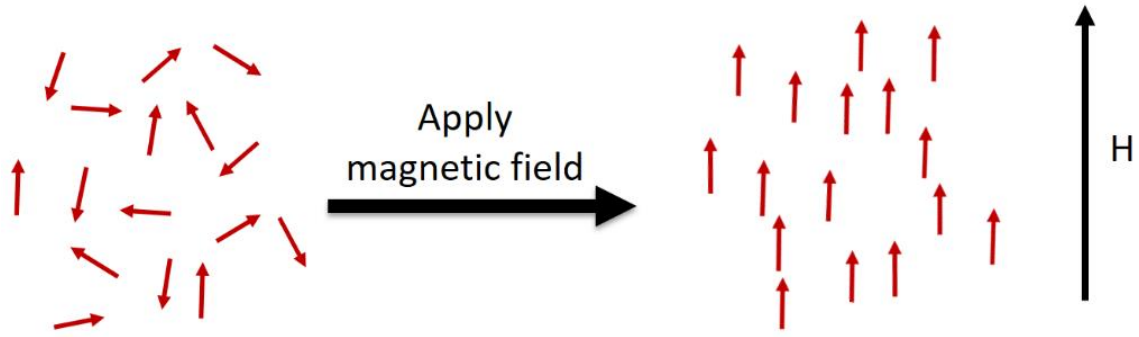
Figure 2.6: Illustration of the parallel alignment of magnetic moment spins along direction of an external magnetic field within a paramagnetic material.

Ferromagnetism occurs when the unpaired electrons in materials form parallel alignments shown in Figure 2.7 a; when this ordering occurs over a large number of atoms it creates a magnetic domain. The magnetic ordering persists even when the external field is removed in ferromagnets, this occurs below the Curie temperature, T_C. When at temperatures above the Curie temperature the increased thermal motion disorders the sample overruling the ordering effect of spin interactions resulting in a paramagnet. The magnetic domains relate to the behaviour seen in magnetic susceptibility curves, wherein ferromagnetic materials magnetisation curves lack retraceability and trace out a loop called a hysteresis loop. Ferromagnetic materials when magnetised in one direction, do not relax to zero magnetisation when the field is removed (like in paramagnets) and so to be driven to 0 a field with opposite direction should be applied. Reversing the direction of the magnetic field to the materials results in the creation of the hysteresis loop.

Antiferromagnetic materials consist of the neighbouring spins in antiparallel arrangements below a Néel temperature T_N. Below this temperature, there is a cancellation of the magnetic moment resulting in the susceptibility decreasing (Figure 2.5). Above the ordering temperatures, the susceptibility is described by the Curie-Weiss formula:

$$\chi = \frac{C}{T - \theta} \tag{18}$$

In Curie-Weiss law, θ is known as the Weiss constant, it will be positive in the case of ferromagnets and negative for antiferromagnets. In layered systems, a variety of different antiferromagnetic ordering can be present; A-, C-, and G-type antiferromagnetism, all with overall net zero magnetisation. G-type AFM ordering of spins occurs when the spins are arranged

70

antiferromagnetically both intraplanar and interplanar, all nearest neighbour spin interactions are antiferromagnetic, (Figure 2.7 b). C-type AFM ordering occurs when the spins have antiferromagnetic intraplanar interactions and ferromagnetic interplanar interactions (Figure 2.7 c). A-type AFM ordering is the inverse of this when spins have ferromagnetic intraplanar interactions and antiferromagnetic interplanar interactions (Figure 2.7 d).
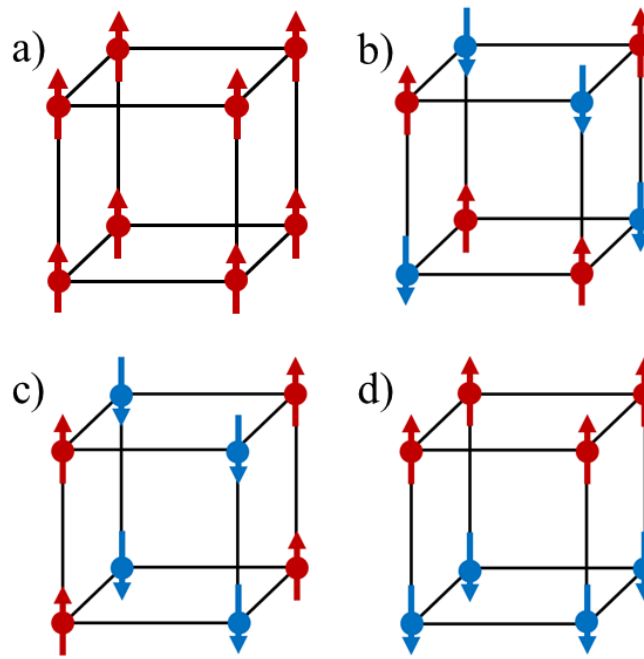
Figure 2.7: Illustration of the different magnetic spin ordering in simple layered systems, a) ferromagnetic ordering, b) G-type AFM ordering, c) C-type AFM ordering, and d) A-type AFM ordering.

Measurements with MPMS were performed for this project on a Quantum design MPMS-XL-7 at the Materials Characterisation Laboratory at ISIS Neutron and Muon Source in Oxford. The later series of samples made with $Ce_{1-x}Sr_xMnSbO$ composition were measured at the Néel institute in Grenoble on the MPMS-XL SQUID. Typically, powder samples are around 100 mg, a few small spatulas full.

References

[1] M. T. Weller, *Inorganic Materials Chemistry*, Oxford University Press, New York, 1994.

[2] A. R. West, *Basic Solid State Chemistry*, John Wiley & Sons Ltd, New York, 1999.

[3] A. R. West, *Solid State Chemistry and its Applications,* John Wiley & Sons Ltd, New York, 1984.

[4] C. Giacovazzo, *Fundamentals of Crystallography*, Oxford University Press, New York, 1992.

[5] M. De Graef and M. E. McHenry, *Structure of Materials*, Cambridge University Press, New York, 2007.

[6] C. Hammond, *The Basics of Crystallography and Diffraction*, Oxford University Press, New York. 1997.

[7] D. S. Sivia, *Elemental Scattering* Theory, Oxford University Press, New York, 2011.

[8] F. Fauth, R. Boer, F. Gil-Ortiz, C. Popescu, O. Vallcorba, I. Peral, D. Fulla, J. Benach and J. Juanhuix, 2015, *Eur. Phys. J. Plus.* **130**, 160.

[9] P. J. E. M. Van der Linden, M. Moretti Sala, C. Henriquet, M. Rossi, K. Ohgushi, F. Fauth, L. Simonelli, C. Marini, E. Fraga, C. Murray, J. Potter and M. Krisch, M., 2016, *Rev. Sci. Instrum.* **87***, 115103.

[10] Pd.chem.ucl.ac.uk, Advanced Certificate in Powder Diffraction on the Web, *Properties Of The Neutron*. url: http://pd.chem.ucl.ac.uk/pdnn/inst3/neutrons.htm, accessed 10/01/21.

[11] B. T. M. Willis and C. J. Carlile, *Experimental Neutron Scattering*, OUP Oxford, Oxford, 2007.

[12] R. Pynn, *Los Alamos Science*, 1990, **19**, 90-114.

[13] H. M. Rietveld, *J. Appl. Cryst.*, 1969, **2**, 65-71.

[14] G. Caglioti, A, Paoletti and F. P. Ricci, *Nucl. Instrum. Methods*, 1958, **135**, 193-195.

[15] L. B. McCusker, R. B. Von Dreele, D. E. Cox, D. Louer and P. Scardi, *J. Appl. Cryst.*, 1999, **32**, 36-50.

[16] R. A. Young, in *The Rietveld Method*, ed. R. A. Young, Oxford University Press, New York, 1993, Chapter 1, 1-38.

[17] Hyperphysics, *Resistance And Resistivity*, url: http://hyperphysics.phy-astr.gsu.edu/hbase/electric/resis.html, accessed on 11/01/21.

[18] M. McElfresh, *Fundamentals of Magnetism and Magnetic Measurements Featuring Quantum Design's Magnetic Property Measurement System*, Purdue University, Quantum Design, 1994, pp. 4.

[19] P. Atkins, J. de Paula, *Elements of Physical Chemistry*, Oxford University Press, Oxford, 4th edn., chapter 15.

[20] M. Weller, T. Overton, J. Rourke and F. Armstrong, *Inorganic Chemistry*, Oxford University Press, 6th edn., chapter 20.

Chapter 3

Synthesis, Electrical and Magnetic Properties of $Sr_2Mn_{2.23}Cr_{0.77}As_2O_2$

3.1: Introduction

The 2322 pnictide system, first discovered in 1991[1], was initially probed as a model system for superconductivity due to the similarity in structure to previously reported high temperature superconductors. Multiple layered pnictide phases $A_2M_3As_2O_2$ (A = Ba, Sr, M_3 = Mn_3, Cr_3, $MnZn_2$, Zn_3, Mn_2Cu) [2, 3, 4, 5, 6, 7] have been studied. The structure has two different transition metal sites present stacking along c direction with alkaline earth cations, A, distributed between them. The first transition metal site, $M(1)$, exists within a square-planar arrangement with oxygen MO_2 similar to the CuO_2 square-planar layering in cuprate superconductors; the second position $M(2)$ is arranged tetrahedrally with arsenic within M_2As_2 layers, like Fe_2As_2 tetrahedra in iron arsenide superconductors. Although there are similarities between this 2322 structure and known high temperature superconductors[8], there has not been evidence of superconductivity within the 2322 pnictide family.

Studies into $Sr_2Mn_3As_2O_2$[9] revealed that the material crystallises with a tetragonal unit cell, space group $I4/mmm$, and down to 4 K no structural phase transitions were detected. The $Mn(2)_2As_2$ sublattice displays long-range G-type AFM order below T_N = 340 K, with the magnetic moments aligned parallel to the c axis. Below 75 K a second magnetic transition occurs, associated with $Mn(1)$ moments rather than the $Mn(2)$ moments. The magnetic reflections seen at low temperature are weak with the strongest peak being of Warren lineshape[9], indicating two-dimensional magnetism. $Sr_2Mn_3As_2O_2$ is revealed as a narrow band gap semiconductor with an activation energy of 147(5) meV through resistivity measurements. $Sr_2Zn_2MnAs_2O_2$ was prepared through substituting some zinc into the manganese 2322 structure[8]. Zn is found to occupy the $M'_2As_2^{2-}$ blocks and the compound is also a semiconductor. Weak magnetic coupling is seen in the Zn_2Mn compound below 38 K as non-magnetic zinc ions disrupt the manganese ordering. A divergence

between ZFC and FC magnetic susceptibility curves confirmed spin-glass type behaviour in the system[10]. $Sr_2Mn_2CuAs_2O_2$ has also been synthesised previously, in this instance copper is substituted into the $Mn(2)_2As_2$ layers, leading to lower Curie temperature of 95(1) K and an A-type ferrimagnetic arrangement of magnetic moments instead of G-type AFM arrangement[2].

$Sr_2Cr_3As_2O_2$ has been synthesised[4] and is isostructural with $Sr_2Mn_3As_2O_2$, consisting of $Cr_2As_2^{2-}$ and CrO_2^{2-} layers. Two magnetic transitions were reported, occurring below 590 K and 291 K, associated with Cr(2) and Cr(1) ordering respectively. At high temperatures, the $Cr(2)^{2+}$ ions form a C-type AFM arrangement parallel to the c axis. In the low temperature region, the $Cr(1)^{2+}$ ions order with a K_2NiF_4-like magnetic structure along c axis. A spin-flip transition is reported to occur within the $Cr_2As_2^{2-}$ sublattice, the moment direction rotates from the c axis to the ab plane. $Sr_2Cr_3As_2O_2$ is metallic, similar to $BaCr_2As_2$[11] and $LaCrAsO$[12]. A more recent study of $Sr_2Cr_3As_2O_2$ and $Ba_2Cr_3As_2O_2$ has been performed[5]. In this instance the strontium analogue is found to undergo a gradual spin reorientation, with the $Cr(1)^{2+}$ magnetic ordering originally appearing in the ab plane rather than along c. The $Cr(1)^{2+}$ spins gradually tilt from the ab plane direction to become parallel to c axis, as this happens the opposite occurs for the $Cr(2)^{2+}$ magnetic moments. The spin reorientation occurs between 297 and 248 K, noted as complete by 247(1) K. As the two chromium moments align in unison, they are thought to be magnetically coupled. The barium analogue of this material does not show any spin reorientation or magnetic coupling, with two magnetic transitions of 473(10) K and 233 K for C-type arrangement of $Cr(2)^{2+}$ ions and long-range AFM ordering of $Cr(1)^{2+}$ ions along c direction respectively.

Following on from this research a mixed manganese and chromium compound was prepared, $Sr_2Mn_2CrAs_2O_2$. Here, the new material was thoroughly investigated with various techniques, including powder X-ray and neutron diffraction, magnetic and resistivity measurements. The major points of interest through this examination were to discover the cation content and if any cation ordering was present for Mn/Cr between the oxide and arsenide layers, as well as compare the magnetic structure to that of the previously studied parent compounds. The results of this study, the nuclear and magnetic structures of $Sr_2Mn_{2.23}Cr_{0.77}As_2O_2$ in particular, are presented in this chapter.

3.2: Experimental

3.2.1: Synthesis

$Sr_2Mn_2CrAs_2O_2$ was made through a solid state reaction method using stoichiometric quantities of Mn (99.98% Aldrich), Cr (99.98% Aldrich) and As pieces (99.97% Alfa Aesar) along with 2% wt. deficiency of SrO (99.99% Aldrich). SrO was prepared through a precursor step involving heating $SrCO_3$ (99.99% Aldrich) at 1200°C for 12 hours to decarbonate it, the material was then cooled in an inert environment to prevent recarbonation. The small oxygen deficiency used is key to increasing purity of the phase, the deficiency was also reported for $Sr_2Cr_3As_2O_2$ synthesis[4]. The starting materials were mixed together in an inert atmosphere in a glove bag using an agate mortar and pestle to grind the powders to a homogeneous mix. The combined powders were then pelleted and placed into an evacuated quartz tube (14mm diameter) to be heated at 800°C for 10 hours and then a further heat at 980°C for 48 hours. The sintered pellet was then ground back into a powder, pelleted and heated at 1000°C for 48 hours. Two $Sr_2Mn_2CrAs_2O_2$ samples were prepared and combined after laboratory XRD found them to have the same structure.

3.2.2: Powder X-ray Diffraction

X-ray powder diffraction patterns were recorded on the PANalytical Empyrean powder diffractometer with Cu Kα1 radiation (λ = 1.540598 Å). Quick scans were performed between range of 5° < 2θ < 70° using a 0.0131° step size for around 12-30 minutes. Longer scans were recorded for Rietveld refinements on the XRD. The same PANalytical Empyrean diffractometer was used for the high-quality scans, with counting time around 16 hours. The patterns were recorded between range of 10 < 2θ < 120°, step size of 0.003°. Synchrotron X-ray diffraction patterns were collected for the $Sr_2Mn_2CrAs_2O_2$ mixture on the BL04-MSPD beamline of the ALBA synchrotron in Barcelona, Spain[13]. The highest angular resolution was obtained using the Multi Analyzer Detection (MAD) setup. Powder diffraction patterns were collected in the angular range 0 < 2θ < 45° with a step size of 0.003°. Low temperatures were achieved using the lHe flow cryostat Dynaflow[14] and data were recorded from 10 - 220 K, λ = 0.4123 Å.

3.2.3 Powder Neutron Diffraction

Neutron diffraction experiments were performed for the $Sr_2Mn_2CrAs_2O_2$ mixture at the Institut Laue Langevin (ILL) in Grenoble, France. D1B, D2B, D20 beamlines were used for analysis of the $Sr_2Mn_2CrAs_2O_2$ sample. For $Sr_2Mn_2CrAs_2O_2$ high-resolution measurements were taken on D2B beamline from 1.5 to 300 K on heating and 200 to 120 K on cooling. Around 1g of sample was inserted into a 8 mm vanadium can for measurements, and data was recorded with $\lambda = 1.594$ Å for 2-3 hours counting per temperature. D20 beamline was used for cooling measurements from 300 - 1.5 K, and D1B recorded on heating from 3 – 446 K. The ramping rates for data recording were 19 seconds per 0.1°.

3.2.4: Magnetic Measurements

Magnetisation measurements of $Sr_2Mn_2CrAs_2O_2$ were recorded on a Quantum Design SQUID magnetometer using an applied field of 1000 Oe after zero field cooling (ZFC) and field cooling (FC) the sample, measuring in the range 4 – 400 K.

3.3: Results and Discussion

3.3.1: Previous Work

The research on $Sr_2Mn_2CrAs_2O_2$ was first undertaken by Dr Eve Wildman as part of postdoctoral studies at the University of Aberdeen. Magnetic susceptibility was recorded for $Sr_2Mn_2CrAs_2O_2$ with varying temperature, the zero-field-cooled (ZFC) and field-cooled (FC) temperature dependence is shown in Figure 3.1. Two magnetic transitions are seen, one at around 150 K and the second around 50 K. The transitions were proposed to correspond to the ordering of $M(2)_2As_2$ and $M(1)O_2$ layers respectively. The magnetic behaviour exhibited is comparable to that of the manganese parent compound $Sr_2Mn_3As_2O_2$, which also shows two antiferromagnetic transitions at $T_N = 350$ K and 50 K[7]. The low temperature transition at 50 K is associated with weak 2-dimensional antiferromagnetic ordering of the $MnO_2{}^{2-}$ layers. The magnetic transition temperatures in the chromium parent compound, $Sr_2Cr_3As_2O_2$ are much higher in contrast, $T_C = 590$ K (Cr_2As_2 layers) and 291 K (CrO_2 layers)[4]. The $Sr_2Mn_2CrAs_2O_2$ sample would be expected to have ordering

temperatures between the two parent phases given the mixed manganese and chromium occupancy, so the 50 K ordering is surprising.
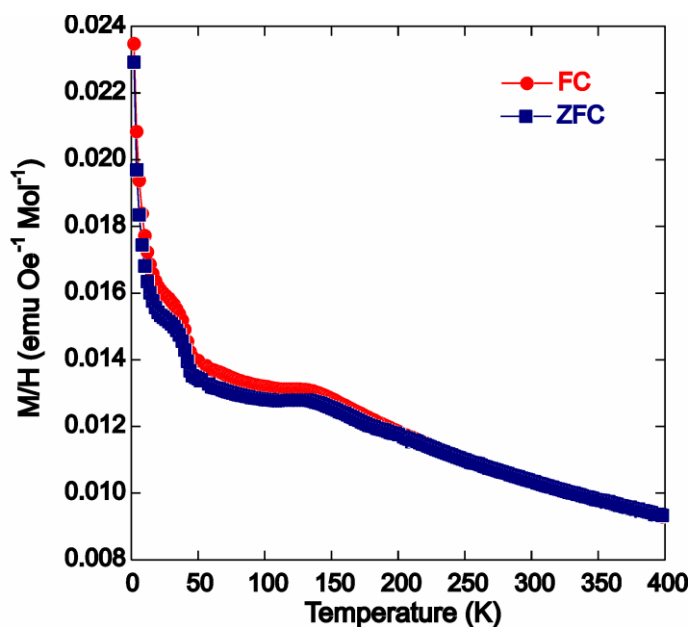
Figure 3.1: The ZFC and FC magnetic susceptibility variation with temperature of $Sr_2Mn_2CrAs_2O_2$ in a field of 1000 Oe.

3.3.2: Crystal Structure Determination from Neutron Diffraction

Initial crystal structure determination for $Sr_2Mn_2CrAs_2O_2$ was performed from laboratory powder X-ray diffraction. The sample was confirmed through Rietveld refinement as being in the tetragonal space group *I4/mmm*, with unit cell parameters $a = 4.1061(1)$ Å and $c = 19.0490(3)$ Å. The crystal structure for $Sr_2Mn_2CrAs_2O_2$ is shown in Figure 3.2. A small impurity was present in the diffraction pattern, indexed as $Cr_{0.7}Mn_{0.3}As$, making up around 5% of the sample (Figure 3.3) was included in the refinement fit.
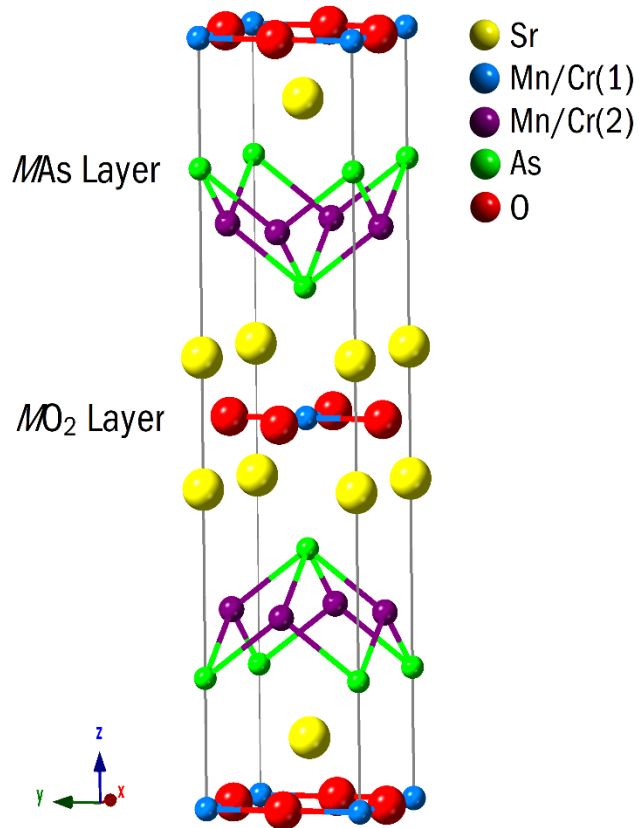
Figure 3.2: Nuclear structure of $Sr_2Mn_2CrAs_2O_2$ with alternating $M(1)O_2$ layers and $M(2)_2As_2$ layers along c, strontium cations are spread between the layers.
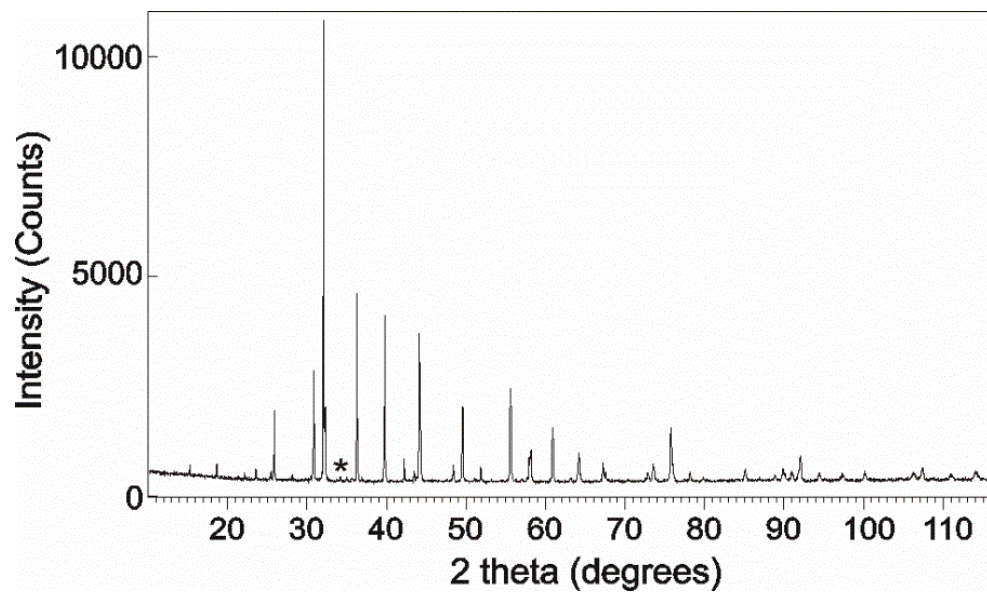
Figure 3.3: XRD pattern of $Sr_2Mn_2CrAs_2O_2$, (*) highlighting the impurity peak assigned to a small (~5%) impurity of $Cr_{0.7}Mn_{0.3}As$.

A problem faced when analysing the XRD data for $Sr_2Mn_2CrAs_2O_2$ is that the site occupancy of Mn and Cr cannot be determined. As they are neighbours in the periodic table, they scatter X-rays similarly and hence cannot be distinguished through this technique. Neutron diffraction was used to determine the cation ordering in this system due to the neighbouring element issue. The $Sr_2M_3As_2O_2$ structure contains two distinct transition metal sites, Wyckoff position $2a$ located in the $M(1)O_2$ layers and $4d$ Wyckoff site is contained within the $M(2)_2As_2$ layers. The distribution of manganese and chromium within these two positions was determined through Rietveld refinement[15] on the high-resolution neutron diffraction data recorded at 300 K using the FullProf Suite package[16].

To perform the refinement, background points were initially selected from the baseline of the datafile only in regions between peaks and then the model refined against the data. The shapes of the diffraction peaks were fitted using a Pseudo-Voigt function. An excellent fit was obtained for the tetragonal $I4/mmm$ space group for the 300 K data file (Figure 3.4), refined parameter values of $a = 4.0935(1)$ Å, $c = 19.0646(6)$ Å; final $\chi^2 = 2.25$, $R_{WP} = 11.1\%$. The fractional occupancies for strontium, oxygen and arsenic were refined and found to be within $\pm 1\%$ of their full occupancy and so were fixed for all further refinements at 1.0.
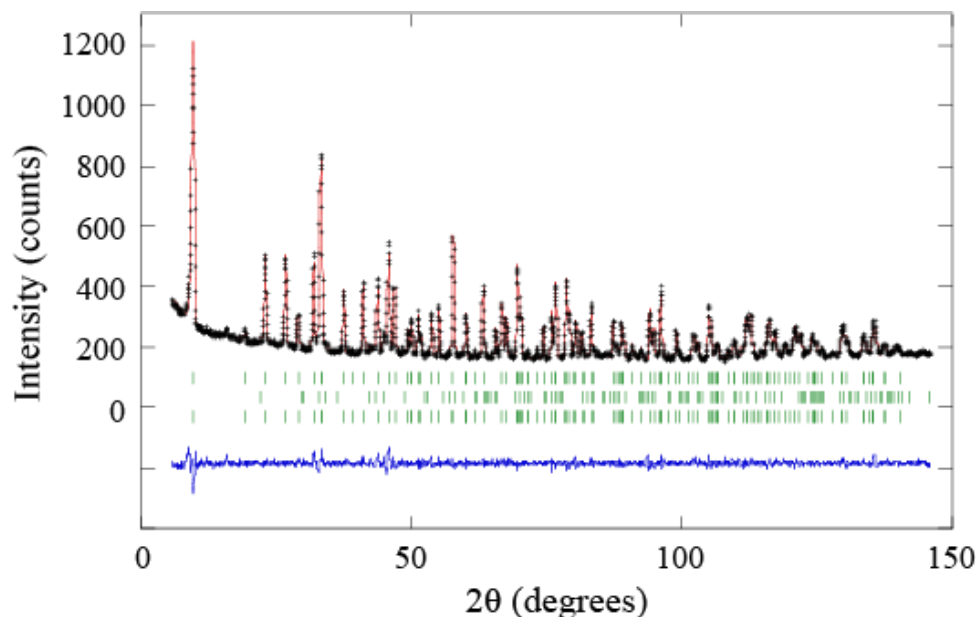
Figure 3.4: Rietveld refinement fit for 300 K data set, fit to the I4/mmm structural model of Sr₂Mn₂CrAs₂O₂ recorded on heating. The impurity phase (Cr₀.₇Mn₀.₃As) is included in the fit as well as the high temperature magnetic phase. The tick marks displayed represent the nuclear phase, impurity phase, and magnetic phase from top to bottom respectively.

To determine the site occupancy, different constraints were used to obtain the best fit. The M(2) site was found to be mainly occupied by manganese ions, a refined occupancy of 96% was obtained. Chromium was found to be predominantly on the M(1) site, the refined occupancies in this square planar arrangement were 68% Cr and 32 % Mn. From these occupancy values, it is clear that the overall stoichiometry is not the intended $Sr_2Mn_2CrAs_2O_2$ but $Sr_2Mn_{2.23}Cr_{0.77}As_2O_2$ instead. As the M(1) site has mixed occupancy of the two transition metal cations, it added a complication to the refinements. Only a small scattering length at M(1) position occurred as a result of the cancellation of the two ion scattering lengths, Mn (-3.73 fm) and Cr (3.635 fm). To resolve this issue the isotropic atomic displacement parameters (B_{iso}) for both M positions were constrained to be the same value. The site occupancies obtained through refinements demonstrate that cation ordering occurs between manganese and chromium ions, resulting in Cr^{2+} predominantly being found on the square planar $M(1)O_2$ site. Chromium with 2+ valence has d^4 electron configuration and so the crystal field stabilisation energy (CFSE) as well as Jahn-Teller distortion leads to the preferential ordering in this system. Cr^{2+}, due to these effects, is principally found in either distorted octahedral or square planar geometry[17]. Manganese ions with 2+ valence (as in this system) is a high-spin d^5 configured system, so there is no CFSE and can occupy either the square planar or tetrahedra layers with no preference, filling in the spaces not occupied by Cr.

Variable temperature neutron diffraction experiments were performed and the Rietveld method was used to refine a model and determine the changes to the crystal structure as temperature changes. The refined values found from D2B data treatments on heating are shown in Table 3.1 with additional refinement fits displayed in Appendix Figures 8.1 and 8.2. The refined values found from D2B data treatments on cooling are displayed in Appendix Table 8.1, with refinement plots displayed in Appendix Figures 8.3, 8.4 and 8.5. As displayed in the table, once the occupancies of Mn and Cr were refined they were then fixed for the remaining refinements. The refinements performed did include the magnetic structure fits, these will be discussed in a later section, it is clear though from the given agreement factors that the refined models are satisfactory. As expected with lowering temperature, the *a* and *c* cell parameters (and thus the unit cell volume) decrease as the lattice contracts. Cyclic refinements were performed on the variable temperature diffraction measurements recorded on D1B and D20 beamlines. With this data, figures of the refined cell parameters could be produced with a larger dataset, see figure Figure 3.5. The region pointed to by

the arrows is consistent with a change in magnetic data to be discussed later; regular cell contraction is seen otherwise.
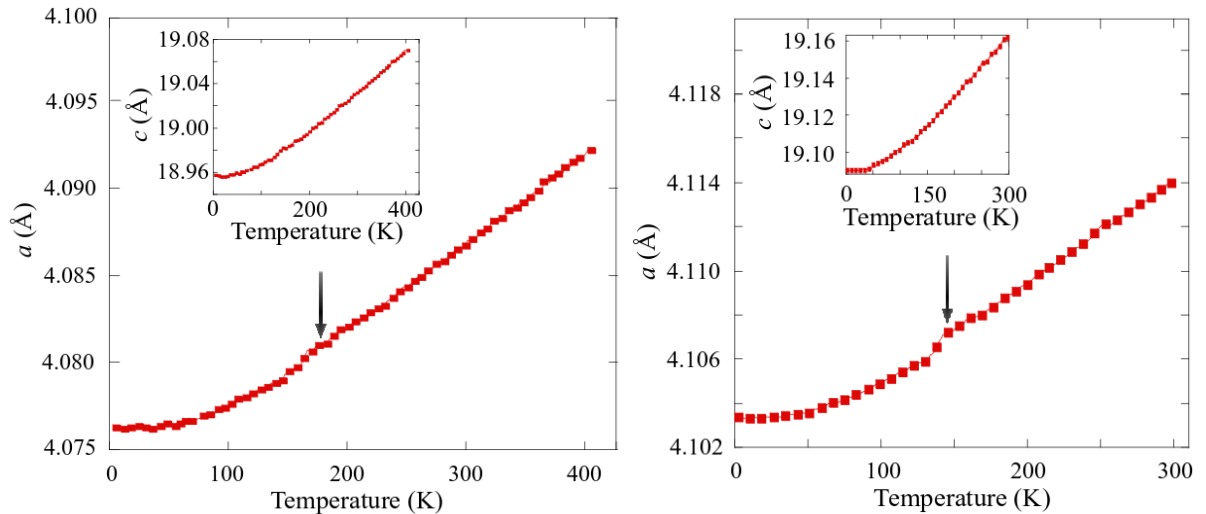
Figure 3.5: Temperature variance of a and c (inset) cell parameters upon heating (left) and cooling (right).Usual cell contraction is seen, other than the areas highlighted by arrows relating to a change in magnetic behaviour to be discussed later.

Selected bond lengths and angles obtained from the high-resolution data refinements on heating are shown in Table 3.2 and Figure 3.6. The bond lengths and angles obtained from data refinements on cooling are shown in Appendix Table 8.2. When the sample undergoes heating, the expected lengthening occurs for multiple bond lengths including Sr-O, Sr-As, M(1)-As and M(1)-O. The M(1)-As bond length variation is shown in Figure 3.6 and the trend of increasing length with raising temperature is seen with a levelling-off occurring around 160 K, matching the temperature of lattice constant change mentioned before. A more visible change is evident when looking at the bond angles, for example Figure 3.6 inset image of M(2)-As-M(2) bond angle variation. When going from 1.5 K to 120 K there is initially a decrease in angle from 69.07(3)° to 69.01(3)°, upon heating above 160 K the angle then increases with angle of 69.06(3)° at 300 K. Similar relationships between bond angle and temperature are witnessed for the two reported angles As-M(2)-As (Table 3.2), so it appears something is occurring within the arsenide tetrahedra around 160 K that could be influencing the cell parameter changes previously mentioned. The changes in bond angles are not statistically significant as they fall within error, so these trends are not the most reliable but they do indicate a change.

Table 3.1: Refined cell parameters, agreement factors and atomic parameters for $Sr_2Mn_{2.23}Cr_{0.77}As_2O_2$ from Rietveld fits against D2B neutron diffraction data recorded at various temperatures on heating. Wyckoff sites for each ions are as follows: Sr and As are at 4e (0, 0, z), Mn(1)/Cr(1) at 2a (0, 0, 0), Mn(2)/Cr(2) at 4d (0, ½, ¼) and O at 4c (0, ½, 0).

	Temperature (K)								
	1.5	**25**	**75**	**100**	**120**	**160**	**200**	**300**	**450**
Sr z	0.41420(9)	0.41437(9)	0.41427(9)	0.41433(10)	0.41433(10)	0.41432(10)	0.41428(9)	0.41444(9)	0.41447(10)
Sr B_{iso}	0.03(3)	0.04(3)	0.11(3)	0.12(4)	0.04(3)	0.21(4)	0.37(3)	0.40(3)	0.91(4)
M1 B_{iso}	0.37(22)	0.23(20)	0.17(21)	0.10(22)	0.06(21)	0.07(22)	0.20(20)	0.20(20)	0.41(22)
M1 Mn occupancy	0.31744	0.31744	0.31744	0.31744	0.31744	0.31744	0.31744	0.31744	0.31744
M1 Cr occupancy	0.68256	0.68256	0.68256	0.68256	0.68256	0.68256	0.68256	0.68256	0.68256
M2 B_{iso}	0.50(6)	0.16(5)	0.29(5)	0.20(6)	0.05(5)	0.31(6)	0.46(5)	0.41(5)	0.95(6)
M2 Mn occupancy	0.978560	0.978560	0.978560	0.978560	0.978560	0.978560	0.978560	0.978560	0.978560
M2 Cr occupancy	0.021440	0.021440	0.021440	0.021440	0.021440	0.021440	0.021440	0.021440	0.021440
As z	0.16985(9)	0.16980(9)	0.16977(9)	0.16972(9)	0.16971(9)	0.16981(10)	0.16974(9)	0.16994(9)	0.16964(10)
As B_{iso}	0.26(3)	0.20(3)	0.28(3)	0.29(3)	0.23(3)	0.39(3)	0.51(3)	0.58(3)	1.04(4)
O B_{iso}	0.04(3)	0.00(3)	0.03(3)	0.05(3)	0.04(4)	0.19(4)	0.32(3)	0.30(3)	0.97(4)
a (Å)	4.08339(6)	4.08329(6)	4.08396(6)	4.08455(6)	4.08499(6)	4.08700(6)	4.08908(11)	4.09354(10)	4.10258(11)
c (Å)	18.9933(3)	18.9936(3)	18.9983(3)	19.0041(3)	19.0071(3)	19.0208(3)	19.0337(6)	19.0646(6)	19.1239(7)
Unit Cell Volume (Å³)	316.697(8)	316.686(8)	316.867(8)	317.056(8)	317.174(8)	317.715(9)	318.253(16)	319.467(14)	321.879(16)
χ^2 (%)	3.12	2.96	2.98	3.11	3.23	3.33	2.73	2.25	2.50
R_{WP} (%)	12.0	12.1	12.4	12.8	13.4	14.0	12.5	11.1	14.0
R_P (%)	11.4	11.4	11.7	12.1	13.0	13.8	12.8	11.6	15.0
R_{Bragg} (%)	2.78	2.55	2.99	2.78	3.52	3.42	3.37	2.13	3.50

Table 3.2: Selected bond length and angle variation with temperature taken from Rietveld refinement fits against D2B neutron diffraction data recorded on heating between 1.5 and 300 K.

	Temperature (K)							
	1.5	**25**	**75**	**100**	**120**	**160**	**200**	**300**
Sr-As(Å)	3.2993(12)	3.3004(12)	3.2998(12)	3.3005(12)	3.3008(12)	3.3034(13)	3.3042(12)	3.3115(12)
Sr-O (Å)	2.6123(11)	2.6103(11)	2.6120(11)	2.6118(12)	2.6121(12)	2.6138(12)	2.6157(11)	2.6172(11)
Sr-M1 (Å)	3.3155(8)	3.3139(8)	3.3154(8)	3.3155(9)	3.3159(9)	3.3178(9)	3.3200(8)	3.3225(8)
Sr-M2 (Å)	3.7276(14)	3.7303(14)	3.7295(14)	3.7314(16)	3.7320(16)	3.7343(16)	3.7360(14)	3.7440(14)
M1-As (Å)	3.2260(17)	3.2251(17)	3.2253(17)	3.2254(17)	3.2257(17)	3.2299(19)	3.2308(17)	3.2398(17)
M1-O (Å)	2.04169(3)	2.04164(2)	2.04197(3)	2.04228(3)	2.04250(3)	2.04350(3)	2.04453(6)	2.04677(5)
M2-As (Å)	2.5468(10)	2.5473(10)	2.5481(10)	2.5492(10)	2.5496(10)	2.5500(11)	2.5522(10)	2.5532(10)
M2-M2 (Å)	2.88739(3)	2.88732(3)	2.88779(3)	2.88821(3)	2.88852(3)	2.88995(3)	2.89141(6)	2.89457(5)
M2-As-M2 (°)	69.07(3)	69.05(3)	69.03(3)	69.01(3)	69.01(3)	69.04(4)	69.01(3)	69.06(3)
As-M2-As 1 (°)	106.58(3)	106.55(3)	106.52(3)	106.48(3)	106.47(3)	106.52(4)	106.47(3)	106.57(3)
As-M2-As 2 (°)	110.93(7)	110.95(7)	110.97(7)	110.99(7)	110.99(7)	110.96(8)	110.99(7)	110.94(7)
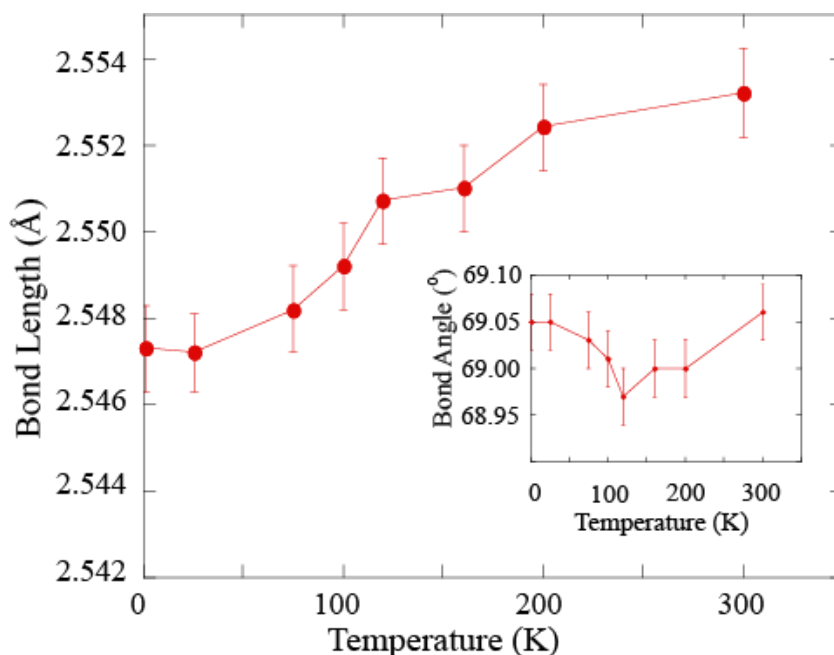
Figure 3.6: Variable temperature plot of M(2)-As bond length and M(2)-As-M(2) bond angle (inset), a clear variation below 160 K is seen for the given bond angle.

3.3.3: Magnetic Structure Determination from Neutron Diffraction

Neutron diffraction is key to determining the magnetic ordering within a crystal structure, thanks to the magnetic dipole of a neutron allowing interactions with magnetic spins of a sample. The process to unearth the magnetic structure was performed in multiple steps. A high-resolution neutron diffraction pattern was needed at a higher temperature than the magnetic ordering temperature, for the high T region in this sample case a pattern recorded at 450 K showed no magnetic Bragg peaks. The magnetic peaks are known as they decrease in intensity as temperature increases and then either disappear if they are at new angles of 2θ or lower, and remain at consistent intensity as the sample continues to be heated if they appear at the same 2θ angle as nuclear Bragg reflections. Comparison is then performed between a pattern with no magnetic reflections and one with clear magnetic reflections (450 K and 300 K high-resolution patterns in the case of the high temperature region for $Sr_2Mn_{2.23}Cr_{0.77}As_2O_2$) and the magnetic peaks are identified and angles 2θ of occurrence recorded. Using an add-on feature of FullProf Suite package, *k*-search, the most likely magnetic propagation vectors (*k*-vectors) were determined. To perform a *k*-search a .sat file is used, which includes the cell parameters and space group, as well as whether to search for

commensurate or incommensurate *k*-vectors, and key is the inclusion of the magnetic Bragg peak positions. Once the most probable *k*-vector is found, this information is then applied in the BasIreps program (also part of FullProf Suite of programs) to analyse the possible symmetry of the magnetic phase (basis vectors) and a trial and error method was employed to attain the best fit[15,16]. In this BasIreps stage, the atomic positions of magnetic ions are required, as well as best fitting *k*-vector and crystal symmetry. The information obtained is easily extracted from this program for use within the FullProf refinements.

High intensity neutron diffraction data between 1.5 and 450 K were recorded, the temperature evolution of magnetic peaks are shown in Figure 3.7. A Néel temperature $T_C = 410$ K was recorded for the high temperature magnetic phase, as evident in the figure the (101) and (103) diffraction peaks are significantly increased. The propagation vector k_1 was determined as $k_1 = 0$ as no new reflections appear. The magnetic ordering at high temperatures was resolved from refinement performed for 300 K high-resolution neutron diffraction data, see Figure 3.4. The refined magnetic structure was a G-type antiferromagnetic ordering of the manganese/chromium ions within the arsenide tetrahedra layers (M(2) position), the magnetic moments align in this arrangement along *c*. This magnetic ordering shown to the right of Figure 3.8 is the same as seen in the $Sr_2Mn_3As_2O_2$ phase at high temperatures, and will be referred to as AFM-HT for the rest of the chapter.
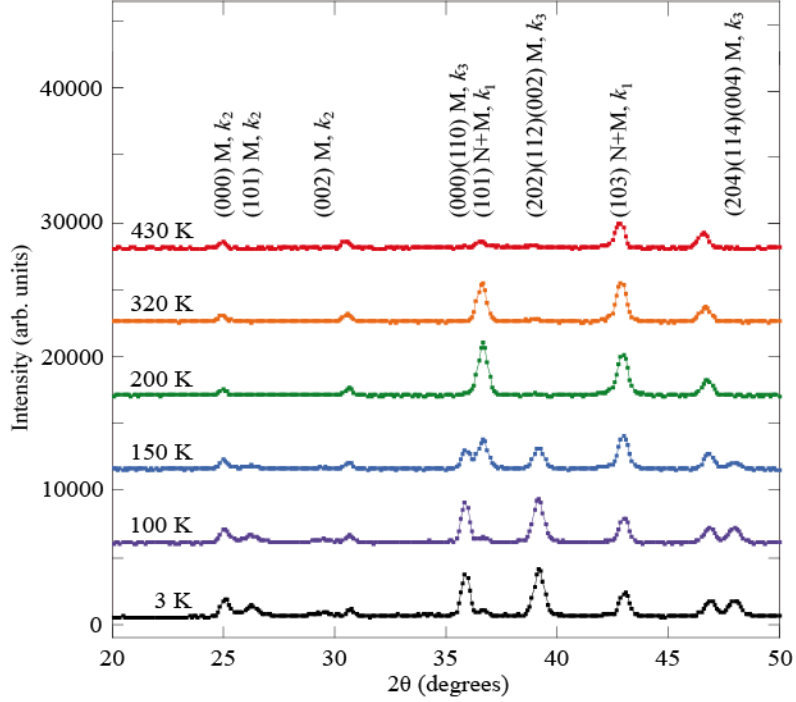
Figure 3.7: Selected high intensity neutron diffraction patterns of $Sr_2Mn_{2.23}Cr_{0.77}As_2O_2$ at varying temperatures between 3 and 430 K on heating. Bragg reflections are labelled and evolution and appearance of magnetic diffraction peaks are evident.

New magnetic Bragg peaks appear in the neutron diffraction patterns recorded below 167 K, as can be seen in Figure 3.7. A portion of the new diffraction peaks seen relate to magnetic ordering within the oxide layers, with long-range antiferromagnetic ordering of the M(1) ion spins along c. The propagation vector is $k_2 = (½, ½, 0)$, as is reported within the CrO_2 layers of $Sr_2Cr_3As_2O_2$[4] at low temperatures, where the M(1) moments order with the La_2CuO_4-like antiferromagnetic structure[18]. Further new reflections were seen at low temperatures, indicating a simultaneous ordering with the established M(1) long-range AFM order. These Bragg reflections are indexed with a new propagation vector $k_3 = (1, 0, 0)$, described as a C-type AFM arrangement of the $M(2)^{2+}$ magnetic moments within the $M(2)_2As_2^{2-}$ sublattice along c. The low temperature magnetic order can be seen on the left of Figure 3.8. The ordering in the arsenide layers for $Sr_2Mn_{2.23}Cr_{0.77}As_2O_2$ below 167 K is the same arrangement as reported for $Sr_2Cr_3As_2O_2$ between 291 and 590 K[4]. The AFM-LT structure as displayed in Figure 3.8 does not display the full magnetic unit cell of $Sr_2Mn_{2.23}Cr_{0.77}As_2O_2$, instead this is a depiction of the magnetic ordering on the nuclear unit cell. As the k_2 propagation vector results in an extension of the unit cell, this new magnetic unit cell is

fully displayed for the low temperature arrangement in Figure 3.9 with new unit cell dimension $a_{MAG} = \sqrt{2}a$, with c remaining unchanged.
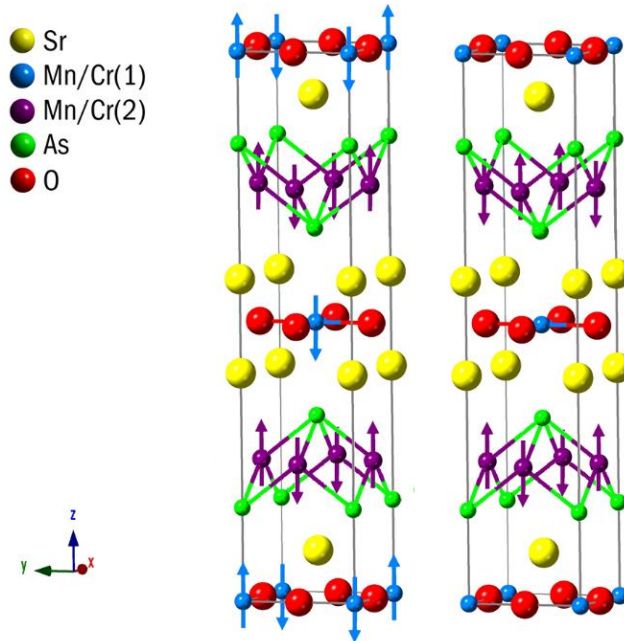
Figure 3.8: The crystal structures of $Sr_2Mn_{2.23}Cr_{0.77}As_2O_2$ showing the magnetic ordering of Mn/Cr^{2+} ions as determined through refinements performed for neutron diffraction data at 1.5 K (left) and 300 K (right). The left magnetic structure is seen below 135 K (AFM-LT) and the right magnetic structure above 167 K (AFM-HT).

There is evidence of magnetic coupling of the two transition metal layers in $Sr_2Mn_{2.23}Cr_{0.77}As_2O_2$, similar to the behaviour exhibited in $Sr_2Cr_3As_2O_2$[5]. In the chromium parent compound, the ordering of the Cr^{2+} in the oxide layers initially in the ab plane results in the gradual spin reorientation of the Cr^{2+} moments in the arsenide tetrahedral layers from parallel alignment to the c axis into the ab plane, with the opposite spin reorientation occurring within the CrO_2 planes[5]. In $Sr_2Mn_{2.23}Cr_{0.77}As_2O_2$ the M(2) site spins flip from a G-type AFM arrangement ($k_1 = 0$) to a C-type AFM arrangement ($k_3 = (1, 0, 0)$) but remain parallel to c. The refinement fit for base temperature neutron diffraction (1.5 K) is shown in Figure 3.10.
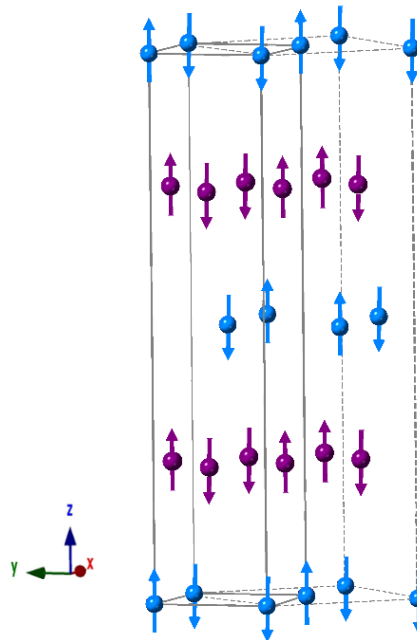
Figure 3.9: The magnetic unit cell of $Sr_2Mn_{2.23}Cr_{0.77}As_2O_2$ at 1.5 K showing the expanded dimensions from the nuclear unit cell due to magnetic propagation vector $k_2 = (\frac{1}{2}, \frac{1}{2}, 0)$. The solid lines represent the nuclear unit cell and the dashed lines show the magnetic unit cell dimensions $a_{MAG} = \sqrt{2}a$, $c_{MAG} = c$.
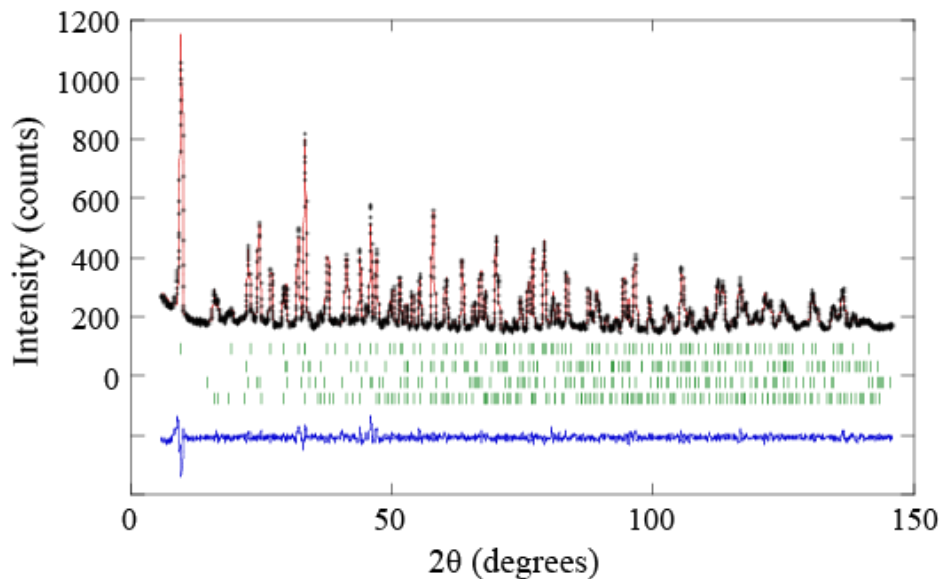
Figure 3.10: The Rietveld refinement fit to the I4/mmm structural model of $Sr_2Mn_{2.23}Cr_{0.77}As_2O_2$ at 1.5 K. The tick marks represent Bragg reflection positions for $Sr_2Mn_{2.23}Cr_{0.77}As_2O_2$ nuclear phase, $Cr_{0.7}Mn_{0.3}As$ impurity, M(2) k_3 magnetic phase, and M(1) k_2 magnetic phase top to bottom respectively.

Interesting behaviour was seen upon analysing the high intensity neutron diffraction temperature scans. Between 135 K and 167 K both the AFM-HT and AFM-LT (Figure 3.8) are present in the material. The so-called magnetic phase separation of the two magnetic structures is clearly evidenced in Figure 3.11. The (101) nuclear and magnetic peak seen at 34.9° and 36.8° 2θ in the top and bottom contour plots respectively, arises in correspondence with the G-type antiferromagnetic arrangement of M(2) ions with propagation vector $k_1 = 0$. The (000) and (202) magnetic peaks in Figure 3.11 bottom at 35.5° and 39° 2θ are due to the $k_3 = (1, 0, 0)$ C-type AFM arrangement of the same M(2) cations within the arsenide tetrahedral layers. Clearly, it can be viewed that both of these magnetic orderings exist within this temperature range ~ 167 – 135 K. The magnetic peaks for the M(1) site ($k_2 = $ (½, ½, 0) are of lower intensity and angle but exhibit the same behaviour as the peaks of the k_3 phase.
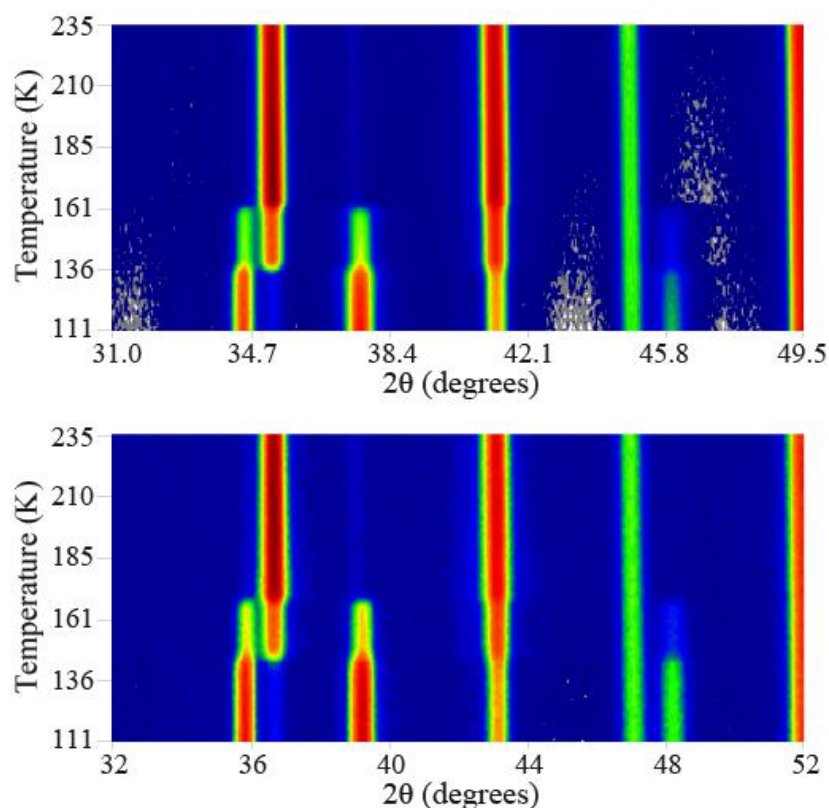
Figure 3.11: Contour plots from D1B (recording data on heating, top) and D20 (recording data on cooling, bottom) neutron diffraction experiments showing the peak intensities of a select 2θ region as temperature is changed. Clear separation between the two magnetic phases is evidenced. The 2θ regions are slightly shifted between the two plots due to the different wavelengths of experiments.

The refined magnetic moments with varying temperature are shown in Figure 3.12 on both heating (left) and cooling (right) of $Sr_2Mn_{2.23}Cr_{0.77}As_2O_2$. The refined magnetic moments for D2B high-resolution neutron diffraction data appear as solid symbols, showing good agreement between the multiple data collections. A slight hysteresis in the magnetic phase transition temperatures is present upon heating and cooling, with the magnetic phase separation occurring between 138 K and 167 K on heating and 164 K and 135 K on cooling. There is a variation in the programs between the two neutron diffraction beamlines, whether they record temperature at the beginning or the end of the measurement, and thus the hysteresis could be as a result of this discrepancy. Upon cooling the sample the M(2) $k_1 = 0$ magnetic phase refined magnetic moment increases until a maximum around 3 μ_B/M ion at 167 K before dropping into a plateau region. In the temperature range ~167 - 138 K the M(2) magnetic moment settles at around 2 μ_B/M ion before this magnetic ordering is fully replaced by the M(2) $k_3 = (1, 0, 0)$ C-type AFM ordering. The AFM-LT order trends in magnetic moment are clearly shown in Figure 3.12 to display the opposite behaviour to the AFM-HT magnetic moment (M(2) k_1). Both magnetic orderings appear at around 167 K but at a lower value and stay in this plateau region with calculated magnetic moments ~2.5 μ_B/M ion until the M(2) k_1 ordering vanishes. At base temperatures the magnetic moments reach 3.94(6) μ_B/M(1) ion and 3.38(2) μ_B/M(2) ion.
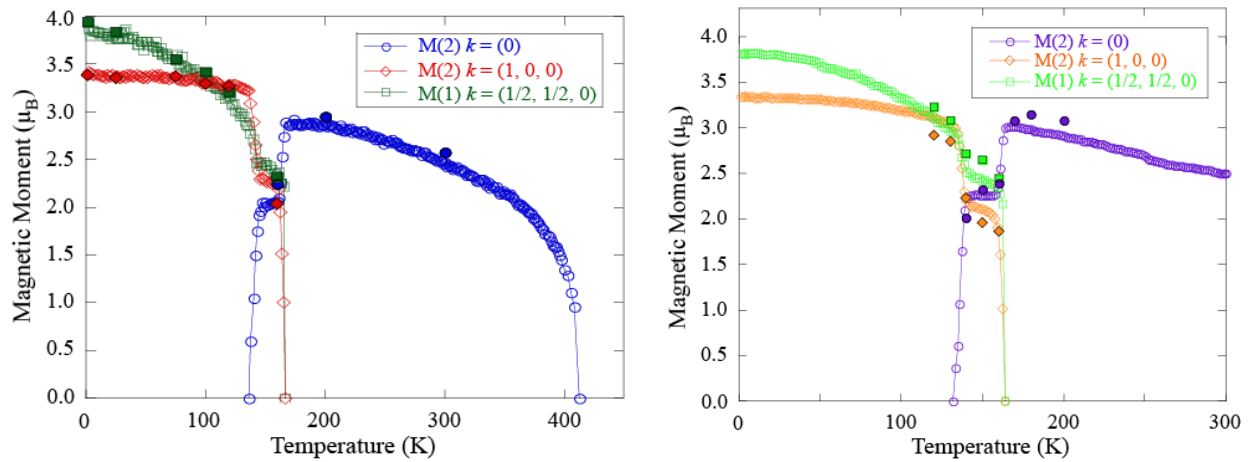
Figure 3.12: Temperature variation of the M(1) and M(2) magnetic moments from D1B (heating, left) and D20 (cooling, right) neutron diffraction data refinements. The filled points on each figure are from D2B high-resolution neutron diffraction data refinements.

In reality, in contrast to the figures above, the magnetic moments of each magnetic phase are not lower in the phase segregation temperature region, but instead only a fraction of the overall sample

is in each conformation (AFM-HT or AFM-LT). During the performed Rietveld refinements, the scale factors of the magnetic phases were all constrained to the same value as the nuclear phase as the magnetic moments and scale factors could not both refine at the same time. To further simplify the overall procedure when performing refinements, magnetic moment calculations were performed by only considering one transition metal ion to occupy the site. For the refinements chromium magnetic form factor was used for the M(1) position and manganese magnetic form factor was used for the M(2) position. The refined magnetic moments from D2B neutron diffraction data on heating are shown in Table 3.3 with the magnetic agreement factors (R factors) also noted. The values obtained from D2B neutron diffraction data on cooling are shown in Appendix Table 8.3.
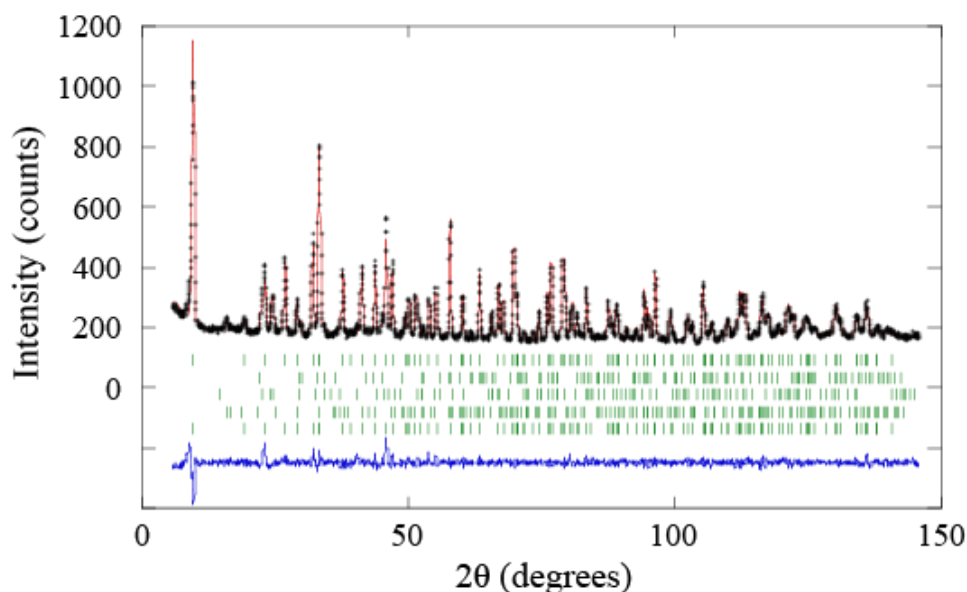
Figure 3.13: The Rietveld refinement fit to the I4/mmm structural model of $Sr_2Mn_{2.23}Cr_{0.77}As_2O_2$ at 160 K. The tick marks represent Bragg reflection positions for $Sr_2Mn_{2.23}Cr_{0.77}As_2O_2$ nuclear phase, $Cr_{0.7}Mn_{0.3}As$ impurity, M(2) k_3 magnetic phase, M(1) k_2 magnetic phase, and M(2) k_1 magnetic phase, top to bottom respectively.

A refinement was performed on the 160 K high-resolution neutron diffraction data which allowed the magnetic phase scale factors to refine while keeping magnetic moment of the M(2) k_1 phase constant (at the value adopted at temperature just above the phase separation); the fit can be seen in Figure 3.13. The phase fractions of the two magnetic phases are 59.8% (AFM-HT) and 40.2% (AFM-LT) at 160 K upon cooling. Refinement of the 160 K data recorded on heating found 56.0%

(AFM-HT) and 44.0% (AFM-LT). The phase fraction for AFM-HT magnetic structure rapidly drops below 146 K, and the magnetic ordering is no longer observed below 135 K. AFM-LT configuration phase fraction shows the opposite behaviour, beginning to increase at 146 K, and is the only magnetic ordering occurring below 135 K. Within the region of 167 and 146 K, very little change is seen in the magnitude of either M(1) or M(2) magnetic moments, or the phase fractions when refined.

The nuclear cell parameters, as mentioned in section 3.3.2, show subtle deviation from general decreasing trend as temperature decreases. The observed deviation to a and c cell parameters occurs at around 160 K, coinciding with the magnetic phase separation, so it appears that the magnetic behaviour is coupled to the crystal structure. The bond angle discrepancies, also previously reported, again occur at around 160 K, indicating that the magnetic transition into this segregated region with both AFM-HT and AFM-LT configurations influences a distortion to the $M(2)_2As_2^{2-}$ tetrahedra layer that subtly influences the a and c parameters. To investigate the observed magnetic phase separation in $Sr_2Mn_{2.23}Cr_{0.77}As_2O_2$ synchrotron X-ray diffraction patterns were recorded.

Table 3.3: Refined magnetic moments of three magnetic phases in $Sr_2Mn_{2.23}Cr_{0.77}As_2O_2$ with increasing temperature, calculated from refinement fits to D2B neutron diffraction data. Magnetic phase agreement factors also presented.

	Temperature (K)							
	1.5	**25**	**75**	**100**	**120**	**160**	**200**	**300**
Ordered moment (μ_B) Cr k_2	3.94(6)	3.84(6)	3.56(7)	3.41(7)	3.20(7)	2.31(13)		
Ordered moment (μ_B) Mn k_1						1.86(1)	2.96(2)	2.57(2)
Ordered moment (μ_B) Mn k_3	3.38(2)	3.36(2)	3.37(2)	3.29(2)	3.26(2)	1.97(3)		
R_{Mag} Cr (%)	3.30	3.13	4.05	4.08	3.99	9.62		
R_{Mag} Mn$_{000}$ (%)						10.0	2.08	1.00
R_{Mag} Mn$_{100}$ (%)	2.79	2.79	3.45	2.95	2.83	9.08		

3.3.4: Synchrotron X-ray Diffraction Analysis

Synchrotron X-ray diffraction was fundamental in this project for understanding the reasoning behind the magnetic phase separation witnessed through neutron diffraction experiments. This technique is key in evidencing subtle peak splitting. The neutron diffraction experiments performed lack the resolution to observe this splitting.

The high-resolution synchrotron X-ray diffraction measurements revealed some interesting behaviour. Throughout the whole temperature region investigated (10 K – 220 K), a subtle splitting of diffraction peaks is observed, see Figure 3.14. The peak splitting is due to the presence of two nuclear phases within the sample, each phase crystallising in the tetragonal *I4/mmm* symmetry space group with marginally diverse cell parameters. The results of Rietveld refinement fits to the synchrotron X-ray diffraction data are shown in Table 3.4. At 220 K (see full refinement fit in Figure 3.15) the cell parameters determined from the refined model of each phase are $a = 4.09082(2)$ Å, $c = 19.0785(1)$ Å for phase 1 and $a = 4.09884(2)$ Å, $c = 19.0288(1)$ Å for phase 2. The refined scale factors for the two phases showed that around 60% of the sample consists of phase 1, and 40% of it is phase 2.
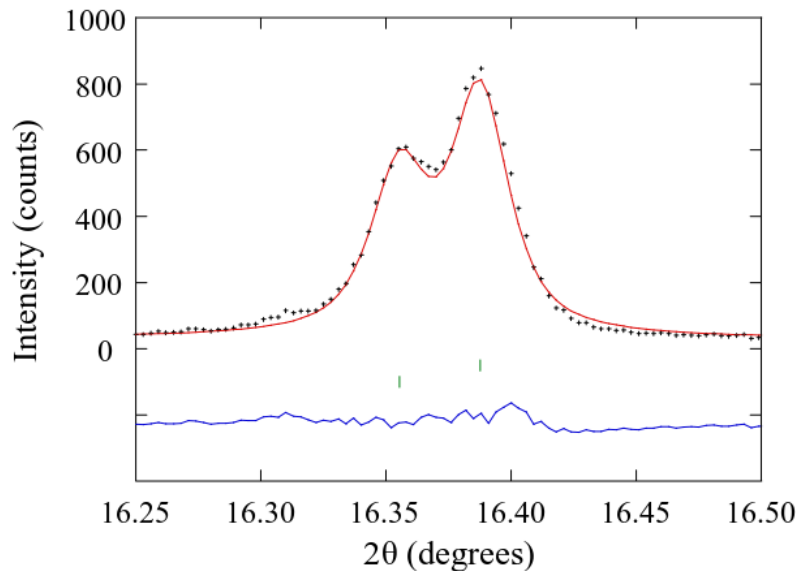
Figure 3.14: Rietveld refinement fit of the split (220) reflection of 220 K $Sr_2Mn_{2.23}Cr_{0.77}As_2O_2$ synchrotron data. The two phases have slightly different angles that the reflection falls at, so the tick marks are for phase one and phase two going from top to bottom respectively.
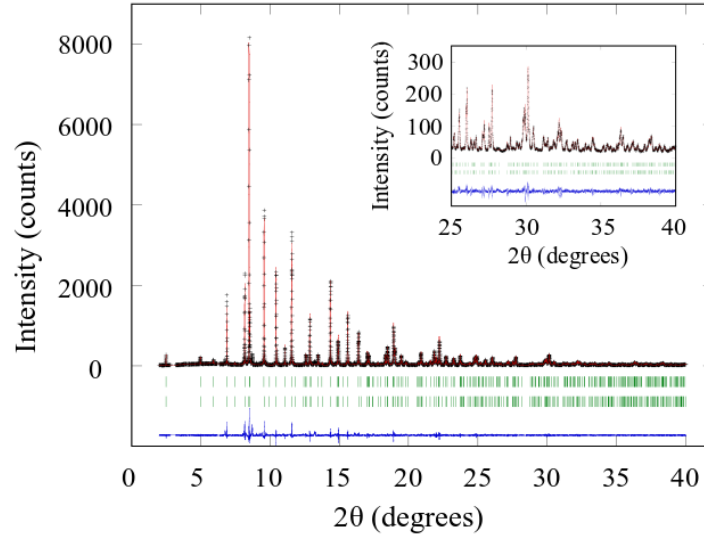
Figure 3.15: Rietveld refinement fit to the 220 K synchrotron X-ray diffraction data, inset displaying a zoomed portion of the higher angle portion of the refinement. Tick marks represent the Bragg reflections for phase 1 and phase 2 top to bottom respectively. There is a visible gap in the fit at low angle, where an instrumental peak has been removed from the model.

The lattice parameters determined from synchrotron X-ray diffraction data refinements show the expected decrease with temperature as the lattice contracts for both nuclear phases, see Table 3.4. The additional refinement fit plots are displayed in Appendix Figure 8.6. Selected bond lengths and angles obtained from the synchrotron X-ray diffraction data refinements are shown in Table 3.5, Figure 3.16 and Figure 3.17. As seen with the refinements performed for the neutron diffraction data, as the sample undergoes heating the expected lengthening occurs for multiple bond lengths for both phases including Sr-As, Sr-M(1), Sr-M(2), M(1)-O, M(1)-As and M(2)-M(2). The trends seen for some other bond lengths not only vary from the usual linear trends, but also the two phases show variation, as seen in Figure 3.16. The M(2)-As bond lengths reported show interesting variation, for phase 2 the usual linear increase with temperature is seen other than a slight bump at 155 K but this falls within the errors. Phase 1 Mn(2)-As values display a clear gradient change after the temperature is increased above 155 K, see Figure 3.16. The M(2)-As bond length remains somewhat constant when temperature is increased from 10 to 155 K, only at higher temperatures a rapid increase to the bond length is witnessed, with similar trend seen for phase 2 Sr-O bond length. All the bond angles reported deviate at temperatures above 155 K. The M(2)-As-M(2) (Figure 3.17) and first As-M(2)-As bond angles exhibit the same behaviour with the two bond angles for phase

95

1 increasing to a maximum value at 155 K before decreasing with further increasing temperature. For phase 2, the opposing trend is seen with a minima at 155K as the angles decrease with increasing temperature until 155 K then an increase is seen with higher temperatures. The second As-M(2)-As bond angle behaves in the opposite way, in this case the value for phase 1 has a minimum at 155 K and phase 2 value reaches a maximum at 155 K. It is key to keep in mind that 155 K is within the region of magnetic phase separation so both nuclear phases display different magnetic ordering at 155 K. This further indicates that the magnetic transition into the region of magnetic phase separation influences a distortion of the $M(2)_2As_2$ tetrahedra.

Table 3.4: Refined cell parameters, agreement factors and atomic parameters for both nuclear phases of $Sr_2Mn_{2.23}Cr_{0.77}As_2O_2$ sample from Rietveld fits against synchrotron X-ray diffraction data between 10 K and 220 K on heating.

		Temperature (K)				
		10	120	155	180	220
	χ^2 (%)	8.34	7.25	7.16	7.11	7.22
	R_{WP} (%)	19.0	18.2	18.6	18.5	18.7
	R_P (%)	14.5	13.9	14.3	14.2	14.3
Phase 1	a (Å)	4.08451(2)	4.08622(2)	4.08768(1)	4.08901(2)	4.09082(2)
	c (Å)	19.0382(1)	19.0491(1)	19.0594(1)	19.0671(1)	19.0785(1)
	Unit Cell Volume (Å³)	317.618(6)	318.066(5)	318.466(4)	318.801(5)	319.276(5)
	Scale (%)	55.1(5)	57.0(4)	60.2(4)	60.9(4)	60.8(4)
	R_{Bragg} (%)	3.65	3.46	3.68	3.72	3.79
	Sr z	0.41436(9)	0.41440(8)	0.41445(8)	0.41437(8)	0.41438(8)
	Sr B_{iso}	0.15(3)	0.27(3)	0.29(3)	0.35(3)	0.41(3)
	M B_{iso}	0.33(5)	0.45(4)	0.47(4)	0.54(4)	0.59(4)
	As z	0.16975(10)	0.16972(9)	0.16971(9)	0.16981(9)	0.16986(9)
	As/O B_{iso}	0.30(4)	0.44(4)	0.46(3)	0.52(3)	0.57(3)
Phase 2	a (Å)	4.09239(2)	4.09426(2)	4.09601(2)	4.09705(2)	4.09884(2)
	c (Å)	18.9851(1)	18.9974(1)	19.0084(1)	19.0163(1)	19.0288(1)
	Unit Cell Volume (Å³)	317.956(6)	318.453(6)	318.910(5)	319.205(6)	319.694(6)
	Scale (%)	44.9(5)	43.0(4)	39.8(4)	39.1(4)	39.2(4)
	R_{Bragg} (%)	4.02	3.64	3.95	3.80	4.03
	Sr z	0.41472(10)	0.41473(10)	0.41474(12)	0.41484(11)	0.41484(12)
	Sr B_{iso}	0.17(4)	0.28(4)	0.29(4)	0.32(4)	0.45(4)
	M B_{iso}	0.25(5)	0.35(6)	0.35(6)	0.39(6)	0.48(6)
	As z	0.16909(12)	0.16920(29)	0.16932(13)	0.16917(13)	0.16915(13)
	As/O B_{iso}	0.20(4)	0.28(4)	0.24(4)	0.31(5)	0.40(5)

Table 3.5: Selected bond length and angle variation with temperature, taken from Rietveld refinement fits against synchrotron X-ray diffraction data recorded on heating between 10 and 220 K.

		Temperature (K)				
		10	**120**	**155**	**180**	**220**
Phase 1	**Sr-As(Å)**	2.6133(11)	2.6140(10)	2.6146(10)	2.6164(10)	2.6176(10)
	Sr-O (Å)	3.3024(12)	3.3040(11)	3.3057(11)	3.3070(11)	3.3091(11)
	Sr-M1 (Å)	3.3166(8)	3.3177(7)	3.3186(7)	3.3205(8)	3.3220(8)
	Sr-M2 (Å)	3.7366(14)	3.7392(13)	3.7418(13)	3.7420(13)	3.7442(13)
	M1-As (Å)	3.2317(19)	3.2330(17)	3.2346(17)	3.2378(17)	3.2407(17)
	M1-O (Å)	2.042255(10)	2.043111(10)	2.043840(7)	2.044502(9)	2.045411(9)
	M2-As (Å)	2.5505(11)	2.5520(10)	2.5532(10)	2.5530(10)	2.5537(10)
	M2-M2 (Å)	2.888185(10)	2.889395(10)	2.890427(7)	2.891363(9)	2.892648(9)
	M2-As-M2 (°)	68.97(4)	68.96(3)	68.95(3)	68.98(3)	68.99(3)
	As-M2-As 1 (°)	106.40(4)	106.37(3)	106.35(3)	106.42(3)	106.44(3)
	As-M2-As 2 (°)	111.03(8)	111.04(7)	111.05(7)	111.02(7)	111.01(7)
Phase 2	**Sr-As(Å)**	2.6093(12)	2.6105(13)	2.6117(14)	2.6113(13)	2.6127(14)
	Sr-O (Å)	3.3024(14)	3.3051(14)	3.3078(16)	3.3083(16)	3.3098(16)
	Sr-M1 (Å)	3.3159(9)	3.3175(9)	3.3189(11)	3.3190(10)	3.3206(11)
	Sr-M2 (Å)	3.7372(16)	3.7395(16)	3.7417(19)	3.7447(18)	3.7469(19)
	M1-As (Å)	3.2100(20)	3.2140(20)	3.2190(20)	3.2170(20)	3.2190(20)
	M1-O (Å)	2.046195(10)	2.047130(10)	2.048004(9)	2.048525(10)	2.049420(10)
	M2-As (Å)	2.5586(14)	2.5587(14)	2.5586(15)	2.5611(15)	2.5626(15)
	M2-M2 (Å)	2.893757(10)	2.895079(10)	2.896315(9)	2.897052(10)	2.898318(10)
	M2-As-M2 (°)	68.87(4)	68.91(4)	68.94(5)	68.89(5)	68.87(5)
	As-M2-As 1 (°)	106.21(4)	106.27(4)	106.35(5)	106.24(5)	106.21(5)
	As-M2-As 2 (°)	111.13(10)	111.09(10)	111.06(10)	111.11(10)	111.13(11)
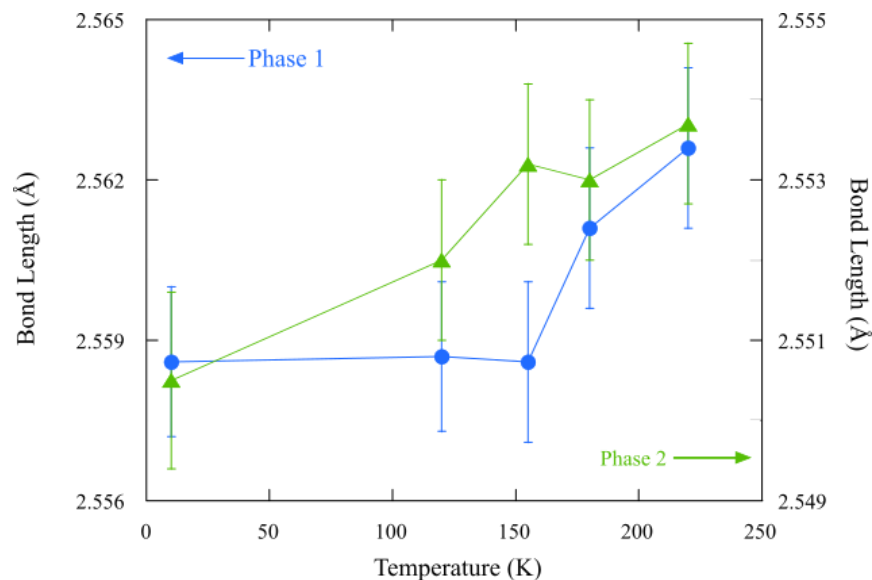
Figure 3.16: Variable temperature plot of M(2)-As bond length for both nuclear phases; a change is seen for the phase 1 values with minimal variation from 10 to 155 K but a rapid increase is seen at higher temperatures.
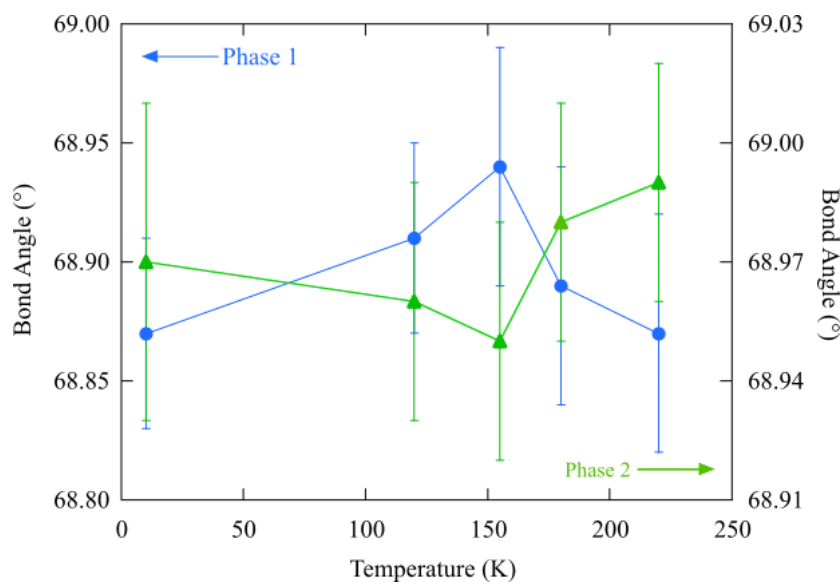
Figure 3.17: Variable temperature plot of M(2)-As-M(2) bond angle for both nuclear phases; a subtle variation below 155 K is seen for the given bond angle.

Looking at previous research within this system it is clear that when the x content is increased in $Sr_2Mn_{3-x}Cr_xAs_2O_2$ from 0 to 3, the unit cell parameters at 300 K decrease from $a = 4.2267(5)$ Å and $c = 20.159(3)$ Å [9] to $a = 4.00671(6)$ Å and $c = 18.8310(3)$ Å [4]. Comparing this trend to the two

phases seen in $Sr_2Mn_{2.23}Cr_{0.77}As_2O_2$, it suggests that the different cell parameters reported for the two nuclear phases are caused by slightly different chromium and manganese stoichiometry in the two phases. Through reexamination of the neutron diffraction data it is possible to observe very subtle peak broadening in the diffraction patterns for some (h00) or (00l) reflections, see Figure 3.18 for the (006) reflection refinement fit. At the tip of the peak in the (006) reflection profile fit, it can be seen that the observed data is slightly flattened and that a broadening occurs, this is, however, not of high enough resolution to index multiple Bragg reflections or perform a refinement for the two nuclear structures. Due to both the inability of X-ray diffraction techniques to distinguish neighbouring elements and the lack of resolution in neutron diffraction to see both nuclear phases, it is not possible to define the exact Cr/Mn stoichiometries of the two phases.
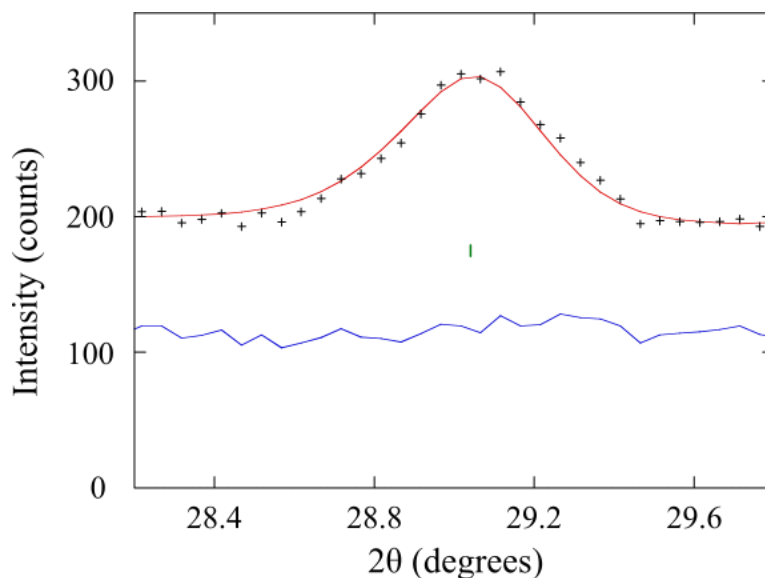
Figure 3.18: Rietveld refinement fit of the (006) reflection of 300 K $Sr_2Mn_2CrAs_2O_2$ neutron diffraction data showing slight broadening of the peak due to the presence of two nuclear phases.

The magnetic phase separation seen through neutron diffraction data in Figure 3.11 and Figure 3.12 can be explained through the nuclear phase separations seen through synchrotron X-ray diffraction data. The phase fractions found for both magnetic phase separation (neutron diffraction data) and nuclear phase separation (synchrotron X-ray diffraction data) have very similar values. At 160 K the two magnetic phase fractions were refined to 59.8% (AFM-HT ordering) and 40.2% (AFM-LT ordering), agreeing well with the 155 K nuclear phase fractions of 60.2% (phase 1) and 39.8% (phase 2) obtained from the synchrotron X-ray diffraction data. From these fractions, it can be rationalized that nuclear phase 2 orders at higher temperatures into the AFM-LT configuration,

with $M(1)^{2+}$ ions in the $M(1)O_2^{2-}$ planes ordering at 167 K. Phase 1 therefore changes to the AFM-LT structure at the lower temperature of 135 K. It is clear through these findings that the $M(1)^{2+}$ ion magnetic ordering is very sensitive to small changes in sample stoichiometry. As $Sr_2Cr_3As_2O_2$[4] has a higher M(1) ordering temperatures than $Sr_2Mn_3As_2O_2$[9] it can be deduced that phase 2, which orders at 167 K into the AFM-LT configuration, has a higher chromium content than phase 1 (ordering at lower temperature of 135 K).

3.4: Conclusions

A new sample with mixed manganese and chromium occupancy in the $Sr_2M_3As_2O_2$ family was made. The structural, electronic and magnetic properties of the prepared $Sr_2Mn_2CrAs_2O_2$ sample were investigated. Similar results to the parent compounds of $Sr_2M_3As_2O_2$ were found for the physical and structural properties, the significant difference seen between the materials was in the magnetic ordering adopted.

The magnetisation measurements revealed two antiferromagnetic transitions at 150 and 50 K and no divergence between the ZFC and FC recordings. The 50 K transition is not observed in the neutron diffraction measurements and so it could be due to the small impurity phase.

$Sr_2Mn_2CrAs_2O_2$ crystallises in the $I4/mmm$ tetragonal space group, as previously reported for $Sr_2M_3As_2O_2$ phases, at 300 K cell parameters are $a = 4.0935(1)$ Å and $c = 19.0646(6)$ Å. A small impurity indexed as $Cr_{0.7}Mn_{0.3}As$ was found to represent ~5% of the overall sample mass, the impurity is assumed to be responsible for the 50 K AFM transition seen in magnetisation measurements that is not visible with neutron diffraction experiments. The $Sr_2Mn_2CrAs_2O_2$ structure contains two distinct transition metal sites, $M(1)O_2$ layers and $M(2)_2As_2$ layers. Manganese was found to mainly occupy the M(2) position with 96% occupancy, the M(1) position is mainly occupied by chromium with 68% Cr occupancy and 32% Mn occupancy. Cr^{2+} has d^4 electron configuration, the CFSE as well as Jahn-Teller distortion leads to the preferential ordering of chromium in the square-planar oxide layers. From the data collected from Rietveld refinement, the overall stoichiometry of the sample was clearly not the intended $Sr_2Mn_2CrAs_2O_2$ but instead $Sr_2Mn_{2.23}Cr_{0.77}As_2O_2$. A likely cause for the nonstoichiometry is the reaction of chromium with the silica tube but there was no visible evidence of a reaction in the tube.

Powder neutron diffraction data reveal two magnetic transition temperatures of 410 K and 167 K. Below 410 K the M(2) ions in M(2)$_2$As$_2$ layers order antiferromagnetically in a G-type arrangement of spins, with $k_1 = (0,0,0)$. At temperatures below 167 K the M(1) magnetic moments order into a long-range AFM phase with $k_2 = (½, ½, 0)$, this ordering results in a simultaneous flip of the spins of Mn^{2+}/Cr^{2+} moments in the M(2) position. The spin-flip results in the M(2) ordering changing from G-type AFM ordering to C-type AFM ordering, with both ordering spins parallel to the c axis of the crystal lattice. Between 167 K and 135 K both AFM-HT and AFM-LT ordering coexist, and through neutron diffraction refinements the sample at 160 K was determined to contain 59.8% AFM-HT and 40.2% AFM-LT ordering.

Powder synchrotron X-ray diffraction data revealed that two different nuclear phases coexist for the entire temperature region recorded 10 – 220 K. Both phases crystallise with $I4$/mmm tetragonal space group, but have slightly different cell parameters. Phase 1 was found at 155 K to occupy 60.2(4)% of the sample, and phase 2 occupies 39.8(4)% of the sample. Comparing the results from both neutron and synchrotron data there is a clear correlation between the nuclear phase data and magnetic separation, meaning that phase 2 (occupying around 40% of the sample) can be deduced to order into AFM-LT configuration at 167 K. As Sr$_2$Cr$_3$As$_2$O$_2$[4] has previously been reported to order at higher temperatures than Sr$_2$Mn$_3$As$_2$O$_2$[9], phase 2, which orders at higher temperature is thought to have slightly higher chromium content than phase 1. Due to the limitations of synchrotron X-ray and neutron diffraction, the exact Cr/Mn content of each phase is unknown. The presence of two nuclear phases is expected to be a result of mixing two samples that laboratory X-ray diffraction could not differentiate prior to all measurements.

Some further work should be carried out on the system to better understand the behaviour seen. Variable-pressure neutron diffraction studies of Sr$_2$M$_3$As$_2$O$_2$ phases would be interesting to further investigate the superexchange interactions as a function of unit cell size.

References

[1] N. T. Stetson and S. M. Kauzlarich, 1991, *Inorg. Chem.* **30**, 3969-3971.

[2] R. Nath, V. O. Garlea, A. I. Goldman and D. C. Johnston, 2010, *Phys. Rev. B.* **81**, 224513.

[3] T. C. Ozawa, M. M. Olmstead, S. L. Brock, S. M. Kauzlarich and D. M. Young, 1998, *Chem. Mater.* **10**, 392-396.

[4] J. Liu, J. Wang, J. Sheng, F. Ye, K. M. Taddei, J. A. Fernandez-Baca, W. Luo, G.-A. Sun, Z.-C. Wang, H. Jiang, G.-H. Cao and W. Bao, 2018, *Phys. Rev. B.* **98**, 134416.

[5] X. Xu, M. A. Jones, S. J. Cassidy, P. Manuel, F. Orlandi, M. Batuk, J. Hadermann and S. J. Clarke, 2020, *Inorg. Chem.* **59**, 15898-15912.

[6] E. Brechtel, G. Cordier and H. Schaefer, 1979, *Z. Naturforsch. B.* **34**, 777-780.

[7] S. L. Brock and S. M. Kauzlarich, 1996, *J. Alloy. Compd.* **241**, 82-88.

[8] T. C. Ozawa, S. M. Kauzlarich, M. Bieringer, C. R. Wiebe and J. E. Greedan, 2001, *Chem. Mater.* **13**, 973-980.

[9] S. L. Brock, N. P. Raju, J. E. Greedan and S. M. Kauzlarich, 1996, *J. Alloy. Compd.* **237**, 9-19.

[10] A. Matsushita, T. C. Ozawa, J. Tang and S. M. Kauzlarich, 2000, *Physica B.* **284-288**, 1424-1425.

[11] D. J. Singh, A. S. Sefat, M. A. McGuire, B. C. Sales, D. Mandrus, L. H. VanBebber and V. Keppens, 2009, *Phys. Rev. B.* **79**, 094429.

[12] S.-W. Park, H. Mizoguchi, K. Kodama, S. Shamoto, T. Otomo, S. Matsuishi, T. Kamiya and H. Hosono, 2013, *Inorg. Chem.* **52**, 13363-13368.

[13] F. Fauth, R. Boer, F. Gil-Ortiz, C. Popescu, O. Vallcorba, I. Peral, D. Fulla, J. Benach and J. Juanhuix, 2015, *Eur. Phys. J. Plus.* **130**, 160.

[14] P. J. E. M. Van der Linden, M. Moretti Sala, C. Henriquet, M. Rossi, K. Ohgushi, F. Fauth, L. Simonelli, C. Marini, E. Fraga, C. Murray, J. Potter and M. Krisch, M., 2016, *Rev. Sci. Instrum.* **87**, 115103.

[15] H. Rietveld, 1969, *J. Appl. Crystallogr.* **2**, 65-71.

[16] J. Rodríguez-Carvajal, 1993, *Physica B.* **192**, 55-69.

[17] D. Waroquiers, X. Gonze, G. Rignanese, C. Welker-Nieuwoudt, F. Rosowski, M. Göbel, S. Schenk, P. Degelmann, R. André, R. Glaum and G. Hautier, 2017, *Chem. Mater.* **29**, 8346-8360.

[18] D. Vaknin, S. Sinha, D. Moncton, D. Johnston, J. Newsam, C. Safinya and H. King, 1987, *Phys. Rev. Lett.* **58**, 2802-2805.

Chapter 4

Synthesis and Physical Properties of $CeMnAsO_{1-x}F_x$ series

4.1: Introduction

The recent discovery of a new family of superconductors, the iron oxyarsenides, has led to widespread research into the structure. The highest superconducting transition temperature T_C found so far is within the 1111 family of iron arsenides, the first of which reported was $LaFeAsO$[1]. The 1111 structure consists of alternating layers of iron arsenide tetrahedra ($Fe^{2+}As^{3-}$) and lanthanide oxides tetrahedra ($La^{3+}O^{2-}$) in the $P4/nmm$ symmetry space group. In this structure lanthanum and arsenic are located on the $2c$ Wyckoff site (¼, ¼, z), iron at $2b$ (¾, ¼, ½), and oxygen at $2a$ (¼, ¾, 0). $LaFeAsO_{1-x}F_x$ series displays a highest T_C of 26 K, with only the fluorine doped samples (above 4 atom %) undergoing a superconducting transition. Applying pressure to the system results in the transition temperature shifting to higher values, a maximum $T_C = 43$ K is achieved for 11 atom % $LaFeAsO_{1-x}F_x$ under 4 GPa[2].

Changing the lanthanide ion in the $LnFeAsO_{1-x}F_x$ system has led to differences in the superconductivity. The same layered structure is adopted by all rare earth 1111 iron oxyarsenides, with tetrahedral FeAs layers. $PrFeAsO_{1-x}F_x$ was the first non-cuprate material to have a superconducting T_C above 50 K[3]. The 11 atom % sample shows a drop in resistivity at 52 K and is unmeasurable at 44 K, the application of a magnetic field shifts the temperature of zero resistance to a lower temperature while the onset of superconductivity remains the same. Neodymium[4], Cerium[5], and Samarium[6] analogues have been studied, with $SmFeAsO_{1-x}F_x$ having the highest recorded T_C. The samarium 1111 iron oxyarsenide material have the highest critical temperature of all other known materials so far, outside of the copper oxide family. A high $T_C = 55$ K for 10 atom % fluorine doped $SmFeAsO_{1-x}F_x$[6].

The 1111 family has been further investigated through swapping the iron for other transition metals, with varying properties exhibited outside of superconductivity. The nickel analogues display superconductivity at low temperature; the other transition metal analogues of the 1111 family do not. Superconductivity was reported for the undoped La and Pr *Ln*NiAsO phases; however, in Ce and Sm undoped phases superconductivity is absent. Fluorine doping into LaNiAsO structure resulted in a shift of the superconducting transition to slightly higher temperatures, with the superconducting quality improving also[7]. Zinc, cobalt and chromium analogues of the *LnM*AsO system do not show superconductivity. The samples have been found to exhibit multiple different properties; semiconducting behaviour (*Ln*ZnAsO, *Ln* = La, Ce, Pr) [8], ferromagnetism (*Ln*CoAsO)[9, 10], and metallic-like conduction with AFM ordering (LaCrAsO)[11].

Manganese pnictides have been recently studied, with 1111 structures also adopting the *P*4/*nmm* symmetry space group where the alternating layer structure is maintained. The early system studied, LaMnAsO[12], was found to display a significant magnetoresistance (MR) over a large temperature range, implying strong spin-charge couplings of the $3d^5$ electrons. The conductivity for LaMnAsO was modelled by three-dimensional variable range hopping (3D VRH) of charge carriers, a localisation temperature of 102 K was found.

NdMnAsO is a semiconductor, and the conductivity can also be modelled through 3D VRH of charge carriers[12]. Fluorine doping on the NdMnAsO system induces a rare phenomenon, colossal magnetoresistance (CMR), with the electrical resistivity of samples decreasing by multiple orders of magnitude with application of a magnetic field[13]. The conduction carriers in the system are thought to be only within the manganese arsenide layers and the electronic behaviour is greatly altered by the presence of 5% fluorine doping. As CMR does not occur in the undoped parent phase, the charge carriers are deduced as electrons created through the replacement of O^{2-} ions with F^- ions. The highest value of MR recorded is -95% at 3 K when a 9 T field is applied and the electronic behaviour was fitted to 3D VRH below 75 K but a subtle deviation below 20 K can be modelled by Efros Shkovskii (ES) VRH. A spin reorientation of the Mn^{2+} magnetic moments occurs at 23 K in the NdMnAsO system, the magnetic ordering results in enhanced Coulomb correlations so ES VRH is observed with diminished transport.

Changing from NdMnAsO to PrMnAsO results in different electrical properties exhibited, as CMR is lost[14]. The fluorine doped PrMnAsO samples are semiconducting, with a sizeable $-$MR present

below a structural transition around 35 K. The −MR reaches a maximum peak at 12 K in the 5 atom % fluorine doped sample, before reducing so that the MR at 4 K is −0.9% at 7 T. The absence of CMR in this material can be a result of multiple factors, for example the lack of Efros Shkovskii VRH as the electron correlations are weakened due to the increase of the Mn-As bond lengths below the structural transition. Changing the lanthanide in the 1111 family of Mn oxyarsenides is clearly shown to effect the electronic properties, with multiple MR mechanisms present[14].

4.2: Experimental

<u>4.2.1: Synthesis</u>

CeMnAsO$_{1-x}$F$_x$ (x = 0 – 0.075) were made through a one-step solid state reaction method using stoichiometric quantities of CeAs (prepared), MnO$_2$ (99+% Aldrich), MnF$_2$ (98% Aldrich) and Mn powder (99.99% Aldrich). CeAs was prepared through a precursor step involving reacting small chips of Ce ingot (99% Alfa Aesar) and As (99.97% Alfa Aesar) in a vacuum sealed silica tube 980°C for around 33h, the precursor was then ground in an inert atmosphere to a powder ready for sample preparation. Cerium chips were prepared in a glove bag by first filing the oxidized surface of the larger ingot pieces, then cut using pliers before being weighed and placed in a silica tube. The starting materials were combined in an inert atmosphere in a glove bag using an agate mortar and pestle to grind the powders to a homogeneous mix. The combined powders were then pelleted and placed in a tantalum crucible then into an evacuated silica tube. The tantalum crucible was used to prohibit contact between the pellet and the silica tube as fluorine ion diffusion would occur otherwise. The pellets were then sintered through the following heating procedure:

106
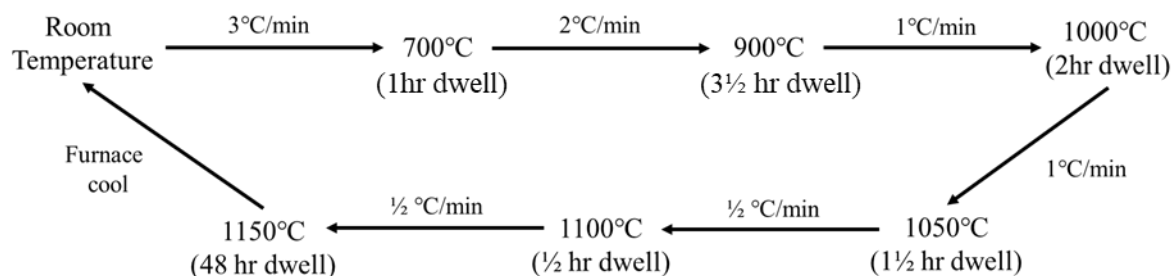
4.2.2: Powder X-ray Diffraction

X-ray powder diffraction patterns were recorded on the PANalytical Empyrean powder diffractometer with Cu Kα1 radiation (λ = 1.540598 Å). Quick scans were performed between range of 5° < 2θ < 70° using a 0.0131° step size for around 12-30 minutes. Longer scans were recorded for Rietveld refinements of the XRD. The same PANalytical Empyrean diffractometer was used for the high quality scans, with counting time around 16 hours. The patterns were recorded between range of 10 < 2θ < 120°, step size of 0.003°.

4.2.3: Resistivity Measurements

Electrical resistance dependence on temperature for the $CeMnAsO_{1-x}F_x$ series was measured using a Quantum Design physical property measurement system (PPMS) in the range 4 - 300 K. Variable temperature AC transport measurements were also performed using the same PPMS system, from 10 – 300 K with frequencies between 1 Hz and 1000 Hz.

4.2.4: Magnetic Measurements

Magnetisation measurements of $CeMnAsO_{1-x}F_x$ were recorded on a Quantum Design SQUID magnetometer using an applied field of 1000 Oe after zero field cooling (ZFC) and field cooling (FC) the sample, measuring in the range 2 – 400 K.

4.3: Results and Discussion

4.3.1: Synthesis and Stoichiometry

Throughout the investigation into the $CeMnAsO_{1-x}F_x$ series, the initial synthesis success proved to be a difficult hurdle to overcome. Any samples with impurities were discarded as only one heating step is implemented. Impurities were greatly reduced through improvement of the precursor quality, a comparison between a pure and impure CeAs precursor and the resultant products XRD patterns can be seen in Figure 4.1 and Figure 4.2. A clear hump can be seen at around 29° 2θ for the impurity containing CeAs sample in purple, this is indexed as a cerium oxide impurity. As is clear by Figure 4.2, the resultant product ($CeMnAsO_{1-x}F_x$) contains extra Bragg reflections caused by impurities in the material (around 27.5° and 30.5° 2θ). Cerium oxide is easily introduced into the precursor through the preparation method, as the cerium ingot oxidises on the surface. The surface oxide is removed with the use of files but some contamination can occur. The oxide is not as a result of cerium reacting with the oxygen in air when the precursor heating occurs, as the tube is fully evacuated and any breakages to the tube would result in complete oxidation.
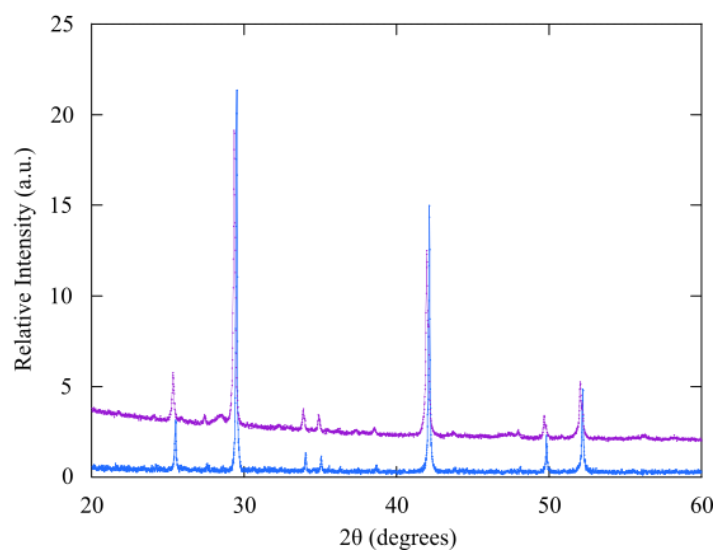
Figure 4.1: Comparison of laboratory X-ray diffraction data from a CeAs sample containing some cerium oxide impurity at around 29° 2θ (purple) and a CeAs sample without the oxide impurity (blue).
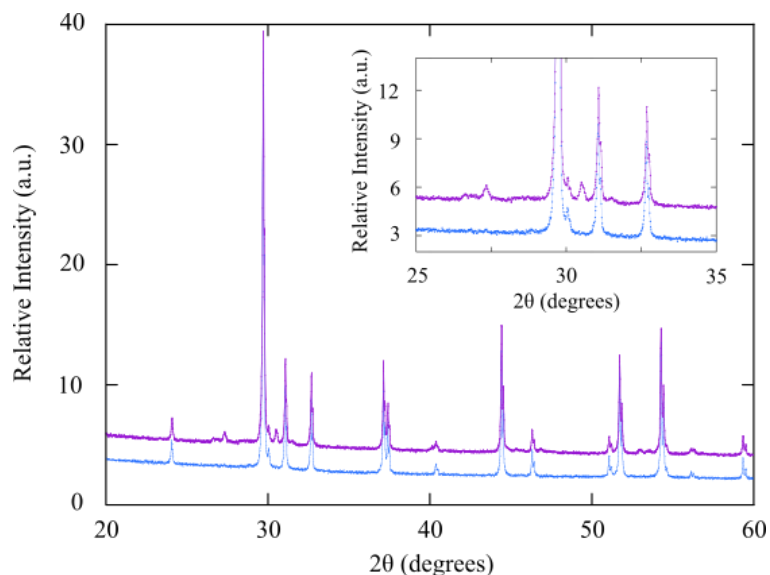
Figure 4.2: Comparison of laboratory X-ray diffraction data from a CeMnAsO$_{1-x}$F$_x$ sample prepared using a CeAs precursor containing some cerium oxide impurity (purple) and a CeMnAsO$_{1-x}$F$_x$ sample prepared using a CeAs precursor without the oxide impurity (blue).

A second issue arose with the sample preparation, it was discovered that the samples prepared often had issues of non-stoichiometry. The problem was noted when performing Rietveld analysis of long-scan laboratory X-ray diffraction patterns. By allowing the occupancy of Ce and Mn to refine, if they fall below 0.99 then the sample is non-stoichiometric, if they stay above 0.99 then the occupancies are set back to one and samples are regarded as pure. The non-stoichiometry resulted in some interesting changes to the physical properties, to be discussed later.

The samples to be mainly discussed within this chapter were found to be phase pure with stoichiometries CeMnAsO$_{1-x}$F$_x$ (x = 0, 0.03, 0.035, 0.05). The 7.5 atom % fluorine doped sample did unfortunately contain a CeOF impurity but this was only around 1.5% by mass of the material so this sample was used going forward. The presence of the impurity suggests that the desired fluorine content may not have been attained. The Rietveld refinement fits for all samples are shown in Figure 4.3, with all crystallising in *P*4/*nmm* tetragonal space group as seen for other aforementioned 1111 pnictides. No cation/anion disorder is present within the samples, each atom fully occupying (split occupancy of O and F) the expected position with Ce and As on the 2*c* Wyckoff site (¼, ¼ *z*), Mn on 2*b* site (¾, ¼, ½) and O/F occupying the 2*a* site (¾, ¼, 0). Selected values from the room temperature X-ray diffraction refinement fits are shown in Table 4.1, as with the refinement plots it is clear from the refinement parameters that the fits are good in each case.
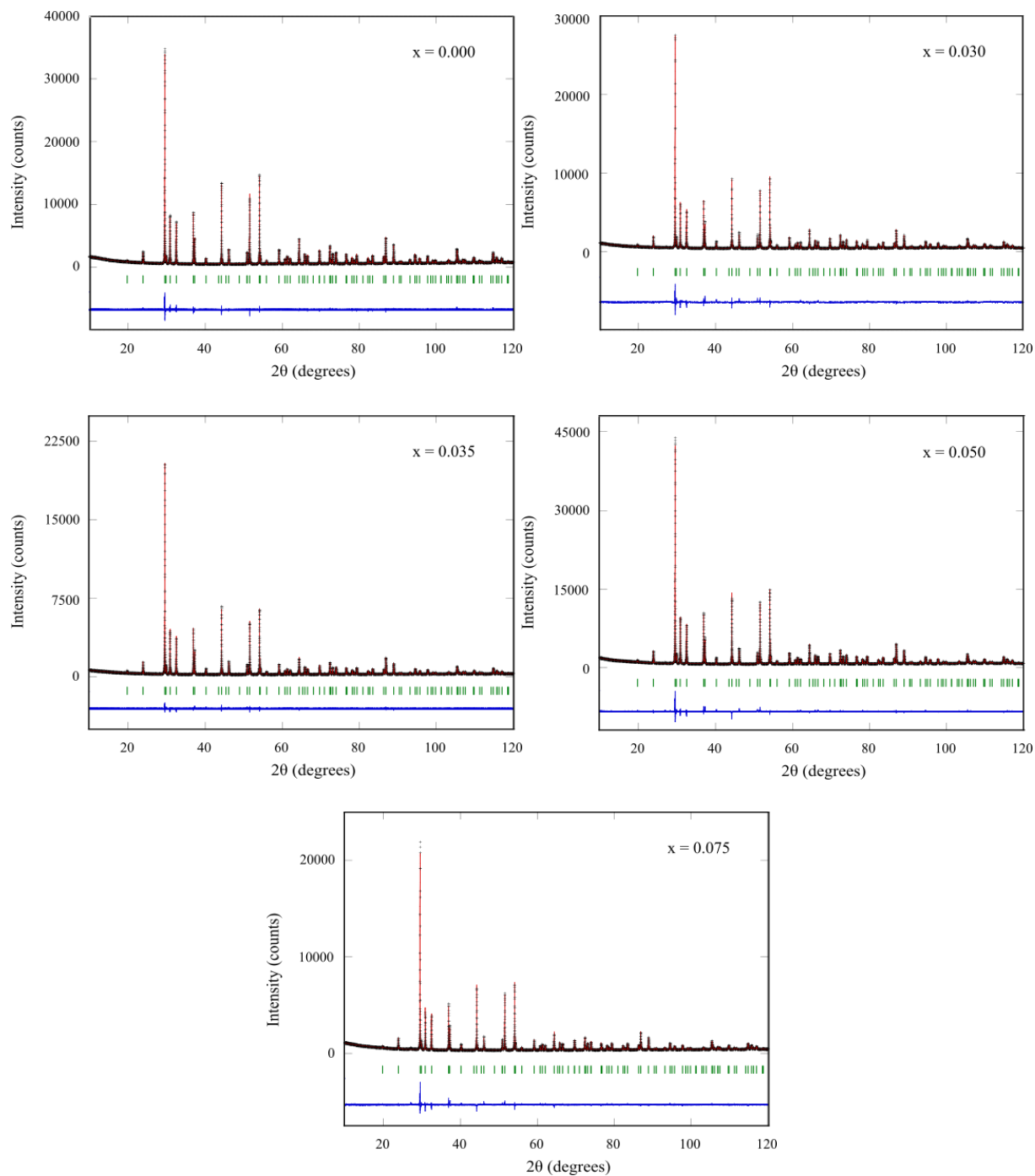
Figure 4.3: Rietveld refinement plots from laboratory X-ray diffraction data recorded at room temperature on various fluorine doped samples of CeMnAsO$_{1-x}$F$_x$ series (x = 0, 0.03, 0.035, 0.05, 0.075).

Table 4.1: Selected refined cell parameters, agreement factors and atomic parameters for CeMnAsO₁₋ₓFₓ series (x = 0 – 0.075) from Rietveld fits against laboratory X-ray diffraction data recorded at room temperature. Wyckoff sites for each ions are as follows: Ce and As are at 2a (¼, ¼, z), Mn at 2b (¾, ¼, ½) and O at 2c (0, ½, 0).

	x				
	0	**0.03**	**0.035**	**0.05**	**0.075**
a (Å)	4.09010(1)	4.08756(1)	4.08834(1)	4.08812(1)	4.08873(1)
c (Å)	8.96544(2)	8.95738(4)	8.95975(2)	8.95908(2)	8.96135(4)
Volume (Å³)	149.982(1)	149.661(2)	149.758(1)	149.730(1)	149.813(1)
Ce z	0.13163(3)	0.13218(6)	0.13217(4)	0.13224(3)	0.13217(5)
As z	0.67136(6)	0.67159(10)	0.67137(7)	0.67093(6)	0.67077(9)
R$_{WP}$ (%)	4.7	5.97	5.86	4.84	5.8
R$_P$ (%)	3.5	4.51	4.6	3.59	4.08
χ^2	1.86	2.13	1.26	2.25	2.67

The overall trend of cell parameters is a reduction upon partial substitution of O^{2-} ions with F^- ions, however there are some discrepancies. Firstly, the 3 atom % fluorine doped sample XRD pattern was recorded using a different step size to the other samples as it was recorded earlier in this study. The other samples were prepared all in close succession with XRD recorded on the same 16 hr run time and so are more comparable. As fluorine has a smaller ionic radius it is expected that the lattice will shrink upon substitution of oxygen, there is an increase observed however in the 7.5 atom % fluorine doped sample which would suggest that the nominal fluorine content might not been achieved.

A selection of bond lengths and angles are shown in Figure 4.4. Clear trends are observed in the Ce-O/F bond which increases with the fluorine content up to 7.5 atom % and this can be used as a better indication that the fluorine content is still increasing even if the cell parameters do not indicate that. In the CeFeAsO₁₋ₓFₓ series, the same increase in the Ce-O/F bond length occurs with F^- doping. The effect of fluorine doping has been suggested to bring the CeO/F charge transfer layer closer to the conducting layer (FeAs tetrahedra) allowing electron charge transfer[15]. A clear trend is also observed in the CeMnAsO₁₋ₓFₓ series within the Mn₂As₂ tetrahedral layers, with the

Mn-As bond lengths decreasing with increasing fluorine content. The manganese arsenide tetrahedra shrink with increasing fluorine doping, where the cerium oxide/fluoride tetrahedra expand. The bond angles all display trends reflecting those seen in the bond angles, with all increasing/decreasing towards a more ideal tetrahedra angle of 109.47°. In the iron superconductors, a link between high transition temperatures and FeAs tetrahedral angles was found with the highest T$_{CS}$ recorded when angles are close to 109.47[16]. The trend observed in the CeMnAsO$_{1-x}$F$_x$ could therefore prove key to physical properties to be discussed. It is not understood why the cell parameters begin to increase at high fluorine content, this trend is not seen in the NdMnAsO$_{1-x}$F$_x$ series as the expected cell contraction occurs with increasing x content[13]. The trends in cell parameters and crystal structure will be further explored in the next chapter, where neutron and synchrotron X-ray diffraction data are analysed.
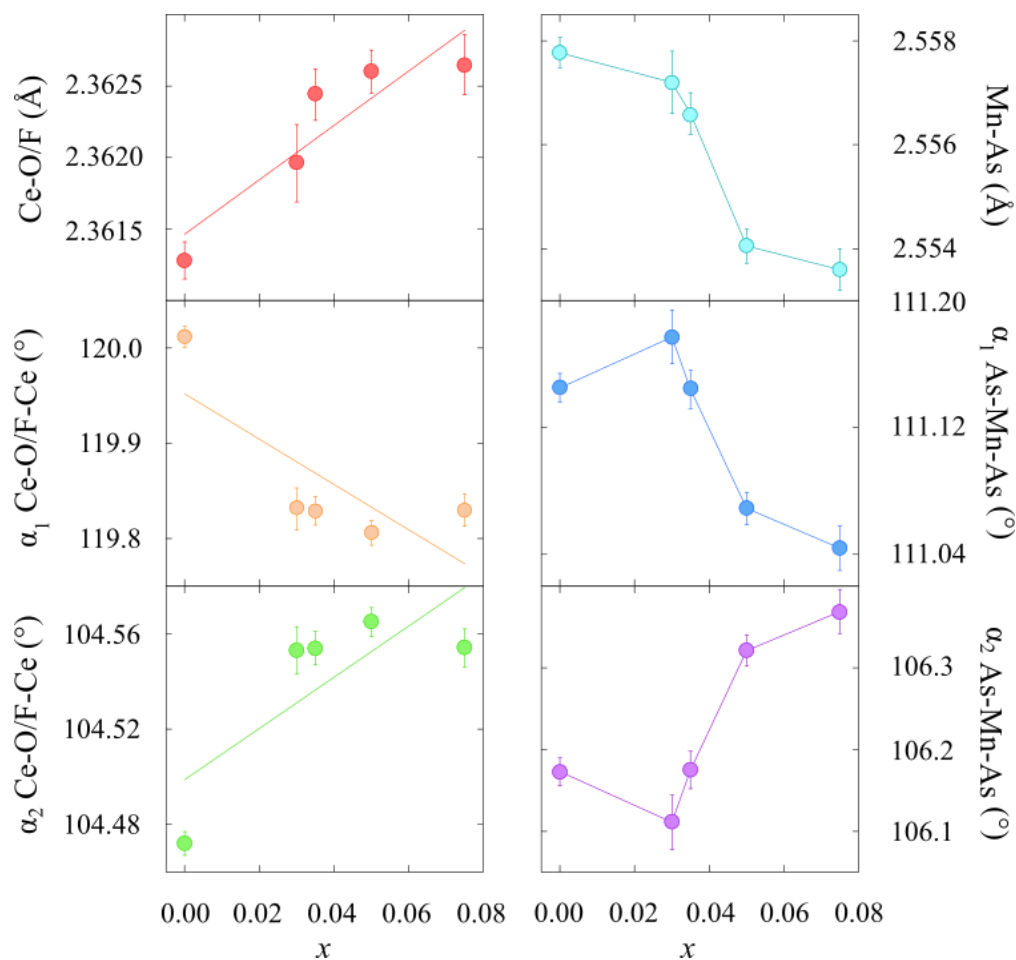
Figure 4.4: Selection of bond length and angles with varying fluorine content (x) in CeMnAsO$_{1-x}$F$_x$ series, values obtained from the refinement using laboratory X-ray diffraction data.

4.3.2: Resistivity Analysis

Within the *Ln*MnAsO series of materials previously studied, Mott insulating ground states are observed[17, 18, 19]. For the CeMnAsO$_{1-x}$F$_x$ series (x = 0, 0.03, 0.035, 0.05, 0.075) variable temperature DC resistivity (ρ) measurements were recorded, shown in Figure 4.5 and Figure 4.6. As in previous reports[19,20], the parent compound CeMnAsO is a Mott insulator with room temperature resistivity of 1.76 × 10^4 Ω.cm, Figure 4.5. When the fluorine content is increased above 3 atom % an extraordinary insulator to insulator transition is seen. As evidenced in the plot (Figure 4.6), the resistivity of these samples (x > 0.03) increases by over two orders of magnitude within a narrow 2 K temperature interval below a transition temperature, T$_{MBL}$. The samples that display the transition become too resistive to measure below the transition temperature.
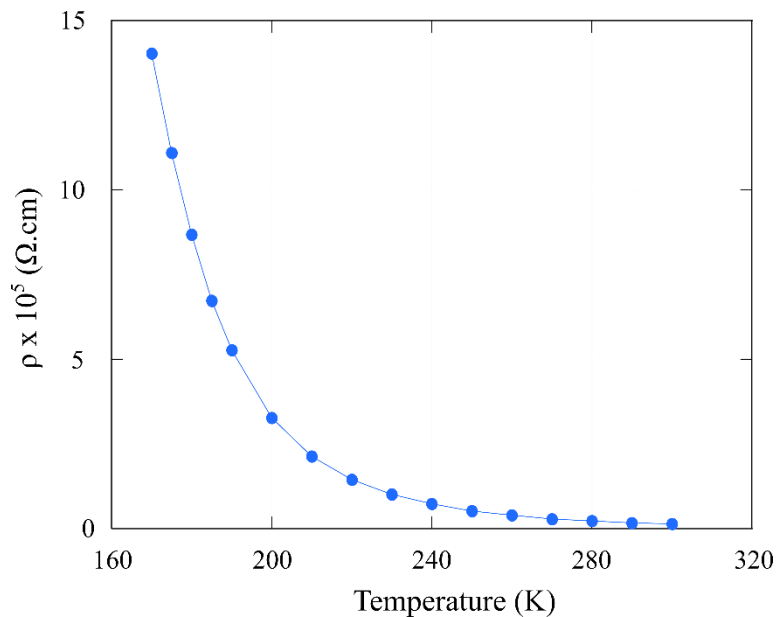
Figure 4.5: Variable temperature resistivity data for undoped parent compound CeMnAsO. CeMnAsO displays Mott insulating behaviour and the resistivity is too high to measure below 170 K.
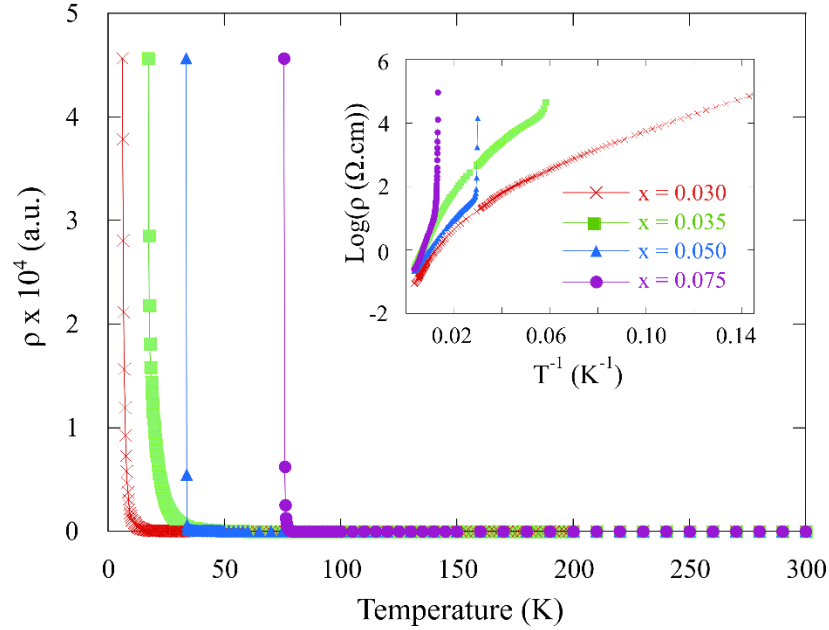
Figure 4.6: Variable temperature resistivity data of CeMnAsO$_{1-x}$F$_x$, showing an insulator-insulator transition when x > 0.03. The data are normalised to the x = 0.035 data set so that the transitions are more apparent. The inset shows the variation of log(ρ) versus inverse temperature where the insulator-insulator transition is apparent for x = 0.035, 0.050 and 0.075.

It is clear from Figure 4.6 that the transition temperature from Mott insulator to the novel insulating phase is reliant on the fluorine content of the samples with the lowest fluorine content required to induce the transition of x = 0.035. The electronic phase diagram of the CeMnAsO$_{1-x}$F$_x$ series is shown in Figure 4.7; the T$_{MBL}$ for each sample is reported in Table 4.2. The composition of samples is key to the control of T$_{MBL}$, with non-stoichiometry greatly influencing the transition. In the phase diagram the highest T$_{MBL}$ shown is the square data point, this is a cerium deficient sample Ce$_{0.98}$MnAsO$_{0.95}$F$_{0.05}$ that was reproducibly made by Dr Eve Wildman, but the focus of my work has been on producing phase pure materials. The 2 atom % deficiency of cerium, determined through Rietveld refinement, increases the T$_{MBL}$ from 34 K to 104 K, demonstrating that a deficiency of cerium significantly increases the transition temperature.
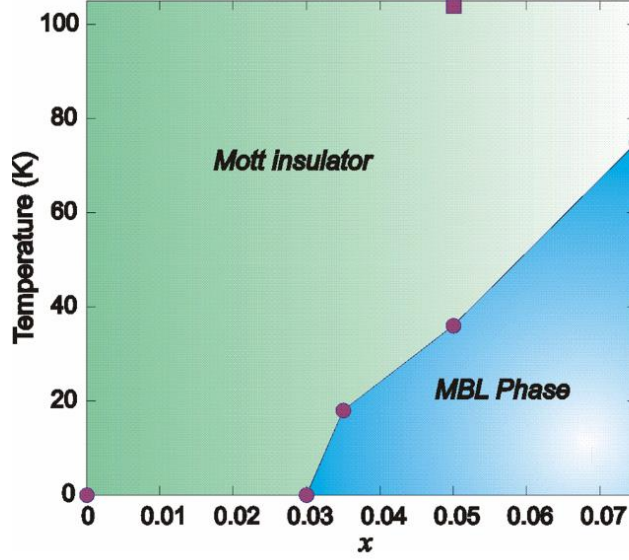
Figure 4.7: Phase diagram showing the boundary between Mott insulating and new insulating phase (many body localised, MBL) for x = 0.00 - 0.075 in CeMnAsO$_{1-x}$F$_x$ series. The circle points are for the stoichiometric samples, with the square data point the T$_{MBL}$ recorded for a Ce$_{0.98}$MnAsO$_{0.95}$F$_{0.05}$ sample.

*Table 4.2: Variation of room temperature resistivity (ρ$_{290 K}$), band gap (E$_g$), localisation temperature T$_0$ and insulator-insulator transition temperature (T$_{MBL}$) with x for the CeMnAsO$_{1-x}$F$_x$ solid solution series. * There was not a large enough range of temperature to obtain a reliable T$_0$ value for the 7.5 atom % fluorine doped CeMnAsO$_{1-x}$F$_x$ sample as the T$_{MBL}$ is at a higher temperature.*

x	$\rho_{290 K}$ (Ω.cm)	E$_g$ (eV)	T$_0$ (K)	T$_{MBL}$ (K)
0.000	17600	0.31(5)	-	-
0.030	0.09	0.05(3)	$1.88(3) \times 10^6$	-
0.035	0.30	0.07(5)	$6.73(3) \times 10^6$	18
0.050	0.23	0.04(2)	$2.51(2) \times 10^6$	34
0.075	0.25	0.08(1)	-*	76

Numerous samples synthesised contained manganese deficiencies, which was identified as a problem after resistivity measurements on these materials were performed, see Figure 4.8. No insulator-to-insulator transition is present for these materials so it is concluded that Mn deficiencies destroy the transition. Further assessment of these materials is required to determine how the sample stoichiometry influences the behaviour exhibited.
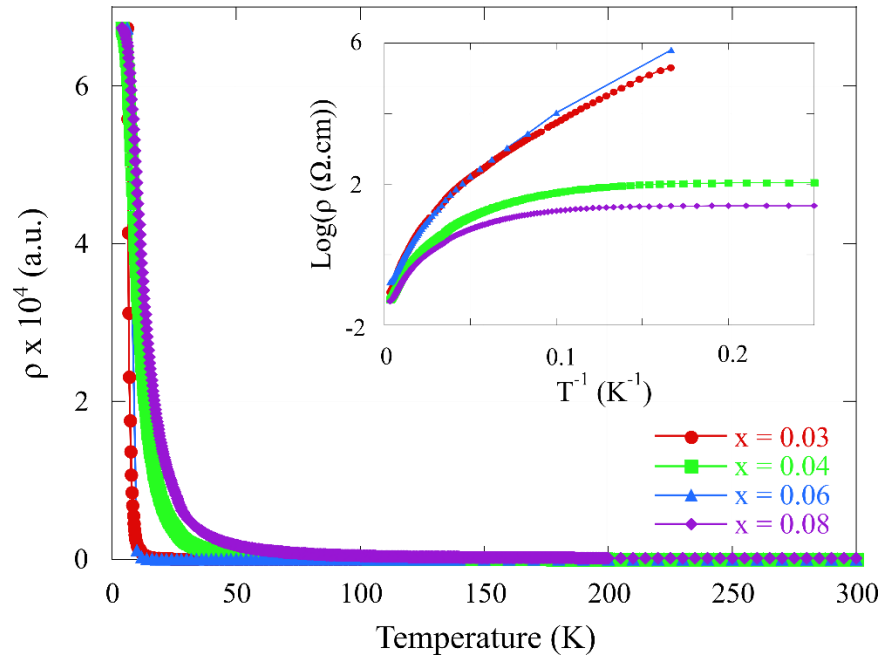
Figure 4.8: Variable temperature resistivity data of CeMnAsO$_{1-x}$F$_x$ samples with manganese deficiencies for x = 0.04, 0.06 and 0.08. The data are normalised to the stoichiometric x = 0.03 data set. The inset shows the variation of log(ρ) versus inverse temperature and it is clear that no insulator – insulator transition occurs in these samples.

The 290 K resistivity values are shown in Table 4.2, and overall there is a general trend of decreasing ρ$_{290\ K}$ when fluorine content increases from x = 0 to x = 0.075. For all samples, from ~250 K to 100 K the electron transport of the CeMnAsO$_{1-x}$F$_x$ series is governed by thermally activated charge carriers across a band gap (E$_g$), values shown in Table 4.2. The Arrhenius relationship of $\rho = \rho_0 \exp(E_g/2kT)$ is employed for this temperature region, where ρ is the measured resistivity, k the Boltzmann constant and T is temperature, an Arrhenius plot of the CeMnAsO sample is shown in Figure 4.9. The Arrhenius plot of x = 0.03 – 0.075 samples between 250 and 100 K is displayed in Appendix 8.7. The E$_g$ values decrease an order of magnitude with electron doping of the CeMnAsO$_{1-x}$F$_x$ system, from 0.31 eV when x = 0 to 0.08 eV when x = 0.075. The

decrease in band gap energy suggests that electron doping of CeMnAsO system results in the creation of a mid-gap state within the Mott-Hubbard gap, like in $LaMnPO_{1-x}F_x$ system where a reduction in band gap magnitude with electron doping occurs[18].
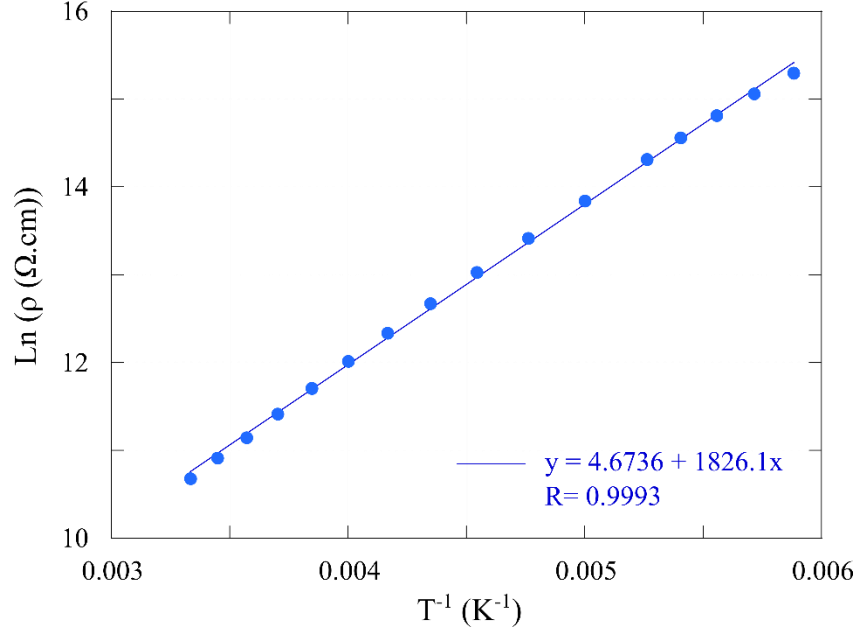
Figure 4.9: Arrhenius plot of CeMnAsO sample from 300 – 170 K before the sample becomes too resistive to measure.

The electron doped samples undergo a transition below ~85 K from Arrhenius behaviour stated above, to Mott three-dimensional variable range hopping (3D VRH). In this lower temperature region the transport can be described by phonon assisted tunneling of electrons between localised states with resistivity ρ defined as $\rho = \rho_0 exp(T_0/T)^{0.25}$ and $T_0 = \lambda\alpha^3/kN(E_F)$. The localisation temperatures (T_0) are displayed in Table 4.2; this is the degree of electronic disorder of the system. For the $CeMnAsO_{0.925}F_{0.075}$ sample, there was not a large enough temperature range between the Arrhenius region and T_{MBL} to determine a reliable T_0. The linear fits to 3D VRH for x = 0.03, 0.035 and 0.05 are displayed in Figure 4.10, with T_0 calculated from the gradient. All localisation temperatures for the samples that undergo the insulator-to-insulator transition are in magnitude 10^6 K, which indicates a strongly electronically disordered system. Previous electron doping studies into manganese oxypnictides ($LnMnAsO_{1-x}Y_x$, Ln = lanthanide; Y = F⁻, H⁻ or vacancies) have been performed[13, 17, 18, 21]. Variable range hopping of electrons has been reported in these materials with x < 0.2 below ~ 100 K. The T_0 values found for $LnMnAsO_{1-x}F_x$ (Ln = Pr, Nd) samples are reported

as $4 - 7 \times 10^5$ K for x = 0.05 - 0.08, these samples display large negative magnetoresistances[13, 14]. For the stoichiometric $CeMnAsO_{1-x}F_x$ series, the T_0 values range from around $2 - 7 \times 10^6$ K which suggests the system has a much greater degree of electronic disorder.
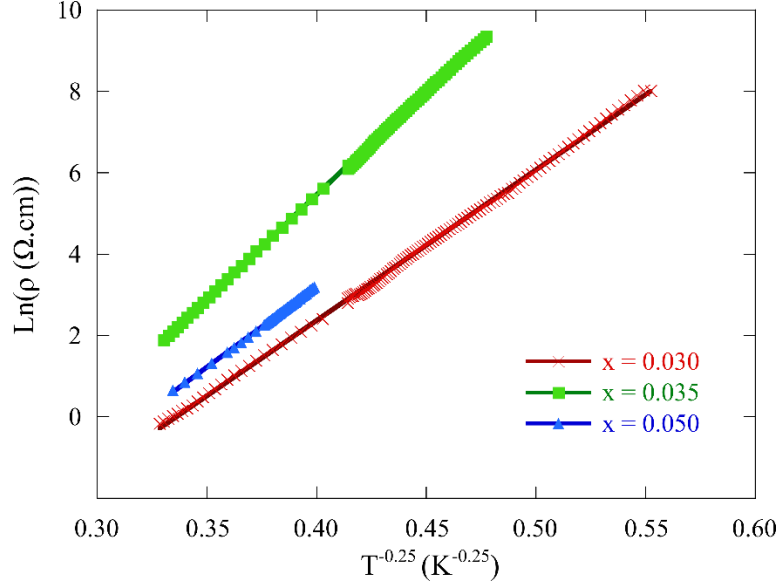
Figure 4.10: The fits to the 3-dimensional VRH equation for $CeMnAsO_{1-x}F_x$ with x = 0.030, 0.035 and 0.050.

The new insulator to insulator transition observed for x > 0.3 in $CeMnAsO_{1-x}F_x$ is unusual and found to be distinct from Efros Shklovskii (ES) VRH as fitting to model was unsuccessful. ES VRH occurs when a soft Coulomb gap pinned at the Fermi level opens up at lower temperatures due to heightened Coulomb correlations; this behaviour was reported to occur for the $NdMnAsO_{1-x}F_x$ series[13]. The new insulating phase occurring in $CeMnAsO_{1-x}F_x$ appears to have very low DC conductance, so they become perfect insulators below the T_{MBL}. The transition temperature is labelled at T_{MBL} as this insulating behaviour is believed to match to that expected for a many-body localised phase (MBL) where the disappearance of DC transport is a helpful indicator of its appearance[22]. MBL systems are highly disordered, so they are unable to thermally equilibrate and the electrons are fully localised below the transition. The MBL effect has previously only been theorised within 1D and 2D systems and witnessed experimentally in ultra-cold atoms in isolated systems[23]. MBL has been predicted to appear in systems that have strong electronic disorder (2D systems), like disordered $CeMnAsO_{1-x}F_x$[24].

Another feature expected for MBL (as was investigated for $CeMnAsO_{1-x}F_x$) are glassy dynamics around the transition with the relaxation times slowing down around T_{MBL}[25, 26]. Variable temperature and frequency AC transport measurements were recorded on the cerium deficient $Ce_{0.98}MnAsO_{0.95}F_{0.05}$ sample, shown in Figure 4.11. A broad peak is seen at around 112 K, which is higher than the T_{MBL} for this sample 104 K, and there is a clear effect of frequency on the peak. Such change in behaviour with frequency is typical of a glassy system. A similar shift in peak position with frequency is observed in other materials that show dynamic phenomena, like spin-glasses such as $Sn_{0.9}Fe_{3.1}N$[27]. These AC transport results together with DC resistivity measurements indicate that MBL could be present within these materials below the electron localisation transition. Some further investigation into this behaviour is necessary to confirm the glassy dynamics.
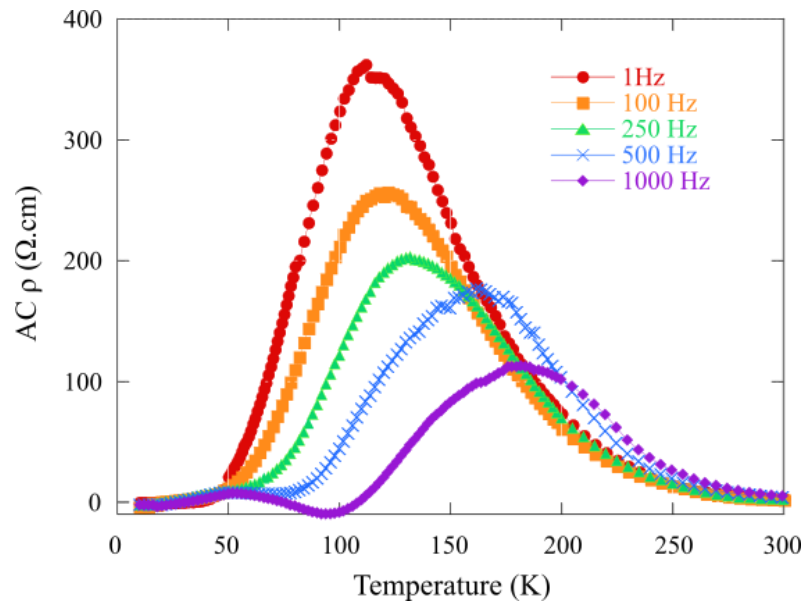
Figure 4.11: The temperature variation of the dissipative part of AC transport for $Ce_{0.98}MnAsO_{0.95}F_{0.05}$ sample at selected frequencies.

4.3.3: SQUID Analysis

The magnetic behaviour of the parent CeMnAsO compound has been previously reported[19, 20, 28]. At high temperatures the manganese magnetic moments form long-range order (T_{Mn} = 347(1) K) into a C-type antiferromagnetic arrangement of spins along c. A spin reorientation transition of Mn^{2+} ions occurs at 34 K with simultaneous long-range ordering of Ce^{3+} magnetic moments into a C-type arrangement with both along a axis. Another transition occurs below 10 K into a non-collinear magnetic structure (T_{NC}).

The five $CeMnAsO_{1-x}F_x$ (x = 0, 0.03, 0.035, 0.05, 0.075) samples prepared had variable temperature magnetic susceptibility measurements performed, zero-field cooled (ZFC) susceptibility curves shown for all in Figure 4.12. It is clear that for all samples the spin reorientation transition occurs around the same temperature T_{SR} ~34 K, with the fluorine content not changing the magnetic behaviour. The high temperature magnetic transition (T_{Mn}) is not visible within these magnetic susceptibility measurements. There also is no evidence of any transition occurring magnetically around the T_{MBL} in this variable temperature magnetic susceptibility data. A plot of the 3.5 atom % fluorine doped $CeMnAsO_{1-x}F_x$ sample ZFC and FC curves is shown in Figure 4.13. The plot of the x = 0.03 sample ZFC and FC curves is visible in Appendix Figure 8.8. There is no evidence of the ZFC and FC curves splitting, meaning that there is no appearance of a spin glass component or a ferromagnetic transition.

In these materials, 2D magnetic correlations arise at temperatures above T_{Mn} which means detection of the magnetic ordering with SQUID is not possible[28]. To determine the T_{Mn} in the $CeMnAsO_{1-x}F_x$ series it was therefore necessary to perform variable temperature neutron diffraction experiments, to be discussed in the following chapter. These measurements are also key to identifying the magnetic ordering occurring within the materials, and further analyse if any magnetic anomalies occur around the novel insulator-insulator transition (T_{MBL}).
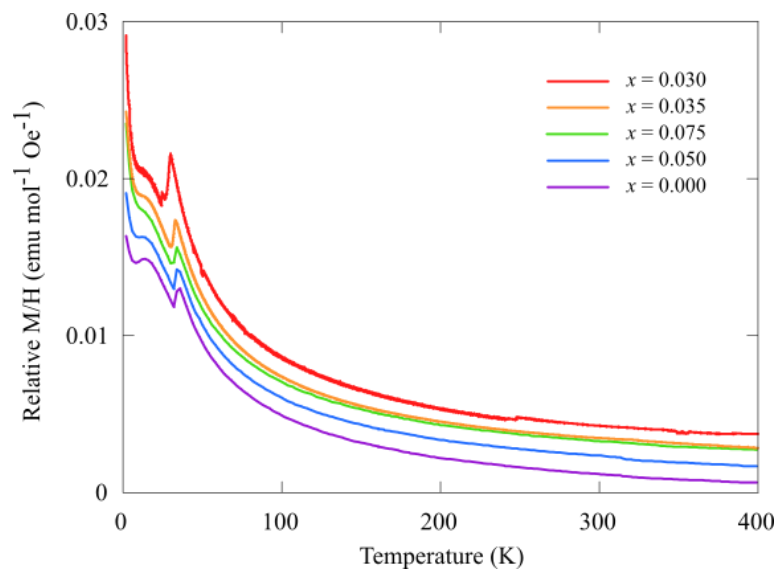
Figure 4.12: ZFC variable temperature magnetic susceptibility of CeMnAsO$_{1-x}$F$_x$ (x = 0, 0.03, 0.035, 0.05 and 0.075) all showing a magnetic transition around T$_{SR}$ = 34 K.
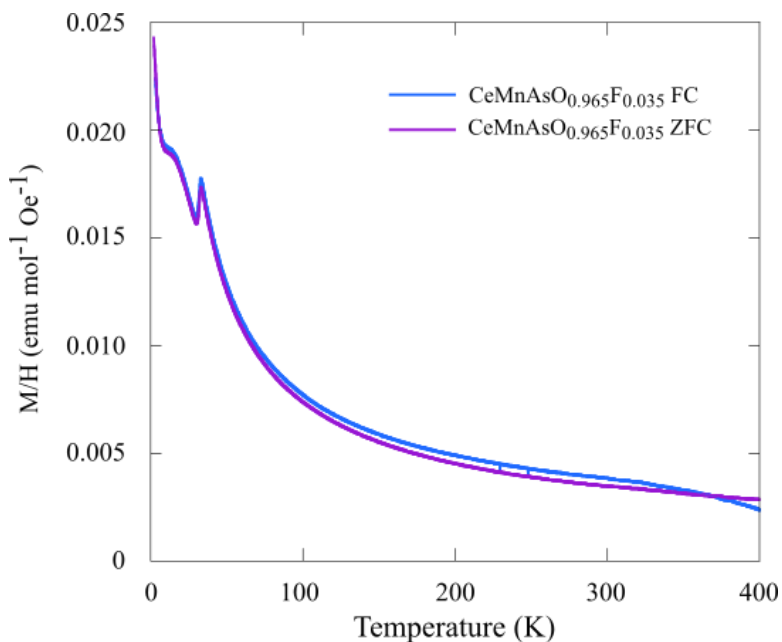
Figure 4.13: Variable temperature magnetic susceptibility plots of CeMnAsO$_{0.965}$F$_{0.035}$ for both ZFC and FC data, no splitting of the data sets is apparent.

4.4: Conclusions

A new series of CeMnAsO$_{1-x}$F$_x$ samples (x = 0, 0.03, 0.035, 0.05, 0.075) were successfully synthesised, with some issues of synthesis addressed through this project. It was determined that purity of the CeAs precursor was key to diminishing the possibility of cerium oxide in the final product. Non-stoichiometry was an issue often faced, with Mn deficiencies commonly occurring and these samples were disposed of after determination through Rietveld refinement fits against the laboratory X-ray diffraction data. The manganese deficient samples were discarded as they do not show the insulator-to-insulator transition of interest, as evidenced through resistivity measurements of 4, 6, and 8 atom % fluorine doped CeMnAsO$_{1-x}$F$_x$ samples with Mn content refined as > 0.99 occupancy.

The cell parameters found through these fits show an overall trend of reducing with partial substitution of O^{2-} with F$^-$ indicating successful fluorine doping. The 7.5 atom % sample cell parameters did not follow the trend and so the success of synthesis was inconclusive from the *a* and *c* parameter trends. The bond lengths within the series do show clear trends as the fluorine content increases. The Ce-O/F bond lengths increase as x increases from 0 to 0.075, whereas the Mn-As bond lengths decrease. The tetrahedral bond angles all display clear trends and as fluorine content increases they all grow/shrink closer to the 'ideal' tetrahedral angle of 109.47°.

Variable DC resistivity measurements revealed a new and exciting property observed within the CeMnAsO$_{1-x}$F$_x$ system when x > 0.03. Parent compound CeMnAsO is a Mott insulator as previously reported, with room temperature resistivity of 1.76×10^4 Ω.cm. When x > 0.03 a new insulator-to-insulator transition occurs, with resistivity increasing by over 2 orders of magnitude within a narrow 2 K temperature range. Below the transition temperature (T$_{MBL}$) into the new insulating phase, the resistivity is too high to measure. The transition is sensitive to x content, with T$_{MBL}$ increasing from 18 K for x = 0.035 to 76 K for x = 0.075. As previously stated, with increasing x the tetrahedra angles trend towards more 'ideal' values, so a link between crystal structure and T$_{MBL}$ could be present. In the iron superconductor families a link between T$_C$ and crystal structure has been established, therefore something similar could be displayed for this insulator-to-insulator transition. The transition is also sensitive to composition, with a slightly cerium deficient sample Ce$_{0.98}$MnAsO$_{0.95}$F$_{0.05}$ showing the highest T$_{MBL}$ of 104 K in comparison to the phase pure sample

CeMnAsO$_{0.95}$F$_{0.05}$ with T$_{MBL}$ = 34 K. Samples containing manganese deficiencies do not show any insulator-insulator transitions.

For all x values, the electronic transport between ~250 and 100 K is governed by thermally activated charge carriers across a band gap (E$_g$) with Arrhenius behaviour followed. The E$_g$ value decreases an order of magnitude through electron doping of CeMnAsO system from 0.31 eV for x = 0 to 0.08 eV for x = 0.075. The electron doped samples undergo a transition into Mott 3D VRH behaviour below ~85 K with localisation temperatures all in order of 10^6 K. The high T$_0$ indicate a great degree of disorder in this system.

The DC resistivity behaviour observed in samples x > 0.03 is new and agrees with the theorised properties expected for a Many-Body Localised state. A key indicator for a MBL phase is the appearance of zero DC conductance. In the CeMnAsO$_{1-x}$F$_x$ (x = 0.035, 0.05, 0.075) series a transition to high DC resistivity is observed and although zero conductance cannot be measured due to the instrumental limitations, the dramatic jump in resistivity (before an inability to measure further) is an indication that loss of conductance occurs as expected for MBL systems. A further indicator of MBL behaviour is the display of glassy dynamics. The AC transport measurements of Ce$_{0.98}$MnAsO$_{0.95}$F$_{0.05}$ sample display glassy behaviour, the peaks shift when frequency increases similar to the behaviour observed in spin-glass materials.

SQUID magnetometry measurements were recorded to investigate the magnetic transitions in the CeMnAsO$_{1-x}$F$_x$ system. Previous reports indicate that manganese ions order at high temperature (T$_{Mn}$ = 347(1) K) with a spin reorientation occurring at 34 K with a simultaneous ordering of Ce^{3+} ions. The spin reorientation temperature in the fluorine doped samples was also observed at 34 K with no shift in temperature with increasing F$^-$ concentration. The high temperature manganese ordering is not visible in the magnetisation plots, and ZFC and FC curves show no splitting indicative of ferromagnetism or a spin-glass component. No evidence was found of a magnetic anomaly around the T$_{MBL}$.

A further investigation is required to determine if any deviations occur to the crystal structure or magnetic structure around the T$_{MBL}$, this was performed using neutron and synchrotron X-ray diffraction to be discussed in the following chapter.

References

[1] Y. Kamihara, T. Watanabe, M. Hirano and H. Hosono, 2008, *J. Am. Chem. Soc*. **130**, 3296-3297.

[2] H. Takahashi, K. Igawa, K. Arii, Y. Kamihara, M. Hirano and H. Hosono, 2008, *Nature*, **453**, 376-378.

[3] Z. A. Ren, J. Yang, W. Lu, W. Yi, G. C. Che, X. L. Dong, L. L. Sun and Z. X. Zhao, 2008, *Mater. Res. Innov*. **12**, 105-106.

[4] Z. A. Ren, J. Yang, W. Lu, W. Yi, X. L. Shen, Z. C. Li, G. C. Che, X. L. Dong, L. L. Sun, F. Zhou and Z. X. Zhao, 2008, *Chin. Phys. Lett.* **25**, 57002.

[5] G. F. Chen, Z. Li, D. Wu, G. Li, W. Z. Hu, J. Dong, P. Zheng, J. L. Luo and N. L. Wang, 2008, *Phys. Rev. Lett*. **100**, 247002.

[6] Z. A. Ren, W. Lu, J. Yang, W. Yi, X. L. Shen, Z. C. Li, G. C. Che, X. L. Dong, L. L. Sun, F. Zhou and Z. X. Zhao, 2008, *Chin. Phys. Lett.* **25**, 2215.

[7] Z. Li, G. Chen, J. Dong, G. Li, W. Hu, D. Wu, S. Su, P. Zheng, T. Xiang, N. Wang and J. Luo, 2008, *Phys. Rev. B*. **78**, 060504.

[8] Y. Takano, S. Komatsuzaki, H. Komasaki, T. Watanabe, Y. Takahashi and K. Takase, 2008, *J. Alloy. Comp.* **451**, 467-469.

[9] X. Jin, T. Masubuchi, T. Watanabe, K. Takase and Y. Takano, 2009, *J. Phys. Conf. Ser.* **150**, 052085.

[10] H. Ohta and K. Yoshimura, 2009, *Phy, Rev. B*. **80**, 184409.

[11] S.-W. Park, H. Mizoguchi, K. Kodama, S. Shamoto, T. Otomo, S. Matsuishi, T. Kamiya and H. Hosono, 2013, *Inorg. Chem.* **52**, 13363-13368.

[12] N. Emery, E. J. Wildman, J. M. S. Skakle, G. Giriat, R. I. Smith and A. C. Mclaughlin, 2010, *Chem. Commun.* **46**, 6777-6779.

[13] E. J. Wildman, J. M. S. Skakle, N. Emery and A. C. Mclaughlin, 2012, *J. Am. Chem. Soc.* **134**, 8766-8769.

[14] E. J. Wildman, F. Sher and A. C. Mclaughlin, 2015, *Inorg. Chem*. **54**, 2536-2542.

[15] J. Zhao, Q. Huang, C. De La Cruz, S. Li, J. W. Lynn, Y. Chen, M. A. Green, G. F. Chen, G. Li, Z. Li, J. L. Luo, N. L. Wang and P. Dai, 2008, *Nat. Mater*. **7**, 953-959.

[16] C. H. Lee, A. Iyo, H. Eisaka, H. Kito, M. T. Fernandez-Diaz, T. Ito, K. Kihou, H. Matsuhata, M. Braden and K. Yamada, 2008, *J. Phys. Soc. Jpn.* **77**, 083704.

[17] Y. Shiomi, S. Ishiwata, Y. Taguchi and Y. Tokura, 2011, *Phys. Rev. B*. **84**, 054519.

[18] J. W. Simonson, K. Post, C. Marques, G. Smith, O. Khatib, D. N. Basov and M. C. Aronson, 2011, *Phys. Rev. B*. **84**, 165129.

[19] A. J. Corkett, D. G. Free and S. J. Clarke, 2015, *Inorg. Chem.* **54**, 1178-1184.

[20] Y. Tsukamoto, Y. Okamoto, K. Matsuhira, M. Whangbo and A. A. Hirio, 2011,*J. Phys. Soc. Jpn*. **80**, 094708.

[21] T. Hanna, S. Matsuishi, K. Kodama, T. Otomo, S. Shamoto and H. Hosono, 2013, *Phys. Rev. B.* **87**, 020401.

[22] R. Nandkishore and D. A. Huse, 2015, *Annu. Rev. Condens. Matter Phys.* **6**, 15-38.

[23] M. Schreiber, S. S. Hodgman, P. Bordia, H. P. Luschen, M. H. Fisher, R. Vosk, E. Altman, U. Schneider and I. Bloch, 2015, *Science*, **349**, 842-845.

[24] T. B. Wahl, A. Pal and S. H. Simon, 2019, *Nature Phys.* **15**, 164-169.

[25] D. M. Basko, I. L. Aleiner and B. L. Altshuler, 2006, *Ann. Phys.* **321**, 1126-1205.

[26] G. Carleo, F. Becca, M. Schiro and M. Fabrizio, 2012, *Sci. Rep*. **2**, 243.

[27] T. Scholz and R. Dronskowski, 2016, *AIP Adv.* **6**, 055107.

[28] Q. Zhang, W. Tian, S. G. Peterson, K. W. Dennis and D. Vaknin, 2015, *Phys. Rev. B*. **91**, 064418.

Chapter 5

Neutron and Synchrotron X-ray Diffraction Studies of CeMnAsO$_{1-x}$F$_x$

5.1: Introduction

The 1111 family of pnictides have been extensively studied due to their interesting physical properties, including superconductivity (LaFeAsO$_{1-x}$F$_x$[1]) and colossal magnetoresistance (NdMnAsO$_{1-x}$F$_x$[2]). The 1111 structure consists of alternating layers of Ln^{3+}(O^{2-}/F$^-$) and Mn^{2+}As^{3-} tetrahedra with nearly all phases reported crystallising in the $P4/nmm$ space group, exceptions with LnZnPO phases that crystallise in the triclinic $R\overline{3}m$ space group.

In the SmFeAsO$_{1-x}$F$_x$ series a transition from tetrahedral to orthorhombic symmetry occurs, with the $Cmma$ space group adopted for $0 \leq x \leq 0.12$[3]. As the doping level is increased, the temperature of the structural transition drops accompanied by a monotonic decrease in lattice constants. The SmFeAsO$_{1-x}$F$_x$ series has the highest T$_C$ outside of the cuprate superconductors, more than any other lanthanide iron arsenide. Samarium has a smaller radius than other lanthanides, and so the unit cell is reduced in size; this cell shrinkage is thought to cause internal chemical pressure that enhance T$_C$[4]. A key feature of the iron arsenide superconductors is the correlation between superconducting transition temperatures and the crystal structure, specifically the tetrahedral bond angle in FeAs$_4$ layers[5,6]. The transition temperature is found to have highest values when a regular tetrahedron is achieved, α As-Fe-As bond angle of 109.47°.

Other transition metal 1111 arsenides have been studied, with only nickel analogues displaying superconducting transitions[7,8]. Some varying magnetic behaviour is recorded in the 1111 structure for the non-superconductors, CeNiAsO has two AFM transitions related to the cerium ions ordering, first in a G-type arrangement of spins then a change to a C-type arrangement of spins at low temperatures[9]. Ferromagnetism is observed for some cobalt pnictides, with formula

*Ln*CoAsO[10], and the ferromagnetism is thought to suppress superconductivity. The ferromagnetic transition temperature is shown to increase with changing lanthanide, and the expected cell shrinkage with decreasing Ln^{3+} size is seen. Nd, Sm and Gd analogues of the cobalt 1111 arsenides have a drop in their magnetization at low temperatures donating a ferromagnetic-antiferromagnetic transition[11]. The *Ln*CrAsO series displays antiferromagnetic ordering only, with a high temperature ordering of Cr^{2+} spins into a G-type AFM arrangement[12].

The magnetic ordering observed for manganese 1111 pnictides is antiferromagnetic, with each *Ln*MnAsO sample at high temperatures having antiferromagnetic arrangement of Mn^{2+} ions in the *ab* plane and ferromagnetic interactions translated in *c* direction, with moments parallel to the *c* axis. A spin reorientation occurs at low temperatures for NdMnAsO samples, the Nd^{3+} ions order at lower temperatures antiferromagnetically along the *ab* plane and simultaneously the Mn^{2+} magnetic moments reorient from along the *c* axis into the *ab* plane[13]. Fluorine doping into the NdMnAsO structure does not alter the magnetic ordering, however cell contraction occurs as fluorine content increases due to the smaller size of fluoride ions[2]. Applying pressure to the system resulted in the reduction of Mn-As bond length and the interlayer spacing, which enhances the superexchange between the manganese centres, this results in the magnetic ordering temperature increasing[14].

In the $PrMnAsO_{1-x}F_x$ series, the crystal structure undergoes a transformation with lowering temperature[15]. The samples change from tetragonal *P*4/*nmm* to orthorhombic *Pmmn* symmetry at low temperatures. The high temperature magnetic ordering of Mn^{2+} spins is the same as seen for $NdMnAsO_{1-x}F_x$ series. Similar to the neodymium study a Mn^{2+} spin reorientation occurs but in this instance the spins change from ordering parallel to *c* to parallel with *a* axis not the *ab* plane. The reorientation of spins occurs over a large temperature range inducing the Pr^{3+} moment ordering, with Pr^{3+} spins ordering antiferromagnetically parallel to *a*.

The $NdMnAsO_{1-x}F_x$ and $PrMnAsO_{1-x}F_x$ have very differing electrical properties, with Nd analogues displaying CMR when Pr analogues do not. The absence of CMR in $PrMnAsO_{1-x}F_x$ is surprising and multiple factors could be the cause, one of which being the difference in crystal structure. As $PrMnAsO_{1-x}F_x$ series undergoes a structural distortion as temperature lowers, the unit cell is extended resulting in the increase of Mn-As bond length. The change in Mn-As bond length results in weakened electron correlations that have been linked to the CMR appearance in

NdMnAsO$_{1-x}$F$_x$ series[15]. Here we investigate the cerium analogue of the 1111 structure oxypnictide, showing the nuclear and magnetic structural changes across the series with varying fluorine doping level.

5.2: Experimental

5.2.1: Powder Neutron Diffraction

Neutron diffraction experiments were performed for the CeMnAsO$_{1-x}$F$_x$ series (x = 0, 0.035, 0.05, 0.075) at the Institut Laue Langevin (ILL) in Grenoble, France. The D2B and D20 beamlines were used for analysis of the CeMnAsO$_{1-x}$F$_x$ series. For CeMnAsO$_{1-x}$F$_x$ high-resolution measurements were taken on the D2B beamline from 1.5 to 400 K on heating. Around 0.7 g of sample was inserted into a 8 mm vanadium can for measurements, and data were recorded with λ = 1.594 Å for 2-3 hours counting per temperature. The D20 beamline was used for variable temperature measurements, with temperature ranges dependant on the dopant level but all recorded between 1.5 and 380 K. The ramping rates for data recording were 19 seconds per 0.1°.

5.2.2: Powder X-ray Diffraction

X-ray powder diffraction patterns were recorded on the PANalytical Empyrean powder diffractometer with Cu Kα1 radiation (λ = 1.540598 Å). Long scans were recorded for Rietveld refinements of the XRD using the PANalytical Empyrean diffractometer, with counting time around 16 hours. The patterns were recorded between range of $10 < 2\theta < 120°$, step size of 0.003°. Synchrotron X-ray diffraction patterns of CeMnAsO$_{0.95}$F$_{0.05}$ were collected on the BL04-MSPD beamline of the ALBA synchrotron in Barcelona, Spain[16]. The highest angular resolution was obtained using the Multi Analyzer Detection (MAD) setup. Powder diffraction patterns were collected in the angular range $0 < 2\theta < 45°$ with a step size of 0.003°. Low temperatures were achieved using the lHe flow cryostat Dynaflow[17] and data were recorded from 8 - 290 K, λ = 0.3252 Å.

5.3: Results and Discussion

In the previous chapter, a new insulator-to-insulator transition was shown to appear in the $CeMnAsO_{1-x}F_x$ series when $x \geq 0.035$. The transition temperature (T_{MBL}) of the new insulating phase increases upon increasing fluorine doping level, from 18 K in $x = 0.035$ to 76 K in $x = 0.075$. The next step was to investigate fully the crystal and magnetic structure of the series, as well as identify if there were any significant changes occurring around T_{MBL}. The investigation was performed using neutron and synchrotron X-ray diffraction, to be discussed in this chapter.

5.3.1: Crystal Structure Determination from Neutron Diffraction

Room temperature XRD patterns, as previously discussed, confirm that all $CeMnAsO_{1-x}F_x$ samples could be indexed to the *P4/nmm* space group as shown in Figure 5.1. The XRD patterns revealed the samples to be of high purity with a small CeOF impurity detected in the $x = 0.075$ sample. $CeMnAsO_{1-x}F_x$ ($x = 0, 0.035, 0.05, 0.075$) samples with high purity were used to collect the neutron powder diffraction patterns to be discussed.
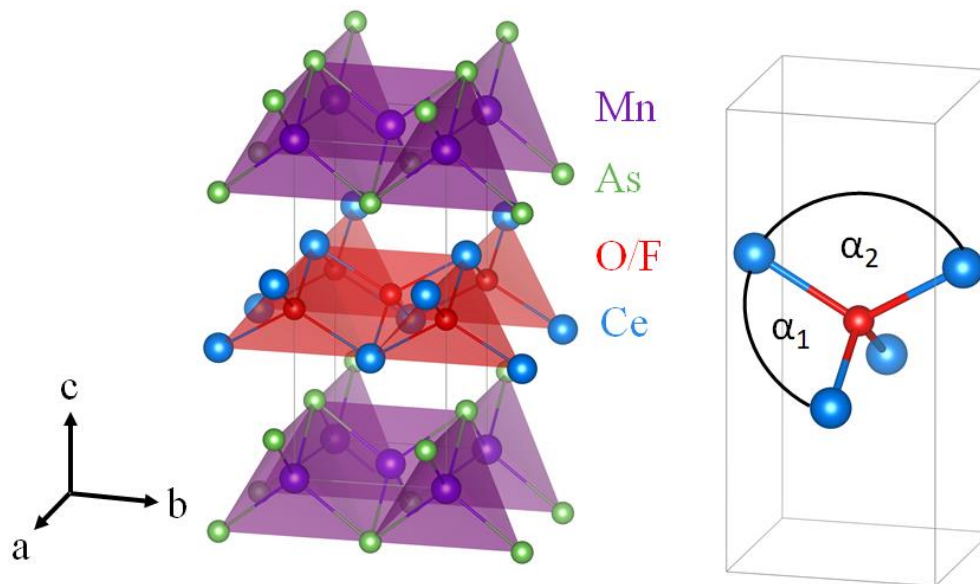
Figure 5.1: Crystal structure of CeMnAsO$_{1-x}$F$_x$ series at 300 K. On the right is an isolated Ce$_4$(O/F) tetrahedron labelling the two different α angles.

Room temperature neutron diffraction patterns and the corresponding Rietveld refinement fits for $CeMnAsO_{1-x}F_x$ series are shown in Figure 5.2. The obtained cell parameters, agreement factors and atomic parameters from refinements of the room temperature data are presented in Table 5.1. A fellow PhD student, Struan Simpson, performed the room temperature refinements and prepared the tables and figures. We were collaborating for a publication, he was responsible for the room temperature data, and I was responsible for the low temperature data. The refined structural model from X-ray diffraction data was found to fit very well for the full series. The occupancies of Ce, Mn and O could be refined to within $\pm 1\%$ of their nominal values, and so were fixed to 1 for the remaining refinements. A deficiency of arsenic was discovered through the neutron diffraction data refinements.

No linear trend is observed for the As deficiency across the series; tantalum is a known arsenic 'getter' and so the deficiencies are likely to be a result of using tantalum crucibles during the synthesis. In the previous chapter, a sensitivity of T_{MBL} to stoichiometry is reported. Ce, Mn and F content have been shown to affect the transition temperatures observed. No correlation is present between T_{MBL} and the As occupancy across the series, this suggests that the transition is not sensitive to arsenic deficiencies. The deficiency was not apparent in the refinements fits to the laboratory X-ray diffraction data. The deficiency could possibly be simply missed by the X-ray diffraction data as it is not as sensitive for refinements as the neutron diffraction data recorded.

Figure 5.2: Rietveld refinement fits to the 300 K D2B neutron diffraction patterns for CeMnAsO$_{1-x}$F$_x$ series. The asterisks on the patterns denotes the positions of additional peaks in the pattern that arise from the sample environment. The tick marks displayed represent the nuclear phase and magnetic phase from top to bottom respectively.

Table 5.1: Refined cell parameters, atomic parameters and agreement factors obtained for CeMnAsO$_{1-x}$O$_x$ series from Rietveld refinement fits to D2B neutron powder diffraction data 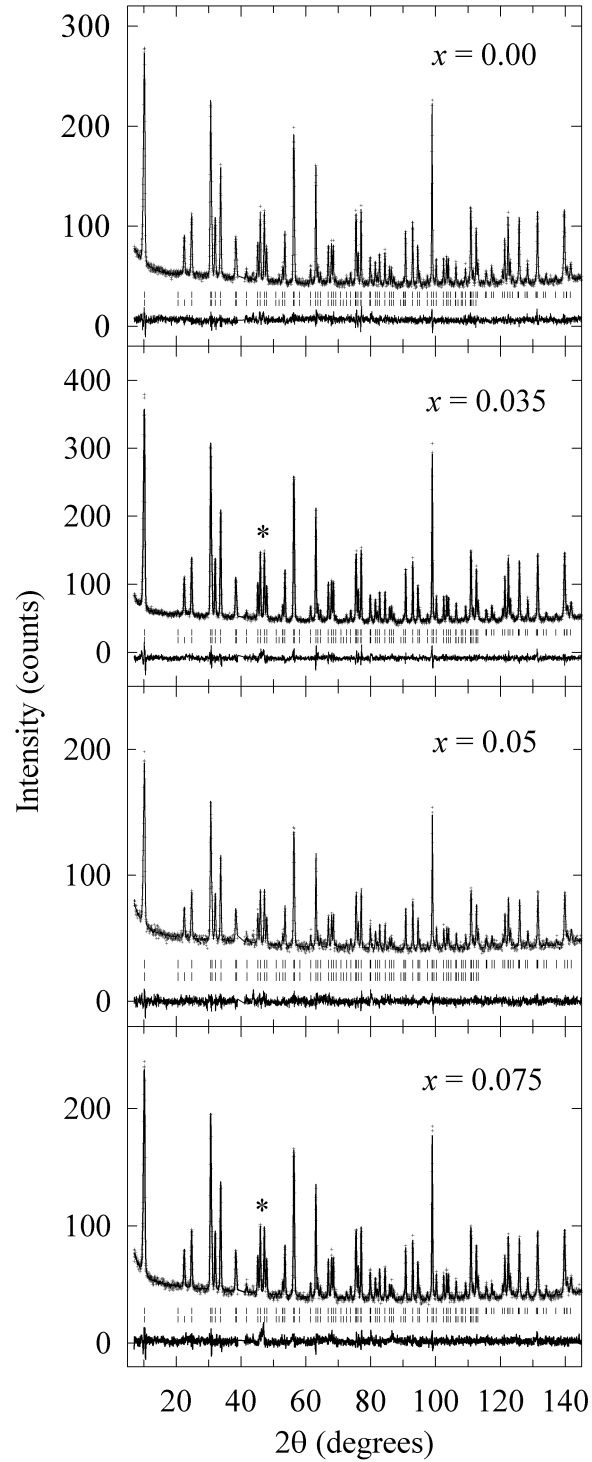at 300 K. The refinement is to the space group P4/nmm with origin choice 2. Ce and As occupy Wyckoff site 2c (¼, ¼, z), Mn occupies position 2b (¾, ¼, ½) and O/F occupy 2a site (¼, ¾, 0). The samples were all determined to be phase pure with the exception of CeMnAsO$_{0.925}$F$_{0.075}$ that contains a small CeOF impurity (~1.5% by volume). The arsenic occupancy is fixed to the low temperature values.

Atom		CeMnAsO$_{1-x}$F$_x$			
	x	0.000	0.035	0.050	0.075
Ce	z	0.1319(2)	0.1321(2)	0.1326(3)	0.1329(3)
	U_{iso} (Å^2)	0.0050(5)	0.0047(5)	0.0033(9)	0.0038(8)
Mn	U_{iso} (Å^2)	0.0055(5)	0.0070(5)	0.0066(8)	0.0063(7)
As	Occupancy	0.989(6)	0.988(6)	1	0.986(7)
	z	0.6714(2)	0.6713(2)	0.6720(2)	0.6713(2)
	U_{iso} (Å^2)	0.0065(4)	0.0058(4)	0.0064(6)	0.0063(5)
O/F	U_{iso} (Å^2)	0.0055(4)	0.0052(4)	0.0043(7)	0.0051(6)
	a (Å)	4.09196(2)	4.09071(5)	4.09012(8)	4.09106(7)
	c (Å)	8.9718(2)	8.9675(2)	8.9644(2)	8.9678(2)
	χ^2	1.32	1.72	1.13	1.36
	R_P (%)	3.38	3.41	3.30	3.66
	R_{WP} (%)	4.27	4.48	4.16	4.75
	V (Å^3)	150.225(4)	150.061(5)	149.967(8)	150.092(7)

The *a* and *c* cell parameters found through refinements to the neutron diffraction data display the same behaviour as the X-ray diffraction data, shown in Table 5.1. Upon increasing the fluorine content from 0 to 5 atom % the *a* and *c* cell parameters decrease. The behaviour is expected as F$^-$ has a smaller ionic radius than O^{2-} (1.31 Å compared to 1.38 Å), therefore the lattice should contract with increased fluorine doping. The CeMnAsO$_{0.925}$F$_{0.075}$ sample cell parameters abruptly increase, as previously seen in refinements of the X-ray diffraction data, which breaks from the predicted trend. Arsenic occupancies can have strong influence on the lattice parameters of pnictide

materials[18]; however, the change seen in As occupancies across this series does not directly link to the cell parameter variation observed but there may be an indirect link. The trend in lattice constants would suggest that nominal doping in the 7.5 atom % fluorine sample has not occurred given the sudden increase of a and c values; examination of the bond angles and lengths are required.

Some selected bond lengths and angles are displayed in Table 5.2. Clear trends occur within the Ce(O/F) tetrahedral layers, see Figure 5.3. As found in the refinement fits to the X-ray data, the Ce-O/F bond length shows an increase with increasing fluorine content. This consistent trend in the Ce-O/F bond length is a good indication that the fluorine content is increasing through the series, when the cell parameters show ambiguity. This behaviour was seen in the $CeFeAsO_{1-x}F_x$ series, as the fluorine content increases the Ce-O/F bond length increases[19] resulting in the Ce-O/F charge transfer layer becoming closer to the superconducting iron arsenide layer. The α_1 Ce-(O/F)-Ce bond angle decreases from 119.93(8)° to 119.53(10)° as x increases from 0 to 0.075. Correspondingly the α_2 Ce-(O/F)-Ce bond angle increases from 104.51(4)° to 104.69(4)°, both angles are trending towards the ideal tetrahedral angle of 109.47°. The Ce(O/F) tetrahedra in $CeMnAsO_{1-x}F_x$ samples clearly become slightly more regular in shape going from x = 0 to x = 0.075.

There are no clear trends in the MnAs tetrahedral layers within these neutron diffraction results. The results seen do however reflect the As content of the samples, so the sharp jump in Mn-As bond length seen for x = 0.05 is in relation to this sample having full occupancy. In these room temperature neutron diffraction results the correlation between the MnAs layer and arsenic occupancies is clearest when comparing x = 0.035 and 0.075 samples that have very similar As content. The bond angles determined for these two samples are very similar to one another (111.14(3)° and 111.14(4)° for α_1 and 106.19(6)° and 106.18(7)° for α_2 As-Mn-As angles) so it is evident that a link occurs between arsenic content and MnAs layer structure. Focusing on the three arsenic deficient samples there is a more apparent trend, with the As-Mn-As bond angles trending towards more regular tetrahedral angles. The same bond lengths and angles from refinements fits to X-ray diffraction data are displayed in Table 5.3, within the MnAs layers clear trends were found with the tetrahedra becoming more regular in shape at higher fluorine levels as discussed in the previous chapter.

Table 5.2: Selected bond lengths and angles for CeMnAsO$_{1-x}$F$_x$ series obtained through Rietveld refinement fits to D2B neutron diffraction data recorded at 300 K. The bond angles are labelled according to the diagram in Figure 5.1.

x	0	0.035	0.05	0.075
Bond length (Å)				
Ce–O/F	2.3634(10)	2.3636(9)	2.3653(14)	2.3676(12)
Mn–As	2.5599(10)	2.5579(9)	2.5614(15)	2.5582(12)
Ce–As	3.3890(10)	3.3876(9)	3.3812(14)	3.3837(12)
Mn–Mn	2.89345(2)	2.89257(8)	2.89215(11)	2.89282(10)
Bond angles (°)				
α_1 Ce–O/F–Ce	119.93(8)	119.85(7)	119.67(12)	119.53(10)
α_2 Ce–O/F–Ce	104.51(4)	104.55(3)	104.62(5)	104.69(4)
α_1 As–Mn–As	111.17(3)	111.14(3)	111.25(4)	111.14(4)
α_2 As–Mn–As	106.12(6)	106.19(6)	105.96(9)	106.18(7)

Table 5.3: Selected bond lengths and angles for CeMnAsO$_{1-x}$F$_x$ series obtained through Rietveld refinement fits to laboratory X-ray diffraction data recorded at room temperature taken from Chapter 4.

x	0	0.035	0.05	0.075
Bond length (Å)				
Ce–O/F	2.36128(13)	2.36244(18)	2.36260(15)	2.36265(21)
Mn–As	2.5578(3)	2.5566(4)	2.5541(3)	2.5536(4)
Ce–As	3.3887(3)	3.3846(4)	3.3862(3)	3.3879(4)
Mn–Mn	2.89214(0)	2.89090(0)	2.89074(0)	2.89117(1)
Bond angles (°)				
α_1 Ce–O/F–Ce	120.01(1)	119.83(2)	119.81(1)	119.83(2)
α_2 Ce–O/F–Ce	104.472(5)	104.554(7)	104.565(6)	104.554(8)
α_1 As–Mn–As	111.145(9)	111.144(12)	111.069(10)	111.044(14)
α_2 As–Mn–As	106.173(17)	106.175(23)	106.321(19)	106.368(27)
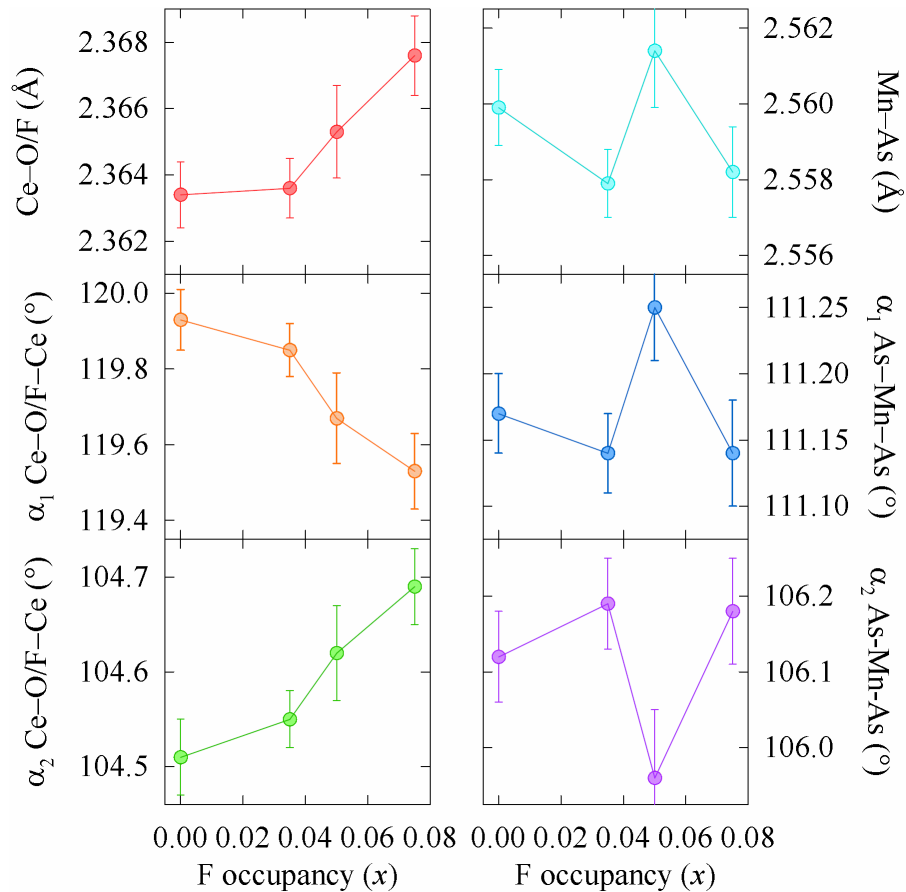
Figure 5.3: Selection of bond length and angles with varying fluorine content (x) in CeMnAsO$_{1-x}$F$_x$ series, values obtained from the Rietveld fits to D2B neutron diffraction data at 300 K.

Low temperature high-resolution neutron diffraction measurements were recorded on the four samples, a problem with the cryostat resulted in each sample being measured at a slightly different temperature. The samples were measured between 1.5 and 10 K; this small temperature difference should not be significant enough to affect the refinement results reported. The Rietveld refinement fits for the CeMnAsO$_{1-x}$F$_x$ samples are shown in Figure 5.4. The obtained cell parameters, agreement factors and atomic parameters from refinements of the low temperature data are presented in Table 5.4. The previously refined structural model was found to fit very well for the full series at low temperatures, no structural transition to different symmetry space group is observed as in some other 1111 pnictides[3, 15].
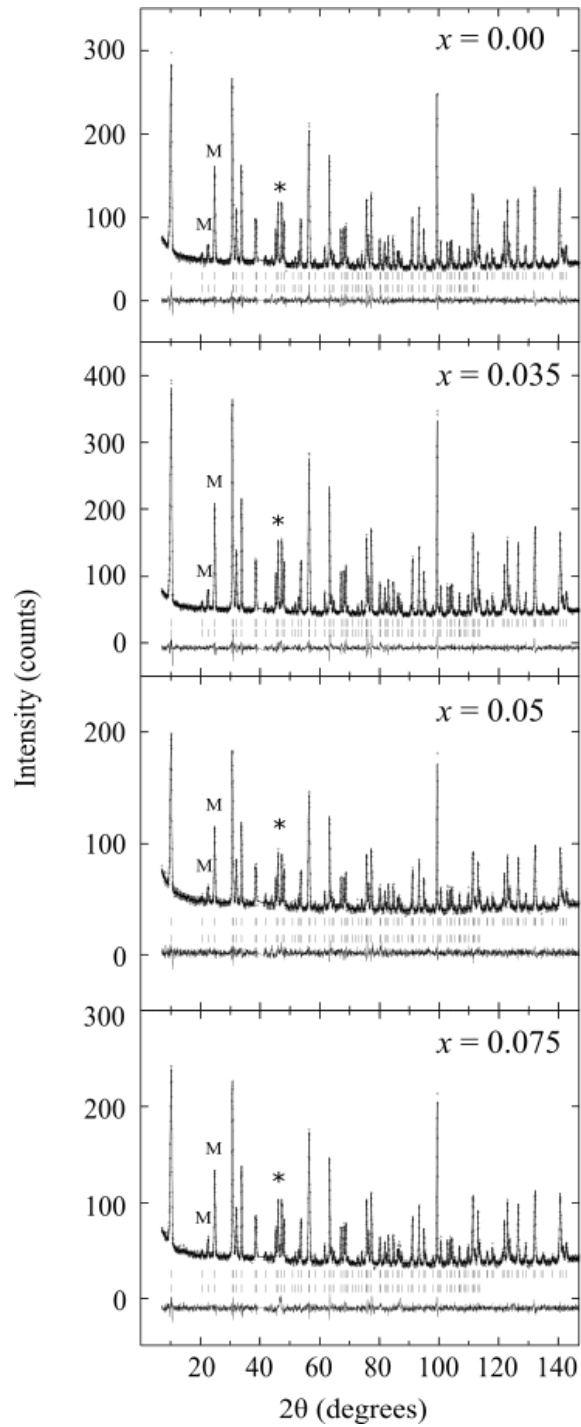
Figure 5.4: Rietveld refinement fits to the low temperature (1.5 – 10 K) D2B neutron diffraction patterns for CeMnAsO$_{1-x}$F$_x$ series. The asterisks on the patterns denotes the positions of additional peaks in the pattern that arise from the sample environment. The tick marks displayed represent the nuclear phase and magnetic phase from top to bottom respectively. M labels donate magnetic Bragg peaks.

Table 5.4: *Refined cell parameters, atomic parameters and agreement factors obtained for* CeMnAsO$_{1-x}$O$_x$ *series from Rietveld refinement fits to D2B neutron powder diffraction data at low temperature (1.5 – 10 K). The refinement is to the space group P4/nmm with origin choice 2. Ce and As occupy Wyckoff site 2c (¼, ¼, z), Mn occupies position 2b (¾, ¼, ½) and O/F occupy 2a site (¼, ¾, 0).*

Atom		CeMnAsO$_{1-x}$F$_x$			
	x	0.000	0.035	0.050	0.075
Ce	z	0.1323(2)	0.1325(2)	0.1336(3)	0.1327(2)
	U_{iso} (Å^2)	0.0007(6)	0.0030(5)	0.0011(8)	0.0010(7)
Mn	U_{iso} (Å^2)	0.0013(5)	0.0021(4)	0.0007(7)	0.0013(6)
As	Occupancy	0.989(6)	0.988(6)	1	0.986(7)
	z	0.6716(2)	0.6716(2)	0.6720(2)	0.6716(2)
	U_{iso} (Å^2)	0.0006(5)	0.0007(4)	0.0006(6)	0.0001(6)
O/F	U_{iso} (Å^2)	0.0022(4)	0.0022(4)	0.0019(6)	0.0021(5)
	a (Å)	4.08282(5)	4.08156(4)	4.08081(5)	4.08193(5)
	c (Å)	8.9460(1)	8.9418(1)	8.9379(2)	8.9420(2)
	χ^2 (%)	1.33	1.84	1.16	1.38
	R_P (%)	3.33	3.60	3.34	3.75
	R_{WP} (%)	4.34	4.70	4.28	4.91
	V (Å^3)	149.124(6)	148.963(5)	148.842(7)	148.993(6)

The lattice parameters show the same behaviour at low temperature as at room temperature. Increasing the fluorine content from the parent compound to the 5 atom % sample the *a* parameter decreases from 4.08282(5) Å to 4.08081(5) Å; *c* lattice parameter also decreases from 8.9460(1) Å to 8.8379(2) going from x = 0 to 0.05. As reported at room temperature (both neutron and X-ray) the *a* and *c* lattice parameters abruptly increase at high fluorine doping level x = 0.075.

Selected bond lengths and angles from the refinement fits to the low temperature neutron diffraction data are shown in Table 5.5 and Figure 5.5. The trends are less clear in these low temperature data, with the Ce(O/F) bond lengths still showing an overall increase with fluorine

doping level. It appears at low temperature the As occupancy might have an effect on the Ce(O/F) layer that is not seen at room temperature, the 5 % sample is the only sample with full occupancy and in this sample there is a slight deviation from the trends observed in the layer. The Ce-As bond lengths show the same general trend at both high and low temperatures with the bond lengths generally decreasing with increasing fluorine content. From all the results it is clear that the expansion of cell parameters is a real effect, and is most likely a result of the Ce(O/F) layer growing and distancing from the MnAs layer. Non-stoichiometry on the As site could also be playing a role, resulting in the cell parameters not obeying Vegard's law upon doping. A previous study of the $NdMn_{1-x}Co_xAsO_{0.95}F_{0.05}$ series observed a similar disobedience of Vegard's law with Co doping due to the presence of arsenic non-stoichiometry in the samples[20].

Table 5.5: Selected bond lengths and angles for $CeMnAsO_{1-x}F_x$ series obtained through Rietveld refinement fits to D2B neutron diffraction data recorded at low temperatures (1.5 – 10 K).

x	0.000	0.035	0.050	0.075
Bond Length (Å)				
Ce-O/F	2.3596(9)	2.3598(8)	2.3641(12)	2.3607(10)
Mn-As	2.5544(9)	2.5533(9)	2.5549(13)	2.5535(11)
Ce-As	3.3781(13)	3.3761(12)	3.3682(17)	3.3755(15)
Mn-Mn	2.88699(3)	2.88610(3)	2.88557(4)	2.88636(3)
Bond Angles (°)				
α_1 Ce-O/F-Ce	119.80(7)	119.72(7)	119.33(10)	119.67(9)
α_2 Ce-O/F-Ce	104.57(3)	104.60(3)	104.78(5)	104.63(4)
α_1 As-Mn-As	111.18(3)	111.17(3)	111.24(4)	111.17(3)
α_2 As-Mn-As	106.11(5)	106.12(5)	106.00(7)	106.12(7)
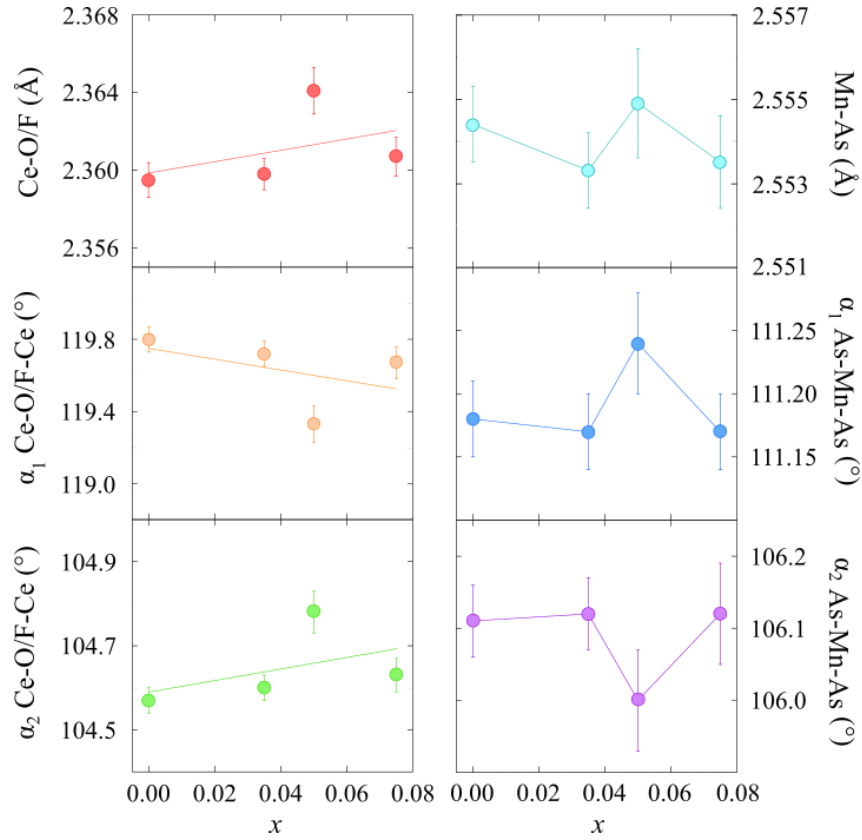
Figure 5.5: Selection of bond length and angles with varying fluorine content (x) in CeMnAsO$_{1-x}$F$_x$ series, values obtained from the Rietveld fits to D2B neutron diffraction data at low temperatures (1.5 – 10 K).

Overall, the parameters at low temperature are lower in value than the room temperature values, as expected as cells contract when temperature decreases. To further investigate this and to determine if any changes occur around T$_{MBL}$, variable temperature scans of samples were recorded. Only the 3.5 and 7.5 atom % fluorine doped samples had full temperature scans recorded using the D20 beamline due to time constraints of the neutron experiment. The lattice parameter variations with temperature for both samples are shown in Figure 5.6 and Figure 5.7. There is no evidence of different behaviour due to the fluorine doping level, as both plots display the same trends. The lattice parameters both show the usual contraction with lowering temperature in each sample, a deviation is highlighted with arrows. The arrows denote the temperature of the magnetic spin reorientation, where the Mn^{2+} ions antiferromagnetic arrangement changes orientation from parallel to the *c* lattice direction into the basal plane. At the spin reorientation temperature, T$_{SR}$,

Ce^{3+} ions also become antiferromagnetically ordered with moments orientated parallel to the basal plane, see Figure 5.16 in section 5.3.3 for the visual representation of the magnetic crystal structure. The break from the trend is therefore due to the magnetic behaviour within the samples.

Figure 5.6: Variable temperature plot of the c lattice parameter determined from Rietveld fits to D20 neutron diffraction data for CeMnAsO$_{0.965}$F$_{0.035}$ sample. Lattice parameter a variation shown inset. Arrow highlighting the T$_{SR}$.

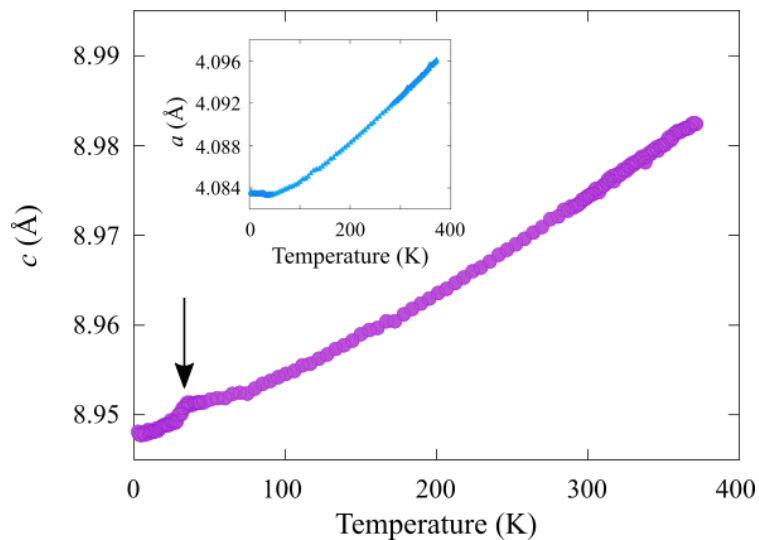*Figure 5.7: Variable temperature plot of the c lattice parameter determined from Rietveld fits to D20 neutron diffraction data for CeMnAsO$_{0.925}$F$_{0.075}$ sample. Lattice parameter a variation shown inset. Arrow highlighting the T$_{SR}$.*

Zoomed plots of the two samples are shown in Figure 5.8; these are to highlight the regions where the T_{MBL} are observed in each sample. There are no present deviations in the parameters at the recorded T_{MBL} for each sample, T_{MBL} = 18 K for x = 0.035 and 76 K for x = 0.075. The only clear deviation to the lattice parameters occurs at the magnetic spin reorientation transition temperature. The T_{SR} as reported in the previous chapter is at around 34 K, with no change with fluorine content; this magnetic structure change is the only factor influencing the nuclear structure of the series. To better determine if any small nuclear structure changes occur that are too sensitive to be observed through the high intensity D20 neutron diffraction measurements, high resolution synchrotron X-ray diffraction measurements are required.

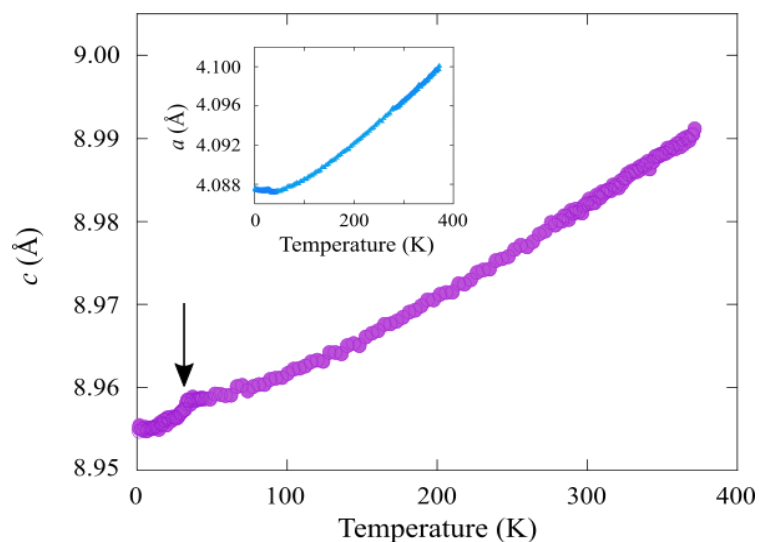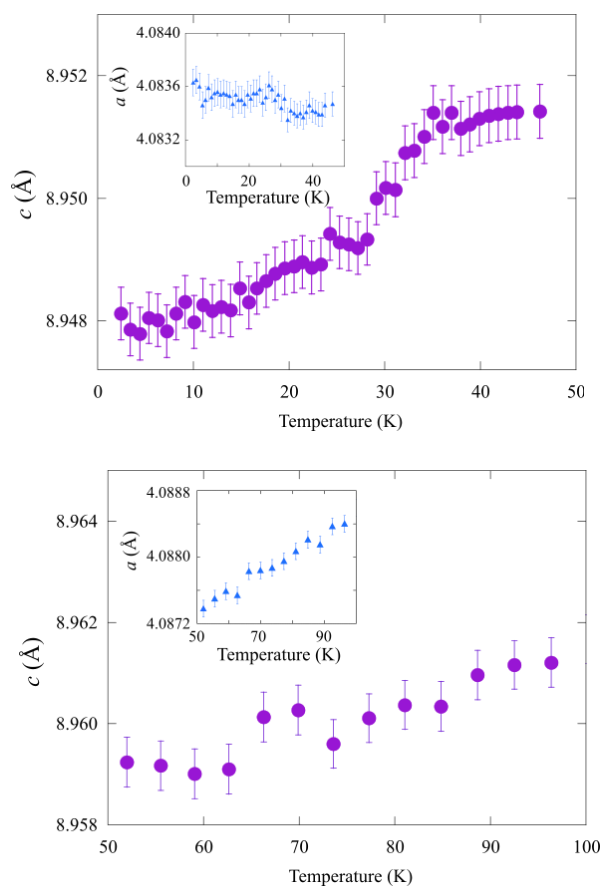*Figure 5.8: Zoomed regions of variable temperature plots of the c lattice parameters determined from Rietveld fits to D20 neutron diffraction data for CeMnAsO$_{0.965}$F$_{0.035}$ (top) and CeMnAsO$_{0.925}$-F$_{0.075}$ (bottom). The inset are a lattice parameters. The temperature regions selected are around the T$_{MBL}$ of each sample (T$_{MBL}$ = 18 K for x = 0.035 and 76 K for x = 0.075).*

5.3.2: Variable Temperature Synchrotron X-ray Diffraction Analysis

Synchrotron X-ray diffraction patterns were recorded between 8 and 290 K on the $CeMnAsO_{0.95}F_{0.05}$ sample on heating, the corresponding Rietveld refinement fits at high and low temperature are shown in Figure 5.9 and Figure 5.10. The refinement fits at interval temperatures (10 – 150 K) are displayed in Appendix Figure 8.9. Over time the samples in the $CeMnAsO_{1-x}F_x$ series degrade, this results in the lowering of T_{MBL}. The 5 atom % sample had further resistivity measurements recorded before the synchrotron experiment was performed, with T_{MBL} now around 16 K due to the sample degradation (see Figure 5.11). A small (~1.5 % by volume) impurity of CeOF was detected in the sample, previously not observed in the neutron diffraction or laboratory X-ray diffraction patterns. The refinement fits included the CeOF impurity as a second phase, a zoomed section of the refinement fit is displayed in Figure 5.12 where the impurity is evident. No cation or anion disorder was found through the refinement fits to the synchrotron X-ray diffraction patterns, with Ce, Mn and As occupancies fixed to 1 for all temperatures. The oxygen and fluorine occupancies were set to 0.95 and 0.05 respectively.

Figure 5.9: Rietveld refinement fits to synchrotron X-ray diffraction pattern for CeMnAsO$_{0.95}$F$_{0.05}$ sample at 8 K. The tick marks displayed represent the nuclear phase and small impurity phase CeOF top and bottom respectively. Inset displays the Rietveld refinements fits to the high angle region of synchrotron X-ray diffraction pattern.

Figure 5.10: Rietveld refinement fits to synchrotron X-ray diffraction pattern for CeMnAsO$_{0.95}$F$_{0.05}$ sample at 290 K. The tick marks displayed represent the nuclear phase and small impurity phase CeOF top and bottom respectively. Inset displays the Rietveld refinements fits to the high angle region of synchrotron X-ray diffraction pattern.

Figure 5.11: New resistance plot for CeMnAsO$_{0.095}$F$_{0.05}$ sample recorded at the time of synchrotron X-ray diffraction experiment. Inset displays the natural log plot versus the inverse temperature displaying the new transition temperature clearer. Two line fits are present in the inset image for high and low temperature regions, where the lines intersect is taken as the T$_{MBL}$, 16 K.

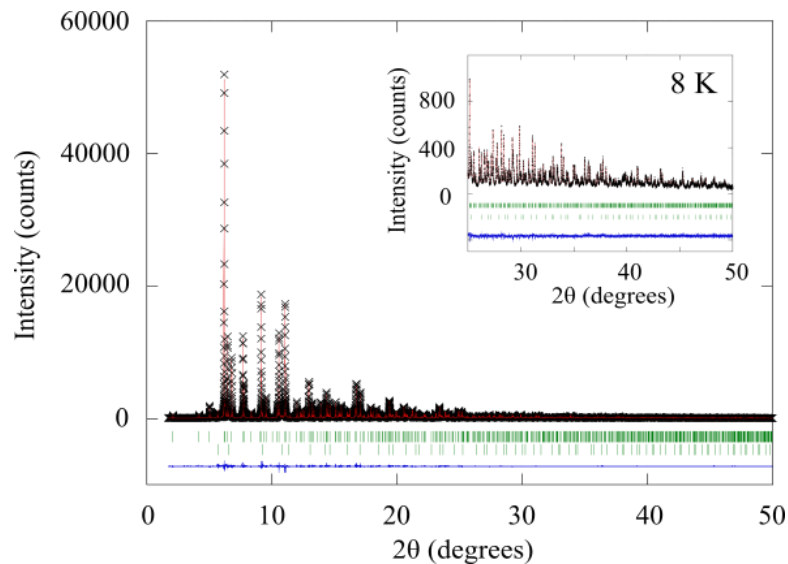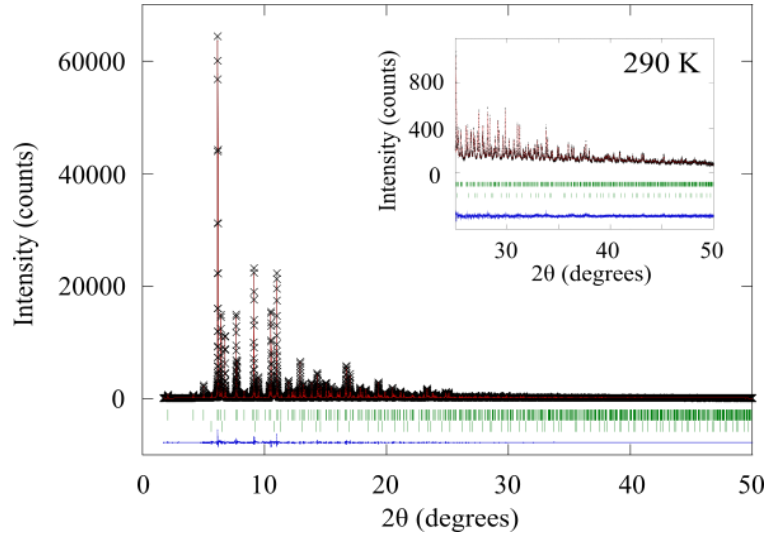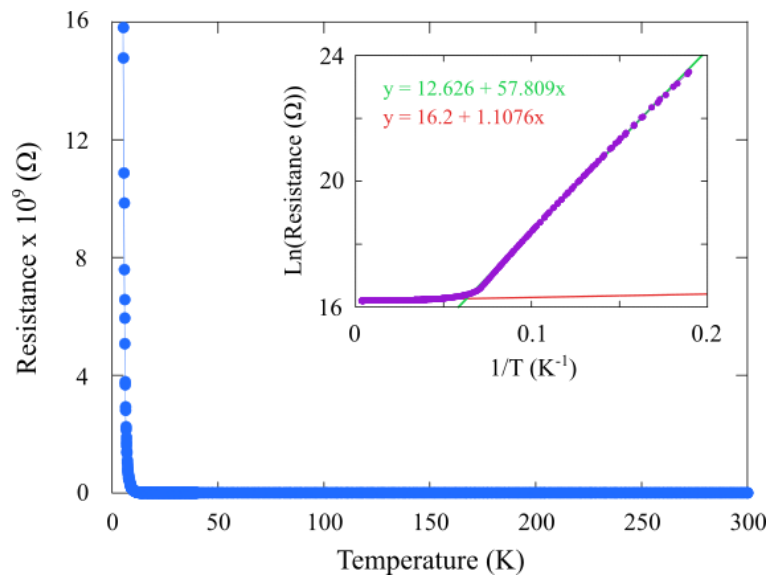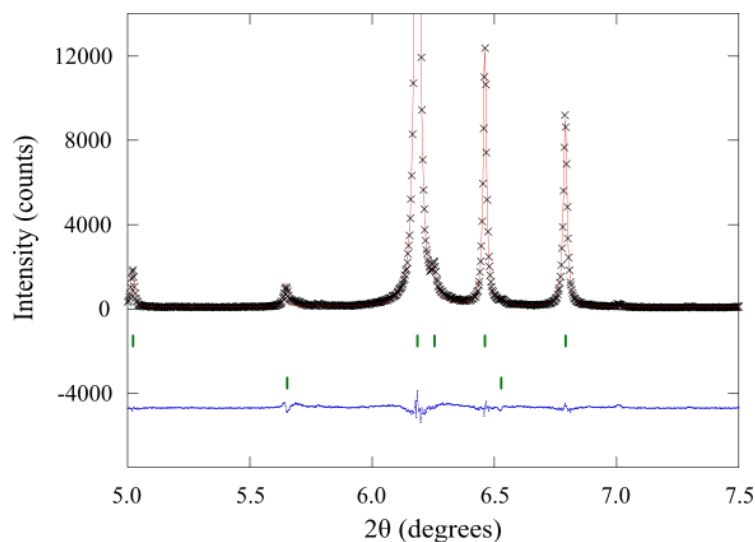*Figure 5.12: Zoomed region of Rietveld refinement fit to synchrotron X-ray diffraction pattern for CeMnAsO$_{0.95}$F$_{0.05}$ sample at 8 K. The tick marks displayed represent the nuclear phase and small impurity phase CeOF top and bottom respectively.*

The obtained cell parameters, agreement factors and atomic parameters from refinements of the variable temperature data are presented in Table 5.6. For the whole temperature range investigated, a good fit was obtained to the tetragonal space group *P4/nmm*. Within these recorded patterns, there is no evidence of peak splitting or superstructure peaks to suggest that any alteration of the symmetry occurs on cooling the material. The neutron diffraction results also saw no evidence of a symmetry change and so different behaviour occurs for the CeMnAsO$_{1-x}$F$_x$ series compared to the PrMnAsO$_{1-x}$F$_x$ series[15], where a change to orthorhombic symmetry occurs upon cooling.

The temperature variation of *a* and *c* lattice parameters are shown in Figure 5.13 and Figure 5.14. The cell parameters in the CeMnAsO$_{0.95}$F$_{0.05}$ sample show the contraction with lowering temperature as expected until around 30 K. The inset to each image highlights the low temperature region so the changes in lattice behaviour are more apparent. The change in slope of *a* and *c* lattice parameters below the T$_{SR}$ is similar to the reported behaviour of NdMnAsO$_{0.95}$F$_{0.05}$[21], discovered through a synchrotron X-ray diffraction study. The variation of slope in CeMnAsO$_{0.95}$F$_{0.05}$ is evident below ~ 30 K, with the T$_{SR}$ around 34 K in this material; as reported for NdMnAsO$_{0.95}$F$_{0.05}$ sample, the CeMnAsO$_{0.95}$F$_{0.05}$ sample has coupling between the lattice and magnetic order. There is no evidence of a link between the crystal lattice size and the electronic behaviour as no significant change occurs to the *a* or *c* lattice parameters around the T$_{MBL}$ =16 K.

144

Figure 5.13: Variable temperature plot of the a lattice parameter determined from Rietveld fits to synchrotron X-ray diffraction data for CeMnAsO$_{0.95}$F$_{0.05}$ sample.

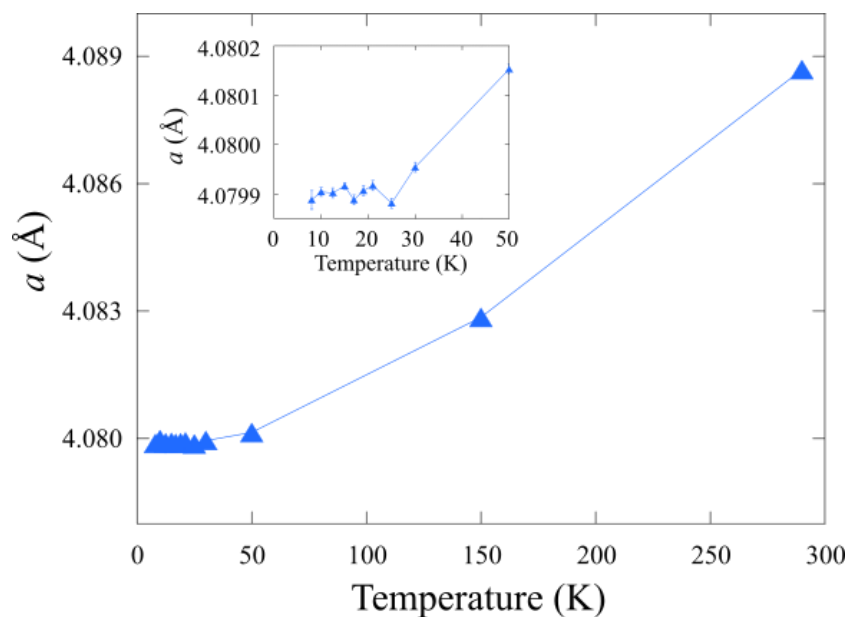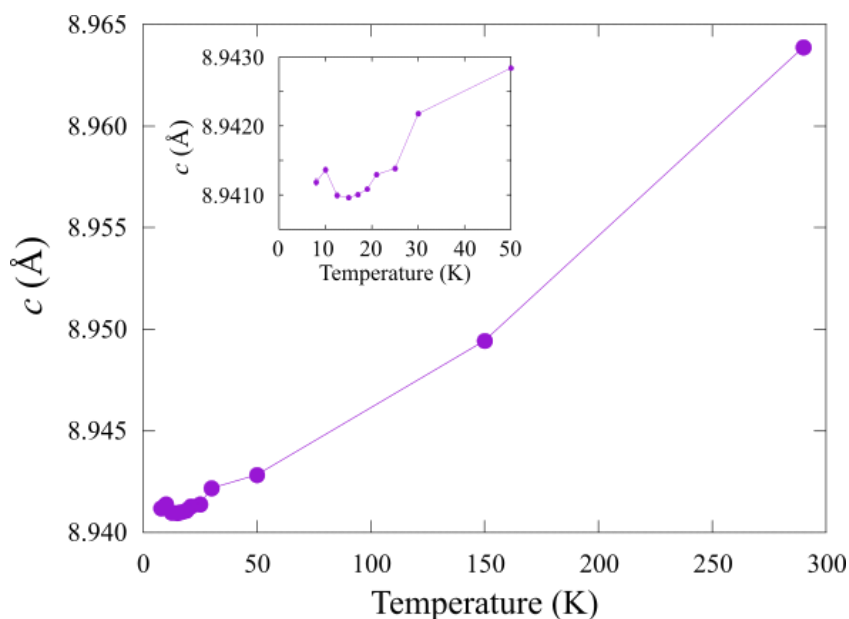*Figure 5.14: Variable temperature plot of the c lattice parameter determined from Rietveld fits to synchrotron X-ray diffraction data for CeMnAsO$_{0.95}$F$_{0.05}$ sample.*

Table 5.6: Refined cell parameters, atomic parameters and agreement factors obtained for CeMnAsO$_{0.95}$O$_{0.05}$ sample from Rietveld refinement fits to synchrotron X-ray powder diffraction data with varying temperature (290 – 8 K). The refinement is to the space group P4/nmm with origin choice 2. Ce and As occupy Wyckoff site 2c (¼, ¼, z), Mn occupies position 2b (¾, ¼, ½) and O/F occupy 2a site (¼, ¾, 0).

Atom		Temperature (K)					
		290	150	50	30	25	21
Ce	z	0.13189(3)	0.13219(3)	0.13237(3)	0.13238(3)	0.13240(3)	0.13237(3)
	U_{iso}	0.625(5)	0.384(4)	0.227(4)	0.210(4)	0.193(4)	0.183(3)
Mn	U_{iso}	0.922(15)	0.544(11)	0.337(9)	0.307(9)	0.303(9)	0.282(9)
As	z	0.67108(5)	0.67116(5)	0.67120(5)	0.67124(4)	0.67124(4)	0.67125(4)
	U_{iso}	0.849(11)	0.511(8)	0.305(7)	0.263(7)	0.253(7)	0.248(7)
O/F	U_{iso}	0.91(7)	0.59(5)	0.50(5)	0.46(5)	0.42(5)	0.47(5)
	a (Å)	4.08869(1)	4.08286(1)	4.08015(1)	4.07995(1)	4.07988(1)	4.07992(1)
	c (Å)	8.96388(4)	8.94943(4)	8.94284(4)	8.94218(4)	8.94138(4)	8.94130(4)
	χ^2 (%)	3.21	3.23	3.43	2.999	4.23	2.83
	R_P (%)	5.55	5.48	5.41	5.25	4.98	5.12
	R_{WP} (%)	7.49	7.55	7.57	7.42	7.10	7.25
	V (Å^3)	149.852(2)	149.184(1)	148.877(1)	148.852(1)	148.833(1)	148.834(1)

Atom		Temperature (K)					
		19	17	15	12.5	10	8
Ce	z	0.13237(3)	0.13238(2)	0.13240(3)	0.13237(3)	0.13233(3)	0.13236(3)
	U_{iso}	0.188(3)	0.188(3)	0.162(4)	0.161(3)	0.200(4)	0.182(4)
Mn	U_{iso}	0.387(9)	0.293(8)	0.264(9)	0.266(9)	0.276(11)	0.286(10)
As	z	0.67123(4)	0.67123(4)	0.67132(5)	0.67126(4)	0.67121(5)	0.67129(5)
	U_{iso}	0.250(7)	0.249(6)	0.214(7)	0.219(7)	0.275(8)	0.240(7)
O/F	U_{iso}	0.42(5)	0.45(4)	0.41(5)	0.36(4)	0.23(5)	0.42(5)
	a (Å)	4.07991(1)	4.07989(1)	4.07992(1)	4.07990(1)	4.07990(1)	4.07989(2)
	c (Å)	8.94108(3)	8.94101(3)	8.94096(3)	8.94099(4)	8.94136(4)	8.94118(5)
	χ^2 (%)	2.73	3.93	2.94	5.03	2.18	2.51
	R_P (%)	5.08	4.82	5.29	4.85	7.16	5.56
	R_{WP} (%)	7.22	6.84	7.58	7.03	9.01	7.79
	V (Å^3)	148.830(1)	148.827(1)	148.829(1)	148.828(1)	148.834(2)	148.830(2)

Selected bond lengths and angles form refinement fits to the synchrotron X-ray diffraction data at variable temperature are displayed in Table 5.7 and Figure 5.15. As reported for the NdMnAsO$_{0.95}$F$_{0.05}$ sample, the bond lengths in both tetrahedra of CeMnAsO$_{0.95}$F$_{0.05}$ shrink with lowering temperature as expected with cell contraction. The plots have a polynomial function fitted to them; highlighting that at low temperatures (below the T$_{SR}$) the parameters level off with a change in gradient. As shown in Figure 5.15, the Ce(O/F) layer bond lengths and angles follow the usual contraction down to ~30 K. Below T$_{SR}$, the refined Ce-O/F bond lengths follow linear behaviour with a steeper gradient. The tetrahedral angles in the Ce(O/F) layers trend towards the ideal tetrahedral angle (109.47°) upon cooling until the T$_{SR}$, below the magnetic transition there is a change so the angles follow linear trends away from the ideal tetrahedral angles. The magnetic order of Ce^{3+} ions is shown to shorten the Ce-O/F bond length and effect the tetrahedral angles so they become less ideal, so, the magnetic order clearly distorts the Ce(O/F) tetrahedra.

The higher temperature Mn^{2+} ordering has no influence on the lattice parameters (as shown in neutron diffraction discussion), this temperature region was not investigated with synchrotron X-ray diffraction. In the MnAs layers the angles do not have clear trends upon cooling the sample, as evident the errors are larger and there is no significant change in the values for the full temperature range. The magnetic ordering of Mn is shown therefore to have little influence on the crystal structure of the sample. The magnetic transition occurring at 34 K is both the spin reorientation of Mn^{2+} spins and introduction of the Ce^{3+} magnetic order. The behaviour of the Ce(O/F) layer matches well to the lattice behaviour observed, so it is apparent that the Ce^{3+} magnetic ordering influences the lattice constants.

Table 5.7: Selected bond lengths and angles for CeMnAsO$_{0.95}$F$_{0.05}$ sample obtained through Rietveld refinement fits to synchrotron X-ray diffraction data recorded at varying temperatures (8 – 290 K).

Temperature (K)	290	150	50	30	25	21
Bond Length (Å)						
Ce-O/F	2.3616(1)	2.3594(1)	2.3586(1)	2.3586(1)	2.3586(1)	2.3584(1)
Mn-As	2.5556(3)	2.5522(3)	2.5507(2)	2.5508(2)	2.5506(2)	2.5507(2)
Ce-As	3.3879(3)	3.3812(3)	3.3778(3)	3.3774(2)	3.3772(2)	3.3773(2)
Mn-Mn	2.89114(1)	2.88702(1)	2.88510(1)	2.88496(1)	2.88491(1)	2.88494(1)
Bond Angles (°)						
α_1 Ce-O/F-Ce	119.919(12)	119.815(11)	119.752(10)	119.747(10)	119.743(9)	119.757(9)
α_2 Ce-O/F-Ce	104.514(5)	104.561(5)	104.589(4)	104.591(4)	104.593(4)	104.586(4)
α_1 As-Mn-As	111.105(9)	111.113(8)	111.118(7)	111.124(7)	111.121(7)	111.123(7)
α_2 As-Mn-As	106.251(17)	106.236(16)	106.225(15)	106.213(14)	106.219(14)	106.215(14)

Temperature (K)	19	17	15	12.5	10	8
Bond Length (Å)						
Ce-O/F	2.3584(1)	2.3585(1)	2.3586(1)	2.3584(1)	2.3583(1)	2.3584(1)
Mn-As	2.5506(2)	2.5505(2)	2.5510(2)	2.5507(2)	2.5505(3)	2.5509(3)
Ce-As	3.3773(2)	3.3773(2)	3.3768(3)	3.3772(2)	3.3777(3)	3.3771(3)
Mn-Mn	2.88493(1)	2.88492(1)	2.88494(1)	2.88493(1)	2.88493(1)	2.88492(1)
Bond Angles (°)						
α_1 Ce-O/F-Ce	119.757(9)	119.754(9)	119.747(10)	119.758(9)	119.772(12)	119.762(10)
α_2 Ce-O/F-Ce	104.586(4)	104.588(4)	104.591(4)	104.586(4)	104.580(5)	104.584(5)
α_1 As-Mn-As	111.120(7)	111.118(7)	111.134(7)	111.123(7)	111.116(9)	111.130(8)
α_2 As-Mn-As	106.222(14)	106.225(13)	106.195(14)	106.215(14)	106.229(17)	106.202(15)
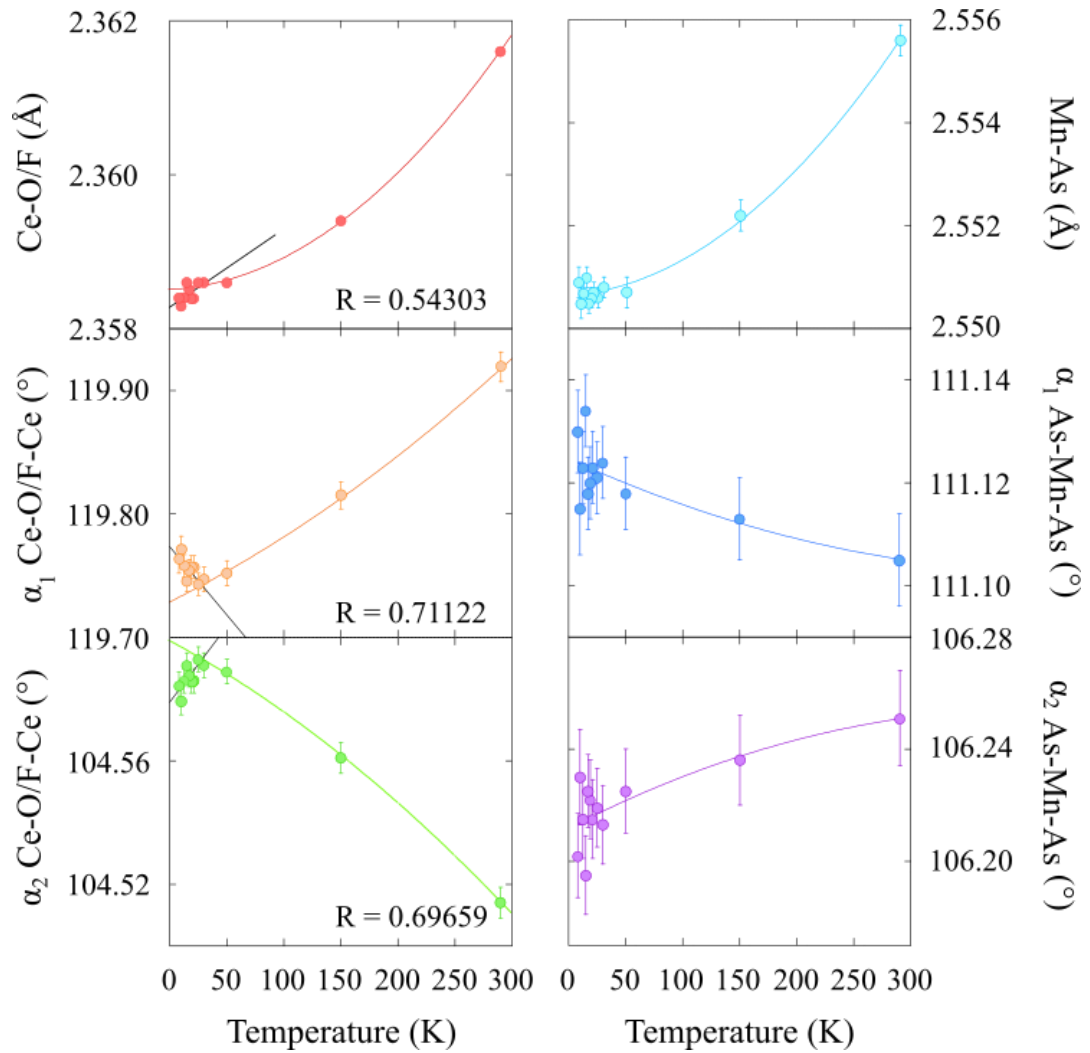
Figure 5.15: Selection of bond lengths and angles with varying temperature in CeMnAsO$_{0.95}$F$_{0.05}$ sample, values obtained from the Rietveld fits to synchrotron X-ray diffraction data. Polynomial fits to the data are displayed for the MnAs layer parameters for the full temperature range, in the Ce(O/F) layer the bond length and angles have polynomial fits from room temperature down to 30 K. Below 30 K in the Ce(O/F) layer the bond length and angles have linear fits displayed in black with R values of straight line fit displayed.

5.3.3: Magnetic Structure Determination from Neutron Diffraction

The magnetic structure of $CeMnAsO_{1-x}F_x$ series was investigated through high resolution and variable temperature high intensity neutron diffraction experiments. The high and low temperature magnetic structures are displayed in Figure 5.16.
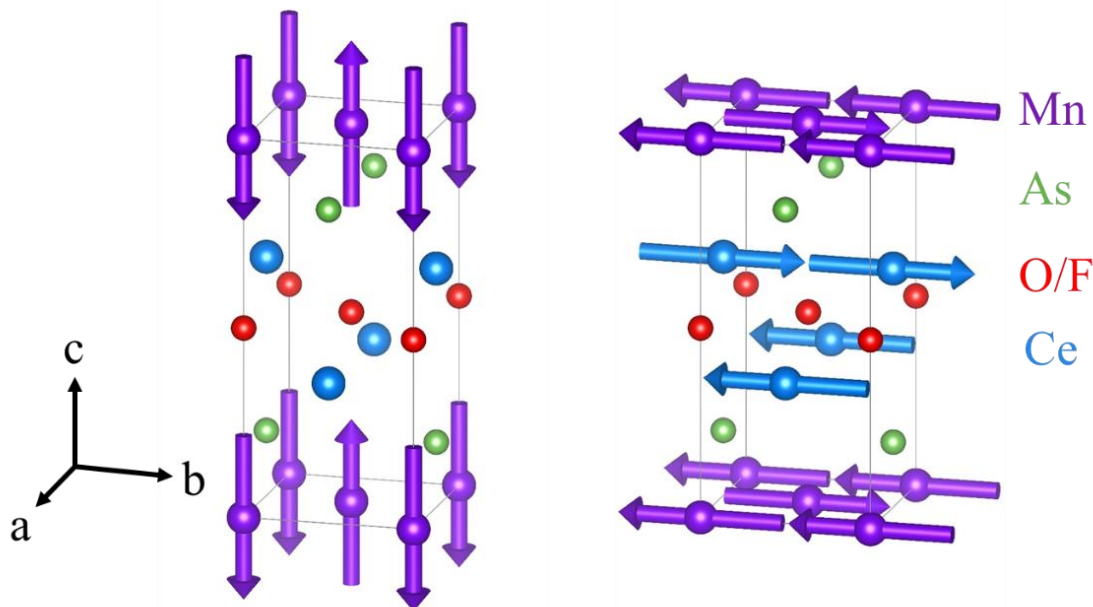
Figure 5.16: The crystal structures of $CeMnAsO_{1-x}F_x$ showing the magnetic ordering of Mn^{2+} and Ce^{3+} ions as determined through refinements performed for neutron diffraction data at 300 K (left) and 1.5 K (right).

At 300 K, the Mn^{2+} ions are ordered antiferromagnetically in a C-type arrangement parallel to the *c* lattice direction. Intraplanar interactions are antiferromagnetic but interplanar the interactions are ferromagnetic. At low temperature there is a rearrangement of Mn^{2+} spins, the same antiferromagnetic arrangement is maintained but now the spins are aligned parallel to the *ab* plane. The Ce^{3+} ions also magnetically order at low temperature, the ordering is antiferromagnetic with spins aligned parallel to the basal plane. The magnetic ordering is the same as reported for the $NdMnAsO_{1-x}F_x$ system[2] and the parent compound $CeMnAsO$[22].

The refined magnetic moments for each sample in the $CeMnAsO_{1-x}F_x$ series are shown in Table 5.8. Fluorine doping does not have a significant effect on the magnetic behaviour of the samples.

The Ce^{3+} magnetic moments do show interesting behaviour with fluorine content, a general decrease of magnetic moment is observed as the fluorine content increases, with the x = 0.05 sample deviating slightly from the linear trend. The trend seen appears to be linked to the Ce(O/F) bond length and angle observations with doping level at low temperature. The 5 atom % F⁻ doped sample deviated from linear trends in calculated bond length and angles, with the largest Ce-O/F bond length observed in that sample at low temperature. Increased lengths, and more ideal tetrahedral angles in the Ce(O/F) layer clearly result in a reduction of the Ce^{3+} ordered magnetic moment as the layer becomes more covalent.

Table 5.8: Refined magnetic moments of CeMnAsO$_{1-x}$F$_x$ with increasing doping level, calculated from refinement fits to D2B neutron diffraction data at high and low temperature.

Temperature	x	0	0.035	0.05	0.075
High (300 K)	Mn^{2+} μ_B(z)	2.54(2)	2.52(2)	2.54(3)	2.49(3)
Low (1.5 – 10 K)	Ce^{3+} μ_B(y)	1.15(4)	1.06(3)	0.97(5)	0.98(5)
	Mn^{2+} μ_B(y)	3.66(3)	3.66(3)	3.66(4)	3.65(4)

Variable temperature neutron diffraction measurements were performed in order to determine the magnetic transition temperatures of the CeMnAsO$_{1-x}$F$_x$ samples and to investigate if there was any change in the magnetic structure at T_{MBL}. Full temperature scans were performed on the x = 0.035 and 0.075 samples, due to time constraints only higher temperature scans were performed on the x = 0 and x = 0.05 samples. A plot of all four CeMnAsO$_{1-x}$F$_x$ samples Mn^{2+} (z) magnetic moments is shown in Figure 5.17. The magnetic transition temperatures found through SQUID magnetometry and neutron diffraction data are presented in Table 5.9. The T_{Mn} for all fluorine doped samples are very similar, with no correlation between F⁻ content and transition temperature. The T_{Mn} of the parent compound is higher, so the introduction of electron doping to the system is shown to lower the magnetic transition for very small amounts of F doping.
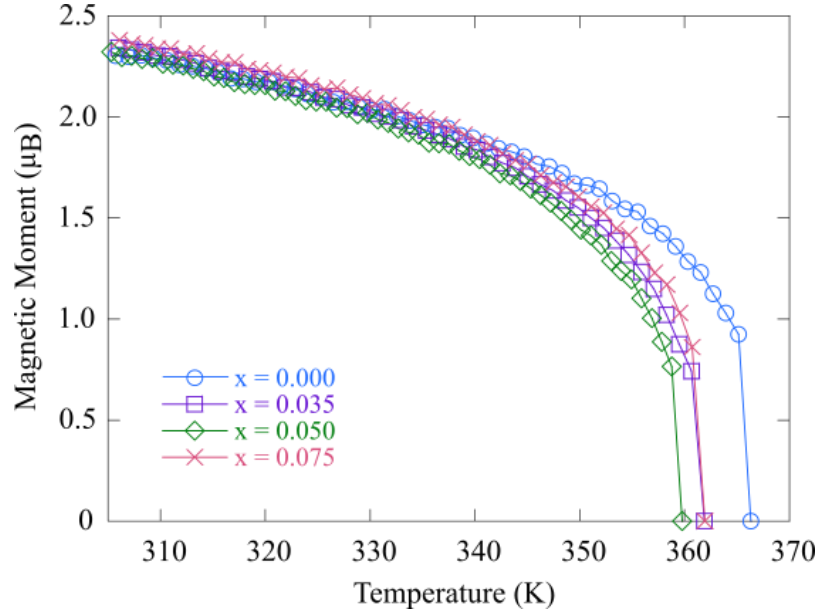
Figure 5.17: Refined magnetic moments of Mn^{2+} ions along c direction variation with temperature for the $CeMnAsO_{1-x}F_x$ series. T_{MN} of each sample is visible, all between 359 and 367 K.

No significant change in the spin reorientation temperature (T_{SR}) is observed throughout the series, with good agreement between the SQUID and neutron diffraction results. The temperature variation of the three different magnetic moment (Ce (y), Mn (y) and Mn (z)) for $CeMnAsO_{0.965-}$ $F_{0.035}$ and $CeMnAsO_{0.925}F_{0.075}$ samples are shown in Figure 5.18 and Figure 5.19 respectively. As is clear from the figures the magnetic behaviour of both samples is the same, as the Ce^{3+} magnetic moments order, the Mn^{2+} moments gradually rearrange from parallel to *c* direction of the lattice into the basal plane. The reorientation occurs within a 10 K region so that the Mn^{2+} moments are fully rearranged by 27 K for both samples.

The T_{MBL} of the 3.5 atom % doped sample was recorded as 18 K, no change in the trend of magnetic moments occurs at this insulator to insulator transition. For the $CeMnAsO_{0.925}F_{0.075}$ sample, there is also no change in magnetic behaviour at the T_{MBL} (76 K). There is no evidence of a link between the magnetic structure and electrical properties evident in this series of materials. The novel transition discovered in this new series of manganese oxypnictides, through these crystal and magnetic structure studies, has therefore been confirmed to be independent of any structural or magnetic structural changes of the sample.

152

Table 5.9: Magnetic transition temperatures of CeMnAsO$_{1-x}$F$_x$ samples. T$_{MN}$ is the temperature at which Mn^{2+} ions order in an antiferromagnetic arrangement along c lattice direction. T$_{SR}$ is the temperature where the Mn^{2+}magnetic ions reorient so they are now parallel to the basal plane. The rearrangement of Mn^{2+} spins occurs simultaneously with the magnetic ordering of Ce^{3+} spins. T$_{SR}$ SQUID were determined from differential plots of the magnetometry data.

x	0	0.035	0.05	0.075
T$_{Mn}$	366	362	360	362
T$_{SR}$ Neutron	-	35.08	-	35.58
T$_{SR}$ SQUID	34	32	34	34

Figure 5.18: Temperature variation of magnetic moments determined from Rietveld refinements of D20 neutron diffraction data for CeMnAsO$_{0.965}$F$_{0.035}$.
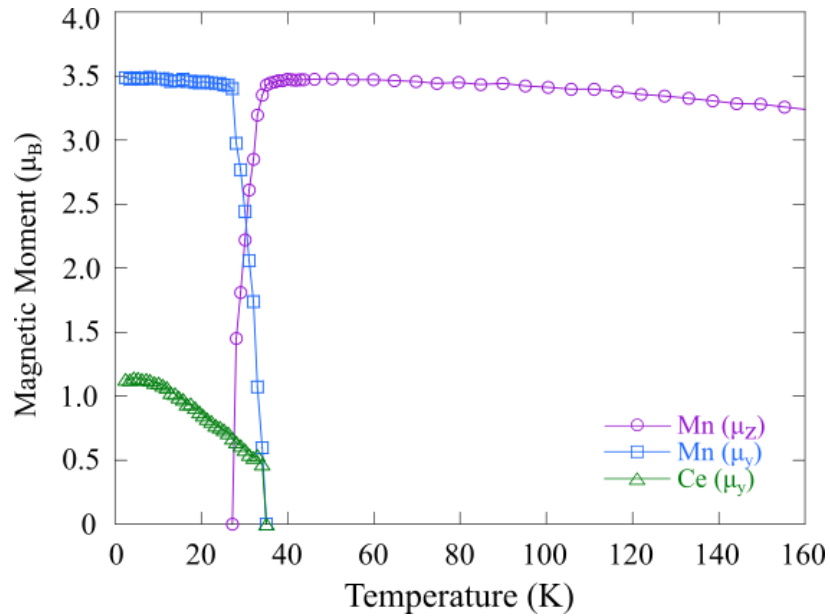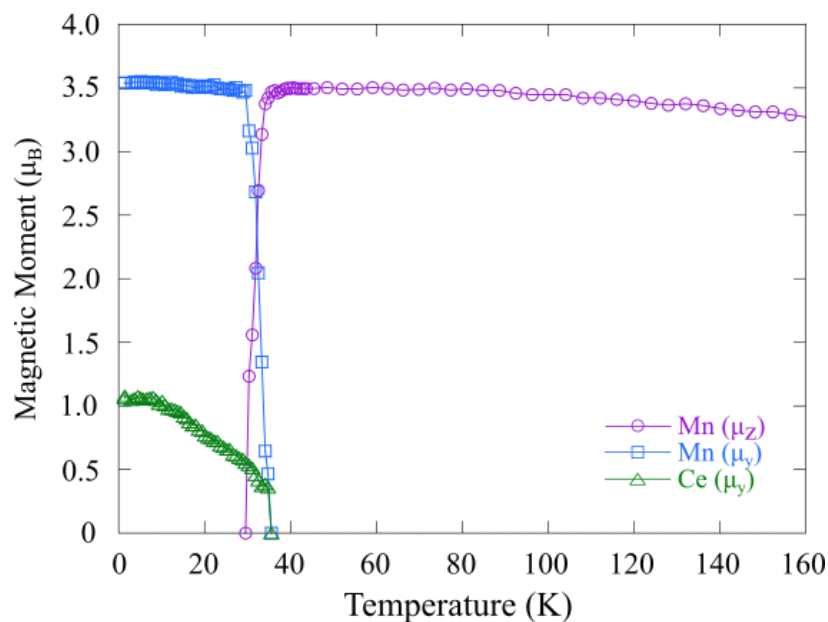
Figure 5.19: Temperature variation of magnetic moments determined from Rietveld refinements of D20 neutron diffraction data for CeMnAsO$_{0.925}$F$_{0.075}$.

5.4: Conclusions

An extensive structure study on the CeMnAsO$_{1-x}$F$_x$ (x = 0, 0.035, 0.05, 0.075) series has been performed using variable temperature neutron and synchrotron X-ray diffraction. Refinement fits for all samples at all temperatures were to the tetragonal space group *P4/nmm*, as previously reported for the 1111 structure. Small (~1.5 % by volume) CeOF impurities were visible in the 7.5 atom % doped fluorine sample (through laboratory X –ray experiments and neutron experiments) and 5 atom % fluorine doped sample (through synchrotron X-ray experiments).

Room temperature neutron diffraction data presented was a result of refinements performed by fellow PhD student Struan Simpson, I originally performed all refinements using the FullProf Suite package but a switch to GSAS occurred and the work was split between high and low temperature. Through neutron diffraction, a deficiency of As was discovered, not previously seen in the refinements to X-ray data. The deficiency could possibly be a result of sample degradation between the time of sample preparation and the neutron experiments. As tantalum is an arsenic getter, this could also explain the slight deficiency. Sample degradation has been observed to occur in the

154

series, with T_{MBL} shifting to lower temperatures with time, from 34 K to 16 K in the CeMnAsO$_{0.95}$F$_{0.05}$ sample. Arsenic occupancy does not show any correlation to the T_{MBL} of the samples, unlike cerium, manganese and fluorine occupancies that were previously shown to have influence on the insulator-to-insulator transition temperature. The same trends in lattice parameters are observed in both sets of neutron diffraction data as seen in the refinement fits to X-ray diffraction data, with *a* and *c* both decreasing with increasing F⁻ content until x = 0.05, then a sudden increase at high dopant level (x – 0.075). This behaviour would suggest that the nominal doping had not occurred for x = 0.075.

However, at room temperature the refined parameters within the Ce(O/F) layers display clear trends. The Ce-O/F bond length shows continuous increase with F⁻ content, as seen in CeFeAsO$_{1-x}$F$_x$ series, confirming that the x = 0.075 does in fact contain the highest dopant level. Both α tetrahedral angles in the Ce(O/F) layer display clear trends with x level, they become more 'ideal' tetrahedral angles as both increase/decrease towards 109.47°. At low temperature the Ce(O/F) layer behaviour shows a deviation at x = 0.05, the sample where As occupancy is 1. The higher As level in the MnAs layer results in a more negatively charged tetrahedra which attracts the Ce^{3+} ions, resulting in a stretch of the Ce-O/F bonds seen.

In the MnAs layers, the same trends are reported at both high and low temperature, with As occupancy having a large impact on the values. The trends in all As deficient samples are similar to those reported from the laboratory X-ray diffraction data set, with MnAs tetrahedra trending towards more regular angles with increasing fluorine content and shrinking bond length. At low temperatures the behaviour in the MnAs layers is the same, with the x = 0.05 sample deviating from near linear trends.

Variable temperature neutron diffraction patterns were recorded showing a clear reduction of cell parameters upon cooling. A deviation in the linear trends is observed below the T_{SR} of the samples (~34 K), where the gradient of the slope is altered. At T_{MBL} there is no observed change in the crystal structure from neutron diffraction results. Closer inspection of the crystal structure was performed through synchrotron X-ray diffraction experiments. No peak splitting or superstructure peaks appear on cooling the CeMnAsO$_{0.95}$F$_{0.05}$ sample. The same contraction of *a* and *c* parameters with temperature was observed, with the gradient of the plotted slopes again shown to change below the T_{SR}. The Ce(O/F) layer trends in bond lengths and angles match those in the lattice

parameters but the MnAs layer angles do not have clear trends. No change to the structural trends occurs at high temperature (T_{Mn}) where the Mn^{2+} magnetic moments originally order so it is clear the introduction of Ce^{3+} magnetic order is the influence behind the lattice behaviour observed. No link between the crystal structure and the insulator transition was found through both neutron and synchrotron X-ray diffraction experiments, which would suggest that the origin of the insulator-insulator transition is of a more exotic nature. We propose that a transition into a many-body localised state could be present, but further experiments are required.

The magnetic behaviour of the $CeMnAsO_{1-x}F_x$ series matches that of the parent compound previously studied, and the neodymium analogue of the series $NdMnAsO_{1-x}F_x$. At high temperatures the Mn^{2+} ions antiferromagnetically order in a C-type AFM structure parallel to the c lattice direction. At low temperatures the Mn^{2+} ions have now undergone a spin reorientation so they are in the same AFM arrangement but parallel to the basal plane of the lattice. Ce^{3+} ions are also magnetically ordered at low temperature, with the same AFM arrangement in the basal plane. Variable temperature neutron diffraction experiments allowed for the determination of the T_{Mn} and T_{SR} in $CeMnAsO_{1-x}F_x$ series. The undoped CeMnAsO sample displays the highest T_{Mn}, with all fluorine doped samples displaying lower transition temperatures. There is no clear trend in T_{Mn} with increasing F^- content present. The x = 0.035 and 0.075 samples have similar As occupancies and the T_{Mn} recorded for both are 362 K, showing that a link may exist between the As content and the T_{Mn}. The T_{SR} is invariant of the fluorine content of the samples, showing that the presence of electron doping of the structure has little effect on the Ce^{3+} order but a stronger influence on the magnetic order of Mn^{2+} ions. No fluctuation of the magnetic moments is evident at the T_{MBL} of the measured samples.

There is evidence of coupling in the $CeMnAsO_{1-x}F_x$ series between the magnetic structure and the crystal structure. The link is clear as when cooling the sample below T_{SR} as the lattice constants (a and c) are shown to deviate from the linear trend. No change is observed in the data, both nuclear structure and magnetic structure, at temperatures close to the insulator-to-insulator transition. The novel transition is therefore independent of structural deviations in the series.

References

[1] Y. Kamihara, T. Watanabe, M. Hirano and H. Hosono, 2008, *J. Am. Chem. Soc*. **130**, 3296-3297.

[2] E. J. Wildman, J. M. S. Skakle, N. Emery and A. C. Mclaughlin, 2012, *J. Am. Chem. Soc.* **134**, 8766-8769.

[3] S. Margadonna, Y. Takabayashi, M. T. McDonald, M. Brunelli, G. Wu, R. H. Liu, X. H. Chen and K. Prassides, 2009, *Phys. Rev. B.* **79***, 014503.

[4] W. Lu, J. Yang, X. L. Dong, Z. A. Ren, G. C. Che and Z. X. Zhao, 2008, *New J. Phys.* **10**, 063026.

[5] C. H. Lee, A. Iyo, H. Eisaka, H. Kito, M. T. Fernandez-Diaz, T. Ito, K. Kihou, H. Matsuhata, M. Braden and K. Yamada, 2008, *J. Phys. Soc. Jpn.* **77**, 083704.

[6] C. H. Lee, K. Kihou, A. Iyo, H. Kito, P. M. Shirage and H. Eisaki, 2012, *Solid State Commun.* **152**, 644-648.

[7] T. Watanabe, H. Yanagi, Y. Kamihara, T. Kamiya, M. Hirano and H. Hosono, 2008, *J. Solid State Chem.* **181**, 2117-2120.

[8] Y. Luo, H. Han, H. Tan, X. Lin, Y. Li, S. Jiang, C. Feng, J. Dai, G. Cao, Z. Xu and S. Li, 2011, *J. Phys.: Condens. Mat.* **23**, 175701.

[9] Y. Li, Y. Luo, L. Li, B. Chen, X. Xu, J. Dai, X. Yang, L. Zhang, G. Cao and Z. Xu, 2014, *J. Phys.: Condens, Mat*. **26**, 425701.

[10] X. Jin, T. Masubuchi, T. Watanabe, K. Takase and Y. Takano, 2009, *J. Phys. Conf. Ser.* **150**, 052085.

[11] H. Ohta and K. Yoshimura, 2009, *Phy, Rev. B.* **80**, 184409.

[12] S.-W. Park, H. Mizoguchi, K. Kodama, S. Shamoto, T. Otomo, S. Matsuishi, T. Kamiya and H. Hosono, 2013, *Inorg. Chem.* **52**, 13363-13368.

[13] N. Emery, E. J. Wildman, J. M. S. Skakle and A. C. Mclaughlin, 2011, *Phys. Rev. B.* **83***, 144429.

[14] E. J. Wildman, M. G. Tucker and A. C. Mclaughlin, 2015, *J. Phys.:Condens. Mat.* **27**, 116001.

[15] E. J. Wildman, F. Sher and A. C. Mclaughlin, 2015, *Inorg. Chem*. **54**, 2536-2542.

[16] F. Fauth, R. Boer, F. Gil-Ortiz, C. Popescu, O. Vallcorba, I. Peral, D. Fulla, J. Benach and J. Juanhuix, 2015, *Eur. Phys. J. Plus.* **130**, 160.

[17] P. J. E. M. Van der Linden, M. Moretti Sala, C. Henriquet, M. Rossi, K. Ohgushi, F. Fauth, L. Simonelli, C. Marini, E. Fraga, C. Murray, J. Potter and M. Krisch, M., 2016, *Rev. Sci. Instrum.* **87***, 115103.

[18] E. J. Wildman, K. S. McCombie, G. B. G. Stenning and A. C. Mclaughlin, *Dalton Trans.*, 2018, **47**, 14726.

[19] J. Zhao, Q. Huang, C. De La Cruz, S. Li, J. W. Lynn, Y. Chen, M. A. Green, G. F. Chen, G. Li, Z. Li, J. L. Luo, N. L. Wang and P. Dai, 2008, *Nat. Mater.* **7**, 953-959.

[20] E. J. Wildman, K. S. McCombie, G. B. G. Stenning and A. C. Mclaughlin, 2018, *Dalton T.* **41**, 14726-14733.

[21] E. J. Wildman and A. C. Mclaughlin, 2016, *Sci. Rep.* **6**, 20705.

[22] A.J. Corkett, D. G. Free and S. J. Clarke, 2015, *Inorg. Chem.* **54**, 1178-1184.

Chapter 6

Synthesis and Preliminary Studies of Manganese Antimonides

6.1: Introduction

Many different substitution methods have been explored within the 1111 family of oxypnictides. The discovery of superconductivity within iron arsenides was first made within both the parent and fluorine doped LaFePO sample [1,2]. The samples share the ZrCuSiAs type structure, with alternating layers of lanthanum oxide and iron phosphide tetrahedra, crystallising in the $P4/nmm$ tetragonal space group. The pure and fluorine doped samples both display a superconducting transition at low temperatures (T_C ~5 K). Upon replacing phosphorus with arsenic in this system, the superconducting transition shifts to much higher temperatures. $LaFeAsO_{1-x}F_x$ was found to have zero resistance at 26 K [3], demonstrating that the pnictide ion has a large influence on the electrical properties of the system.

Replacement of the pnictide ion can also have an influence on the magnetic transitions within the 1111 structure. $LaCoPnO$ (Pn = P, As) samples were studied[4], with the lattice constants increasing as expected with increasing ionic radius of Pn. The two samples display metallic behaviour down to 3 K and no evidence of superconductivity is recorded. The $LaCoPnO$ system displays ferromagnetism and the Curie temperature is dependent on the pnictide ion (34 K for P analogue, 59 K for As analogue) showing that the magnetic transitions are heavily influenced by the Pn ion.

The structure and magnetic properties of $LnMnSbO$ (Ln = La and Ce) have been investigated, with both crystallising in the expected $P4/nmm$ tetragonal space group[5]. High temperature ordering of Mn^{2+} ions occurs in both samples into a C-type AFM arrangement of spins, with T_{Mn} = 255 K and 240 K for La and Ce analogues respectively. These T_{Mn} values are lower than those reported for the arsenic analogues, 317 K for $LaMnAsO$[6] and 347 K for $CeMnAsO$[7], which indicates that the Mn-Pn (Pn = As or Sb) d-p hybridization is weaker in the samples containing Sb. Weaker hybridization between Mn d orbitals and Sb p orbitals results in weakened superexchange Mn-Mn

coupling. The CeMnSbO sample undergoes a spin reorientation transition alongside ordering of Ce^{3+} spins, similar to that seen in the arsenic analogue but at lower temperature, ~ 4.5 K in comparison to ~ 34 K.

The success of electron doping of the 1111 structure led to experimentation with the opposing technique of hole doping. In the iron arsenide materials, superconductivity was found with both doping strategies. The electron doped $LnFeAsO_{1-x}F_x$ samples were first reported, with T_{CS} found over 50 K[8, 9]. From that success, this hole doping approach was further explored, with substitution of trivalent lanthanide ions (Ln^{3+}) with divalent strontium ions (Sr^{2+}). In the $La_{1-x}Sr_xFeAsO$ series a maximum T_C of 25 K was found when x = 0.13, therefore the superconducting transition is slightly lower in these materials even if the doping levels possible are higher (solubility of fluorine into the 1111 structure is limited to x < 0.2)[10]. In the PrFeAsO series, the doping strategy has a much larger effect on the superconducting transition temperature. $PrFeAsO_{1-x}F_x$ displays a transition into a superconducting state at 52 K when x = 0.11[8], the hole doped equivalent $Pr_{1-x}Sr_xFeAsO$ only shows a maximum T_C of 16.3 K when x= 0.20 – 0.25[11]. The use of differing doping techniques in the iron arsenides does not destroy the superconductivity behaviour, but this does appear to affect the transition temperature.
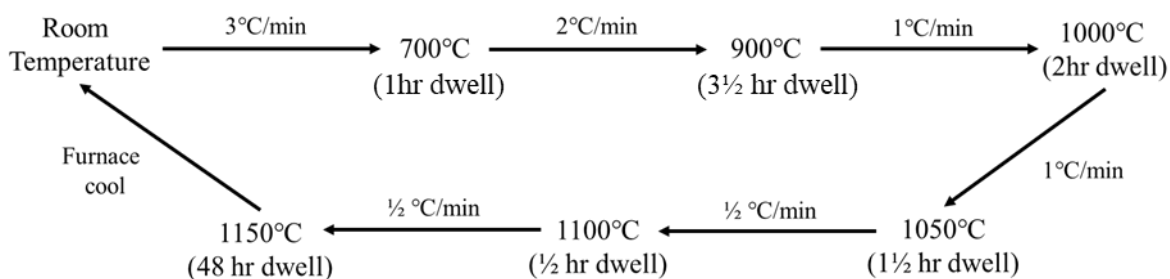
Within the 1111 manganese arsenides, doping strategy has been shown to change the electrical properties of the materials. Electron doping of the NdMnAsO system through partial substitution of oxygen with fluorine resulted in the emergence of colossal magnetoresistance[12]. The charge carriers are reported as electrons produced through the replacement of O^{2-} ions with F^- ions, hence a change in the doping strategy would be expected to result in differing properties. A series of $Nd_{1-x}Sr_xMnAsO$ samples exhibited metallic behaviour, unlike the semiconducting NdMnAsO parent compound, and no large negative MR[13]. At low temperatures the strontium doped materials have positive MR with peaks around 15 K. The positive MR in $Nd_{1-x}Sr_xMnAsO$ series is unrelated to the magnetic transitions in the material unlike the CMR in $NdMnAsO_{1-x}F_x$ samples. The two doping strategies clearly display that multiple different MR mechanisms occur in $LnMnAsO$ samples.

Furthermore, some preliminary synthesis and study into new manganese antimonide materials has been performed. The intention was to investigate the effect of hole and electron doping on the structure and magnetic properties of the CeMnSbO system.

6.2: Experimental

6.2.1: Synthesis

$Ce_{1-x}Sr_xMnSbO$ (x = 0 – 0.075) samples were made through a one-step solid state reaction method using stoichiometric quantities of CeSb (prepared), MnO (99.99% Alfa Aesar), Sb (99.5% Alfa Aesar), Mn powder (99.99% Aldrich), and SrO (prepared). SrO was prepared through a precursor step involving heating $SrCO_3$ (99.99% Aldrich) at 1200°C for 12h and the decarbonated material was then cooled within an inert environment. $CeMnSbO_{1-x}$ (x = 0 – 0.075) and $NdMnSbO_{1-x}F_x$ (x = 0 – 0.05) samples were made through a one-step solid state reaction method using stoichiometric quantities of CeSb/NdSb (prepared), MnO (99.99% Alfa Aesar), Mn powder (99.99% Aldrich), and MnF_2 (98% Aldrich). CeSb and NdSb were prepared through a precursor step involving grinding and pelleting powdered Ce ingot (99% Alfa Aesar) or Nd (99.99% Aldrich) with Sb (99.5% Alfa Aesar) before reacting in a vacuum sealed silica tube at 980°C for around 33h. The precursor was then ground in an inert atmosphere to a powder ready for sample preparation. The starting materials were mixed together in an inert atmosphere in a glove bag using an agate mortar and pestle to grind the powders into a homogeneous mix. The combined powders were then pelleted and placed in a tantalum crucible, then transferred into an evacuated quartz tube. The tantalum crucible was used to prohibit contact between the pellet and the silica tube as fluorine ion diffusion would occur otherwise. The pellets were subsequently sintered through the following heating procedure:

Room Temperature → 3°C/min → 700°C (1hr dwell) → 2°C/min → 900°C (3½ hr dwell) → 1°C/min → 1000°C (2hr dwell)

1000°C → 1°C/min → 1050°C (1½ hr dwell)

1050°C → ½ °C/min → 1100°C (½ hr dwell) → ½ °C/min → 1150°C (48 hr dwell)

1150°C → Furnace cool → Room Temperature

161

X-ray powder diffraction patterns were recorded on the PANalytical Empyrean powder diffractometer with Cu Kα1 radiation (λ = 1.540598 Å). Quick scans were performed between range of 5° < 2θ < 70° using a 0.0131° step size for around 12-30 minutes. Longer scans were recorded for Rietveld refinements of the XRD. The same PANalytical Empyrean diffractometer was used to perform the high-quality scans, with counting times around 16 hours. The patterns were recorded between range of 10 < 2θ < 120°, with step size of 0.003°.

6.2.3: Magnetic Measurements

Magnetisation measurements of $Ce_{1-x}Sr_xMnSbO$ samples were recorded on a MPMS-XL SQUID using an applied field of 1000 Oe after zero field cooling (ZFC) and field cooling (FC) the sample, measuring in the range 2 – 300 K.

6.3: Results and Discussion

6.3.1: Synthesis of Electron Doped Manganese Antimonides

Due to the successful synthesis of $CeMnAsO_{1-x}F_x$ (as discussed in Chapters 4 and 5), preparation of the same series was attempted with arsenic substituted with antimony. The X-ray diffraction profiles for $CeMnSbO_{1-x}F_x$ samples (x = 0.03 – 0.075) are shown in Figure 6.1. Only a short time was available to prepare these samples and as is clear from the diffraction profiles, impurities were present throughout the series highlighted with asterisks in the figure (*). The impurities are the same as those often seen in the arsenic analogues, CeOF and Ce_2O_3, with the purity decreasing as the F^- content increases. A further impurity phase is present within the x = 0.075 sample, denoted by (★) in Figure 6.1, which indexes as Sb_2O_5. Nominal doping of F^- is unlikely to have occurred due to the fluorine containing impurity.

The Bragg peaks appear to shift to lower 2θ angle, indicating the increase of cell parameters in the $CeMnSbO_{1-x}F_x$ series as x increases. Rietveld refinements were performed on the samples, revealing all have Ce and Sb deficiencies, the refinement fits are displayed in Appendix Figure 8.10. Selected parameters from the room temperature X-ray diffraction refinement fits are shown in Appendix Table 8.4, with bond lengths and angles in Appendix Table 8.5. There are no observable trends throughout the series, so further research is needed to improve the synthesis and ensure that proper incorporation of F^- occurs.

Synthesis of the $NdMnSbO_{1-x}F_x$ series was examined. Quick X-ray diffraction scans of the materials, however, revealed impurities and the preparation of samples was unsuccessful. A limited time period of availability to perform synthesis stopped any further study of $LnMnSbO_{1-x}F_x$ ($Ln =$ Ce, Nd) samples.

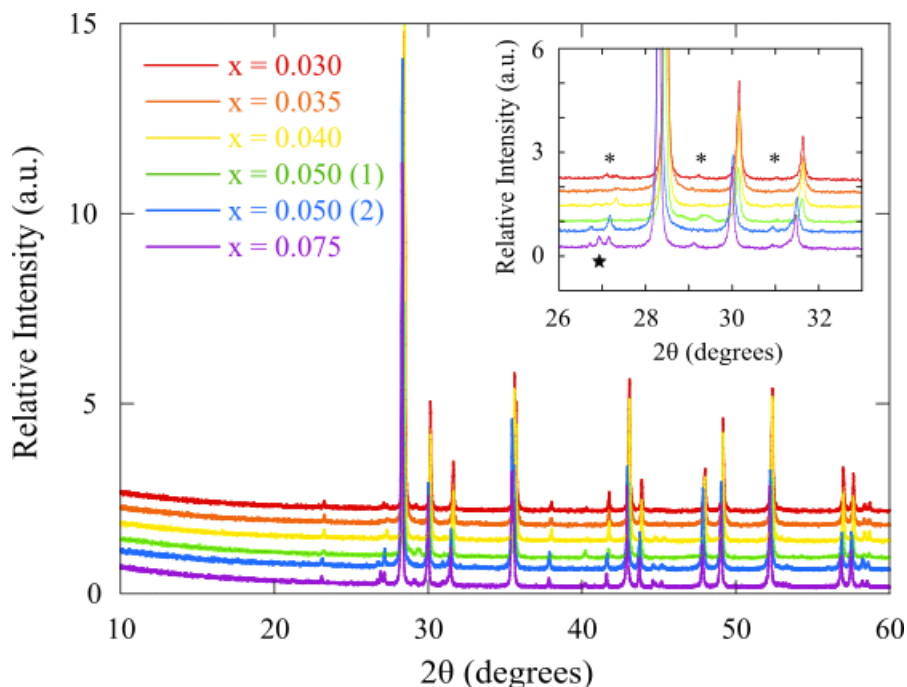*Figure 6.1: Comparison of the X-ray diffraction patterns for $CeMnSbO_{1-x}F_x$ series. Inset shows zoomed 2 theta region where visible impurities are present in the samples highlighted with * which are a mix of CeOF and Ce_2O_3 impurity phases. The ★ denotes a Sb_2O_5 impurity present in the $CeMnSbO_{0.925}F_{0.075}$ sample.*

6.3.2: Crystal Structure Determination from X-ray Diffraction

Synthesis of another series of CeMnSbO samples was performed, in this case hole doping was assessed through partial substitution of Ce with Sr, rather than the electron doping which was previously performed. $Ce_{1-x}Sr_xMnSbO$ samples were synthesised with doping levels x = 0 to 0.075, with Rietveld refinement fits to laboratory X-ray diffraction patterns carried out (Figure 6.2). All phases crystallise in *P*4/*nmm* tetragonal space group. Ce/Sr and Sb occupy the 2*c* Wyckoff site (¼, ¼ z), Mn on 2*b* site (¾, ¼, ½) and O occupying the 2*a* site (¾, ¼, 0). Selected cell parameters, agreement parameters and atomic parameters from the room temperature X-ray diffraction refinement fits are shown in Table 6.1. From the refinement parameters, it is clear that the fits are good in each case. All of the prepared samples contain small impurities, the x = 0.025 and 0.05 samples contain the same small Ce_2O_3 impurity. The x = 0 and 0.075 samples contain a different impurity phase that is not easily identified, and could potentially be the MnSb phase.

Table 6.1: Selected refined cell parameters, agreement factors and atomic parameters for Ce₁₋ₓSrₓMnSbO series (x = 0 – 0.075) from Rietveld fits against laboratory X-ray diffraction data recorded at room temperature. Wyckoff sites for each ions are as follows: Ce/Sr and Sb are at 2a (¼, ¼, z), Mn at 2b (¾, ¼, ½) and O at 2c (0, ½, 0).

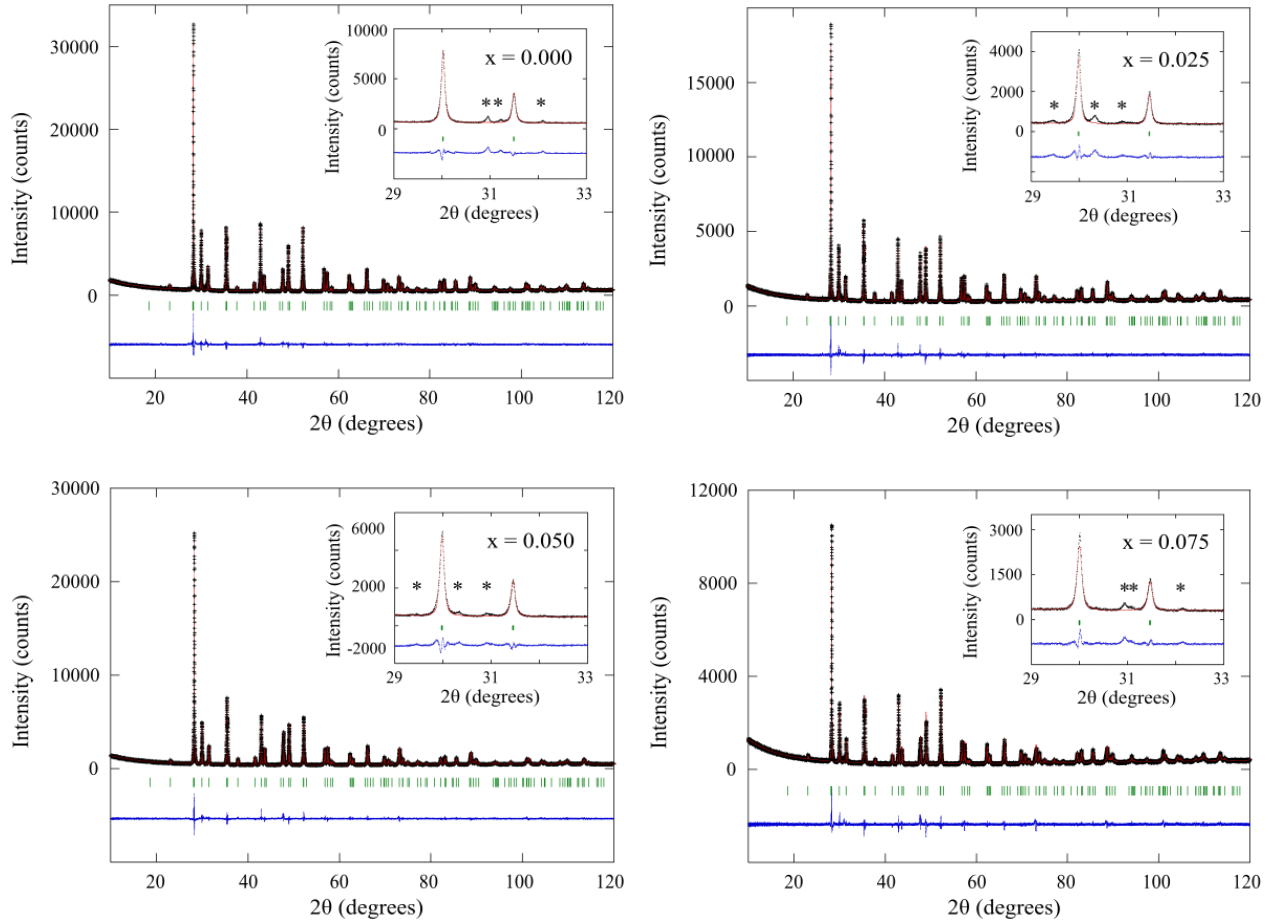|	x			
	0.000	**0.025**	**0.050**	**0.075**
a **(Å)**	4.20963(2)	4.21002(2)	4.20988(2)	4.21052(3)
c **(Å)**	9.50385(4)	9.50503(4)	9.50841(5)	9.51471(8)
Volume (Å³)	168.418(2)	168.469(2)	168.518(3)	168.681(4)
Ce z	0.1181(1)	0.1179(2)	0.1179(1)	0.1176(1)
Sb z	0.6832(1)	0.6835(1)	0.6835(1)	0.6831(1)
R_WP (%)	6.15	6.77	6.03	7.60
R_P (%)	4.45	5.00	4.53	5.51
χ^2	2.97	2.40	2.41	2.49

Figure 6.2: Rietveld refinement fits to the laboratory X-ray diffraction patterns of $Ce_{1-x}Sr_xMnSbO$ series ($x = 0 - 0.075$). Inset is a zoomed region of the refinement fits, impurity peaks are highlighted with asterisks (*).

The cell parameters display overall trends; increasing upon partial substitution of Ce^{3+} ions with Sr^{2+} ions, see Figure 6.3. The ionic radius of Sr^{2+} is larger than that of Ce^{3+} (1.32 Å rather than 1.15 Å) and thus an expansion of the cell parameters is expected upon increasing the strontium content. The trend in cell parameters confirms that the strontium content is increasing across the series as desired.
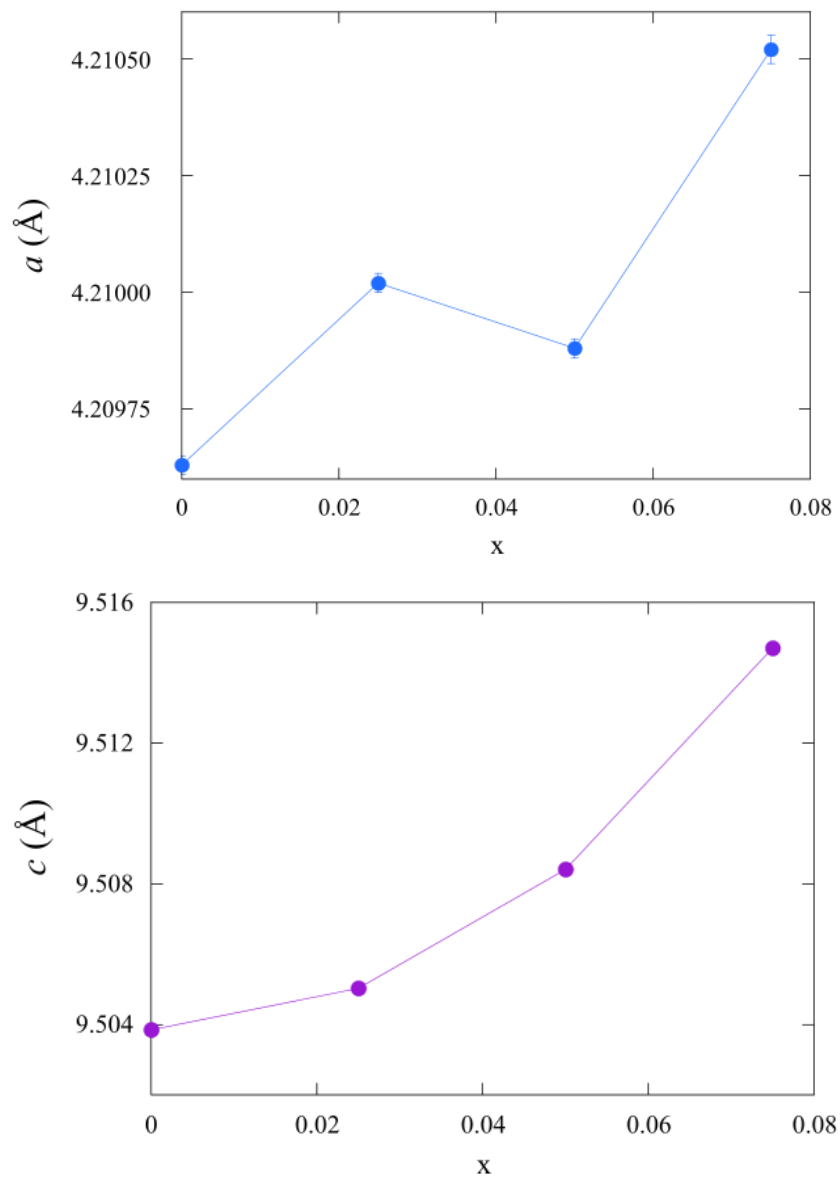
Figure 6.3: Plots displaying the variation of a and c cell parameters with increasing Sr content in the Ce$_{1-x}$Sr$_x$MnSbO series.

A selection of bond lengths and angles are shown in Table 6.2 and Figure 6.4. Within the Ce/Sr-O layers there are general trends observed with increasing x content. The Ce/Sr-O bond decreases as Sr content increases, further validating that the nominal doping of strontium was successful. The Ce/Sr-O-Ce/Sr bond lengths trend away from the ideal tetrahedral angles (109.47°) with increasing doping level, this opposes what is seen within the $CeMnAsO_{1-x}F_x$ family. In the MnSb layers there are not distinct trends observed, this could be a result of the impurities as well as the non-stoichiometry within the samples. All $Ce_{1-x}Sr_xMnSbO$ samples had their Mn content refined to below 0.99 occupancy so they are all deficient in manganese, this non-stoichiometry may be causing the lack of trends as seen in the $NdMn_{1-x}Co_xAs_{0.95}O_{0.05}$ series[14]. Further studies into the $Ce_{1-x}Sr_xMnSbO$ series would be necessary to better understand the crystal structure using neutron and synchrotron X-ray diffraction techniques, as employed for the $CeMnAsO_{1-x}F_x$ series.

Table 6.2: Selected bond lengths and angles for $Ce_{1-x}Sr_xMnSbO$ series obtained through Rietveld refinement fits to X-ray diffraction data recorded at room temperature.

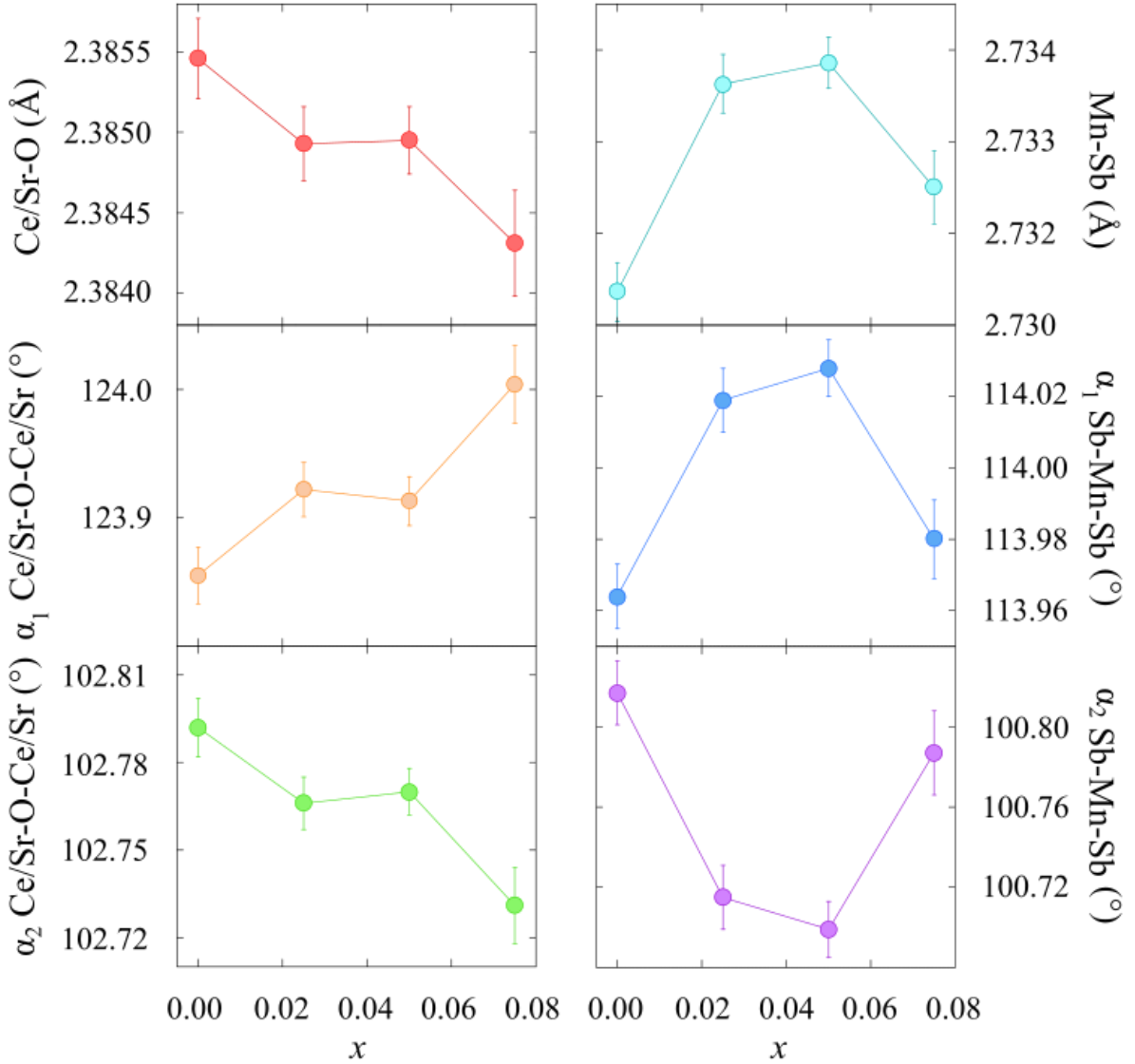| x	0	0.025	0.05	0.075
Bond length (Å)				
Ce/Sr–O	2.3854(3)	2.3849(2)	2.3850(2)	2.3843(3)
Mn–Sb	2.7314(3)	2.7336(3)	2.7339(3)	2.7325(4)
Ce–Sb	3.5253(4)	3.5248(4)	3.5253(4)	3.5298(6)
Mn–Mn	2.97666(1)	2.97693(1)	2.97683(2)	2.97729(2)
Bond angles (°)				
α_1 Ce/Sr–O–Ce/Sr	123.86(2)	123.92(2)	123.91(2)	124.00(3)
α_2 Ce/Sr–O–Ce/Sr	102.79(1)	102.77(1)	102.77(1)	102.73(1)
α_1 Sb–Mn–Sb	113.96(1)	114.02(1)	114.03(1)	113.98(1)
α_2 Sb–Mn–Sb	100.82(2)	100.72(2)	100.70(1)	100.79(2)

Figure 6.4: Selection of bond length and angles with varying strontium content (x) in $Ce_{1-x}Sr_xMnSbO$ series, values obtained from the refinement using laboratory X-ray diffraction data.

6.3.3: Magnetic Properties

The magnetic behaviour of the parent CeMnSbO compound has been previously investigated[5]. The magnetic structure of CeMnSbO is the same as that reported for CeMnAsO, at high temperatures, in that the manganese magnetic moments form long-range order into a C-type antiferromagnetic arrangement of spins along c (T_{Mn} = 240(4) K). Below 4 K there is a spin-reorientation transition

of Mn^{2+} ions, with the C-type AFM arrangement maintained but now oriented in the *ab* plane. Simultaneously, the Ce^{3+} magnetic moments align in an antiferromagnetic arrangement in the basal plane. The magnetic behaviour displayed is similar to that reported for the CeMnAsO system, however, the magnetic transition temperatures are lowered as a result of substituting arsenic with antimony.

Variable temperature magnetic susceptibility measurements were performed on the four $Ce_{1-x}Sr_xMnSbO$ (x = 0, 0.025, 0.05, 0.075) samples. Zero-field cooled (ZFC) susceptibility curves are shown in Figure 6.5. It is evident that for all samples the spin reorientation transition, as previously found for the parent compound, occurs at around the same temperature T_{SR} ~ 4 K. Strontium doping does not appear to change the magnetic behaviour. The high temperature magnetic transition (T_{Mn}) is not visible within these magnetic susceptibility measurements. As in the CeMnAsO series, 2D magnetic correlations arise at temperatures above the T_{Mn} in the $Ce_{1-x}Sr_xMnSbO$ series, resulting in the transition not being visible through SQUID measurements[7]. Moreover, it was not possible to fit the magnetic susceptibility plots to Curie-Weiss behaviour, this is presumed to be due to the 2D manganese magnetic correlations.

A plot of the 2.5 atom % strontium doped $Ce_{1-x}Sr_xMnSbO$ sample ZFC and FC curves is shown in Figure 6.6. The parent compound (CeMnSbO) ZFC and FC curves plot is shown in Appendix 8.11 There is no evidence of a spin glass component or a ferromagnetic transition in this series as the ZFC and FC curves show no splitting. To fully explore the magnetic behaviour of the new series, variable temperature neutron diffraction measurements would be required.
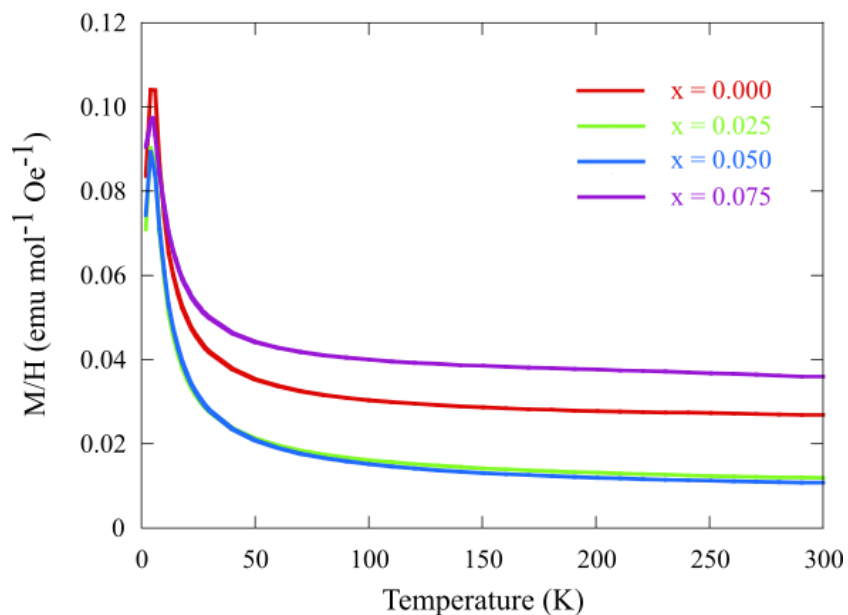
Figure 6.5: ZFC variable temperature magnetic susceptibility of Ce1-xSrxMnSbO (x = 0, 0.025, 0.050 and 0.075) all showing a magnetic transition around T_{SR} = 4 K.
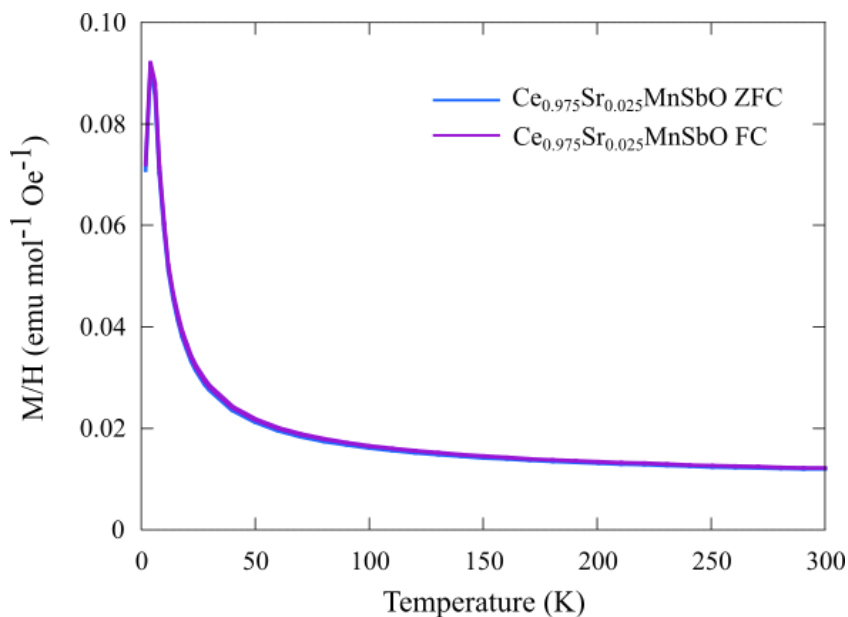

Figure 6.6: Variable temperature magnetic susceptibility plots of Ce0.975Sr0.025MnSbO for both ZFC and FC data, no splitting of the data sets occurs.

6.4: Conclusions

A new series of 1111 type manganese oxyantimonides was synthesised. There was no success within the synthesis of the $NdMnSbO_{1-x}F_x$ series, with impurity peaks evident in short X-ray diffraction scans. Within the $CeMnSbO_{1-x}F_x$ series, impurities (CeOF and Ce_2O_3) were present as has often been detected in arsenide analogues. The impurity content rose as the doping level was increased in the samples and given the presence of a CeOF impurity, nominal doping in the series is unlikely to have occurred. The Bragg peaks apparent in X-ray diffraction patterns were shown to shift to lower 2 theta angle, indicating there is the increase of cell parameters in the $CeMnSbO_{1-x}F_x$ series with increasing doping level. Preliminary Rietveld refinement fits to the X-ray diffraction data revealed Ce and Sb deficiencies, with no observable trends in the crystal structure across the series. These samples had no further analysis performed.

A series of hole doped samples were prepared with formula $Ce_{1-x}Sr_xMnSbO$ (x = 0 – 0.075). All of the samples contain small impurities, so the synthesis was not entirely successful. The cell parameters exhibit clear trends with an increase in strontium content, as was expected given the larger ionic radius of Sr^{2+} than Ce^{3+}. The increasing cell parameters is an indication that the strontium content is successfully increasing across the series, even if nominal doping is unlikely given the presence of impurities. No trends are present within the bond lengths and angles in the MnSb layers. The (Ce/Sr)O layers display observable trends, with the bond lengths decreasing with increasing strontium content as well as tetrahedral angles showing clear trends away from the ideal angle of 109.47°.

Variable temperature magnetic susceptibility measurements were performed on the $Ce_{1-x}Sr_xMnSbO$ (x = 0, 0.025, 0.05, 0.075) samples. The spin reorientation transition, as previously reported for the parent compound, is shown to occur around the same temperature T_{SR} ~ 4 K. Strontium doping does not appear to change the magnetic transition temperature. The transition of Mn^{2+} ions from paramagnetic into antiferromagnetic arrangement at high temperatures is not visible within the magnetic susceptibility measurements. No evidence of a spin glass component or a ferromagnetic transition is displayed in this series. Further investigation of the series through neutron diffraction measurements would be required to better determine the structural and magnetic

behaviour in the series. It would be interesting to perform physical property measurements on the series to determine the electronic properties upon hole doping with strontium.

References

[1] B. I. Zimmer, W. Jeitschko, J. H. Albering, R. Glaum and M. Reehuis, 1995, *J. Alloy. Compd.* **229**, 238-242.

[2] Y. Kamihara, H. Hiramatsu, M. Hirano, R. Kawamura, H. Yanagi, T. Kamiya and H. Hosono, 2006, *J. Am. Chem. Soc.* **128**, 10012-10013.

[3] Y. Kamihara, T. Watanabe, M. Hirano and H. Hosono, 2008, *J. Am. Chem. Soc*. **130**, 3296-3297.

[4] X. Jin, T. Masubuchi, T. Watanabe, K. Takase and Y. Takano, 2009, *J. Phys.: Conf. Ser.* **150**, 052085.

[5] Q. Zhang, C. M. N. Kumar, W. Tian, K. W. Dennis, A. I. Goldman and D. Vaknin, 2016, *Phys. Rev. B.* **93**, 094413.

[6] N. Emery, E. J. Wildman, J. M. S. Skakle, G. Giriat, R. I. Smith and A. C. Mclaughlin, 2010, *Chem. Commun.* **46**, 6777-6779.

[7] Q. Zhang, W. Tian, S. G. Peterson, K. W. Dennis and D. Vaknin, 2015, *Phys. Rev. B.* **91**, 064418.

[8] Z. A. Ren, J. Yang, W. Lu, W. Yi, G. C. Che, X. L. Dong, L. L. Sun and Z. X. Zhao, 2008, *Mater. Res. Innov*. **12**, 105-106.

[9] Z. A. Ren, W. Lu, J. Yang, W. Yi, X. L. Shen, Z. C. Li, G. C. Che, X. L. Dong, L. L. Sun, F. Zhou and Z. X. Zhao, 2008, *Chin. Phys. Lett.* **25**, 2215.

[10] H. Hosono and S. Matsuishi, 2013, *Curr. Opin. Solid St. M.* **17**, 49-58.

[11] G. Mu, B. Zeng, X. Zhu, F. Han, P. Cheng, B. Shen and H.-H. Wen, 2009, *Phys. Rev.B.* **79**, 104501.

[12] E. J. Wildman, J. M. S. Skakle, N. Emery and A. C. Mclaughlin, 2012, *J. Am. Chem. Soc.* **134**, 8766-8769.

[13] E. J. Wildman, N. Emery and A. C. Mclaughlin, 2014, *Phys. Rev. B.* **90**, 224413.

[14] E. J. Wildman, K. S. McCombie, G. B. G. Stenning and A. C. Mclaughlin, 2018, *Dalton T.* **47**, 14726-14733.

Chapter 7

Conclusions & Further work

Fascinating properties have been observed within LnMnPnO oxypnictides, with lanthanide ion substitution and doping strategy effecting the behaviour observed. NdMnAsO samples with F$^-$ doping are reported to display CMR, whereas Sr^{2+} doped samples display positive MR. In PrMnAsO$_{1-x}$F$_x$ series a sizeable -MR occurs below a structural transition in the material, this change of lattice symmetry is not observed in the other manganese oxyarsenides.

The novel phase Sr$_2$Mn$_{2.23}$Cr$_{0.77}$As$_2$O$_2$ has been synthesized and investigated, this structure is described as a 2322 oxypnictide. The 2322 structure consists of two distinct layers; square-planar oxide layers (M(1)O$_2$) and pnictide tetrahedral layers (M(2)$_2$$Pn_2$) stack along the c axis with alkali earth cations distributed between them. The phase crystallises within the $I4/mmm$ tetragonal space group, with cation order discovered within the two transition metal sites of the structure. Cr^{2+} ions mainly occupy the M(1) positions (68%) and Mn^{2+} ions nearly fully occupying the tetrahedral M(2)$_2$As$_2$ layers (96%). The preference of chromium for the square-planar arrangement is thanks to a combination of CFSE and Jahn-teller distortions, given Cr^{2+} has a d^4 electronic configuration. The actual formula of the sample was Sr$_2$Mn$_{2.23}$Cr$_{0.77}$As$_2$O$_2$, the desired Mn$_2$Cr stoichiometry was not achieved.

Two magnetic transitions occur in Sr$_2$Mn$_{2.23}$Cr$_{0.77}$As$_2$O$_2$ at 410 and 167 K. Below 410 K M(2)$^{2+}$ ions are ordered in a G-type AFM arrangement of spins parallel to the c axis. The lower temperature transition occurs as a result of the M(1)$^{2+}$ ions forming long-range AFM ordering along c lattice direction, simultaneously there is a spin-reorientation of M(2)$^{2+}$ spins into a C-type AFM arrangement still parallel to c lattice. Between 167 K and 135 K both the high temperature (AFM-HT) and low temperature (AFM-LT) antiferromagnetic arrangements occur. At 160 K, 59.8% of the sample is in AFM-HT and 40.3% AFM-LT arrangement. The magnetic phase coexistence occurs as a result of two different nuclear phases, as discovered through synchrotron X-ray diffraction. One phase orders into the AFM-LT configuration at 167 K, while the other orders at

135 K; this difference in magnetic ordering temperature is due to differing chromium content within the phases. In the $Sr_2Cr_3As_2O_2$ sample, two magnetic transitions occur at 590 K and 291 K, associated with the ordering of Cr(2) and Cr(1) ions respectively. $Sr_2Mn_3As_2O_2$ also displays two magnetic transitions but at lower temperatures (340 and 75 K). Of the two nuclear phases present in $Sr_2Mn_{2.23}Cr_{0.77}As_2O_2$, the phase which occupies 40% of the total sample and undergoes the spin reorientation at 167 K is deduced to contain a higher chromium content than the other nuclear phase which orders at 135 K. The magnetic order present within $Sr_2Mn_{2.23}Cr_{0.77}As_2O_2$ is distinct from both the parent compounds; the manganese analogue displays G-type AFM order in the arsenide layers and only 2D ordering of the Mn(1) moments at lower temperature, no spin reorientation occurs. In $Sr_2Cr_3As_2O_2$, the Cr(2) magnetic moments order into a C-type arrangement along c at high temperature, with long-range order of Cr(1) moments occurring at lower temperature (291 K). Spin reorientation does occur in the Cr_3 analogue, but rather than a change of antiferromagnetic ordering type, the direction of spins rotates from the c axis to the ab plane.

Investigation of the novel $CeMnAsO_{1-x}F_x$ series discovered a new insulator to insulator transition within the resistivity measurements when $x \geq 0.035$. The new transition is sensitive to the stoichiometry of the samples, with higher F^- content and small Ce deficiencies increasing the transition temperature and Mn deficiencies destroying the transition. Arsenic nonstoichiometry does not affect the transition. The cell parameters in the series show the expected contraction upon doping until $x = 0.075$, where an unexpected increase is observed. The refined bond length and angles display clear trends with increasing doping level, so the nominal doping is successful. The tetrahedra bond angles within the samples trend towards 'ideal' tetrahedral angles of 109.47° with increasing doping level. A link appears to be present between ideal tetrahedral angle and the insulator to insulator transition temperature in $CeMnAsO_{1-x}F_x$ series, as observed in 1111 iron arsenide superconductors.

The electronic transport within the $CeMnAsO_{1-x}F_x$ series fits to Arrhenius behaviour at high temperatures (~250 K – 100 K) with the transport dominated by thermally activated charge carriers across a band gap. Through doping, the band gap (E_g) value decreases from 0.31 eV for the undoped sample to 0.08 eV for $CeMnAsO_{0.925}F_{0.075}$. Below 85 K there is a transition into Mott 3D VRH behaviour within the electron doped samples, all localisation temperatures are in the order of 10^6 K so that a high degree of disorder exists within the series. A transition into the new insulating

174

phase from the Mott insulating phase occurs in x ≥ 0.035 samples, where a jump to high DC resistivity is observed. The resistivity values increase by four orders of magnitude at the transition before the resistivity becomes immeasurable. The transition is an indicator that conductance is lost in the $CeMnAsO_{1-x}F_x$ series at low temperature, as expected for a many-body localised (MBL) state. AC transport measurements of the $Ce_{0.98}MnAsO_{0.95}F_{0.05}$ sample display glassy behaviour as the peaks shift with increasing frequency. Glassy dynamics are also an indicator of a MBL state.

Variable temperature neutron and synchrotron X-ray diffraction studies revealed the nuclear and magnetic structure trends within the $CeMnAsO_{1-x}F_x$ series. Doping of the CeMnAsO structure does not result in a change of the magnetic structure with Mn^{2+} ions forming C-type AFM arrangement parallel to c at high temperatures (T_{Mn}). The Mn^{2+} ordering undergoes a spin reorientation around 34 K (T_{SR}) so the spins are now parallel to the basal plane. At the spin reorientation temperature, the Ce^{3+} ions also magnetically order in the same way as Mn^{2+}, parallel to the basal plane. The T_{Mn} shows no clear trend with fluorine doping level and is possibly influenced by the As deficiencies in the samples. T_{SR} is unchanged by increasing fluorine content. No change is visible in the magnetic moments of the samples at the temperature of the insulator to insulator transition.

No peak splitting or superstructure peaks are present in the synchrotron X-ray diffraction profiles. The lattice parameters display the usual contraction upon cooling, with a subtle anomaly around 34 K, T_{SR}. Within the Ce(O/F) layers, trends matching those of the lattice parameters are observed, no trends occur in the MnAs layers. There is a clear coupling between the magnetic structure and crystal structure in the $CeMnAsO_{1-x}F_x$ series given the change of a and c lattice constants below T_{SR}. At T_{MBL} there are no observed changes to the structural or magnetic trends and so there is no correlation between the nuclear and magnetic structures and the novel insulator to insulator transition.

Synthesis of 1111 oxyantimonides was attempted, the $NdMnSbO_{1-x}F_x$ series could not be successfully synthesised without impurities. The $CeMnSbO_{1-x}F_x$ samples prepared contained some small impurities, with the impurity content increasing with doping level. No clear trends are present within the results of Rietveld refinement fits to the XRD data. Ce and Sb deficiencies are observed in the series and no further analysis was performed.

Hole doped $Ce_{1-x}Sr_xMnSbO$ (x = 0 – 0.075) samples were prepared, all phases contain small impurities. Rietveld refinement fits to laboratory X-ray diffraction data revealed clear trends in the

cell parameters with strontium content. The a and c lattice parameters are shown to increase with increasing x, which is a strong indicator that the doping was successful given the larger ionic radii of Sr^{2+} ions compared to that of Ce^{3+}. No trends are visible within the bond lengths and angles of the MnSb layers. Some trends are present in the (Ce/Sr)O layers, with bond lengths decreasing with increasing Sr level and the tetrahedral angles trend away from the ideal tetrahedral angle of 109.47°. Magnetic susceptibility measurements of the series reveal the same spin reorientation transition at ~4 K as reported for the parent phase CeMnSbO; strontium doping does not change the transition temperature in the series. The high temperature Mn^{2+} magnetic ordering transition is not visible in the magnetic susceptibility measurements and there is no evidence of a spin glass component or ferromagnetic transition in the series.

Further work within these different systems is clearly warranted to gain a better understanding of the behaviour being exhibited. In the 2322 system, a solid solution series could be investigated to further analyse the changes to magnetic behaviour upon substitution of manganese for chromium. A closer examination of the spin reorientation transition could be performed on $Sr_2Mn_{2.23}Cr_{0.77}As_2O_2$ through powder neutron diffraction measurements at smaller temperature intervals, as performed on the $Sr_2Cr_3As_2O_2$ sample. Variable-pressure neutron diffraction studies would also be of interest to further investigate the superexchange interaction as a function of the unit cell size.

Within the 1111 system, more analysis on the $CeMnAsO_{1-x}F_x$ is warranted to fully examine the origin of the novel insulator-insulator transition. Synthesis of intentionally non-stoichiometric samples for analysis could be performed so the conditions required for the new transition are discovered. We currently believe the new insulator to insulator transition is a sign of a many-body localised state within the series but more measurements are required to further confirm this. Hall measurements and thermal transport measurements could be used to further evidence the MBL transition; Hall measurements can be used to check the carrier content and electron mobility within samples, thermal transport measurements would be interesting to determine whether the transition is observed through different measurement techniques.

The antimonide samples were only prepared in short visits to the laboratories with limited time, so preparing them again with more time to work on improving the purity would be key. After synthesis is successful in the new series the research could move forward into measurement and analysis

using the same techniques explored within the $CeMnAsO_{1-x}F_x$ series. Resistivity measurements of the antimonide samples would be key to identify if any MR or other exotic phenomena are present.

The introduction chapter of this thesis outlines a selection of the vast studies performed into pnictide materials so far, with the discovery of high temperature superconductivity within iron pnictide materials being a huge drive to continue research. Superconductivity is widely regarded as a key discovery with the aim of solving the energy crisis. This thesis project, focused on manganese pnictides, has unearthed new electronic behaviour, which may lead to advancements in the field of quantum computing and quantum memory if many-body localisation is confirmed and a product can be mass-produced. Moreover, this body of work has highlighted further the sensitivity of magnetic and electronic behaviour in manganese pnictide materials to the chemistry of the system.

Chapter 8

Appendix

8.1: Additional results from Chapter 3

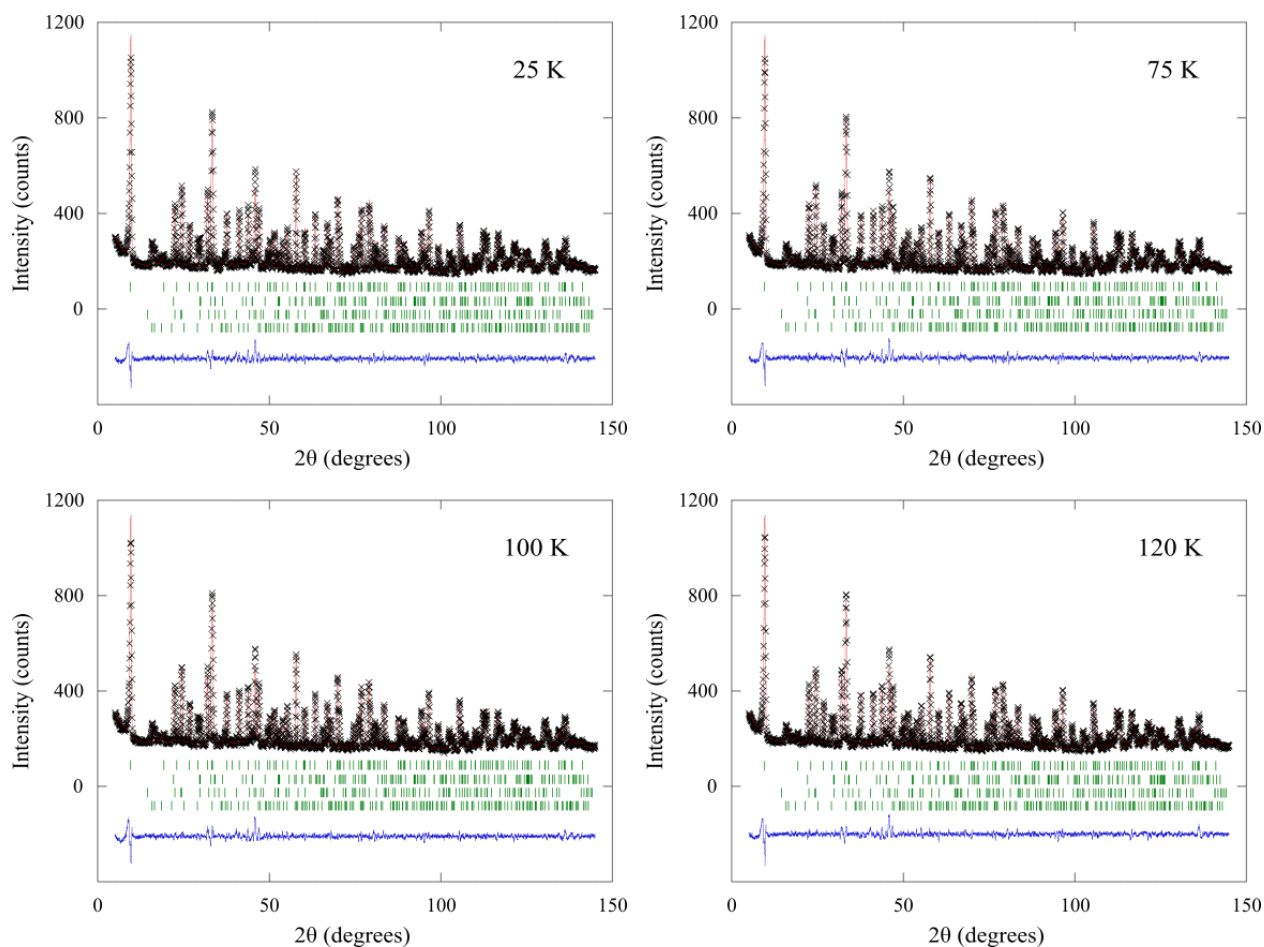*Figure 8.1: Rietveld refinement fits to the I4/mmm structural model of $Sr_2Mn_{2.23}Cr_{0.77}As_2O_2$ recorded on heating from 25 – 120 K. The tick marks represent Bragg reflection positions for $Sr_2Mn_{2.23}Cr_{0.77}As_2O_2$ nuclear phase, $Cr_{0.7}Mn_{0.3}As$ impurity, M(2) k_3 magnetic phase, and M(1) k_2 magnetic phase top to bottom respectively.*
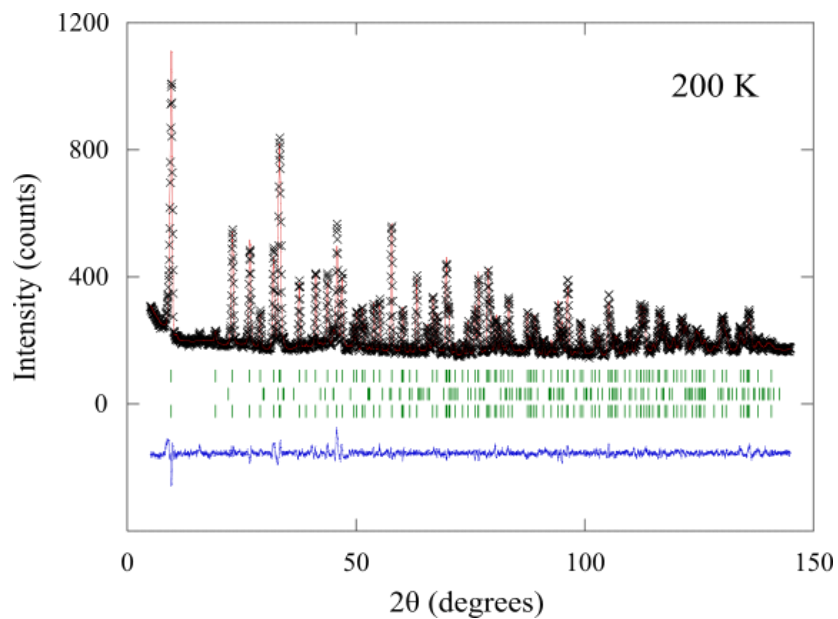
Figure 8.2: Rietveld refinement fit for 200 K data set, fit to the I4/mmm structural model of Sr$_2$Mn$_{2.23}$Cr$_{0.77}$As$_2$O$_2$ recorded on heating. The tick marks represent Bragg reflection positions for Sr$_2$Mn$_{2.23}$Cr$_{0.77}$As$_2$O$_2$ nuclear phase, Cr$_{0.7}$Mn$_{0.3}$As impurity and M(2) k$_1$ magnetic phase top to bottom respectively.

*Table 8.1: Refined cell parameters, agreement factors and atomic parameters for $Sr_2Mn_{2.23}Cr_{0.77}As_2O_2$ from Rietveld fits against D2B neutron diffraction data recorded at various temperatures on cooling. Wyckoff sites for each ions are as follows: Sr and As are at 4e (0, 0, z), Mn(1)/Cr(1) at 2a (0, 0, 0), Mn(2)/Cr(2) at 4d (0, ½, ¼) and O at 4c (0, ½, 0). *Isotropic atomic displacement parameters (B_{iso}) for both M positions were constrained to be the same value.*

	Temperature (K)							
	120	**130**	**140**	**150**	**160**	**170**	**180**	**200**
Sr z	0.41459(9)	0.41445(9)	0.41433(9)	0.41443(9)	0.41440(9)	0.41442(9)	0.41438(9)	0.41439(9)
Sr B_{iso}	0.49(3)	0.49(3)	0.49(3)	0.53(3)	0.52(3)	0.58(3)	0.53(3)	0.46(3)
M B_{iso} *	0.46(5)	0.37(4)	0.47(5)	0.49(5)	0.40(4)	0.54(5)	0.77(5)	0.45(4)
As z	0.16901(8)	0.16923(8)	0.16947(9)	0.16954(8)	0.16958(8)	0.16958(9)	0.16980(9)	0.16981(9)
As B_{iso}	0.45(3)	0.44(3)	0.45(3)	0.48(3)	0.53(3)	0.54(3)	0.62(3)	0.63(3)
O B_{iso}	0.65(3)	0.60(3)	0.51(3)	0.50(3)	0.51(3)	0.45(3)	0.44(3)	0.42(3)
a (Å)	4.08612(11)	4.08641(11)	4.08691(11)	4.08740(11)	4.08765(10)	4.08837(11)	4.08881(11)	4.08945(10)
c (Å)	19.0145(6)	19.066(6)	19.0163(7)	19.0198(6)	19.0230(6)	19.0272(6)	19.0307(6)	19.0370(6)
Unit Cell Volume (Å³)	317.473(28)	317.553(28)	317.623(28)	317.762(27)	317.853(26)	318.034(27)	318.162(27)	318.367(25)
χ^2 (%)	1.95	1.97	2.00	1.88	1.83	1.99	2.04	1.97
R_{WP} (%)	12.0	12.2	12.3	12.1	12.3	12.4	12.7	12.7
R_P (%)	11.9	12.1	12.0	12.0	12.4	12.5	13.1	13.1

Table 8.2: Selected bond length and angle variation with temperature taken from Rietveld refinement fits against D2B neutron diffraction data recorded on cooling between 200 and 120 K.

	Temperature (K)							
	120	130	140	150	160	170	180	200
Sr-As(Å)	3.2977(11)	3.2987(11)	3.3001(12)	3.3021(11)	3.3025(11)	3.3033(12)	3.3054(12)	3.3062(12)
Sr-O (Å)	2.6099(11)	2.6118(11)	2.6134(11)	2.6126(11)	2.6132(11)	2.6135(11)	2.6143(11)	2.6148(11)
Sr-M1 (Å)	3.3145(8)	3.3160(8)	3.3174(8)	3.3170(8)	3.3175(8)	3.3180(8)	3.3188(8)	3.3193(8)
Sr-M2 (Å)	3.7374(14)	3.7356(14)	3.7338(14)	3.7360(14)	3.7360(14)	3.7371(14)	3.7371(14)	3.7383(14)
M1-As (Å)	3.2136(15)	3.2182(15)	3.2227(17)	3.2246(15)	3.2259(15)	3.2266(17)	3.2314(17)	3.2327(17)
M1-O (Å)	2.04306(6)	2.04321(6)	2.04345(6)	2.04370(6)	2.04382(5)	2.04418(5)	2.04440(6)	2.04472(5)
M2-As (Å)	2.5484(9)	2.5561(9)	2.5536(10)	2.5532(9)	2.5530(9)	2.5534(10)	2.5513(10)	2.5517(10)
M2-M2 (Å)	2.88932(6)	2.88953(6)	2.88988(6)	2.89023(6)	2.89040(5)	2.89091(5)	2.89123(6)	2.89168(5)
M2-As-M2 (°)	68.76(3)	68.83(3)	68.92(3)	68.94(3)	68.96(3)	68.95(3)	69.03(3)	69.03(3)
As-M2-As 1 (°)	105.98(3)	106.13(3)	106.30(3)	106.35(3)	106.37(3)	106.37(3)	106.51(3)	106.51(3)
As-M2-As 2 (°)	111.24(6)	111.17(6)	111.08(7)	111.06(6)	111.04(6)	111.05(7)	110.97(7)	110.97(7)

Table 8.3: Refined magnetic moments of three magnetic phases in $Sr_2Mn_{2.23}Cr_{0.77}As_2O_2$ with decreasing temperature, calculated from refinement fits to D2B neutron diffraction data. Magnetic phase agreement factors also presented.

	Temperature (K)							
	120	**130**	**140**	**150**	**160**	**170**	**180**	**200**
Ordered moment (μ_B) Cr k_2	3.25(6)	3.11(7)	2.73(8)	2.66(8)	2.50(9)			
Ordered moment (μ_B) Mn k_1			2.01(3)	2.32(2)	2.41(2)	3.07(2)	3.14(2)	3.07(2)
Ordered moment (μ_B) Mn k_3	2.92(2)	2.85(2)	2.23(2)	1.97(2)	1.85(2)			
R_{Mag} Cr (%)				5.11	6.30	6.72	7.93	7.03
R_{Mag} Mn$_{000}$ (%)	1.43	1.79	3.27	7.02	3.19	4.82		
R_{Mag} Mn$_{100}$ (%)				2.95	6.42	7.94	7.93	7.05
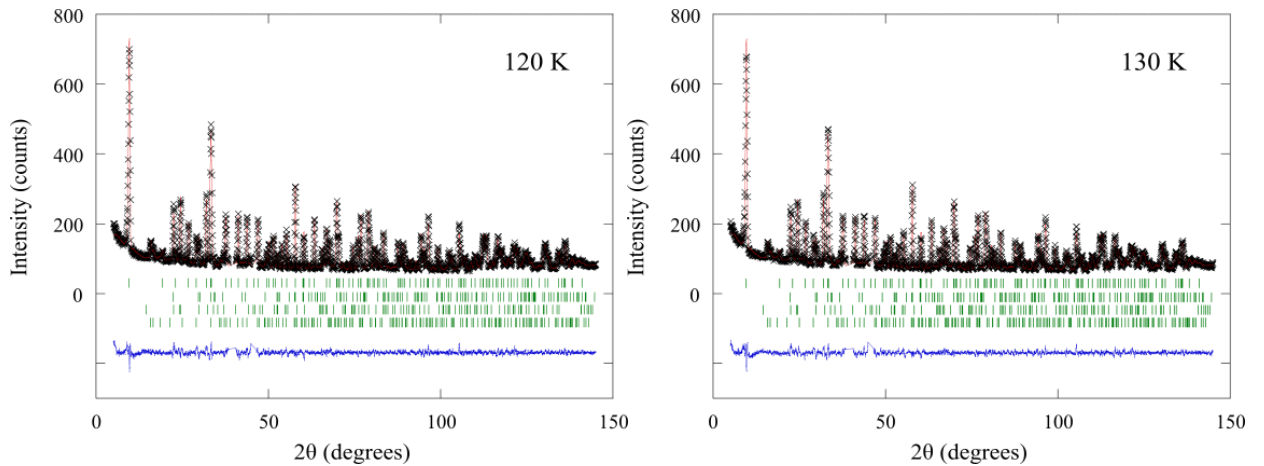
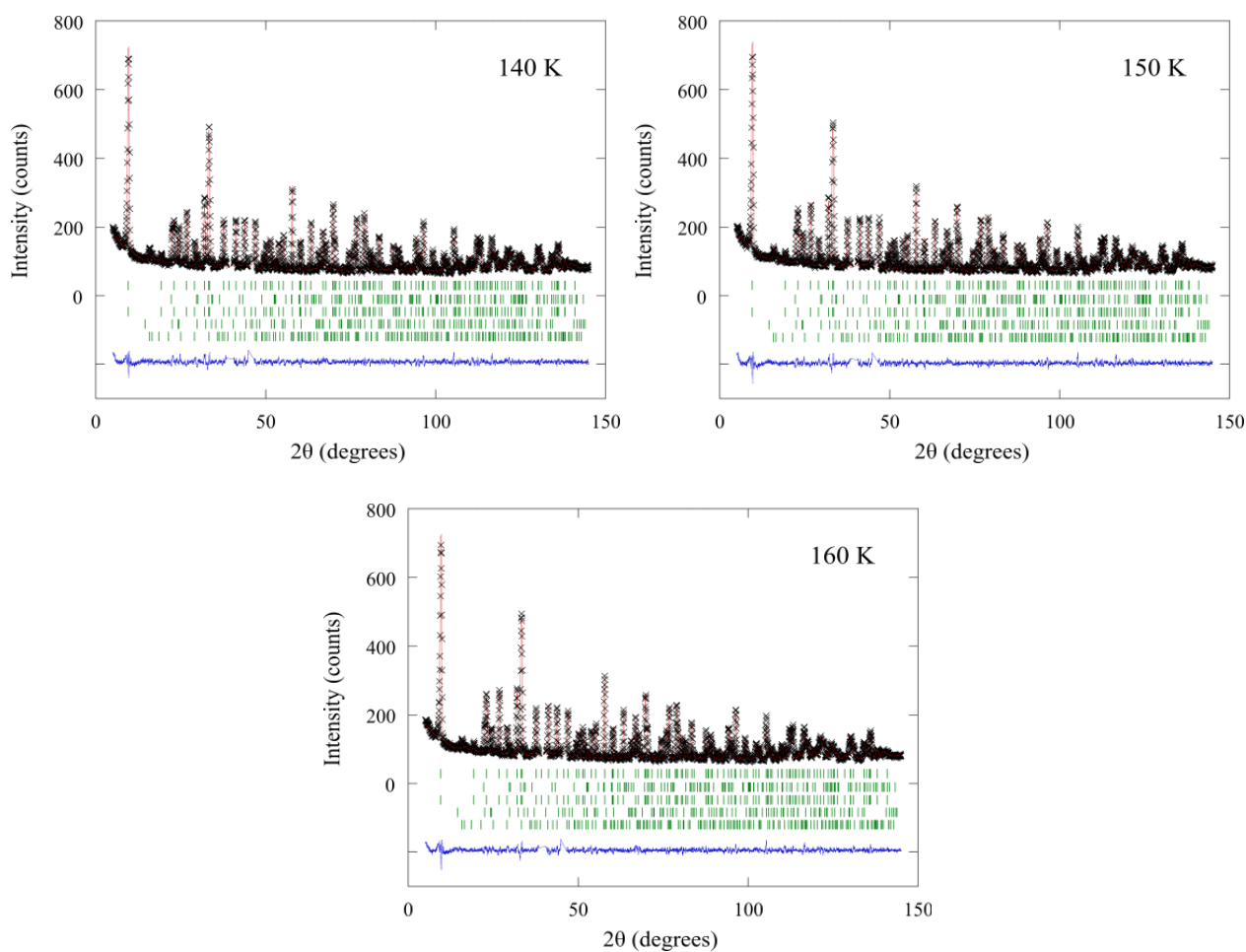
Figure 8.3: Rietveld refinement fits for the 120 and 130 K data sets, fit to the I4/mmm structural model of $Sr_2Mn_{2.23}Cr_{0.77}As_2O_2$ recorded on cooling. The tick marks represent Bragg reflection positions for $Sr_2Mn_{2.23}Cr_{0.77}As_2O_2$ nuclear phase, $Cr_{0.7}Mn_{0.3}As$ impurity, M(2) k_3 magnetic phase, and M(1) k_2 magnetic phase top to bottom respectively. There are visible gaps in the fit between 38.5-40.5° and 45-46.5°, where instrumental peaks have been removed from the model.
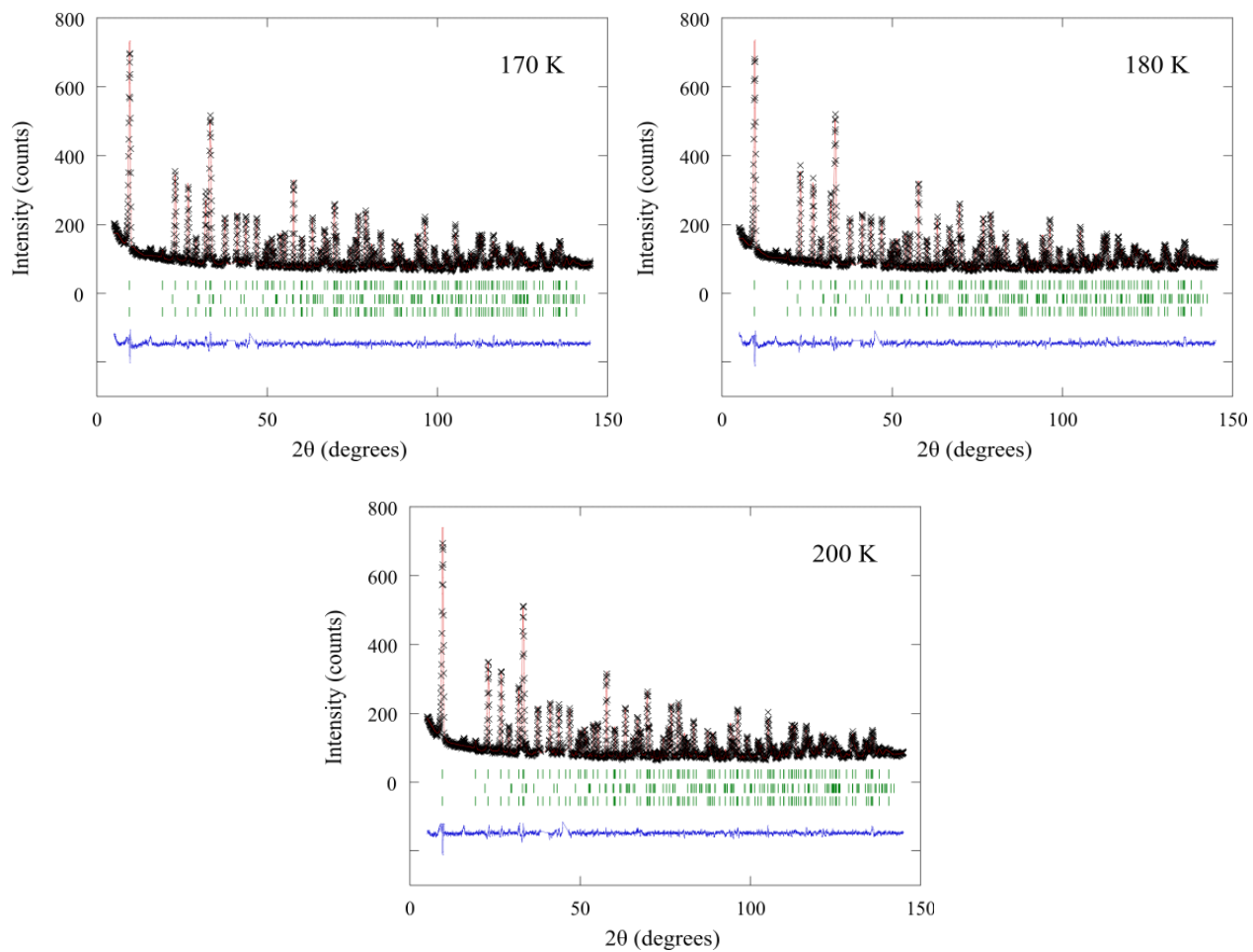
Figure 8.4: Rietveld refinement fits for the 140, 150 and 160 K data sets, fit to the I4/mmm structural model of $Sr_2Mn_{2.23}Cr_{0.77}As_2O_2$ recorded on cooling. The tick marks represent Bragg reflection positions for $Sr_2Mn_{2.23}Cr_{0.77}As_2O_2$ nuclear phase, $Cr_{0.7}Mn_{0.3}As$ impurity, M(2) k_1 magnetic phase, M(2) k_3 magnetic phase, and M(1) k_2 magnetic phase top to bottom respectively. There are visible gaps in the fit between 38.5-40.5° and 45-46.5°, where instrumental peaks have been removed from the model.
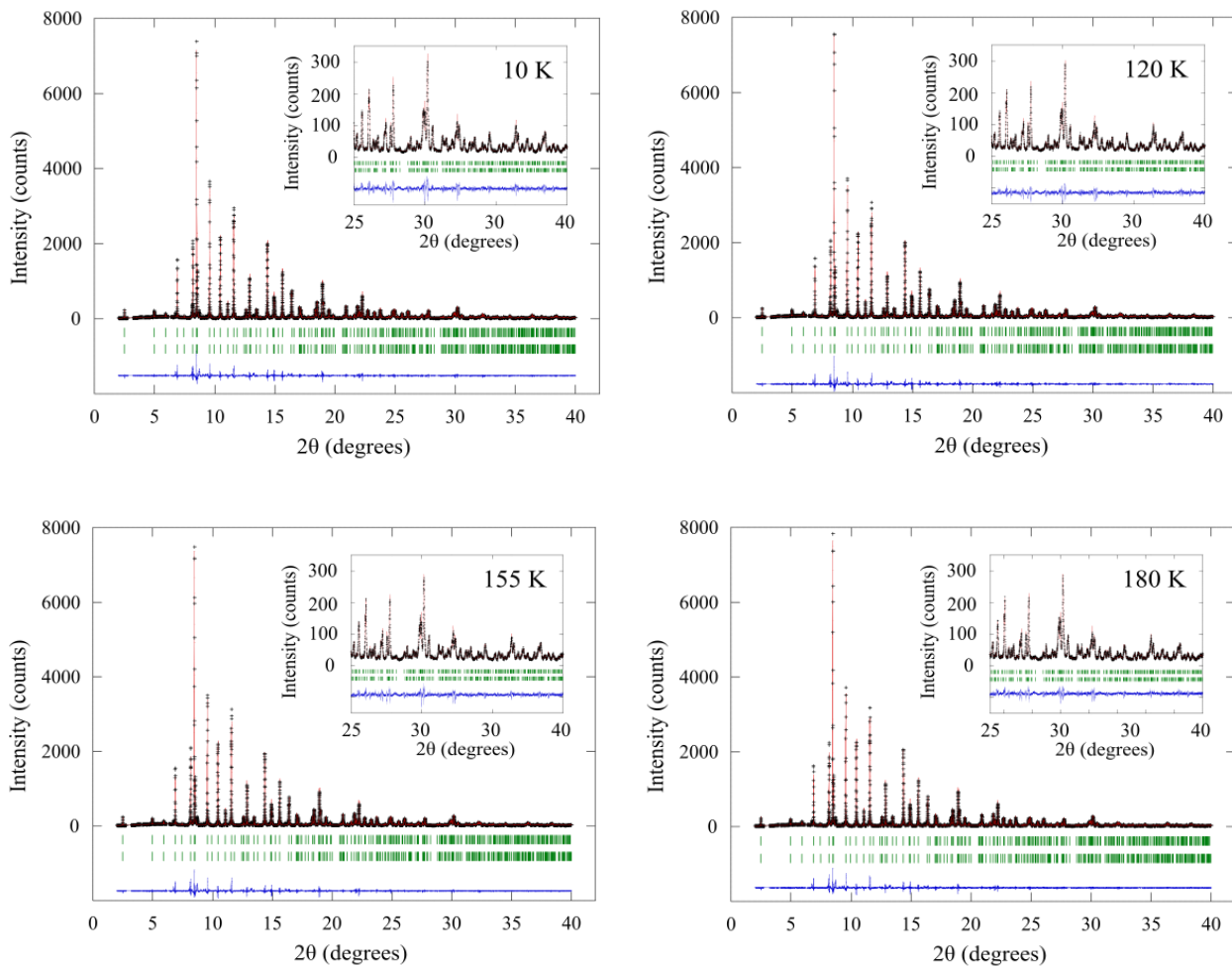
Figure 8.5: Rietveld refinement fits for the 170, 180 and 200 K data sets, fit to the I4/mmm structural model of $Sr_2Mn_{2.23}Cr_{0.77}As_2O_2$ recorded on cooling. The tick marks represent Bragg reflection positions for $Sr_2Mn_{2.23}Cr_{0.77}As_2O_2$ nuclear phase, $Cr_{0.7}Mn_{0.3}As$ impurity and M(2) k_1 magnetic phase top to bottom respectively. There are visible gaps in the fit between 38.5-40.5° and 45-46.5°, where instrumental peaks have been removed from the model.

Figure 8.6: Rietveld refinement fits to the 10, 120, 155 and 180 K synchrotron X-ray diffraction data of $Sr_2Mn_{2.23}Cr_{0.77}As_2O_2$, inset displaying a zoomed portion of the higher angle region of the refinements. Tick marks represent the Bragg reflections for phase 1 and phase 2 top to bottom respectively. There is a visible gap in the fit at low angle, where an instrumental peak has been removed from the model.
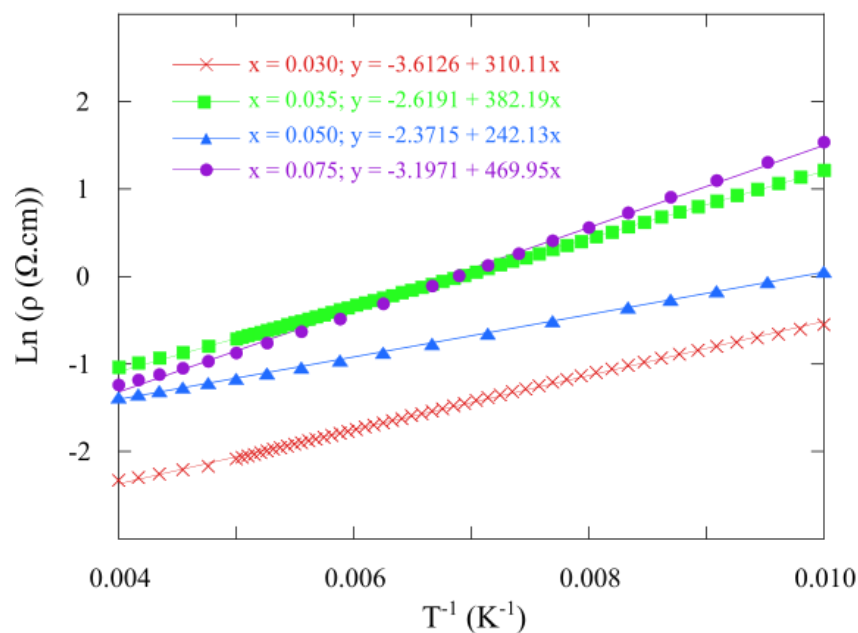
8.2: Additional results from Chapter 4

Figure 8.7: Arrhenius plot of CeMnAsO$_{1-x}$F$_x$ samples from 250 – 100 K, straight line fits displayed for all samples. At lower temperatures the samples undergo a transition from Arrhenius behaviour to Mott three-dimensional variable range hopping.
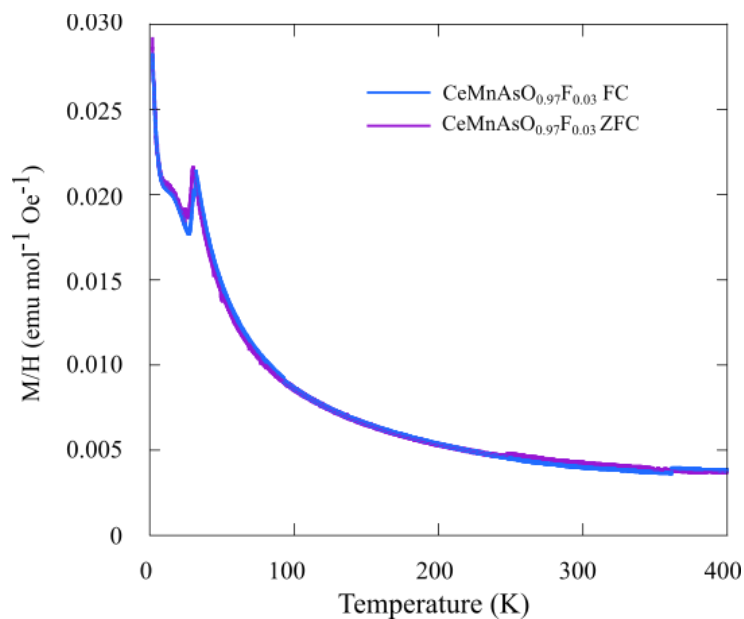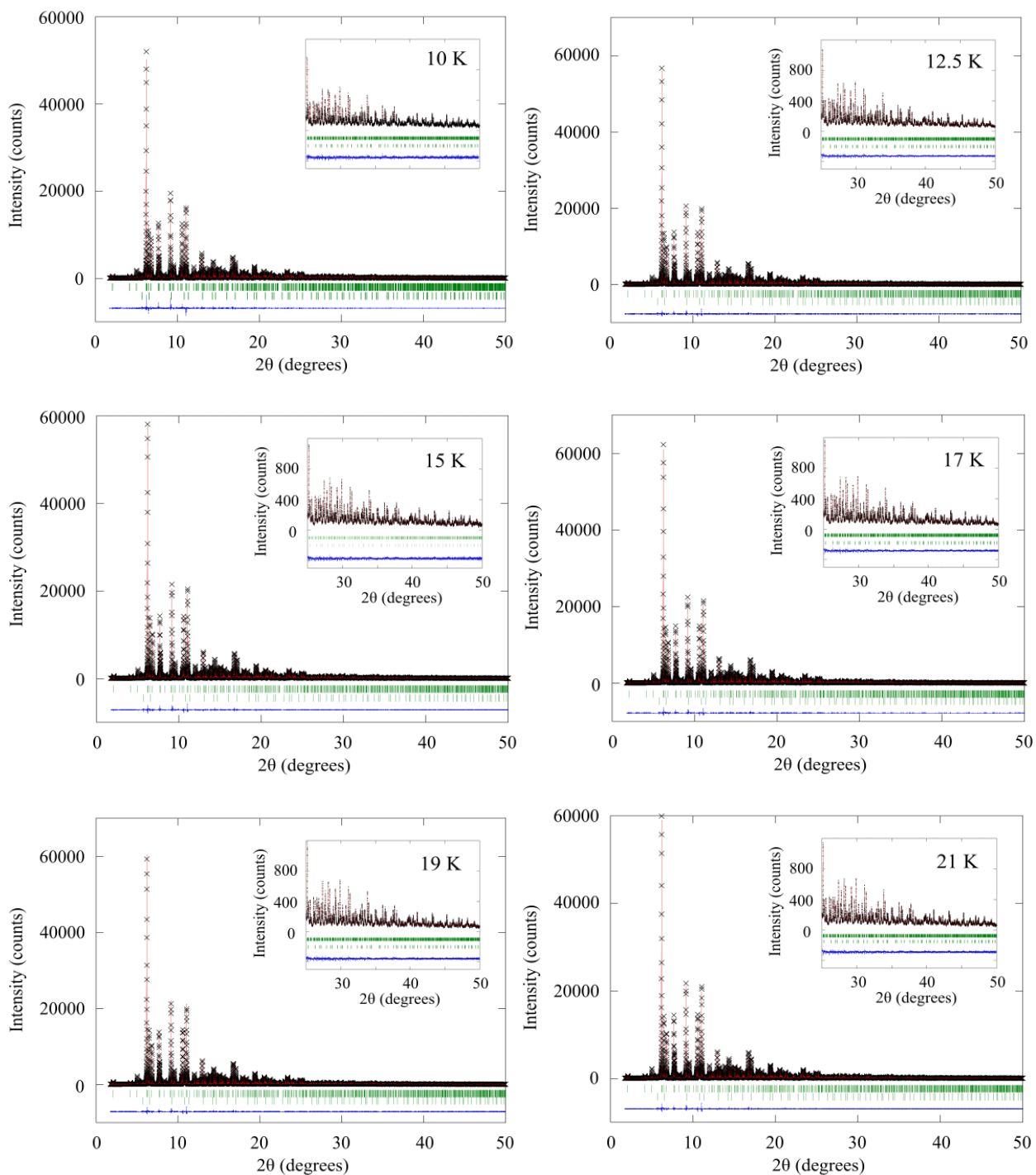

Figure 8.8: Variable temperature magnetic susceptibility plots of CeMnAsO$_{0.97}$F$_{0.03}$ for both ZFC and FC data, no splitting of the data sets is apparent.

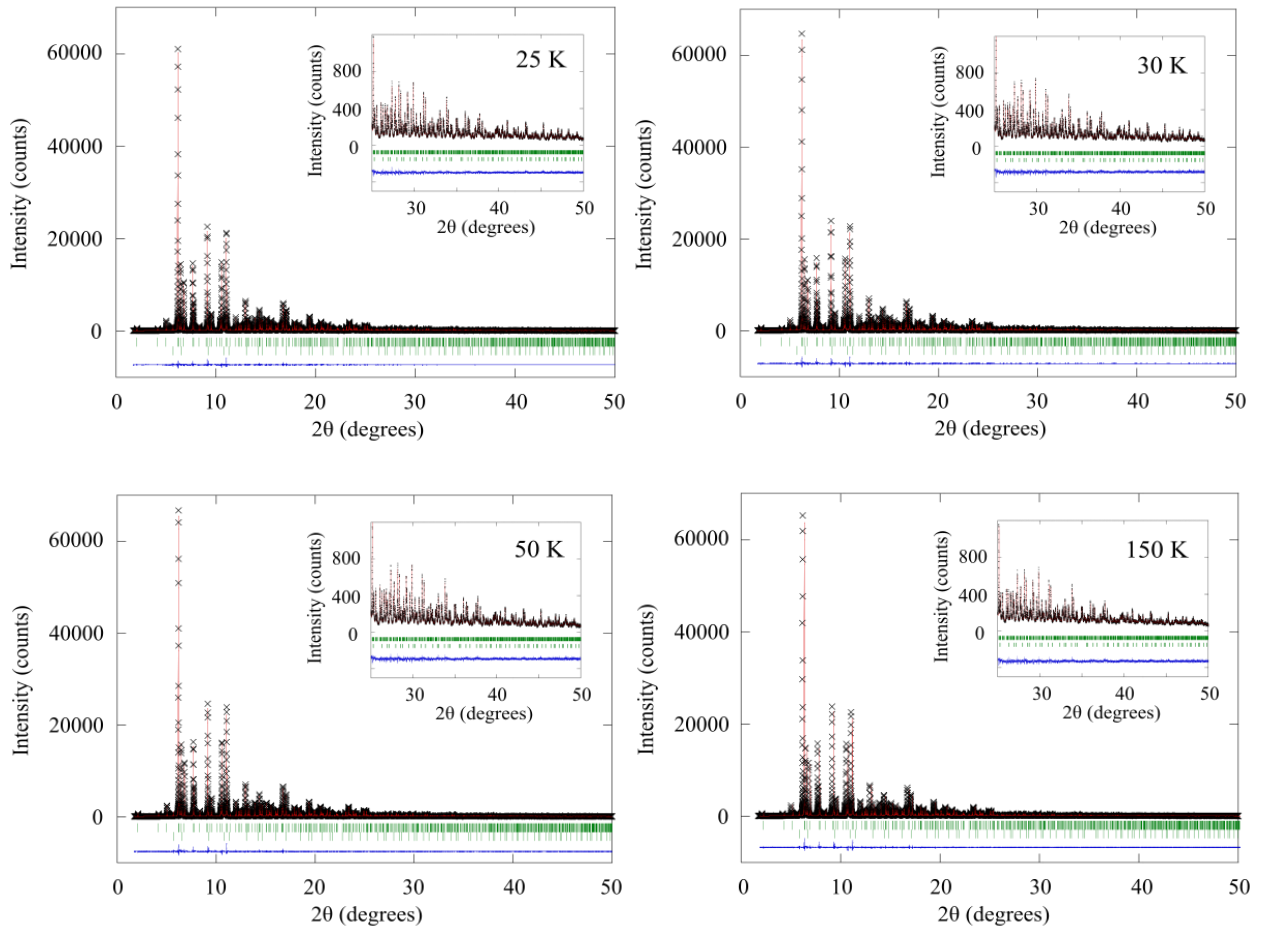## 8.3: Additional results from Chapter 5

Figure 8.9: Rietveld refinement fits to synchrotron X-ray diffraction pattern for CeMnAsO$_{0.95}$F$_{0.05}$ sample from 10 to 150 K. The tick marks displayed represent the nuclear phase and small impurity phase CeOF top and bottom respectively. Inset displays the Rietveld refinements fits to the high angle region of synchrotron X-ray diffraction pattern.
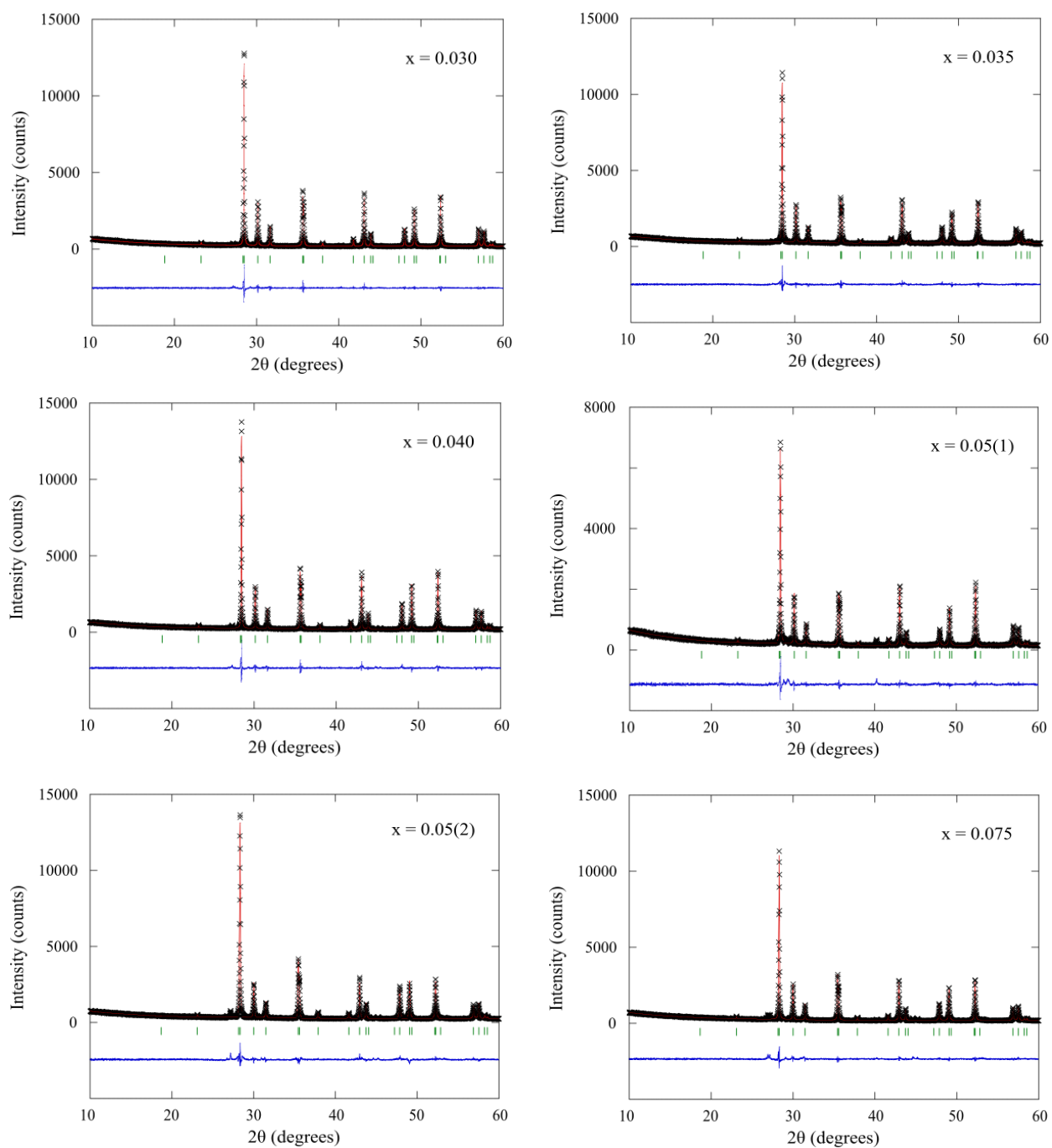
8.4: Additional results from Chapter 6

Figure 8.10: Rietveld refinement fits to the laboratory X-ray diffraction patterns of CeMnSbO$_{1-x}$F$_x$ series (x = 0.030 – 0.075).

Table 8.4: Selected refined cell parameters, agreement factors and atomic parameters for CeMnSbO$_{1-x}$F$_x$ series (x = 0 – 0.075) from Rietveld fits against laboratory X-ray diffraction data recorded at room temperature. Wyckoff sites for each ions are as follows: Ce and Sb are at 2a (¼, ¼, z), Mn at 2b (¾, ¼, ½) and O/F at 2c (0, ½, 0).

	x					
	0.030	**0.035**	**0.040**	**0.05(1)**	**0.05(2)**	**0.075**
a (Å)	4.2108(1)	4.2102(1)	4.2105(1)	4.2102(1)	4.2079(1)	4.2088(1)
c (Å)	9.4994(2)	9.5040(2)	9.5003(2)	9.5018(3)	9.4958(2)	9.4960(2)
Volume (Å^3)	168.42(1)	168.46(1)	168.42(1)	168.42(1)	168.14(1)	168.21(1)
Ce z	0.1187(2)	0.1189(2)	0.1188(2)	0.1193(3)	0.1190(2)	0.1187(3)
Sb z	0.6839(2)	0.6839(2)	0.6841(2)	0.6833(3)	0.6840(2)	0.6838(2)
R$_{WP}$ (%)	7.53	7.99	8.53	8.91	8.59	8.83
R$_P$ (%)	5.85	5.84	6.43	6.34	6.30	6.11
χ^2	2.01	2.45	2.70	2.34	3.34	2.79

Table 8.5: Selected bond lengths and angles for CeMnSbO$_{1-x}$F$_x$ series obtained through Rietveld refinement fits to X-ray diffraction data recorded at room temperature.

| x	**0.030**	**0.035**	**0.040**	**0.05(1)**	**0.05(2)**	**0.075**
Bond length (Å)						
Ce–O/F	2.3882(9)	2.3894(11)	2.3888(10)	2.3907(14)	2.3882(11)	2.3871(12)
Mn–Sb	2.7360(11)	2.7360(12)	2.7369(12)	2.7321(15)	2.7351(13)	2.7342(14)
Ce–Sb	3.5187(16)	3.5178(19)	3.5171(17)	3.5190(24)	3.5144(19)	3.5177(20)
Mn–Mn	2.97746(5)	2.97705(6)	2.97728(5)	2.97708(7)	2.97543(8)	2.97608(6)
Bond angles (°)						
α_1 Ce–O/F–Ce	123.67(8)	123.53(10)	123.60(9)	123.41(13)	123.52(9)	123.67(10)
α_2 Ce–O/F–Ce	102.87(4)	102.93(4)	102.90(4)	102.98(5)	102.94(4)	102.88(4)
α_1 Sb–Mn–Sb	114.07(3)	114.08(3)	114.10(3)	113.97(4)	114.10(4)	114.06(4)
α_2 Sb–Mn–Sb	100.62(6)	100.60(6)	100.57(6)	100.80(8)	100.57(6)	100.64(7)
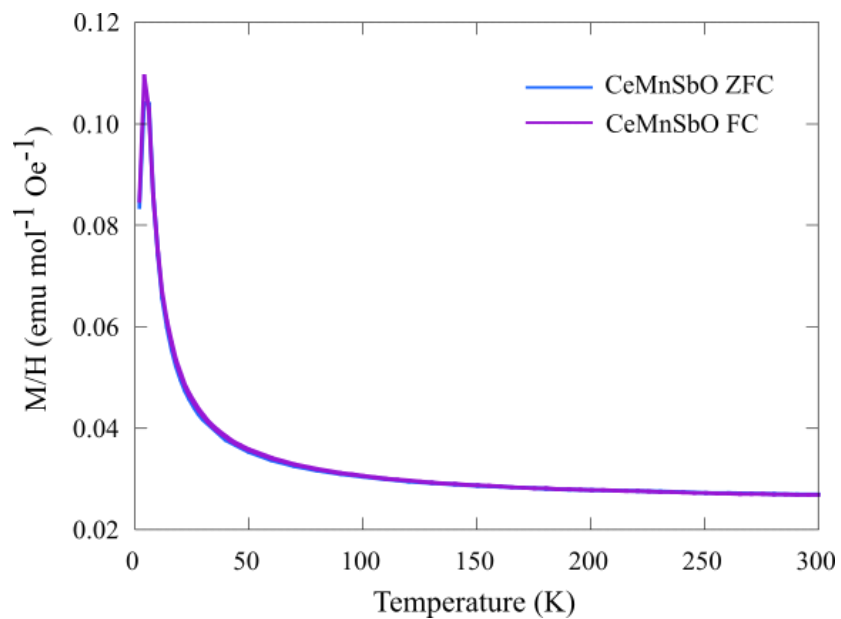
Figure 8.11: Variable temperature magnetic susceptibility plots of parent compound CeMnSbO for both ZFC and FC data, no splitting of the data sets occurs.